Carbon Nanotube Growth on Perovskite Substrates

Jingyu Sun

St Anne's College

A thesis submitted for the degree of

Doctor of Philosophy

Trinity Term 2012

Abstract

This thesis reports on the chemical vapour deposition (CVD) growth of carbon nanostructures (mainly carbon nanotubes (CNTs)) on perovskite oxide surfaces with the aid of various catalysts. Two types of perovskite oxide, single crystal $SrTiO_3$ (001) and polycrystalline $BaSrTiO_3$, have been used as catalyst supports (in metal-catalyst-involved CVD routes) or as catalysts (*via* metal-catalyst-free CVD routes) for the growth of carbon nanostructures.

In metal-catalyst-involved cases, $SrTiO_3$ (001) single crystal has been proven, for the first time, to serve as a substrate for the growth of CNTs. Fe and Ni catalysts can be tailored in a controllable manner on $SrTiO_3$ (001) surfaces prior to the CNT synthesis, forming truncated pyramid shaped nanocrystals with uniform size distributions. The growth of vertically aligned CNT carpets was realised with the aid of Fe on $SrTiO_3$ (001) surfaces, and it was further found that the CNTs grow *via* a base growth model. Furthermore, it is possible to grow helical carbon nanostructures on $BaSrTiO_3$ substrates by introducing a Sn catalyst into the system. The synthesised helical carbon nanostructures follow a tip growth mode, where the structural and chemical aspects of catalyst particles gave rise to a wide range of carbon morphologies.

CNTs were also grown on single crystal $SrTiO_3$ (001) and polycrystalline $BaSrTiO_3$ substrates *via* metal-catalyst-free routes. The surface-roughness-tailored growth of CNTs was surprisingly achieved on a series of engineered $SrTiO_3$ (001) surfaces, where a correlation between the surface roughness/morphology of the substrates and the relevant catalytic activity was revealed. The growth of CNTs arises because the catalyst fabrication methods lead to the formation of $SrTiO_3$ asperities with nanoscale curvatures, over which the CNTs are generated throughout a lift-off process. Facet-selective growth of CNTs was observed on polycrystalline $BaSrTiO_3$ surfaces, where $BaSrTiO_3$ (110) facets lead to the growth of CNTs on them, whereas the (001) facets result in no growth at all. This observation was further analysed in the content of the adsorption and diffusion of carbon species on distinct $BaSrTiO_3$ facets, before reaching the conclusion that the formation of CNTs occurs through a metal-free, stack-up process driven by the assembly of the carbon fragments.

Preface

This work presented in this thesis was carried out by the author under the supervisions of Professor Martin R. Castell and Professor Nicole Grobert. Some of the work reported in this thesis has been presented at several international conferences and in preparation for publications in scientific journals. These include:

Oral presentation:

- The UK Surface Analysis Forum Summer Meeting 2010 - Edinburgh, UK

Poster presentations:

- 'Seeing at the Nanoscale' Conference 2011 - Santa Barbara, USA
- NanoteC10 Conference 2010 - Oxford, UK
- Annual Meeting of the COST Action on Surfaces and Interfaces 2009 - London, UK
- Winter School of the COST Action on Surfaces and Interfaces 2009 - Berlin, Germany.

Publications:

- Surface roughness tailored growth of carbon nanotubes on $SrTiO_3$ (001) surfaces by metal-catalyst-free CVD.
  J. Sun, A.A. Koos, F. Dillon, C. Wu, N. Grobert, and M.R. Castell.
  Journal of the American Chemical Society. In preparation.
- Facet-selective growth of carbon nanotubes on polycrystalline $BaSrTiO_3$ surfaces by metal-catalyst-free CVD.
  J. Sun, A.A. Koos, F. Dillon, C.E. Lekka, Y. Cao, J. Jiang, M.R. Castell, and N. Grobert.
  Chemistry of Materials. In preparation.
- CVD growth of helical carbon nanostructures on $BaSrTiO_3$ substrates with the aid of Sn.
  J. Sun, F. Dillon, A.A. Koos, T.M. Cristea, N. Grobert, and M.R. Castell.
  Carbon. In preparation.

Acknowledgements

This thesis would have never reached its present form without the help and support of many generous people. In what follows, grateful acknowledgement is given to everyone who assisted and inspired me throughout this work.

First and foremost, I would like to thank my supervisors, Professor Martin R. Castell and Professor Nicole Grobert, for their patience, support, encouragement and investment of time over the past few years. I was so fortunate and proud to have them as my supervisors who themselves engage rigorously and earnestly in scientific research and truly care about training their students to become better scientists. During my project, Martin and Nicole were always there to provide valuable advice and instruction when necessary. The fruitful discussions about the details of experimental results and about the directions of future work during the supervisor meetings were always enlightening to me and led to the gradual fulfillment of this project. Furthermore, it was Martin and Nicole who gave me the opportunity to go to different conferences in Germany, Scotland and the United States, thereby allowing me to present my work to an international audience. I would also like to express my great appreciation to my officemate, Dr. Chen Wu, who trained me on STM and always offered helpful suggestions to me on this project. I deeply acknowledge the help and support of Dr. Antal Koos, who trained me in using the CVD apparatus and provided me with tremendous help on TEM characterisation of samples. My sincere gratitude goes to Dr. Frank Dillon, for his generous help and guidance in performing experimental investigations in the Begbroke lab, as well as for proof-reading the whole of this thesis and for his suggestions and corrections to the first two manuscripts of my research papers. I am also thankful to Dr. Jules Gardener and Dr. Matthew Marshall for imparting their knowledge to me and offering their kind help to me during my first two years of DPhil study. I feel very lucky to have had such expertise right at hand. Fatma Dinc and Andrew Searle deserve my gratitude as well, for those inspiring chats about study, entertainment, and Oxford life, as does Teodor-Matei Cristea for those times we spent discussing carbon coil growth, and for his special '$SrTiO_3$' Christmas gift presented to me last winter. It has been an enjoyable experience to work with other colleagues in both the Castell's and Grobert's research groups during my study in Oxford: Dr. Zabeada Aslam, Dr. Olga Shvarova, Dr. Geoffrey Otieno, Adam Shaw, Adrian Murdock, Madhuri Dutta, Sarah Downes, Seyyed Shayan Meysami, Shams ur Rahman, Karl-Sebastian Mandel, and Jodie Melbourne.

I would like to extend my thanks to Professor Yilin Cao at the Henan Normal University, China and Dr. Christina Lekka at the University of Ioannina, Greece, for performing theoretical calculations on my experimental results. I would also like to thank Dr. Kerstin Jurkschat for her considerable help on the TEM-EDX characterisation of my samples in JEOL-JEM 2010, Jun Jiang and Professor Angus

Wilkinson for their valuable time in assisting me with the EBSD measurements, as well as Clive Downing and Hugh Bishop for their generous aid in carrying out XPS. I am greatly indebted to Gabriella Chapman and Dr. Gareth Hughes, who trained me on SEM, as well as to Dr. Colin Johnston, who trained me on Raman spectroscopy. Also, I feel really lucky to have had Chris Spencer around, as he has been extremely helpful to the STM group in taking such excellent care of the JEOL equipments and fixing them in time on many occasions. I am also grateful for the funding from a Chinese Ministry of Education-University of Oxford joint scholarship, which made my life in Oxford much easier.

I would like to express my gratitude to Professor Andrew Briggs for offering me the opportunity of a telephone interview, when I applied to Oxford for a DPhil study in Materials, which has proven to be of great significance for me. I am also deeply indebted for the help and support from the Department of Materials, which has provided an incredibly supportive environment. I would like to thank the administrative staff and the technical support staff: Lyn Richmond, Marion Beckett, Dr. Paul Warren, Dr. Adrian Taylor, Barry Fellows, Richard Cripps, and Ian Sutton. My college, St Anne's College, was a brilliant social environment and its support has enabled me to attend a conference in the United States.

I owe special thanks to John Birkin, a retired teacher from Magdalen College School, Oxford and the current chairman of the Oxford & District Table Tennis Association, for proof-reading my thesis with a view to improving the quality of the writing. I have to express my appreciation to him for introducing me into the Oxford table tennis league, in which I managed to win several team and individual trophies and also had the chance to represent both City and County as No. 1 ranked player in County Championship and inter-town matches over these years. I would also like to thank him for those joyful times we had not only at the table tennis events, but also in the arena of Excel London while watching the Olympic matches. Life in Oxford provided me with opportunities to be part of a vibrant sporting community, extending beyond the borders of academia. I would like to thank all the people with whom I got acquainted through table tennis and football; there are too many to name here, but they know who they are.

My sincere gratitude also goes to Elli Wang who, as a special friend and an important person in my life, has always supported me with all her heart and shared with me every twist and turn during the process of thesis writing-up.

Last but not least, I would like to give my sincere thanks to my beloved family: to my mom, for taking care of me, loving me and always helping me out of difficulties that I encountered during my DPhil study, without a word of complaint; to my dad, for his warm encouragement and unwavering support in my studies as well as in my whole life through the years. Without their support, I would not even have made this thesis into a reality.

List of Acronyms

AFM	Atomic force microscopy
BHF	Buffered hydrofluoric acid
BST	Barium strontium titanate
CMOS	Complementary metal-oxide-semiconductor
CN/MC	Carbon nano/microcoil
CNF	Carbon nanofibre
CNT	Carbon nanotube
CVD	Chemical vapour deposition
DRAM	Dynamic random-access memory
EBSD	Electron backscatter diffraction
ED	Electron diffraction
EDX	Energy-dispersive X-ray spectroscopy
EM	Electron Microscopy
HRTEM	High-resolution transmission electron microscopy
MEMS	Micro-electro-mechanical systems
MF	Metal-catalyst-free
MI	Metal-catalyst-involved
ML	Monolayer
MWNT	Multi-walled nanotube
NP	Nanoparticle
RBM	Radial breathing mode
SEM	Scanning electron microscopy
STM	Scanning tunnelling microscopy
STO	Strontium titanate
SWNT	Single-wall nanotube
TEM	Transmission electron microscopy
UHV	Ultra-high vacuum
VACNT	Vertically-aligned carbon nanotube
XPS	X-ray photoelectron spectroscopy
XRD	X-ray diffraction

Contents

Chapter 1：

Introduction

1.1 Background

Within the past decade, the growth of carbon nanotubes (CNTs) on substrate surfaces has been a topic of extensive interest in both applied technology and fundamental research. CNTs grown on substrates have already found practical applications, for example in the fabrication of novel nanoelectronic devices[1, 2] and in the design of new composite materials with advanced mechanical capabilities.[3, 4] Owing to their unique properties, CNTs also have great potential in the field of bioapplications,[5] Li-batteries,[6, 7] supercapacitors,[9] and energy storages.[10, 11] In research, there are ongoing efforts to investigate and understand the synthesis of CNTs on substrates, which remains vital for CNT science and for industry, and plays a key role in the performance of the resulting materials within various applications.[4] Tremendous progress has been made of late towards synthesising surface-bound[13, 14] carbon nanofilaments, notably in achieving a measure of control over morphological features (wall numbers, defects, chiralities) and in increased knowledge of the growth mechanism and processes.

The synthesis of CNTs cannot be achieved without control over a large array of growth-control parameters, such as temperature, carbon feedstock and growth time. Amongst these, the selection and preparation of the catalyst during the growth of CNTs are of paramount importance, specifically when employing the chemical vapour deposition (CVD) technique. This is due to the fact that the chemical and geometrical aspects of the prepared catalysts dictate the structures and hence the properties of the grown CNTs. To date, the conventional metal-catalyst-involved

routes have been heavily researched, accompanied by a large expansion of the catalyst types developed for CNT growth. For instance, Chiang *et al.*[17] managed to control the single-wall nanotube (SWNT) chiralities by tuning the elemental compositions of Ni/Fe binary catalysts, while Chiu *et al.*[18] coupled the elements of K and Ag to achieve successful synthesis of carbon nanocoils (CNCs). Moreover, new insight into CNT research has also been gained by the metal-catalyst-free route, which proves that CNT growth is possible with no metal catalyst. Examples include the most recent works by Liu *et al.*[19, 20] and Huang *et al.*[21], who demonstrated growth of SWNTs by using SiO_2 nanoparticles. A detailed discussion on the catalysts for CNT growth is presented in Chapter 3.

The role of the catalyst is crucial to the growth of CNTs, especially when the catalyst is supported on a substrate, which affects the size, shape, and activity of the supported catalyst particles. In this thesis, single crystal $SrTiO_3$ (001) and polycrystalline $BaSrTiO_3$ are used as substrates for the growth of CNTs. Interest in the $SrTiO_3$ (001) surface stems from its remarkable ability to support distinct nano-sized metal shapes,[22-27] which in turn would be expected to function as catalysts for the growth of CNTs. Furthermore, the realisation of vertically-aligned CNT growth on doped $SrTiO_3$ substrates (electrically conductive) may herald the beginning of a new age of oxide nanoelectronic devices. As for $BaSrTiO_3$, previous research has indicated that it may be a good candidate for numerous applications, e.g. high-sensitivity sensors and tunable microwave systems, owing to the benefits of its low cost and well-known ferroelectric properties.[29-32] The combination of the CNTs

with BST may create new properties and lead to the fabrication of future MEMS-based devices.[31] Thus, the growth of CNTs on the surface of perovskite oxides ($SrTiO_3$ and $BaSrTiO_3$) presented in this thesis has been studied not only in pursuit of a controlled design for catalysts and a fundamental understanding of the CNT growth mechanisms, but also with the idea of building up novel devices to open up new avenues in nanotechnology.

1.2 Plan of Thesis

This thesis is concerned with the study and understanding of the growth of carbon nanostructures (mainly CNTs) on perovskite oxide surfaces with the aid of CVD techniques. Investigations on utilising $SrTiO_3$ and $BaSrTiO_3$ as catalyst supports, or catalysts, for the growth of carbon nanomaterials are carried out. Based on the focus on the design and fabrication of catalysts, two main threads run through this work: i) the *metal-catalyst-involved* route for growing CNTs on $SrTiO_3$ (001) using Fe and Ni catalysts (Chapter 4) and synthesising CNCs on polycrystalline $BaSrTiO_3$ surfaces with the assistance of Sn (Chapter 7); and ii) the *metal-catalyst-free* route for the growth of CNTs on pure $SrTiO_3$ (001) single crystals and $BaSrTiO_3$ polycrystals (Chapters 5 and 6). An outline of the thesis follows below.

In Chapter 2, a general introduction to the characterisation techniques used to generate the results in this thesis is presented. This is followed by a description of the

instrument and experimental procedures involved in the fabrication of the CNT growth catalysts, as well as the synthesis of CNTs.

A review of the research literature in the field of 'CVD growth of CNTs on substrates' is given in Chapter 3. This contains a background description of the structural features and morphology-property correlation of CNTs, a general introduction of the current methodologies for CNT growth, with a special focus on the 'surface-bound CVD' techniques employed in this thesis, and a detailed review of the growth aspects and formation mechanisms concerning the synthesis of CNTs on substrate surfaces, highlighting the role of catalysts during the CVD processes.

From Chapter 4 onwards, original experimental work performed by the author is presented. The proposed layout of contents for Chapters 4-7 is based on the link-up between these result chapters. Starting from the exploration on the growth of CNTs *via* metal-involved CVD (Chapter 4) is because this investigation accords with the initial aim of the original project proposal. Then it is natural to come up with the idea to investigate the CVD growth of CNTs without the 'tedious' metal-involved routes, since $SrTiO_3$ (001) can present various surface structures with atomic surface roughness, which could be useful to directly grow CNTs on it (Chapter 5). This study is furthered by the investigation in Chapter 6 to see which perovskite facets are the most catalytically active for the growth of CNTs, by using $BaSrTiO_3$ polycrystals. Finally, the investigation of helical carbon growth is included after Sn-residue has been surprisingly found inside the pits of the $BaSrTiO_3$ substrates (Chapter 7).

Chapter 4 is concerned with the growth of CNTs on $SrTiO_3$ (001) substrates *via*

CVD with the aid of Fe and Ni catalysts. Through STM investigation of catalyst design prior to CNT growth and SEM study of the effects of various CVD parameters, the growth conditions are optimised and the synthesis of vertically-aligned CNTs is then realised for the first time. Interesting results are obtained when growing CNTs under unusual conditions (fast-heating, catalyst pretreatment design).

In Chapter 5, different catalyst preparation methods are used in order to investigate the growth of CNTs on $SrTiO_3$ (001) surfaces by metal-catalyst-free CVD. The methods include engineering a series of $SrTiO_3$ substrates to achieve distinct surface structures, preparing particulate $SrTiO_3$ powders and creating scratched $SrTiO_3$ substrates. Using engineered $SrTiO_3$ substrates to grow CNTs, a correlation between the surface roughness/morphology of the substrate and the relevant catalytic activity is revealed. Complementary studies of the growth of CNTs on the $SrTiO_3$ powders and scratched substrates confirm the catalytic capability of $SrTiO_3$ nanoparticulates/nanoasperities. A possible CNT growth mechanism is proposed based on the experimental findings.

Chapter 6 presents the work on the metal-catalyst-free growth of CNTs on polycrystalline $BaSrTiO_3$ surfaces. Facet-selective formation of CNTs on substrate surfaces is observed. Detailed characterisation studies indicate that the orientations and surface roughness of the distinct $BaSrTiO_3$ facets play a critical role in the facet-selective growth behaviour of CNTs. A mechanism of CNT formation is proposed in respect to the assembly of carbon segments.

Chapter 7 focuses on the growth of coiled carbon nanostructures (CNC/CMCs) on $SrTiO_3$ and $BaSrTiO_3$ substrates without/with the aid of Sn, which can be regarded as new catalyst systems for the synthesis of carbon helices. On both scratched $SrTiO_3$ and $BaSrTiO_3$ substrates, observations of grown CNC/CMCs are documented *via* SEM imaging, even though no conventional CNT catalyst are used. With the introduction of Sn into the system, CNC/CMCs can be obtained in much higher yield on the $BaSrTiO_3$ substrate, especially when Fe is used as an additive to Sn.

A summary of the work is presented in Chapter 8, along with concluding remarks. The work contained within this thesis deals with the growth of carbon nanostructures (mainly CNTs) on $SrTiO_3$ and $BaSrTiO_3$ surfaces from an experimental perspective, centering on the selection, design and usage of catalysts, and provides some fundamental understanding of the growth mechanisms of the resulting materials. The usage of perovskite oxides to serve as CNT catalyst supports, or catalysts, is explored. There is scope for future work in investigating the enhanced production of CNTs and their properties *via* the metal-catalyst-involved route, to determine whether they can serve as promising candidates for oxide/CNT-based devices. Moreover, the cases of metal-catalyst-free growth of CNTs on $SrTiO_3$ and $BaSrTiO_3$ substrates might shed further light on the use of perovskite oxides in catalysis.

Chapter 2：

Experimental Techniques

2.1 Background

The growth of carbon nanotubes (CNTs) by chemical vapour deposition (CVD) is a complicated catalytic process. In principle, it involves two main stages: 1) the design and generation of catalysts; 2) the growth of CNTs on these catalysts. In this thesis the CVD process is restricted to the oxide surface-bound[13, 14] type (The CNTs are grown on oxide substrate surfaces with/without metal nanoparticles *via* CVD. The details are given in Chapter 3). The experimental technique is of paramount importance in this particular field, not only because it directly leads to the fabrication-characterisation of obtained carbon nanomaterials, but also because it dictates the structure-property relationship of synthesised CNTs and provide insights into the growth mechanisms to facilitate potential applications.

The catalyst plays a key role throughout the whole synthesis, it deserves thorough characterisation prior to the CVD process. This can be achieved with the aid of specific probes ranging from scanning tunnelling microscopy (STM), atomic force microscopy (AFM), and white light interferometric microscopy (Micro-XAM). Scanning electron microscopy (SEM), transmission electron microscopy (TEM) and Raman spectroscopy are utilised to investigate the final carbonaceous product, whilst energy-dispersive X-ray spectroscopy (EDX) equipped within an SEM or TEM provides elemental constitution/chemical information of given samples.

A broad range of different characterisation techniques are employed in this thesis. These characterisation techniques have been divided into two separate groups: Section 2.2 focuses on depicting ‘main’ techniques which were used to characterise

the materials, whilst Section 2.3 covers 'complementary' techniques in a more succinct way, as these are techniques that were not performed by the author personally. The experimental methodologies and procedures (which are also carried out by the author) are covered in Section 2.4.

2.2 Main Techniques

2.2.1 Scanning Tunnelling Microscopy (STM)

The scientists' long-term aspiration to observe and manipulate surfaces at the atomic level was not fully fulfilled until the invention of STM in 1981.[36, 37] The pioneers, Gerd Binnig and Heinrich Rohrer at the IBM Zürich research laboratory, were subsequently awarded the Nobel Prize in Physics in 1986. To date, STM has been a perfect tool to study surface structures, observe surface dynamics, and monitor catalysis taken place on surfaces.[38, 39] It has been touted to have created a 'revolution in nanoscience and nanotechnology'.[40]

STM is based on the quantum mechanical phenomenon called 'tunnelling'. Normally a perfectly sharpened conductive tip is brought close to the surface to be investigated, a bias applied between the tip and the sample, which gives rise to the tunnelling current, can be described as:

$$I_{tunnel} \propto V\varphi^2 \rho_S \rho_T e^{-Ad\sqrt{\varphi}} \tag{2.1}$$

where I_{tunnel} is the tunnelling current, V is the bias established between the tip and the

sample, φ is the average barrier height (in eV), ρ_S is the density of sample states, ρ_T is the density of tip states, d is the tip-sample separation (in Å), and A is a constant. There is an inverse exponential relationship between the tip-sample separation d and the tunnelling current I_{tunnel} in the expression (2.1), which means that the current density is sensitively affected by the separated distance, which gives rise to the high resolution of the STM. It can also be derived from this relationship that electrons can only tunnel between the atom situated at the tip-apex and atoms on the topmost layer of the sample (as shown by the enlarged view in Figure 2.1) This featured 'surface sensitive' character is the reason why STM is particularly suitable for examining and analysing surfaces.

Figure 2.1 shows the basic instrumentation of an STM. Typically, a metal (tungsten or platinum-iridium alloy) tip is attached to a scanner which is constituted by piezoelectric crystals. The piezoelectric materials expand/contract due to an applied voltage, and the scanner is specifically designated in order to allow independent movement in x, y, and z directions, thus extremely precise control in tip's positions can be achieved. By scanning the surface of the sample, information is gathered with the aid of computer and finally presented in image form.

Equation (2.1) not only reveals that the inverse exponential relationship between tip-sample gap and tunnelling current that leads to the characteristic 'sensitivity' of STM, it also conveys that the tunnelling current is dependent on the local density of states (LDOS) of the tip as well as the sample. Therefore the STM image should not simply be interpreted as a topological map. In fact the STM image needs to be

deemed as a contribution of both textural and electronic information. This means that the regions that appear bright or dark on an STM image might not exactly correspond to a surface protrusion or depression topologically. An example of the STM study of rutile TiO_2 (110) surface[41] substantiates the above statement. The Ti ions at a topologically sunk level on the surface surprisingly appeared as bright rows on the image because the LDOS of un-coordinated Ti ions will 'attract' more electrons to tunnel into themselves under this circumstance.

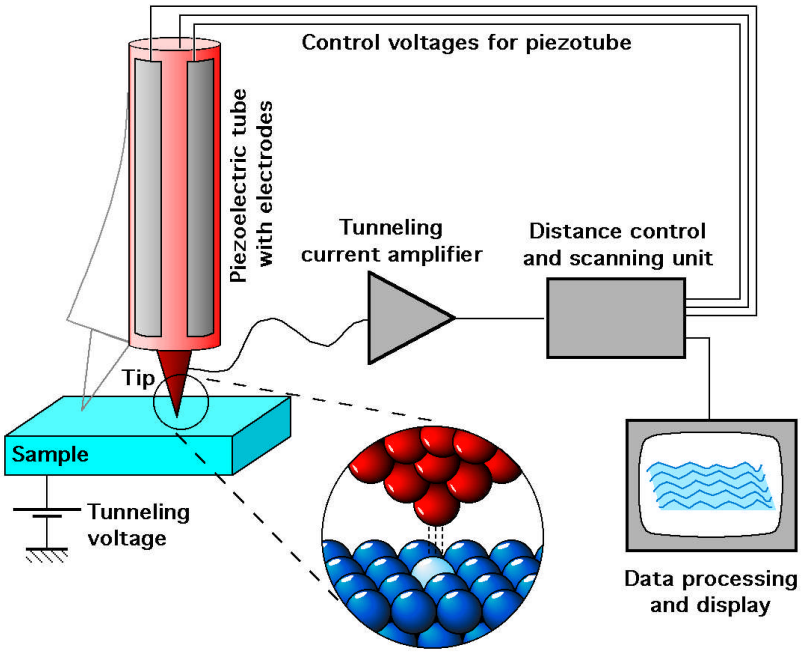

Figure 2.1: A simple sketch of the basic instrumentation of an STM. Image adapted from the TU Wien.

There are two essential modes to be chosen for acquiring a topological STM image. The first mode is called *constant height mode*. This mode is to scan the tip in the *x*-*y* plane over the sample surface without altering in the *z* direction. In this operation the height of the tip is held constant thus the tip-sample separation *d* is varied due to the topology of the surface, creating an image as a tunnelling current map. The other

mode is *constant current mode* which is, by far, the most widely employed method to produce STM images. In this mode the tunnelling current is set by the operator, the height of the tip is adjusted by the feedback loop while scanning in order to maintain the determined current. This leads to variation of tip position in the *z* direction and creates an image as a tip height map. Specifically, the image of the surface employs the voltage applied to the piezoelectric scanner, which changes the *x*, *y*, and *z* parameter, to document a picture of the sample surface. In this thesis the *constant current mode* is used to image surfaces.

2.2.2 Scanning Electron Microscopy (SEM)

An electron microscope (EM) employs a beam of electrons directed at a specimen to get a magnified image of the specimen. SEM is the most widely used type of EM due to its versatility in surface characterisation and practical ease of specimen preparation. It is extremely useful for observing the external morphology of materials and can be used in tandem with other techniques to obtain analytical information on the structural, chemical, and crystallographic properties of samples.[42]

Within an SEM, the electron beam is generated by an electron gun. The most common electron source is the W/LaB_6 filament thermionic emitter, but there is a growing trend toward the use of field emission guns (as within the instrument of the JEOL JSM 840F), as these guns provide higher brightness and better defined electron supplies (narrower energy spread). The benefits engendered from using electrons

instead of light within an EM lie in the following aspects:

(1) An improvement of both resolution and depth of field of the SEM instrument is achieved.

On the Rayleigh criterion the resolving limit r for distinguishing two adjacent points could be interpreted as:

$$r = \frac{0.61\lambda}{\sin\alpha} \tag{2.2}$$

Furthermore, the depth of field of the microscope, h, which is defined as the range along the microscope axis within which the specimen can be moved without blurring the image, is given by:

$$h = \frac{0.61\lambda}{\sin\alpha \tan\alpha} \tag{2.3}$$

where λ is the wavelength, α is the angular aperture of the microscope lens. For a light microscope, α is relatively large, and the wavelength λ of visible light is posited at 400-700 nm, while for an SEM, the electron lenses are so poor that the α is very small thus the approximation $\sin\alpha=\tan\alpha=\alpha$ can be applied. This much reduced value of α gives rise to the greater depth of field in SEM which enables us to build up a clear 3D pattern of specimen topography. However, the resolution of SEM is mainly determined by the electron beam diameter (unlike that of TEM which is determined by the small wavelengths of high-energy electrons), the use of higher beam energy electrons (e.g. 20-25 keV) within an SEM could cause larger beam penetration towards the sample thus more beam damage, leading to poorer resolution.

(2) An enrichment of characterised information in the specimen, e.g. *on chemical composition, crystal orientation, magnetic behavior and electric potentials can be*

obtained.

In comparison with photon radiations, electron radiations can interact more diversely with the specimen surfaces. When an incident beam of electrons hits the surface it can generate many different signals by interacting with the surface atoms. Among these distinct types of signals, are the secondary electrons that are detected for surface topographic imaging. Apart from these originated low-energy electrons, there are backscattered electrons and X-rays *etc.* generated and these can be collected and used to obtain information on the specimen. The backscattered electrons, which consist of high-energy electrons, can be used to overview the sample composition and also help determining the crystallography of the specimen (EBSD). The X-ray emissions can be used for EDX to enable detailed analysis of the chemical make-up of the specimen.

The operation of an SEM commences when an electron beam is initiated from the electron gun. The generated beam (energy ranging 0.5-40 keV) is first demagnified and condensed into a thin, sharp stream of electrons by a series of condenser/objective lenses, and then deflected by magnetic lenses/scanning coils in the *x* and *y* direction to adopt a raster scanning fashion. The incident beam interacts with the specimen and the various types of electrons (SE, BSE, *etc*.) emitted are collected by designated detectors and amplified to provide an electrical signal. Simultaneously, a spot of the cathode ray tube (CRT) is scanned across the display and it is the amplified signal that controls the intensity of the spot. In the SEM, both the electron beam and the CRT spot are scanned in the *raster* pattern; the image is

digitally captured by a computer and regarded as a distribution of the intensities of the electrons emitted from the scanned surface. In this work, a JSM 840F SEM (operates at 5 kV) and a JSM 840A SEM (operates at 10 kV) were used to generate the SEM data.

2.2.3 Raman Spectroscopy

The Nobel Prize in Physics in 1930 was awarded to Indian physicist C.V. Raman, for his discovery of Raman scattering by means of sunlight in 1928. Spurred by this groundbreaking observation, Raman spectroscopy has developed with the progress of technology since and has become an extremely significant spectroscopic tool for the analysis of materials and chemicals.

Raman scattering is an inelastic scattering process, as opposed to the elastic Rayleigh scattering. These different forms of scattering stem from the interaction between the photons in light and the molecular bonds/electron clouds from a molecule, as shown in Figure 2.2. In *Rayleigh scattering* a molecule is excited by a photon and promoted from the ground state to a ‘virtual’ energy state, thereafter it instantly drops back to its ground state and releases a photon, giving rise to scattering. Since the molecule returns to an identical state the scattered light possesses the same wavelength as the incident beam of photons. Raman scattering is a different process because it involves energetic transfers between the photons and molecules during interaction. If the molecule finally drops back to a vibrational state that has higher

energy than ground state then the scattered photon possess less energy (longer wavelength) to keep the whole system energy balanced, this is entitled *Stokes scattering*; If the molecule starts off being raised in a vibrational state and return to its ground state after scattering, then the scattered photon gains energy therefore a shorter wavelength is achieved, this is called *Anti-Stokes scattering*. Operationally, the Raman shift is used for documenting the shifting in energy caused by the vibrational states of the sample. Raman shift is normally expressed in *wavenumbers*, with the typical units of inversed centimeters, which can be interpreted as

$$\Delta\omega\left(cm^{-1}\right)=\left(\frac{1}{\lambda_0\left(nm\right)}-\frac{1}{\lambda_R\left(nm\right)}\right)\times 10^7\,\frac{\left(nm\right)}{\left(cm\right)} \tag{2.4}$$

where $\Delta\omega$ is the Raman shift, λ_0 is the excitation wavelength, λ_R is the Raman spectrum wavelength.

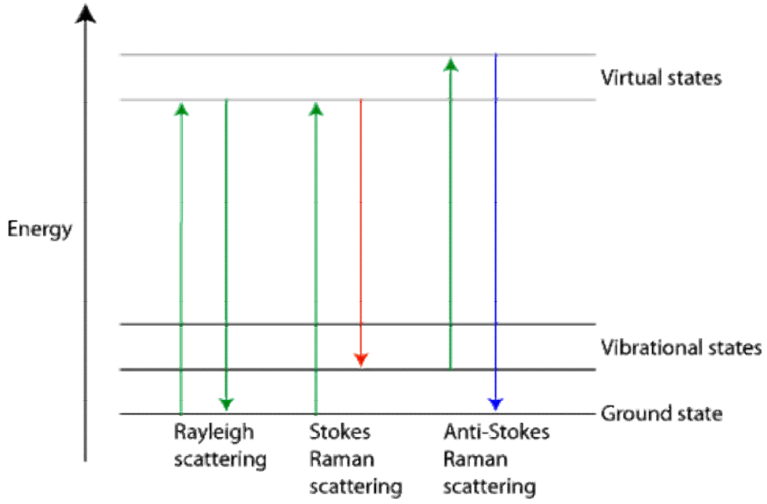

Figure 2.2: A graph showing three forms of visual light scattering. Image adapted from the University of Cambridge.

Raman spectroscopy offers a surface-sensitive technique for studying a wide range of materials and identifying specific molecules. In particular, it is well established

that the quality and intrinsic structure of CNTs can be assessed by Raman spectroscopy.[43] CNT samples possess several peaks at specific frequency positions in Raman spectra (using visible light excitation). Typical Raman spectra of CNTs contain four characteristic Raman bands that are resonance enhanced. The bands are the G-band, the D-band, the 2D (G')-band, and the radial breathing mode (RBM).

The G-band near 1590 cm^{-1} is related to the vibration of sp^2-bonded carbon atoms in a 2D hexagonal lattice, indicating the existence of the graphitic structures. The D-band at around 1310 cm^{-1} is associated with the presence of amorphous carbon and disordered graphite. The 2D/(G')-band near 2700 cm^{-1} indicates the presence of large crystallinity in the sample. The RBMs at low wavenumbers are strong evidence for the presence of SWNTs. Furthermore, the diameter of the SWNTs can be predicted with the aid of ω_{RBM}. More evidence for SWNTs contained in carbon species relies on the fact that a sharp split of G-band into two components (G– and G+) occurs, which is attributed to the curvature effect when the tube diameter is sufficiently small.[44] Therefore, by compiling and analysing the Raman spectral data, decisive information on size, quality and symmetry of CNTs can be attained.[45] In this work, the grown samples were inspected by a Raman spectroscopy (JY Horiba Labram Aramis imaging confocal Raman microscope with a 532 nm frequency doubled Nd:YAG laser).

2.2.4 White Light Interferometric Microscopy (Micro-XAM)

Interference is defined as the change of beam intensity occurring at the moment that two waves of light beam are superpositioned. The use of white light interference leads to the development of white light interferometric microscopy. White light interferometric microscopy has already been employed as a novel tool for characterising and measuring roughness, step heights, and special features of the sample surfaces.[46] The principle of operation involves the splitting a beam of white light into two beams with the aid of upper beam splitter, as shown in Figure 2.3. One beam is directed towards the target sample surface whilst the other beam is brought to reach an internal reference surface/mirror. The lower beam splitter equipped within the objective lenses recombines the light beams reflected from both the sample and reference surfaces, and the interference patterns of bright and dark fringes can be detected and imaged by the CCD sensor. This static fringe map essentially shows the ‘protrusion and depression’ of the sample. By vertically adjusting the objective lenses the distance between the sample and the lower beam splitter varies and dynamic interference fringe images can be created. Once the maximum constructive interference is established, a 3D topography of the sample surface is created and is ready to be imaged.

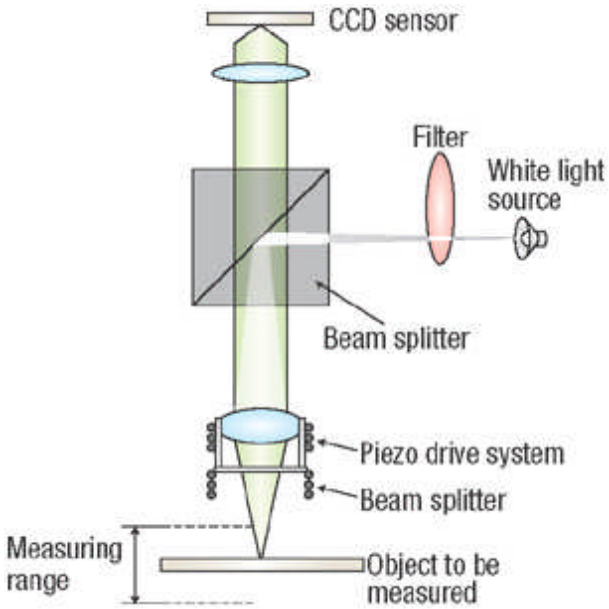

Figure 2.3: A schematic diagram of typical instrumentation of a white light interferometric microscopy.[46]

Conventionally, Atomic force microscopy (AFM) might be the most competent measurement approach for obtaining the *z*-direction information (height, roughness, *etc.*) of provided surfaces out of UHV. However, lengthy setting-up times and sample imaging times, along with the fact that the lateral range of inspection is always limited to an area of several μm^2, limit the use of AFM. Compared to the AFM, white light interferometric microscopy has several advantages including fast measurement speed, facile access of manipulation, long term reproducibility and stability. This truly non-destructive technique is also able to achieve high vertical resolution and good lateral resolution when characterising complex sample surfaces.

Micro-XAM data shown in this thesis were generated on an Omniscan Micro-XAM 5000B 3D interferometric spectroscopy at Begbroke within the Department of Materials, University of Oxford. This instrument can measure field of

view from 84 μm × 63 μm to 8.0 mm × 10.0 mm (depending on the objective lenses employed), and can also quickly and accurately achieve a 3D topographic map of the surface at the nm scale (the capacity of vertical resolution can be better than 0.1 nm) with a sensitive *z*-parameter scan range of up to 10 mm. Experimental data were processed using the provided SPIP^{TM} software, where the advanced data analysis, batch processing, surface roughness (line/area) measurement *etc.* can be realised.[47]

2.2.5 Chemical Vapour Deposition (CVD)

Chemical vapour deposition (CVD) is a chemical process where solid materials are deposited onto substrates from volatile precursors at high temperatures. Generally, CVD process can be employed in different forms, the most frequently used CVD techniques include: atmospheric-pressure thermal CVD, low-pressure thermal CVD, plasma enhanced CVD, and aerosol assisted CVD.

The CVD technique has played a significant role in the nanotechnology boom of the past 20 years where it has been used to synthesise novel materials with fascinating morphologies and tantalising properties. The products fabricated cover a huge range of types, from elements (metals, semiconductors) to compounds (oxides, carbides, nitrides), which can also display in various forms (single crystalline, polycrystalline, amorphous, *etc.*). Specifically, carbon nanotubes (CNT) grown by CVD approach have attracted great interest. It is well known that CNT can be synthesised by a wide range of methods such as arc-discharge, laser ablation, and

CVD. CVD is used due to its low cost, high yield, and ease of scale-up.[48, 49] Moreover, CVD is a versatile approach for CNT synthesis in the sense that it enables precise control of positioning of grown CNTs on patterned substrates and offers control over growth parameters.

The growth of CNTs by CVD technique relies on the catalytic decomposition of carbonaceous precursors and the formation of tubular architectures on catalysts at elevated temperatures (typically 600-950˚C). The catalysts are normally transition metals (or their alloys) and oxides, in the form of substrate supported nanoparticles or thin films. In this thesis the carbon nanostructures were grown by means of CVD process. More detailed information on CVD technique is presented in Section 3.2 of Chapter 3.

2.3 Complementary Techniques

2.3.1 Transmission Electron Microscopy (TEM)

TEM is capable of providing images of given specimens at an extremely high resolution, seeing objects in the order of several angstroms (Å) due to the small *de Broglie* wavelength of electrons (around 2.75 pm at 200 keV). TEM can explore the internal structure of specimens, revealing the details at the nanostructural level, while an SEM can always only illustrate an object's external appearance.

In TEM, a beam of electrons with significantly high energy is transmitted through

a specimen, interacting with the specimen as it passes through. It is those electrons which transmitted through the specimen that form an image. A TEM is composed of an electron gun, a condenser system, a specimen stage, an objective lenses system, the magnification system, the chemical analysis system, and data recording devices.

There is an array of operating modes in the TEM, which the contrast formation depends greatly upon. For instance, in the bright field imaging mode, the formation mechanism of contrast is due to the directly absorption of electrons in the sample, therefore, thicker regions of the sample will appear dark, whilst regions with no sample in the beam path will appear bright. Another basic mode is the dark-field imaging mode, where the images are generated due to the usage of scattered electrons (diffraction contrast). Nowadays the diffraction contrast is a dominant mechanism for imaging dislocations and defects in the samples. Moreover, the phase contrast imaging mode is an advanced operation mode that is based on the variation of phase of electron waves, which is induced by the interaction with sample. In the TEM, phase contrast imaging enables the observation of individual atoms, leading to the high resolution (HR) imaging techniques (HRTEM).

In general, TEM samples need to be sufficiently thin (< 100 nm) to allow electrons to be transmitted through them. To meet this requirement, numerous sample preparation methodologies have been created, the degree of handling difficulty varies from being nearly trivial, such as ultrasonicated dispersion, to procedures involving complex steps, such as focused ion beam milling, mechanical polishing *etc.*.

2.3.2 Energy-Dispersive X-Ray Spectroscopy (EDX)

In this work, EDX has been employed as a probe of chemical information, due to its operational ease and extensive availability within both SEMs and TEMs. This enables EMs equipped with EDX to perform elemental identification especially at local areas/morphologies of interests.

Spectroscopy of the inner shell electrons provides information regarding the elemental constitution of the sample, as the inner electrons are hardly influenced by chemical bonds between atoms. In EDX, a high-energy beam of primary electrons or X-rays (external stimulation) is focused to hit the sample being examined. The incident beam penetrates to excite an electron in an inner shell, releasing it from the shell thus creating a hole. An electron possessing higher energy from an outer shell 'drops' and fills the hole, during this process X-rays are generated with an energy that corresponds to the difference between the higher energy shell and the lower energy shell. The stated principle of EDX is graphically shown in Figure 2.4. Since the energies of the emitted X-rays are characteristic of the atomic structure of the element, EDX is suitable to measure the elemental composition of the sample.

EDX systems are commonly equipped within SEMs and TEMs, where the fine-focused electron beam is used to eject the inner shell electrons. Typically a detector within the EMs is used for converting the energy of the emitted X-rays into voltage symbols (keV), software such as Oxford INCA installed at computer monitors could be functioned as data collector, analyser, and processor.

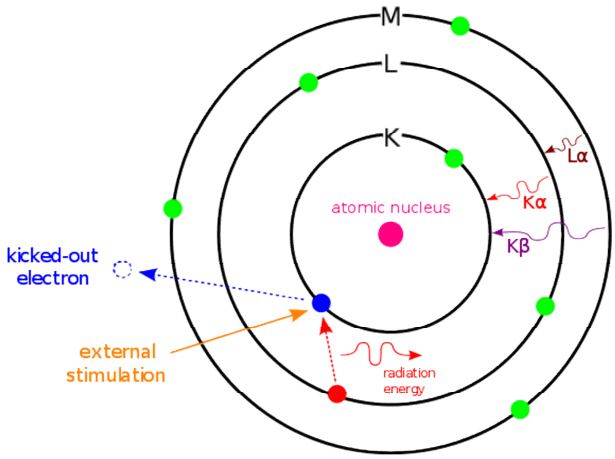

Figure 2.4: A schematic diagram showing the principle of Energy-Dispersive X-Ray Spectroscopy.

2.3.3 Electron Backscatter Diffraction (EBSD)

By making use of backscattered electrons, as mentioned in the above sub-section 2.2.2, the crystal structures of a polycrystalline material can be well elucidated. It is the backscattered electrons generated by incident beam could exit the sample surface in the special fashion that the Bragg diffraction condition is adopted. EBSD has therefore been devised in this sense and becomes a reliable and suitable technique nowadays for identifying the crystallographic orientations and examining the crystalline structures in solid materials.

In general, EBSD is performed by virtue of an SEM equipped with an EBSD detector, which mainly consists of a transmission phosphor screen and a sensitive video camera. In order to conduct an EBSD measurement, the specimen, prior to placement into the SEM chamber, needs to be mechanical/chemical polished to form a flat surface free of damage. This is because, as the electron backscattered patterns

are normally created at relatively shallow depths (~1 μm) within the materials, the crystal lattices close to the surface of specimens need to be clearly presented. The prepared specimen is then mounted inside the SEM and tilted to an angle of ~70˚ relative to normal incidence of the electron beam, and the diffraction pattern named Kikuchi bands are formed on the phosphor screen. It is these Kikuchi bands that can be processed and analysed in the connected PC to generate information on the crystal structures and orientations of the specimen being examined.

2.3.4 Atomic Force Microscopy (AFM)

Following the invention of the STM, there has been a revolution in the field of scanning probe microscopies (SPMs). AFM, has swiftly found widespread uses since its invention in 1986,[50] and is now a ubiquitous tool for observing, imaging and manipulating surfaces at the nanoscale.

The AFM utilises a sharp probe which is mounted on a Si or SiN cantilever to scan and image the sample surfaces. In a typical AFM measurement the probe is placed close enough above the specimen that forces between the atoms of the probe and those of the specimen surface give rise to a deflection of the cantilever. When the specimen is scanned, the cantilever will move up and down in accordance with the surface topography in order to maintain the constant force between the tip and sample. This vertical movement of the tip can be accurately measured by using a laser beam reflected from the cantilever. Moreover, as in the STM, piezoelectric

crystals facilitate the sensitive and precise scan in all the *x*, *y* and *z* directions. The vertical resolution is less than 0.1 nm and hence the atomic imaging of surface structures of the specimen is possible.

The AFM provides clear atomic 3D surface profiling and the measurement can be carried out under ambient conditions (no vacuum is required). However, compared to other techniques such as Micro-XAM and SEM, AFM has a limited scan size (typically up to 10~20 μm in height and 100 μm × 100 μm scanning area limit), a slow scan speed and laborious sample preparation is required.

2.4 Methods and Procedures

2.4.1 The Equipments

In this thesis the UHV-STM system, JSTM-4500XT[51-54] in the Department of Materials at Parks Road was designated to carry out experiments to fabricate and characterise of $SrTiO_3$ catalyst substrates for CNT growth, whereas the aerosol-assisted, atmospheric CVD apparatus in the Department of Materials at the Begbroke Science Park was used for the *ex situ* growth of CNTs on the prepared substrates by means of CVD approach.

2.4.1.1 UHV-STM System

Figure 2.5 shows a general view of the JSTM-4500XT. This JEOL system maintains and operates at pressure of 10^{-8} Pa with the aid of ion pumps as well as titanium sublimation pumps (TSP) when required. It consists of two UHV chambers: a treatment chamber and an STM chamber. The treatment chamber is built up for treating samples (*i.e.* degassing, sputtering, annealing), and can also function as a platform for storing the tips and samples. A loadlock is connected with the treatment chamber and used for tip/sample introduction, which can be opened and pumped down using a turbo molecular pump (TMP) to a pressure around 10^{-6} Pa. The STM chamber contains the STM head for detailed STM imaging, an e-beam evaporator for metal deposition and a K-cell evaporator for organic molecular deposition.

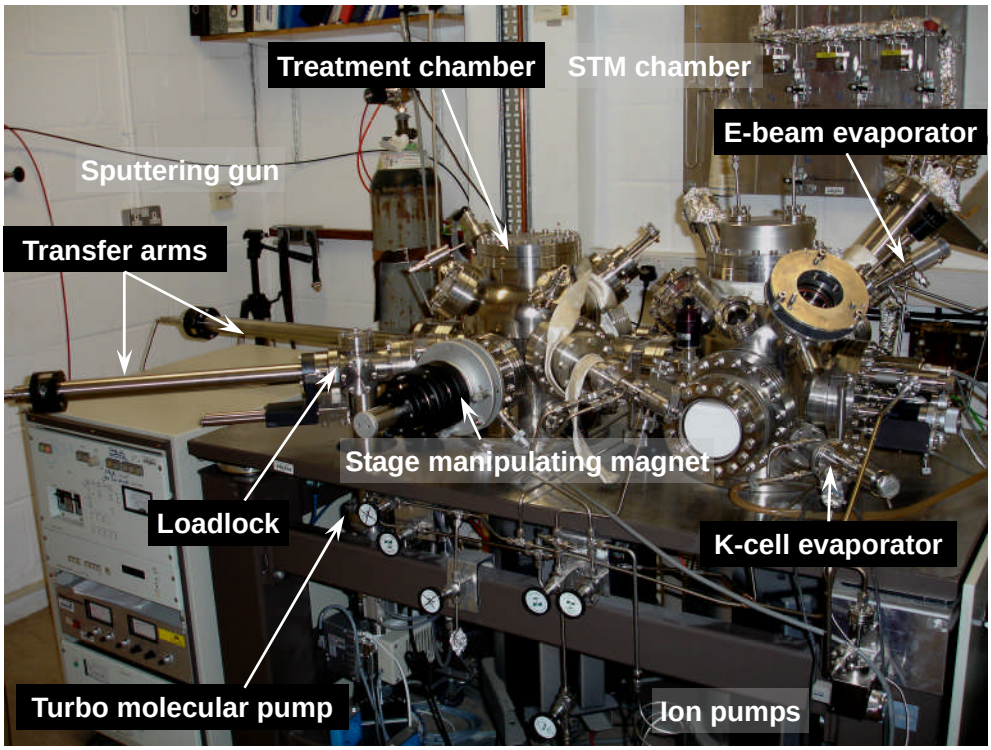

Figure 2.5: Photograph of the JEOL JSTM-4500 XT microscope. A list of key components is labelled on the UHV chambers.

2.4.1.2 Atmospheric CVD Apparatus

The lab designed CVD apparatus[55] consists of a 50 cm long horizontal electrical furnace, a quartz tube (2.2 cm inner diameter) which is typically inserted into the furnace, and a gas exhaustion trap filled with acetone. It should be noted here that the use of acetone at the current set-up has potential danger, in particular when the system functions at high temperatures, since acetone is highly flammable. A diaphragm pump could be used instead for future work. The whole system is equipped with a gas flow controller for governing the used type and flow rate of carrier/feedstock gases. A piezo-driven aerosol generator (RBI Pyrosol 7901) can be incorporated into the system to allow the use of liquid carbon feedstock (such as ethanol) for CNT growth. A picture of the apparatus is shown in Figure 2.6.

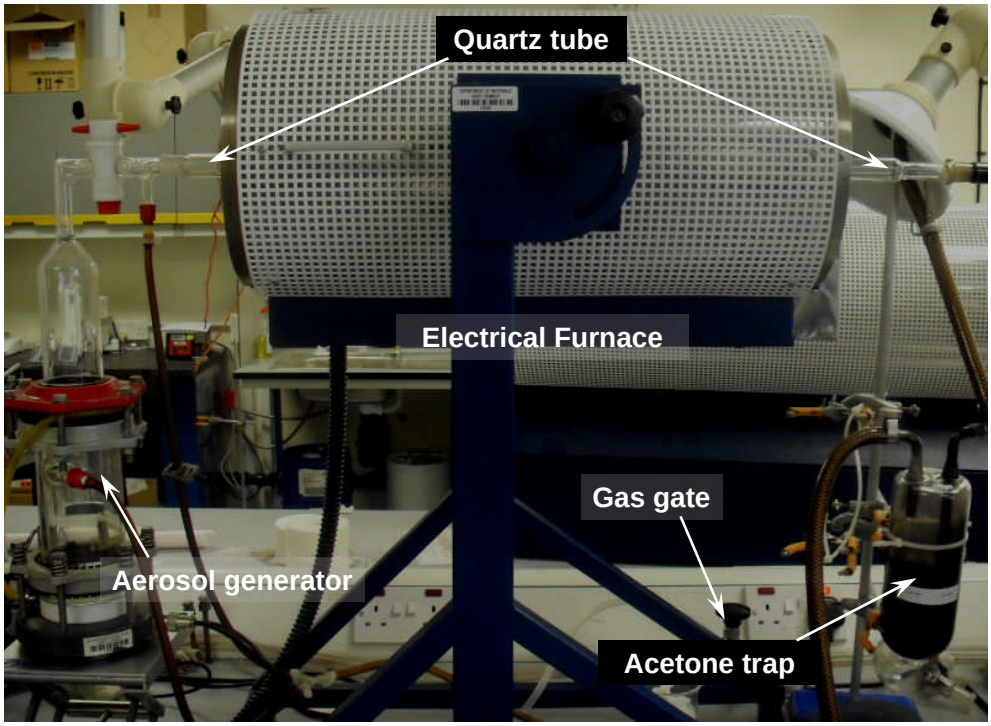

Figure 2.6: Photograph of the atmospheric CVD apparatus at Begbroke lab. A selection of set-ups is labelled.

2.4.2 Buffered-HF Etching

Buffered-HF (BHF) etching remains an effective method to prepare and treat the surface of perovskites, such as $SrTiO_3$ (STO), $BaSrTiO_3$ (BST). The BHF solution used in this work was prepared by dosing the NH_4F solution (60% mass concentration) into the HF solution (40% volume concentration), to make sure the final mixture has a pH value of 4.5. Further details regarding this preparation method were reported by Kawasaki *et al.*[56]

Two kinds of substrates, single crystalline STO (001) and polycrystalline BST, were used in the experiments. Both of the substrates were epi-polished and supplied by PI-KEM, UK. In this work, the substrate samples were typically etched for 10 min in the prepared BHF solution and thoroughly cleansed by ethanol and deionised water afterwards, prior to CNT growth. By using BHF etching, not only can the amorphous layer of polishing damage on the new samples be removed, but the used samples can be regenerated as the sample surfaces are cleansed by etching.

2.4.3 Sputtering and Annealing

Sputtering refers to the process of bombardment of sample surface with noble gas ions. It is a universal and versatile method for surface cleaning. In particular, with regard to the STO (001) surface, sputtering also remains as a key step for producing various kinds of surface nanostructures, as the bombardment can induce specific defects and disorders to the uppermost surface layers.

In this work, argon (Ar) ions served as the sputtering beam. On the JEOL 4500XT, sputtering was performed by using a PSP Vacuum technology ion source ISIS3000, which is incorporated within the treatment chamber. This sputtering gun uses a filament to create plasma from Ar gas before accelerating the Ar^+ ions towards the sample. The ion beam energy can be selected from 0.3 to 3 keV depending on the different surfaces, for example, 0.75 keV could be used for STO sample. The Ar gas pressure should be maintained at ~2×10^{-3} Pa for the sputtering gun to operate. In order to achieve this, the TMP must be in constant operation to control the pressure in both the load lock and the treatment chamber, whilst the ion pump should be switched off beforehand to avoid any possible damage.

Annealing is often necessary after sputtering. Annealing of materials not only serves as a cleaning approach, but also assists the atoms on the uppermost surface layers to rearrange and heals the defects/disorders of crystal surface caused by the bombardment.

The STO sample used in this work is doped with 0.5% wt Nb to become sufficiently conductive for STM measurements. The level of dopants gives rise to a low RT resistivity of 10^{-3} $\Omega \cdot m$, which allows the sample to be heated up resistively through passing a current along their length. In this manner an annealing temperature of up to 1400˚C can be achieved in the UHV chamber. To measure sample temperatures during annealing, an optical pyrometer can be employed to monitor temperatures above 750˚C, while a fit equation[53] is applied to estimate the sample temperatures below 750˚C, as stated in Equation (2.5),

$$T = 1.4739x^3 - 34.546x^2 + 325.3x + 15.58 \quad (2.5)$$

where x is the power supply output (W) of the sample when heating, T is the sample temperature (˚C).

2.4.4 Metal Deposition

Metals, in the form of thin films (nanometer thickness) coated on the substrate surfaces, are capable of producing CNTs. In UHV, in order to deposit metal thin films on substrates, certain types of metals need to be delivered by their evaporated states from the source to the target substrates. This was achieved with the aid of the e-beam evaporator equipped within the JEOL-4500XT in this work, and Fe and Ni were used and deposited with the evaporator.

In the e-beam evaporator, a W filament is positioned close to the top of a metal rod. The metal rod is applied by a positive bias (typically 2 kV). The filament is passed through a current to emit electrons, which can be attracted and collected by the tip of the rod. The emitted electrons, due to thermionic emission, lead to high electron density on the tip of the rod, further inducing local heating at the area of the tip. Hence, the evaporation of source materials is enabled.

In this work, an Oxford Applied Research mini e-beam evaporator ENG4 is used for metal deposition. It has four separate pockets, and each pocket possesses an independent filament, which facilitates replacement of different types of material rods. A water circulation system is provided to cool the instrument when operating

and a shuttle is attached to protect the target substrate from contamination before establishing a steady flux rate and also offer control on the deposition timings.

2.4.5 CVD Procedure

The carbon nanotubes (CNTs) were produced on the STO or BST substrates by EtOH-CVD or C_2H_2-CVD over a range of temperatures (600-800°C) for designed growth periods (normally 30 min). Briefly, samples of STO substrates were placed inside a new quartz tube (2.2 cm inner diameter), which was then positioned in a 50 cm long horizontal furnace. For EtOH-CVD, pure ethanol (C_2H_5OH) as carbon feedstock was introduced by an ultrasonic unit (piezo-driven aerosol generator (RBI Pyrosol 7901)) during the growth period, whilst for C_2H_2-CVD, instead of aerosol generator, plastic tubing directly connected to the quartz tube could deliver C_2H_2 at a requested flow rate. In a typical CVD experiment the furnace was ramped up to the designed growth temperature under the protection of 900 sccm Ar and 100 sccm H_2. Carbon precursors were carried by the Ar/H_2 mixture and introduced to the quartz tube after the furnace reached the growth temperature. The Ar and H_2 gas flow was maintained during the growth stage. After a certain growth time, the furnace was switched off and the quartz tube was cooled down to room temperature in Ar. The as-reacted substrates were collected to be further characterised.

2.5 Summary

This chapter has introduced the characterisation techniques and experimental procedures for investigating the CNT growth on STO surfaces. Since the topic of surface-bound CVD growth of CNTs can be considered as a ‘merged’ area, a wide range of probing tools and dedicated synthetic methods have been employed. Integrated usage of all the techniques enables complementary analysis and leads to more detailed information to be revealed.

Chapter 3：

Growth of Carbon Nanotubes by Surface-Bound CVD: A Literature Review

3.1 Background

This chapter deals with the latest progress and understanding in the field of the growth of carbon nanotubes (CNTs) by surface-bound chemical vapour deposition (CVD). The growth of CNTs on substrate surfaces *via* CVD is of technologically significance for the development of novel devices and composites. In this chapter, the major technique employed in this area is described. Growth parameter-control aspects such as the influences of growth temperature, carbon feedstock, ambient gas, and catalysts (and/or substrates) are reviewed. Emphasis is placed on the selection, design, and usage of different catalysts in CNT growth on substrates by CVD. Current understanding of growth mechanisms of various carbon nanostructures (CNTs, carbon nanofibres (CNFs), carbon nano/micro coils (CNC/CMCs)) are also explored with the aid of different catalyst types and synthetic methodologies.

3.1.1 Structural Features of CNTs

In the last decade, CNTs have been extensively studied, both theoretically and experimentally, because of their unique architecture and fascinating properties.[8, 49, 57-63] Several reviews[59, 60, 64] have shown that CNTs are ideal candidates for electrical, mechanical, thermal, and chemical applications such as nanoelectronic devices,[9, 65, 66] field emission displays,[1, 67] structural composites,[68, 69] scanning probes,[70-72] and sensors.[73, 74] Fundamentally, a CNT can be regarded as a seamless graphene cylinder, obtained from rolling up a planar sheet of graphene.[75] Nanostructures comprising

single graphene cylinders are termed single-wall nanotubes (SWNTs),[76] whereas multi-walled nanotubes (MWNTs) consist of two (double-walled nanotubes (DWNTs)) or more such cylinders that are concentrically positioned[77, 78]. Schematic configurations and real microscopic images of CNTs are shown in Figures 3.1a-3.1e.

Defects incorporated within the hexagonal lattices might lead to varied tubule morphologies, *i.e.* carbon helices, which have been theoretically predicted and target fabricated[18, 78-80] (Figures 3.1f-3.1j). In principle, these shaped CNTs are created by the insertion of pentagon-heptagon atomic paired defects into the regular hexagonal carbon networks.[81, 82]

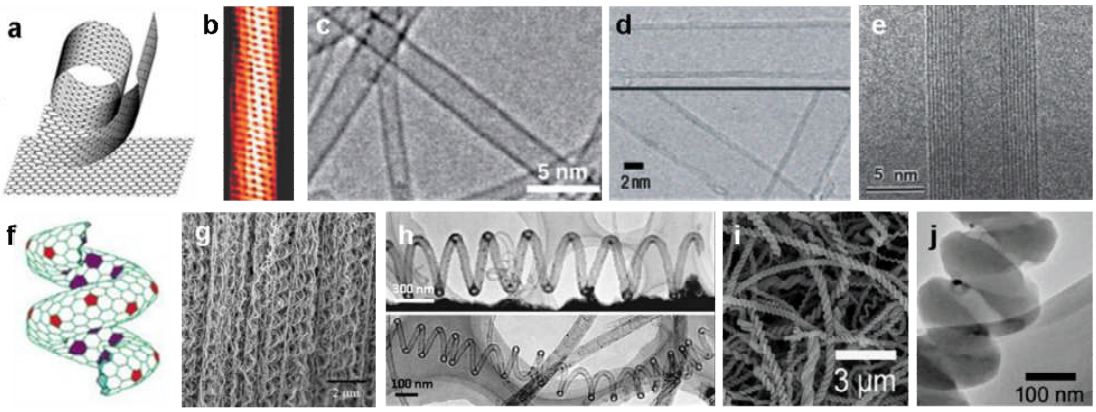

Figure 3.1: Image library of common types of CNTs. (a) Schematic illustrations of ideal graphene sheet, SWNT, and MWNT.[8] (b) STM image of a 1.3 nm diameter SWNT.[12] (c) TEM image of SWNTs.[15] (d) TEM image of DWNTs.[16] (e) TEM image of a nine walled MWNT.[1] (f) Structural model of helically coiled CNT, where the pentagon (red) and heptagon (purple) atomic carbon rings arrange themselves periodically within the hexagonal network.[28] (g) SEM image of a coiled CNT array.[33] (h) TEM images of individual coiled CNTs by different magnifications.[34] (i) SEM image of a large amount of carbon nanocoils (CNCs) produced by CVD.[18] (j) TEM image of an individual helical fibre present in (i).[18]

3.1.2 Morphology-Property Correlation: Importance of CNT Growth Catalysts

It is well known that carbon can be fabricated into a myriad of forms at the nanoscale, and the properties of carbon nanomaterials depend strongly upon the detailed features of their morphologies.[77, 78] Specifically, the morphology-property correlation of CNTs leads to numerous investigations on synthetic routes throughout academic and industrial laboratories worldwide. However, controllable production of CNTs with well-defined morphological features is still beyond reach of the current growth methodologies. The reason for this partially lies in the fact that there are various growth parameters to be adjusted within the synthetic methods, and even tiny fluctuations in the control of growth parameters can alter the morphologies of CNTs drastically.[35, 64, 77] Amongst these, the accurate selection, design, and usage of CNT growth catalysts remains to be a key factor for a rational synthesis of target materials, for the reason that the chemical and geometrical aspects of tailored catalysts could dictate the structures and hence the properties of resulting CNTs.

3.2 CNT Growth Techniques

To date, several techniques have prevailed in the field of CNT synthesis. All the well-developed growth techniques, namely, *arc-discharge*,[83] *laser-ablation*,[84] *and chemical vapour deposition (CVD)*[85] have already been detailed in published reviews,

accounts and books. Regarding the first two techniques, arc-discharge uses an applied electric current to provide heat towards two graphite electrodes, realising the production of different carbon nanostructures even without the presence of metal catalysts;[49] whilst the laser-ablation route uses a laser to vaporise the carbon and the metal catalyst to produce CNTs, especially SWNTs.[49] Here the special focus is placed on the CVD technique, as it is probably the most versatile production method for CNTs and also the technique employed for CNT growth in this thesis.

3.2.1 CNT Growth via CVD

Nowadays, CVD is the most widely used method to produce CNTs.[63, 64] The CVD process relies on using an energy source (*i.e.* an electrical furnace) to decompose carbon feedstocks and to provide heating for the sample substrates. There have been various types of CVD, with different energy sources, developed to facilitate the CNT synthesis. For instance, in thermal CVD, the heat of a furnace aids the precursor cracking as well as affecting the catalytic performance of the sample substrates;[48] plasma-enhanced CVD (PECVD) uses plasma to enable the process of hydrocarbon decomposition and assists the creation of catalytic nanoparticles (NPs) on the substrates;[86] In hot-filament CVD processing, a hot wire is employed to heat the precursor gases to high temperature to grow vertically aligned CNT (VACNT) carpets.[87]

In comparison with the arc-discharge and laser-ablation methods, CVD is a

practical technique for the production of CNTs.[59, 88-92] The major advantages of the CVD technique over the other two lie in the following aspects:

1) It enables growth of CNTs in large quantities at a range of relatively low temperature windows and ambient pressures.

2) It provides more control on the growth parameters and therefore better structural manipulation over the resulting CNT architectures.

3) It allows ease in experimental set-up and synthesis of CNTs in predefined positions on patterned surfaces/substrates, which is suitable for fabrication of electronic devices, field emission displays, gas sensors, etc. and other potential applications.

3.2.2 Surface-Bound CVD

As the name itself states, the surface-bound CVD refers to a technique of synthesising CNTs on substrate surfaces (oxide/semiconductor/metal surfaces) rather than on porous/powder supports.[14, 67, 93, 94] Prior to the furnace-heating process, the fabrication of surface-supported catalysts in the forms of NPs or ultrathin films is involved (*ex situ* generation of catalysts). Compared with the scenarios of synthesis of CNTs using floating catalysts (*in situ* generation of catalysts), the design and preparation of the catalysts in surface-bound CVD becomes more crucial, as the roles of catalysts supported by underneath substrate surfaces are more complex. Even small modifications of surface chemistry and physics of substrates would lead to notable changes in catalyst performances; hence the morphologies and properties of

CNTs. The critical factors that can influence the surface growth of CNTs are not only the catalytic abilities of catalysts themselves, but also the interplay between catalysts and supports and the interactions between catalysts and various processing parameters.[77, 95]

3.3 CNT Synthesis on Substrates: With a Focus on Catalysts

The successful growth of CNTs on catalyst-coated substrates by surface-bound CVD needs smart design of catalysts and precise control of the CVD process.[96, 97] A large array of parameters involved in CNT synthesis, such as growth temperature, carbon feedstocks, ambient gas *etc.* can exert appreciable influences on the catalyst performances as well as the resulting material. Control over catalyst design and growth conditionings in surface-bound CVD processes might therefore enable researchers to obtain the desired production of materials with targeted structural features and properties. A sketch highlighting the importance of catalysts in the course of CVD CNT growth is shown in Figure 3.2.

In this section, I will review a key set of the growth parameters involved in surface-bound CVD synthesis of CNTs, ranging from general aspects on the choice of growth temperatures, carbon feedstocks, and carrier gases, to specific strategies on the design of the catalysts. The aim is to provide brief insights into the impact of

growth-control aspects on CNT production and to illustrate important factors in the role of catalysts.

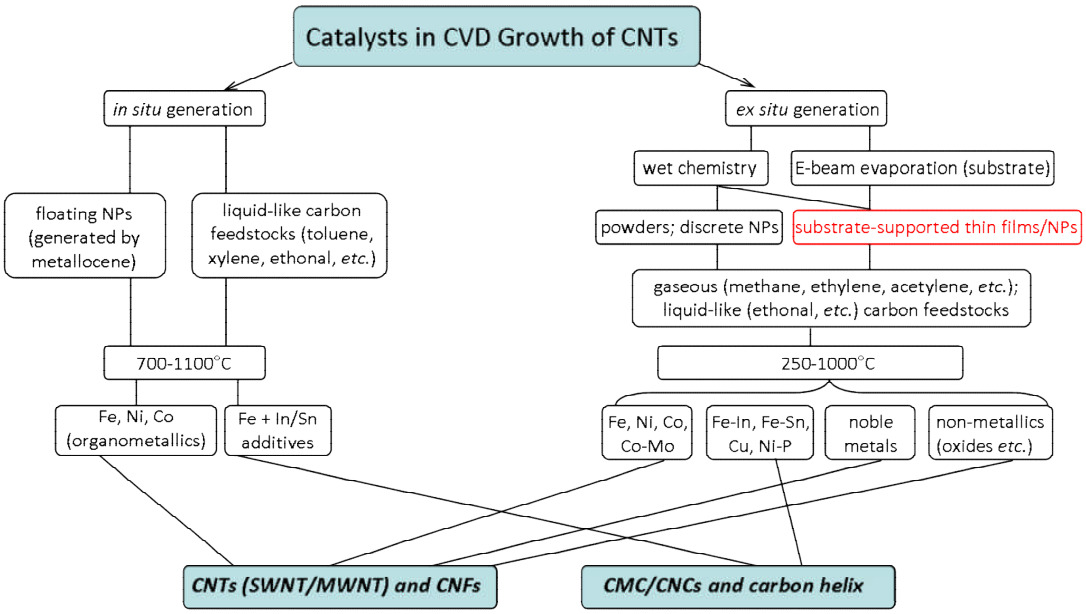

Figure 3.2: A sketch of 'catalysts in CVD growth of CNTs', highlighting the importance of catalysts involved within a CVD process. The focus of this chapter and the whole thesis is positioned on the substrate-supported catalysts (red colour) in terms of CNT growth *via* surface-bound CVD.

3.3.1 Growth Temperature

Selecting growth temperatures for CNT synthesis is of great significance,[64, 77] owing to the two-fold functions of heating in surface-bound CVD process: 1) To influence the surface chemistry and catalysis of catalysts (metal catalyst de-wetting, ripening *etc.*) and the transported diffusion of reagent species; 2) To affect the thermal/catalytic pyrolysis of precursor molecules within the reactor/on the catalyst surfaces. Hence, the effect of growth temperatures is the first to be scrutinised.

Experimental findings have suggested that growth temperature can affect the catalytic performances of catalyst particles during the surface-bound CVD process, thus influencing the production (*i.e.* yield, structure) of CNT outcomes.[98-101] Low temperatures (*i.e.* 500-600°C) hinder the surface diffusion of catalyst atoms and carbon species, whereas excessively high temperatures (*i.e.* greater than 800°C) lead to aggregation of catalyst particles on surfaces and enhancement of thermal decomposition of carbon feedstocks, both of which give rise to sparse yield of CNTs. An investigation of the T dependence of the growth of SWNTs for the alumina supported Ni system indicated that promising growth (grown CNTs covering the whole substrate) took place at ca. 650-700°C (as shown in Figure 3.3);[102] Another interesting phenomenon was that the optimum T was tested to be 650°C for synthesizing the highest VA-MWNT carpets on Fe-SiO_2 substrates.[103] Moreover, the effect of growth temperature may dominate the final morphology of the products. A study conducted by Liu *et al.* on the fabrication of unusual carbon structures illustrated that within the range of reaction temperatures from 430-550°C, the morphologies of carbon deposits grown by Ni on Si wafers evolved from straight CNFs, to helical CNFs, to CNCs.[104]

According to the conventional viewpoint, MWNTs can be generated with relatively low growth temperatures (400-750°C), while SWNT synthesis generally require higher synthesis temperatures (800-1100°C).[64] However, a breakthrough made in 2006 has shown that SWNT can be produced at temperatures as low as 350°C on SiO_2 supported Fe catalyst by low-pressure CVD,[13] which can be

explained by the conjecture that the CNT growth is governed by the surface processes of the Fe catalyst NPs. This technically controllable, economically viable method for SWNT production at low temperature is desirable, because it is compatible with nanoelectronic processing and related applications.[105]

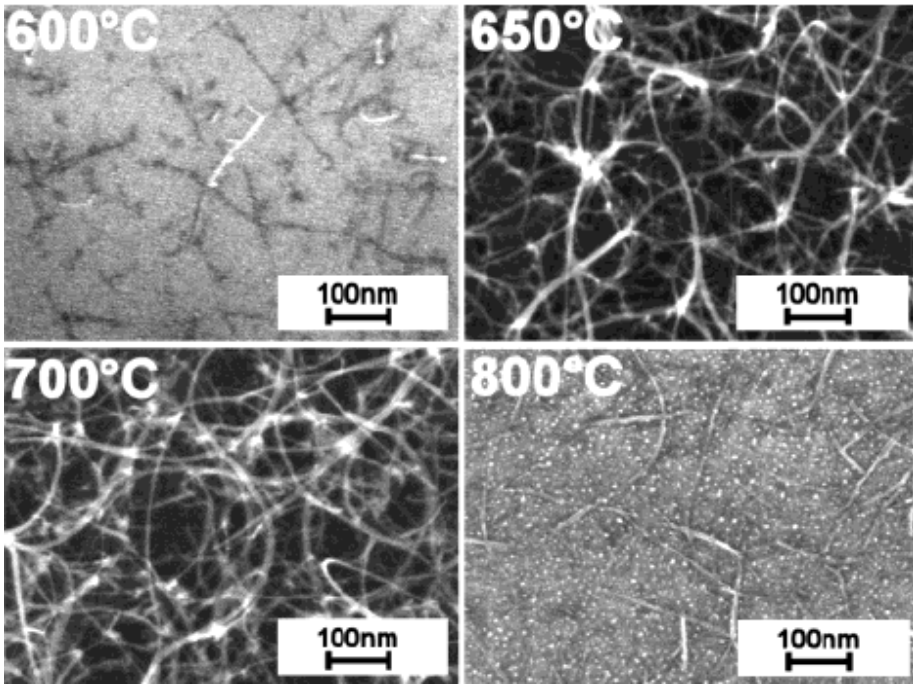

Figure 3.3: SEM investigations of temperature dependence of the SWNT growth on alumina surface-supported Ni catalyst by methane-CVD.[102] At 600°C the growth was sparse (lack of active catalyst sites); promising growth of SWNT was observed for 650°C and 700°C; at 800°C the yield of CNTs clearly decreased (agglomeration of catalysts).

3.3.2 Carbon Feedstock

Controlling the composition of the carbon feedstock crucially impacts upon CNT formation,[106] this is partially due to the fact that different types of carbon feedstocks possess distinct routes/performances of decomposition in a certain CVD condition,

leading to discrepancies in the yield and morphology of the resulting materials. For instance, hydrocarbon sources with exothermic decomposition (such as C_2H_2, C_2H_4) are noticed to achieve low-temperature growth of SWNTs (at 400°C),[13, 107] whereas the use of less active carbon feedstock with endothermic decomposition (CH_4) requires higher growth temperatures (>560°C) for producing SWNTs.[106, 108]

In a CVD process, the decomposition of carbon feedstock depends not only on the intrinsic properties of the precursor, but also on the type and morphology of catalysts used within a reaction. An example given by Mizuno *et al.*[109] found a strong selectivity between carbon sources and elemental catalyst species in terms of SWNT growth on Si substrate. In their study, the matching of two representative carbon feedstocks (ethylene (C_2H_4) and ethanol (C_2H_5OH)) with Fe and Co metal catalysts was investigated, with the result that Fe (Co) catalysts showed high SWNT yields for ethylene (ethanol) CVD, while showing very low yield for ethanol (ethylene) CVD.[109]

Moreover, recent discoveries have revealed that tuning the chemistry of carbon feedstocks exerted strong influences on the crystal structures of grown CNTs. By decoupling the thermal treatments of carbon precursor and substrate-supported catalysts, and through varying the treatment temperature of gaseous feedstocks, Nessim *et al.*[97] observed an interestingly morphological transition of produced carbon filaments (between amorphous CNFs and crystalline CNTs). The similar experimental route has been tried by Plata *et al.*[96, 110] in enhancing the efficiency of CNT synthesis. These investigations suggest that specific gas precursors could

control the structural features of resulting CNTs, thus pinpointing which types of carbon molecule(s) are responsible for building up the tubular architectures and then direct delivering these molecule(s) might enable selective growth of carbon nanostructures in a surface-bound CVD process.

Veering away from the general discussions on the carbon feedstocks above, two specific types of carbon sources are used in this thesis, acetylene (C_2H_2) and ethanol (C_2H_5OH). C_2H_2 has been frequently used for CNT synthesis, and in particular, used to exert coiling efforts on carbon nanostructures with the aid of various catalysts, especially Cu.[111-117] Investigations of the catalytic decomposition of C_2H_2 over Cu NPs have indicated that the shape of Cu NPs changed during the adsorption of C_2H_2 and distinct carbon growth rates from the different facets of NPs were therefore established, contributing to the formation of helical structures.[111, 115]

The use of C_2H_5OH in alcohol-CVD expanded the types of carbon feedstock available for CNT synthesis. It has been claimed that C_2H_5OH serves as the most versatile carbon source for CNT synthesis with various catalyst forms (floated/powdered/supported) NPs.[118] Furthermore, using C_2H_5OH as a carbon feedstock in a CVD reaction guarantees a low-cost, environmentally-friendly process of CNT production;[99, 118] also the liberated oxygen-containing radicals (such as –OH radicals) from C_2H_5OH decomposition during CVD processes can suppress the formation of amorphous carbon, leading to the growth of CNTs of high purity. It is believed that oxygen plays an important role in the CNT synthesis by CVD. Further details are revealed in the following sections (Sections 3.3.3.2 and 3.3.4.3).

3.3.3 Ambient Gas

In CVD experiments, carbon-free gases can function as catalyst pretreatment agents (H_2, NH_3; O_2, H_2O; Ar, He *etc.*) to aid the catalyst conditioning/restructuring, or as reagents (H_2, H_2O *etc.*) to participate within the CVD processes, or simply act as carriers (Ar, He, N_2 *etc.*) to help transport the hydrocarbons.

3.3.3.1 Influence of Catalyst Pretreatment

Catalyst pretreatment can strongly influence CNT growth in surface-bound CVD process.[119] Two competing pathways of catalyst pretreatment have been previously used: reducing and oxidising pretreatment (RP and OP).[120-122]

Hydrogen gas has been proven to be effective, not only in the stage of RP but also in CNT growth. In addition to enabling reduction and formation of the catalyst prior to the introduction of carbon, H_2 helps to suppress the cracking rate of the precursor and also assists in etching away the amorphous carbon accumulating around the catalysts particles during the CVD process. However, excessive H_2 usage, especially at the stage of catalyst pretreatment, results in severe Ostwald ripening, which causes aggregation of the catalyst particles, making them unsuitable for CNT formation.[123-126]

Recent findings have documented that metal catalysts in oxidation states, prepared by OP, promote CNT growth efficiently. Several techniques of conducting OP of samples have been attempted, such as controlled annealing in open air[127] and O_2 plasma sputtering,[120] all of which gave rise to enhanced yield and quality in the CNT

production.

The latest studies on catalyst preparations, which focus on the comparisons between the OP and RP, have become even more interesting. The deep analyses of Esconjauregui *et al.*[122] have revealed that the alignment and growth mode of nanotubes on SiO_2 surfaces can be controlled by careful selection of catalyst pretreatment conditions (OP vs RP); With the aid of *in situ* XPS, they have demonstrated that OP induces strong catalyst-substrate interaction (SCSI) by forming interfacial metal silicates, which can anchor the catalyst particles to substrates, thus hindering the process of catalyst aggregation, and leading to the base growth mode of VACNTs on surfaces. Similar results regarding switching the growth modes of CNTs have also been reported by Dijon *et al.*[121]

Nessim *et al.*[125] dealt with the analysis of the effects of delayed introduction of RP over the Fe/Al_2O_3 catalyst system. They found that varying the timing of H_2 introduction, sometimes even postponing it to after the introduction of the carbon feedstock, significantly dictated the CNT outcomes, as shown in Figure 3.4.

Inert gases such as Ar and He are often used as carriers to transport carbon species during CVD process in general. However, a report appeared in 2009 demonstrated that catalyst treatment by inert gas, with synergetic effects provided by RP or OP, led to a distinction in both morphology and coarsening behaviour of the catalyst NPs, prior to CNT nucleation.[2] As a result, chiral-selective growth of SWNTs was achieved, up to 91% of which were metallic SWNTs. Moreover, the mechanism of catalyst conditioning probed by *in situ* TEM observations suggested that He ambient

can enhance the Fe NP faceting and hinder its ripening, whilst Ar ambient led to degradation of catalyst faceting and induced severe coarsening instead.[2]

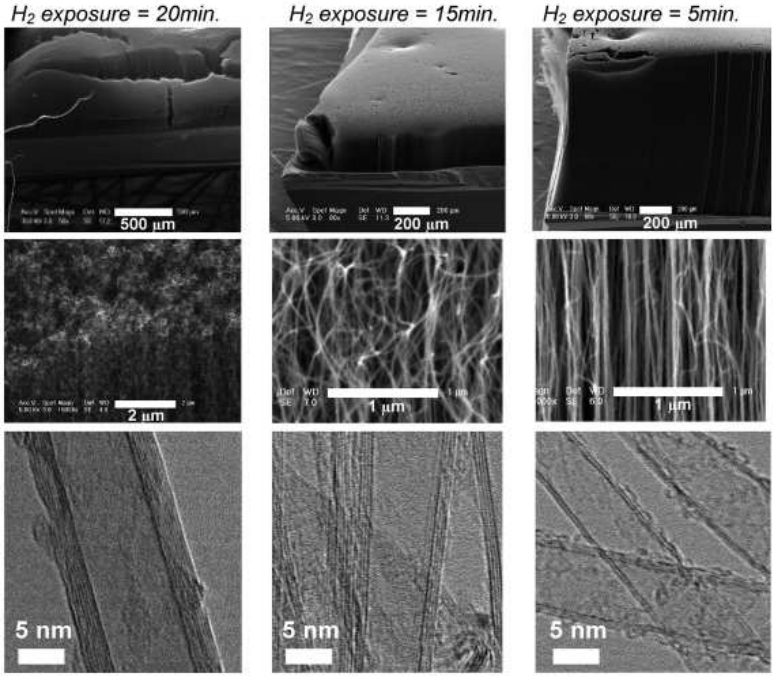

Figure 3.4: SEM and HRTEM images of CNT carpets grown from Fe catalysts on Al_2O_3 surface by C_2H_4-CVD.[125] H_2 has been introduced 5 min before, simultaneously with, and 10 min after C_2H_4 flows in. Delaying H_2 introduction gives rise to taller CNT carpets with better tube alignment and thinner tubular structures with fewer graphitic walls.

3.3.3.2 Influence of Oxygen-Containing Species

It is believed that oxygen plays an important role in the CVD of CNT growth, as various studies have revealed that the synthetic efficiencies of CNT growth have been enhanced by introducing appropriate levels of oxygen (for example, in a water-assisted CVD process, the water concentration was measured to be around 20~500 ppm[15] in the ambient gas) into the systems (*i.e.* into ambient gas, substrate,

even catalyst). Surface-bound SWNT synthesis has been achieved at low growth temperature (450°C) and employed CO as carbon feedstock.[128] A number of investigations also reported that the oxygen-containing species in gas composition benefit the yield of CNT production by drastically improving the CVD reaction.[118, 129-131] In general, there are two routes for introducing oxygen into the CVD process: through the ambient gas (H_2O, CO_2 *etc.*), or *via* carbon precursor (CO, C_2H_5OH *etc.*).

Hata and co-workers[15] demonstrated 'super-growth' of SWNTs by using H_2O in CNT synthesis *via* CVD. Since then, numerous publications have appeared, demonstrating the realisation of large-scale, high-quality VANT carpets with heights on the substrates in the millimeter scale, by means of this 'super-growth' technique.[16, 132-135] Along with researching the reproducibility of super growth, the role of water has also been extensively investigated, and the consensus is that a small amount of water in the ambient gas can keep the surfaces of catalyst particles clean by removing the amorphous carbon coating, thus stimulating and preserving the catalyst abilities as a growth enhancer.[15, 136-138] Amama and co-workers[139] reported that the major role of water in super-growth CVD is in suppressing the Ostwald ripening of catalyst particles, whilst Noda *et al.*[138] have argued *per contra* that water has no effect on that. It would be helpful to initiate possible investigations to observe the interaction of water and catalysts at atomic scales, in order to tackle the discrepancy in the function of water in such super-growth CVD process.

Based on the successful design of super-growth CVD using water, recent works have progressively shown that many materials which contain oxygen could replace

water as a 'growth enhancer'. CO_2[140-143] has been extensively used to build up a flexible approach for CNT synthesis, incorporated with hydrocarbons. The general rules governing the high efficient growth of CNTs proposed by Futaba *et al.*[144] state that two essential ingredients must be present in the growth stage: 1) a carbon source that does not contain oxygen and 2) a growth enhancer containing oxygen. A follow-up study interestingly revealed that using the oxygen-containing aromatics as growth enhancer, synthetic control over CNT structures (size and wall number) can even be realised by C_2H_4-CVD on the Fe/Al_2O_3 substrate,[145] as shown in Figure 3.5.

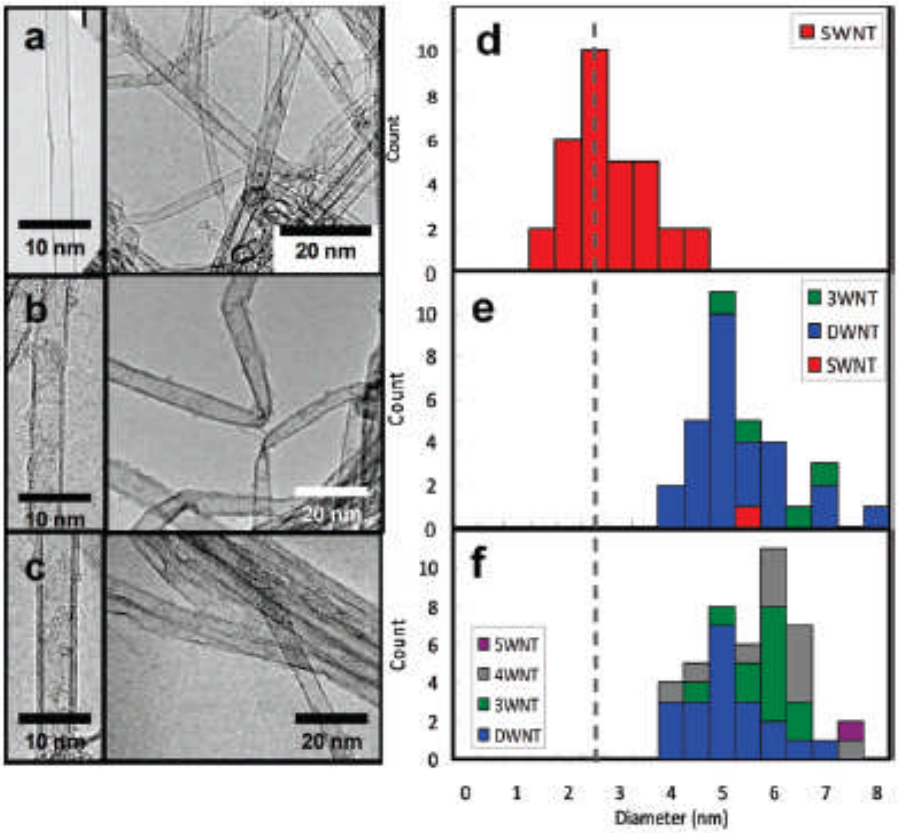

Figure 3.5: CNT structural changes tailored by oxygen-containing aromatics (growth enhancer).[145] TEM images of CNTs using (a) water, (b) methyl-benzoate, and (c) benzoaldehyde growth enhancers. Diameters and wall numbers of CNTs are plotted in the histograms in (d-f), respectively.

3.3.4 Catalyst

The ultimate role of catalysts in the surface-bound CVD process is still in dispute although much time has been spent on this matter. The current understanding is that the functions of catalyst particles during the CVD reaction include decomposing carbon precursor, assisting diffusion of carbon species (over/within the catalyst NP), acting as templates to facilitate tubular nucleation, and dictating tube diameters.[146, 147] The plethora of comprehensive reviews[48, 64, 92, 146, 148-150] dealing with the roles of catalysts in CNT synthesis bears witness to the significance of this area. In this section, effects of catalyst type, catalyst morphology and catalyst substrate are reviewed.

3.3.4.1 Catalyst Type

It is well known that transition metals (such as Fe, Co, and Ni) are effective catalysts for CNT growth. They can be utilised either in their pure form or mixed as binary composites. The first comparative study of the catalytic behaviour of elemental Fe, Co, and Ni was carried out by Huang *et al.*[151], which revealed that the catalyst type strongly influenced the growth rates and structures of CNTs and concluded that Ni was the most suitable catalyst of the three for CNT growth. However, another investigation regarding catalyst activities of Fe, Co, and Ni under the condition of CH_4/H_2/900°C showed clear discrepancies: Fe gave rise to the highest yield of CNTs, while Ni showed the poorest catalytic performance.[152] The reason for this distinction is still unknown, but factors such as the stabilities and properties of their

corresponding metal carbides and the interactions between the catalysts and the substrates are worth taking into consideration.

CNT growth on binary catalyst systems has been reported. Several studies have shown that SWNTs can be grown *via* CVD on a binary FePt alloy,[153-156] which was obtained from gas-phase based and solution-based catalyst preparation methods. Moreover, the addition of Mo to Fe, Co or Ni has been accomplished and these binary catalysts have enhanced the yields of CNTs.[157] Introducing Mo to Co led to formation of bimetallic compounds that can prevent the aggregation of Co, thus resulting in effective CNT production. Mo has also been claimed to be responsible for advancing the (n,m) selectivity of grown SWNTs, when using supported Co-Mo catalysts.[158-160]

Recent investigations in developing metal catalysts for CNT synthesis have broadened the scope of catalyst type: Au,[161-164] Ag,[162] Cu,[162, 164-166] Pd,[162, 164, 167] Ru,[168] Pb,[169] Rh,[170] Zr,[171] Al,[164] Mg[164] have been reported to catalyse CNT growth. Zhou *et al.*[166] pioneered the use of Cu as a catalyst for SWNT growth and achieved a high-quality product; Yuan *et al.*[164] employed a large variety of metals to successfully achieve horizontally aligned SWNT growth on quartz surfaces. Theoretical investigations have succeeded in unravelling the effects of metal catalysts in the growth of CNTs. By analysing carbon-metal binary phase diagrams, Deck and Vecchio[172] proposed that successful metal catalysts were the ones exhibiting sufficient carbon solubility, rapid carbon diffusion capacity, and limited carbide formation. Yazyev and Pasquarello's study[173] on modelling the nucleation and

diffusion stages of CVD-grown CNTs, showed that noble metals, with the aid of surface diffusion of targeted carbon species on catalyst particles, were able to support CNT growth at the synthesis temperature of 900°C.

Additionally, investigations on helical carbon nanostructure growth revealed that 'coiling efforts' can be assigned to specific catalysts, such as In,[33, 174-176] Sn[33, 175-180]. The in-depth exploration of non-linear growth of carbon induced by these kinds of catalysts is featured in Section 3.4.

Lastly, as indicated in previous paragraphs, oxygen has been noticed to benefit CNT growth. The latest development of CNT catalysts shows that non-metallic species, such as oxides, can act as CNT growth catalysts. A breakthrough has been made in reports of the exciting performances of surface-generated SiO_2 NPs in terms of producing SWNTs.[19, 21, 181] Further details of this metal-catalyst-free route are presented in Chapters 5 and 6 of this thesis.

3.3.4.2 Catalyst Morphology

The catalyst geometry in the surface-bound CVD process is as important as catalyst chemistry in tailoring the yield and configuration of CNT production. Herein, the influence of the size and shape of catalysts is discussed.

3.3.4.2.1 Catalyst Size

Quantum size effects of NPs can significantly affect their catalytic performances, when the sizes of particles are below 10 nm; therefore, the solubility of carbon within catalyst particles and the diffusion pattern of carbon governed by catalyst particles

are greatly dependent on the size of catalysts.[146, 148] A groundbreaking investigation, reported by Gohier *et al.*[182], demonstrated that the growth of CNTs were strongly correlated to the catalysts' nanometric dimension, whilst Liu's group[183] discovered that an optimal particle size was required when the carbon feeding rates was fixed, to properly nucleate SWNTs. Smaller NPs were prone to be easily deactivated due to poisoning from feedstock overfeeding, and larger NPs were inactive because of underfeeding.[183]

Several reports have indicated that controlling the size of NPs led to fine tuning of the carbon nanotube diameters as well as wall numbers.[182, 184] Dai's research group[91] was amongst the first to grow CNTs with controlled catalyst size. They made use of an iron-storage protein, ferritin, to synthesise discrete catalytic iron oxide NPs with controllable diameters on SiO_2 surfaces for SWNT growth. Moreover, they observed both ends of CVD grown SWNTs in the TEM for the first time.[91] A similar experiment was conducted by Jeong *et al.*[185] to demonstrate a facile, diameter-controlled growth of SWNTs using Co-filled apoferritins. Recently, a systematic study performed by Schaffel *et al.*[186] has shown that different particle sizes resulted in distinct diameters and number of walls in the resulting CNTs, as indicated in TEM images in Figure 3.6[186]. Hence, at that moment a consensus had been reached that SWNTs were normally generated from small particles. However, Jeong *et al.*[187] observed an atypical phenomenon that larger catalytic particles embedded on SiO_2 substrates also produced SWNTs. It is worth mentioning that by using arc-discharge methods, radially grown SWNTs were observed from the catalyst

particles which have diameters much larger than those of tubes.[188, 189]

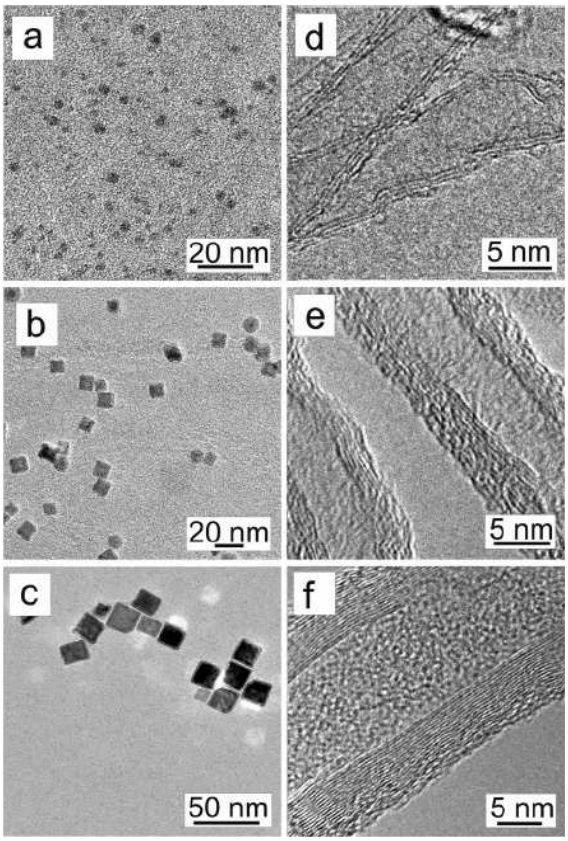

Figure 3.6: Investigation of catalyst size effect on the growth of CNTs.[186] (a-c) TEM images of Fe particles of varying median diameters of 2.7, 10, and 18 nm, respectively. (d-f) Corresponding HRTEM micrographs of grown CNTs with different diameters and wall numbers.

The preparation of the catalyst material is a critical step for CVD CNT growth. To date, enormous efforts have been made to fabricate catalytic NPs with narrow size distributions and high-catalytic activities. Various catalyst patterning methods such as evaporation,[101] dendrimer-templated NPs,[88] reserved micelle,[190] and wet chemistry[191] have been used to achieve this goal. Although thermal evaporation has remained the most common approach in catalyst patterning, thanks to its merits in

precise control of catalyst position and size, other techniques can lead to unexpectedly striking results. In their landmark report on growth of SWNT by CVD, Dai *et al.*[192] synthesised SWNTs over Mo NPs using CO as a carbon source. The results showed close correlation between the diameters of grown tubes and pre-designed catalysts by a wet chemistry method. A recent preparation approach involving ion-implantation has been used in patterning Ni NPs on a silica layer in order for subsequent CNT growth, with their diameters strongly dependent on the size of catalyst particles.[193]

3.3.4.2.2 Catalyst Shape

Besides the size of the catalyst NPs, another morphologic parameter that could have influence in the catalytic process is the shape of the NPs. Controlling nanoparticle shape can be achieved throughout several routes, such as solution-based chemistry,[194] surface energy-controlled substrate growth,[25, 27] and gas-induced restructuring.[2, 115] To serve the purpose of growing desired carbon nanostructures, the gas environment structured preparation methods have mainly been used.[2, 115]

A representative example of catalyst shape effects was reported by Shaikjee and his co-workers,[115] who employed TEM 3D tomography to reveal that the geometry of Cu NPs can control the morphologies of the grown CNFs at a low synthesis temperature (250°C), thus illustrating the critical role of catalyst shapes plays on synthesis, as shown in Figure 3.7.[115]

However, concerns have been raised on how much the desired shapes of metal

catalysts can be preserved in response to the variations in temperatures and surrounding environments. Extensive studies have shown that the shapes of metal nanocrystals can be altered (sometimes irreversible) by heating, molecule adsorbing and so on. The shape transformation of a nanocrystal occurs due to a need to minimise the total interfacial free energy at a given volume. Herein, it will be meaningful in future works to perform investigations on $SrTiO_3$-supported metal shaped nanocrystals to see how the shape could be maintained in CVD conditions (T: 400-800°C; Ambient gas: $Ar/H_2/C_2H_2$).

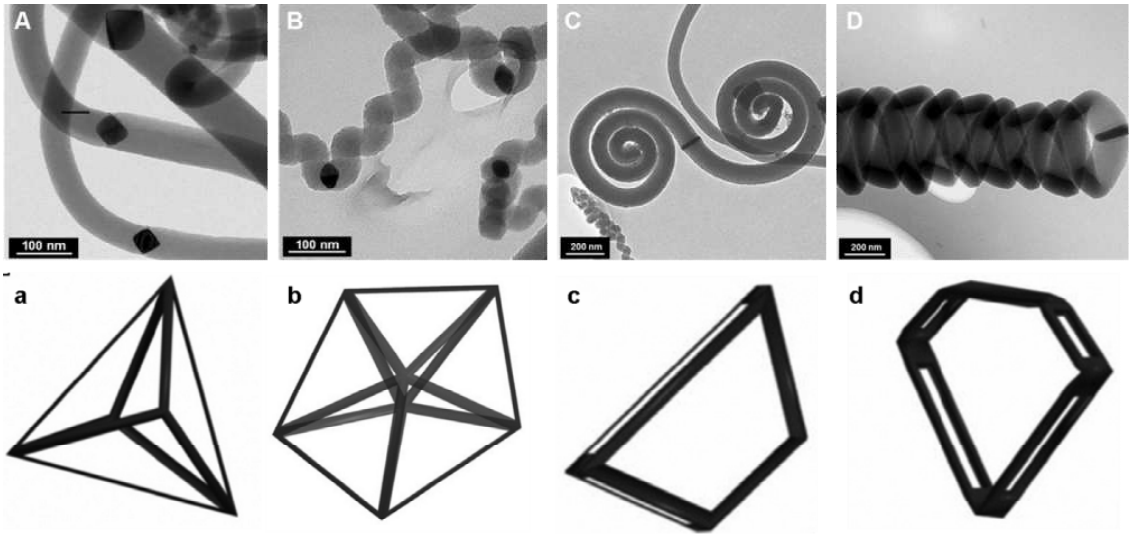

Figure 3.7: The morphologies of CNFs are dictated by the shape of Cu catalyst particles.[115] (A-D) TEM images of CNFs grown from Cu catalysts, which are presented within the structures. (a-d) Simulated particle shapes that correspondingly relate to the distinct CNF growth.

3.3.4.3 Catalyst Substrate

In the surface-bound CVD process, the catalysts are normally deposited on a substrate as a thin film by evaporation. This is followed by ripening to yield NPs via

de-wetting of the substrate under proper heating. To serve as a stage for catalyst dots to perform and also a template to allow the nucleation and growth of CNTs, substrates used in CVD reactions are of great importance in CNT synthesis.

3.3.4.3.1 Choices of Substrate

Nowadays, CNTs can be grown successfully on numerous types of substrates. Silicon oxide, aluminum oxide, and magnesium oxide are among the most popular oxide types used as substrates. From an energy standpoint, it remains critical to obtain optimally-sized and well-dispersed catalyst particles on oxide substrates, as it will influence the morphologies and properties of resulting CNTs. However, this targeting is not easy to achieve, owing to the complicated interplay between catalyst and relating ambient (substrate, gas atmosphere, thermal process *etc.*), which has effects on the de-wetting and agglomerating of catalysts on substrates.[77, 95]

Extensive investigations have been performed using alumina as a catalyst substrate, exploiting the fact that it supports the production of high-quality VACNT carpets, with large tolerance of the process conditions.[195, 196] Recently, with the aid of *in situ* XPS, Hofmann *et al.*[197] have studied the growth of CNT forests, using Fe as catalysts on an Al_2O_3 substrate, and concluded that the enhanced Fe catalytic activities were due to the specific character of Fe/Al_2O_3 interface reaction. A recent, comprehensive study by Amama *et al.*[198] has revealed considerable differences in the activity and lifetime of Fe catalysts, supported on different types of alumina. By using a combination of microscopic and spectroscopic characterisation, they demonstrated

that the complex interplay between Ostwald ripening, subsurface diffusion, and porosity of the alumina supports may be responsible for the observed phenomena.

Growing CNTs on metallic substrates has proven more challenging, and is hence less well-studied, because the occurrences of interdiffusion and alloying between catalyst and metallic substrates could detrimentally affect the de-wetting process, through which catalyst dots form. However, metal-surface-supported synthesis of CNTs is of great importance for electronic applications, because the CMOS industry often requires direct electrical contact between CNTs and the substrates.[77, 199] Nowadays, the identified target for CNTs production on metallic substrates is to synthesise CNTs with vertical-aligned forms at low growth temperatures. To achieve this, several metallic substrates, such as Cu, Ta, Pd, W, Ti and Al, have been experimentally tested.[97, 105, 199] The very latest, detailed study of the Fe-Ta model system presented by Bayer *et al.*[95] has highlighted general selection criteria for CNT growth on metallic substrates.

3.3.4.3.2 Interaction between Catalysts and Substrates

There are two widely accepted growth modes for CNT growth on substrates by surface-bound CVD: tip-growth and base-growth (or root-growth). Interaction between catalysts and substrates has been suggested to account for the two growth modes presented during the CVD process.[200] Specifically, the tip-growth mode corresponds to weak interaction. In this mode, catalyst particles rise with CNT growth, and eventually stay at the tip of the CNTs. In base-growth mode, catalyst

particles bond strongly with the substrate at growth, finally remaining anchored on the substrates and appearing at the bottom of the CNTs. (These growth modes will be further described in Section 3.4). In this way, the growth of CNTs can be tailored by modifying catalyst-substrate interaction prior to conducting CVD.

Wang *et al.*[201] conducted a comparative study in the formation of Fe catalyst NPs on both Ta (metal; with high surface energy) and SiO_2 (oxide; with low surface energy) surfaces for CNT growth by CVD. They observed that Fe particles showed a Volmer-Weber (VW) growth mode on SiO_2 and a Stranski-Krastanov (SK) mode on Ta. In particular, CNT growth on SiO_2 followed a tip-growth mode with a slow growth rate, whilst Ta exhibited a base-growth mode with a fast growth rate. Their conjecture suggested that the CNT growth mode was modified by the adhesion between the catalyst and support.

Interaction between catalysts and substrates has been described, not only as the adhesive forces indicated above, but also as a variety of forms including interfacial chemical reactions[122, 202] and inter-diffusions[198], which can be dictated by specific catalyst prepared methods, *e.g.* gas pretreatment. By inducing strong catalyst-substrate interaction by means of oxidising pretreatment towards catalyst, Robertson's group[122] has managed to manipulate the growth mode and alignment of CNTs. In their study, the interaction between metal catalysts (Fe, Co, and Ni) and SiO_2 substrates was operated by forming interfacial metal silicates, which in turn anchored the catalytic NPs to the substrate, thus restricting their surface mobility and coarsening.[122]

3.3.4.3.3 Functions of Substrate

CNTs synthesised on appropriate substrates have been identified as promising candidates for their integration into novel devices, such as field emitters and nanoelectronics. Several roles that substrates can serve in the growth of CNTs are discussed here.

The basic role of substrates is to support catalyst formation. It has already been found that the relative surface energies of the substrate, the catalyst, and their interfacial energies can tune the sizes, shapes, and curvatures of the particles grown on substrates.[25, 26] This variation would lead to large differences in the morphology, property, and growth mode of resulting CNTs, as already noted.

Another function that substrates can provide is to serve as a template to guide the growth of surface-bound, horizontally-aligned CNTs (HACNT). It has been shown that directional control of CNTs growth on a substrate is essential for the production of high-performance nanodevices, and this becomes achievable once an appropriate substrate is selected.[203] Quite a few recent studies have claimed that single-crystal surfaces, such as sapphire,[204-210] quartz,[203, 211] silicon,[212, 213] and magnesia,[214, 215] enable the controlled production of HACNTs. The CNTs are said to be generated along either atomic steps[205] or lattice directions[206]. Moreover, observations have revealed that the crystalline facet strongly influences not only the growth direction but also the nanotube structure (*i.e.* diameter and chirality distributions).[204, 207]

A hidden role of catalyst supports (especially oxides) is simply to aid nanotube growth. A pivotal effect of oxide substrate in CNT synthesis has been recently

studied by Rümmeli's group, based on their experimental observations.[184, 195, 216, 217] They proposed a striking concept, that the oxide support plays a catalytically active role for CNT growth, while metal particles are solely responsible for CNT nucleation steps. Furthermore, with the aid of HRTEM characterisation, they managed to demonstrate clearly that graphitic nanotube walls directly root on oxide (alumina) supports, as opposed to the catalyst particle.[218] They also pointed out that oxygen species are crucial in the growth of CNTs, following a comparative study of growing CNTs (as indicated in Figure 3.8) on both TiN and Al_2O_3 supports under the same CVD conditions.[195] Apart from their investigations, a Japanese group[196] has claimed that oxide support assisted the adsorption and transportation of carbon flux, thus enhancing the growth rates of CNTs. This is because oxides were key components for hydrocarbon reforming.

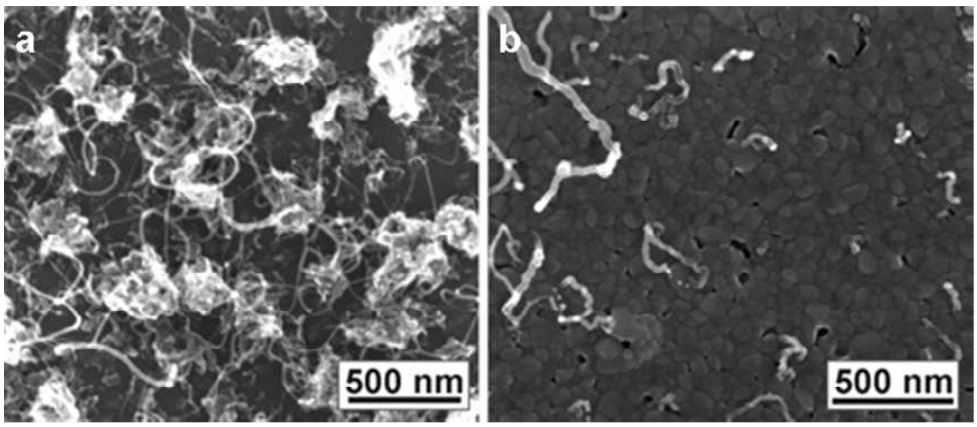

Figure 3.8: A comparison study of growth of CNTs on both oxide and non-oxide substrates.[195] SEM images of CNTs grown on (a) Al_2O_3 surface and (b) TiN surface, suggesting the oxygen within the substrates plays a critical role in CNT formation in surface-bound CVD process.

3.4 Insights into Growth Mechanisms of Carbon Nanostructures

The theme of this thesis centres on *the design and fabrication of different types of catalysts for the growth of carbon nanostructures on perovskite oxide surfaces*. As for the growth methods, two main forms of CVD technique with regard to catalysts have been employed, namely, 'metal-catalyst-involved (MI)' route and 'metal-catalyst-free (MF)'[19] route. In order to achieve an efficient CNT growth and design synthetic routes, it is essential to gain a comprehensive understanding of the underlying science involved in growth mechanisms, which have triggered intense debates over past years. In this section, the growth mechanisms of MI CNTs, MF CNTs, and CNC/CMCs are reviewed.

3.4.1 Growth Mechanisms of CNTs Produced via Metal-Catalyst-Involved Route

3.4.1.1 Growth Modes

Investigating CNT growth mechanisms is difficult especially at the molecular or atomic level. In part this is due to the number of growth parameters at CVD play. However, earlier studies on carbon filament formation of metal catalyst particles shed light on mechanisms of CNT growth, which consists of: (1) absorption and dissociation of gas precursors, (2) carbon diffusion over/into the particle, (3)

formation of carbon filament, and (4) migration of carbon species to form the top area of the filament. Through these proposed procedures, two possible scenarios of growth modes were reported, as discussed in the previous paragraph, the tip-growth mode and the base-growth mode (Figure 3.9).[200]

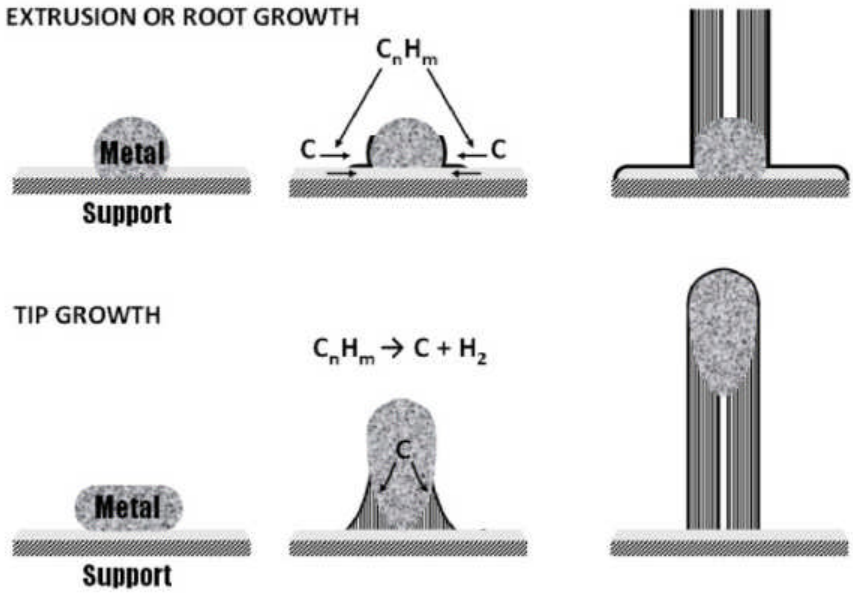

Figure 3.9: Schematics showing the growth modes of base-growth and tip-growth of carbon filaments.[200]

3.4.1.2 Growth Mechanisms Based on Experimental Findings

The mechanisms behind the growth of CNTs *via* metal-involved CVD routes remain a highly debatable topic, despite the considerable efforts invested over the years. From a fundamental point of view, there is still a discord over a consortium of issues, such as the states of the metal catalysts and the diffusion pattern of carbon at growth. To date, experimental findings generated with the aid of sophisticated characterisation techniques (*in situ* HRTEM, *in situ* XPS, *etc.*) have provided numerous insight into the possible mechanisms at play.

The question of the exact chemical and physical state of the active catalyst during CNT growth is yet to be answered.[64, 219] For common metal catalysts, such as Ni and Fe, there is a variety of speculations, none of which has gained ascendency. Several early investigations probing the chemical states of Ni and Fe on the basis of *ex situ* measurements showed conflicting results. Baker and his co-workers proposed that metallic element was the active catalyst for CNF growth;[220, 221] whilst Endo and many others advocated that carbide was responsible for catalysis.[222-224] However, *ex situ* studies mean that the catalyst could have time to undergo phase transition or form carbide upon cooling, owing to excess carbon supply; thus it might not be that accurate in revealing the steady catalyst state at growth.

Recent developments in *in situ* TEM and XPS techniques have enabled extensive investigations of the growth mechanisms of carbon nanostructures from both kinetic and energetic considerations.[225] Helveg *et al.*[226] pioneered the demonstration that Ni catalyst particles remained crystalline with well-faceted shape during low-temperature, *in situ* CVD experiments; Lin *et al.*[227] and Hofmann *et al.*[14, 228] have also arrived at similar conclusions. However, *in situ* TEM and ED observations, performed by Yoshida *et al.*,[229] Sharma *et al.*,[230] and Feng *et al.*[231] showed otherwise, by experimentally confirming that CNTs were generated from metal carbide (iron carbide), although Fe were used in these investigations.

The physical state of metal catalysts at growth is another area where no decisive conclusion has been reached. Are metal catalyst NPs in liquid state, quasi-liquid state (fluctuating crystalline), or in solid form (crystalline)? Recent *in situ* TEM

investigations suggest that the metal catalyst stays in its solid or quasi-liquid form during growth, by presenting clear lattice diffraction patterns.[14, 227, 229-231] However it is worth pointing out that these growth trials took place at relatively low temperatures. Others have concluded that the active catalyst was in a liquid phase, by considering the exothermic nature of hydrocarbon decomposition on metal surfaces and the quenching behaviours of melting point of NPs.[148, 232, 233] Moreover, a few experiments have shown that the catalyst particles experienced structural deformation or re-shaping[14, 222, 234] during the growth of MWNTs, which might lead to the impression that the catalyst was liquid at growth. However, it has been posited that this structural re-shaping was caused by the mechanical forces exerted by the surrounding graphitic layers, while the catalyst particle stayed in its solid form.[222, 234]

A key mechanism, namely the vapour-liquid-solid (VLS) model, was pioneered by Baker[235] and then successfully used by Saito[236] to explain the critical role played by metal NPs in CNT growth. According to this model, the decomposition of carbon-containing gases first takes place on the surface of metal NPs, followed by the diffusion of carbon atoms into liquidised metal particles to form metal carbides. Further supply of carbon sources results in the supersaturated state of nanoclusters with carbon, and finally carbon islands precipitate on the particle surface, and nucleate CNTs.[101, 232, 237] As a characteristic of the VLS process, bulk diffusion of carbon occurring within catalyst particles becomes the major carbon transport mechanism. By means of experimental HRTEM observations and theoretical molecular-dynamic simulations, Gavillet *et al.*[237] suggested a root growth mechanism

for SWNTs based on the VLS model, where carbon atoms were structured into the tube base by a diffusion-segregation process. Another obvious feature of the VLS process was the formation of metal carbides (eutectic compounds), owing to the molten catalysts during CNT synthesis. Homma *et al.*[101] grew SWNTs over Fe and Co NPs on a silica substrate and indicated a carbon-metal eutectic compound formation. They showed that the eutectic point of nanosized Fe, Co and Ni with carbon was reduced to 700-800°C owing to the size effect of NPs, and concluded the CNT growth was mediated by the VLS mechanism. An *in situ* TEM experiment performed by Yoshida *et al.*[229] also suggested that carbon atoms adopted bulk diffusion through iron carbide NPs during the CNT growth. By examining the metal-carbon phase diagrams, Deck and Vecchio proposed that a successful metal candidate for supporting CNT growth would exhibit rapid carbon diffusion, adequate carbon solubility and limited carbide formation.[172]

In contrast, surface diffusion describes the process of migration of absorbed carbon atoms over the catalyst surface. An earlier growth model, related to surface diffusion of carbon species onto catalyst particles, was proposed by Oberlin *et al.*[224] to illustrate the tubular filament growth by catalytic effect. Recently, surface diffusion mechanism has been favoured in surface-bound, low-temperature CVD processes. Seidel *et al.*[102] succeeded in growing SWNTs at 600°C, using different catalysts, and proposed a surface diffusion model. This in particular indicates that rapid diffusion over surfaces (of particles, support, even grown tubes) caused the fast growth rates of SWNTs. Helveg *et al.*[226] demonstrated that carbon atoms were

preferably absorbed at step edges of Ni *via* surface diffusion, by means of *in situ* TEM observation, and density functional theory (DFT) calculations. Moreover, Hoffman *et al.*[238] inferred that sub-surface diffusion and incorporation of carbon in transition metals was more general, through studying the diffusion pattern of carbon on a Ni particle.

The diffusion process has been regarded as the rate-limiting step in CVD growth of CNTs.[238, 239] The two modes of diffusion process, bulk diffusion and surface diffusion, contribute competitively. Wang *et al.*[240] claimed that the relative contribution of the two diffusion pathways depended on the size of the catalyst particle. The smaller the catalyst size was, the more dominant surface diffusion would be.[13, 238] Interestingly, for catalyst NPs with moderate sizes, the surface and bulk diffusion contributed equally to the transportation of carbon species.[227, 240] However, at low temperatures, surface diffusion has been assumed to be the more active diffusion process, compared to bulk diffusion, owing to the lower activation energy for surface diffusion.[102, 173]

Regarding the catalysis of metal NPs, various effects such as melting point depression, higher reactivity, larger surface area to volume ratio, and carbon solubility variation can be applied, owing mainly to the size confinement of NPs, which could give rise to surprising results in the growth of CNTs.[146, 219] As for noble metals, such as Au, Ag, Cu, and Pt, the successful realisation of SWNT growth employing these NPs has led to in-depth exploration of their catalytic activities. Unlike transition-group metals, noble metals have extremely limited solubility for

carbon and negligible carbide formation; thus the VLS model has to be reviewed under this circumstance. However, it has been inferred that noble metals can dissolve carbon effectively for CNT growth, when they are in nanometer scale (<5 nm). This allows the NPs to present many more surface-atoms, which are catalytically active ones with low coordination; furthermore, the oxide-substrate-supported NPs can interact dramatically with the support underneath, which might lead to further charge transfer to activate noble metal NPs to some extent, for example, Au on SiO_2.[146, 219]

3.4.1.3 New Insights into the Growth Models

For CNT growth by means of surface-bound CVD, various models have been proposed on the basis of the synthetic routes and conditions. To date, no single universal mechanism exists that encapsulates the entire range of growth specifics appropriately. In this sub-section, several modern models, describing the growth of CNTs with metal catalysts, are reviewed.

In situ observation of catalyst performance during surface-bound SWNT growth inspired the proposal of the 'catalyst re-shaping' model.[14] Based on the results obtained by *in situ* TEM and XPS, Hofmann *et al.*[14] revealed that Ni nanoclusters remained in crystalline states and re-shaped on the silica support during carbon cap formation and subsequent tube growth. This model highlighted the importance of catalysts' dynamic re-shaping with regard to carbon cap origination and stabilisation, and suggested that the structural selectivity of grown tubes was influenced by the interplay between carbon network formation and catalyst particle deformation.

A novel model proposed by Rümmeli *et al.*[216] has identified the critical role played by oxide substrates during CNT growth *via* surface-bound CVD. By demonstrating the rational synthesis of MWNTs from Fe and Co particles on alumina, they revealed that the grown CNTs exhibited roots anchored directly onto the oxide supports, rather than the metal catalyst particles. In turn, they indicated that the function of catalyst particles was merely to provide nucleation caps of CNTs, but oxide supports played an important role in boosting the growth of CNTs, as evidenced by the TEM micrographs (Figure 3.10),[218] which clearly shows the alignment of CNT graphitic walls with the alumina lattice fringes.

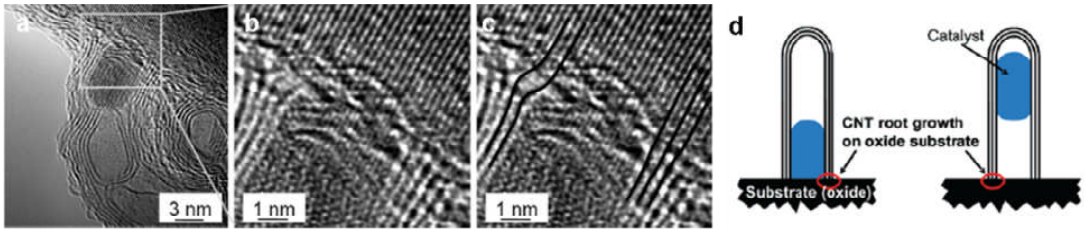

Figure 3.10: Investigations of the function of oxide substrates during CNT growth. (a-c) TEM micrographs showing a cross-section view of a CNT root at the oxide support surface.[218] (a) The Co catalyst particle resides in the core of the tube; the outer walls of the CNT align themselves with the lattice fringes of the alumina support. (b) A magnified image of the boxed region in (a). (c) A copy of (b) with drawing lines added to highlight the alignment of the graphitic planes with the alumina lattice fringes. (d) Schematic models illustrating that CNTs grow directly from the oxide support after nucleation.[216]

Another new mechanism which implied that catalyst supports actively participate in the growth of CNTs has been derived.[241] Therein, the activation of catalyst support for CNT growth can be simply dictated by an efficient chemical treatment, which

changed the acid-base properties of the substrate. Compared to acidic supports, enhanced growth of CNTs was found on basic supports, where the presence of basic sites accelerated the aromatization and reduced the complexity of carbon precursor molecules, as indicated in Figure 3.11.[241] This model also shed new light on the role of water as modifying the acidity of the support surface in the super-growth CVD reactions.

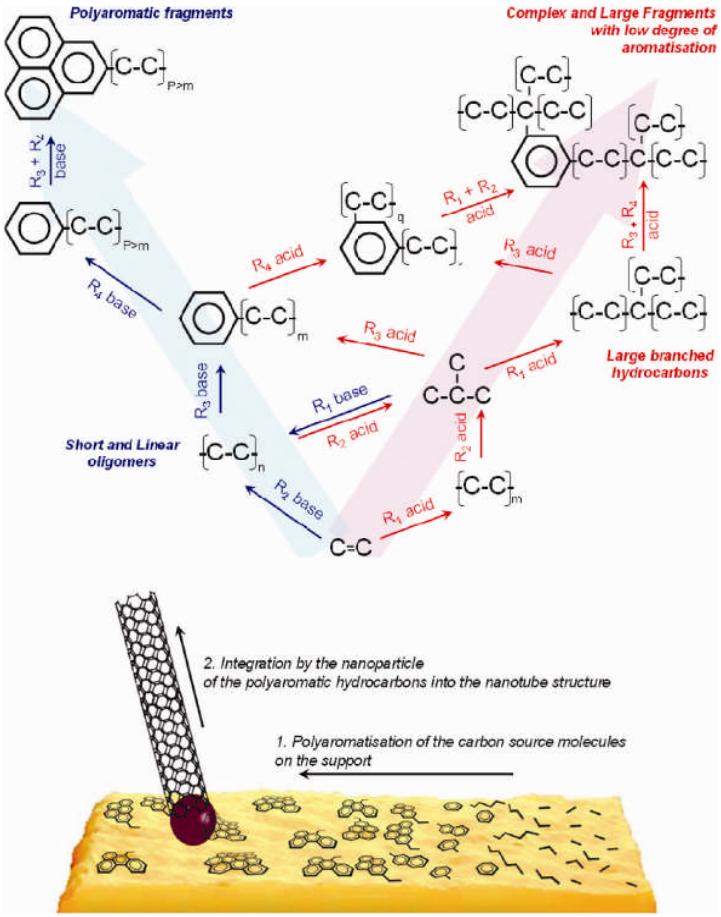

Figure 3.11: (Top) Chemical mechanism undergone by carbon precursors adsorbed on the surface of the supports. Basic supports led to the forming of highly aromatic fragments, whilst acidic supports produced large-branched, complex hydrocarbon segments with low degree of aromatisation. (Bottom) Scheme showing the new growth mechanism of CNTs by surface-bound CVD, which relied on the acid-base properties of surfaces. In this mechanism, CNT growth emanated on the support and continued on the nanoparticles, where aromatic fragments were assembled to form CNTs.[241]

Veering away from the classic VLS model, which laid stress on the dissociation-diffusion-precipitation process of atomic carbons, a polymerization-like mechanism was suggested in the latest studies,[96, 110, 242] where the CNT growth proceeded by adding new aromatic fragments (building blocks), generated from pyrolysis of unsaturated carbon feedstock, such as C_2H_2. The focus on carbon precursors in building up CNTs has also been put forward by Reilly *et al.*,[243] as they came up with a 'free-radical-condensate (FRC)' model, which stated that the presence of radicals in pyrolysed hydrocarbon species enabled rational rearrangement of carbon bonds, leading to the formation of CNTs.

3.4.2 Growth Mechanisms of CNTs Produced via Metal-Catalyst-Free Route

The latest development of CNT synthesis has ignited an entire research field, owing to the fact that the growth of CNTs was realised with no metal at all: the non-metallic species (oxides, carbon species, *etc.*) can act as the catalyst. The metal-catalyst-free route for producing CNTs indeed opened up a new avenue in nanotechnology,[64, 92] however there appears to be no universal, convincing model to represent the growth mechanisms involved.

Various kinds of oxide NPs (such as Al_2O_3,[21, 244] SiO_2,[19, 21, 181, 245-247] ZnO,[248] ZrO_2,[249] Eu_2O_3,[21, 250]) have proven catalytically active in catalysing CNT growth. In particular, there have been several investigations focusing on the CVD synthesis of

CNTs on SiO_2 substrates, with large disagreements over the growth mechanisms. Huang and his co-workers[21] revealed after careful XPS measurements, that the presence of SiO_2 NPs was responsible for the growth of SWNTs at high temperatures. They further suggested that only a nanoscale curvature was needed to generate SWNTs, and the defects and distortions created within the quasi-liquid SiO_2 NPs could also enhance decomposition of hydrocarbons. This result is consistent with Liu and Cheng's findings,[20] where the importance of oxygen-containing SiO_x NPs was highlighted through *in situ* TEM experiments and DFT calculations. Furthermore, Page *et al.*[245] employed quantum-chemical molecular dynamics simulations to investigate the SWNT nucleation on SiO_2 NPs. In their study, a vapour-solid-solid (VSS)[20, 245] mechanism, rather than a VLS mechanism, was suggested to explain SWNT generation on SiO_2 catalysts. However, Bachmatiuk *et al.*[247] observed that the SiO_2 NPs were carbothermally reduced to SiC during the synthesis of CNFs and stated that the VLS mechanism was applicable in this sense; whilst another route of mechanisms has been argued by Liu *et al.*,[246] who proposed that the SiO_2 substrate subjected to high-temperature H_2 annealing would present defects on its surface, which provided stack-up sites for facilitating the deposited carbons to self-assemble into SWNTs.

Most recently, alternative routes for generating CNTs by employing pure carbon species in absence of any metal catalyst have emerged. Investigations have shown that nanodiamond,[251] activated carbon,[252] porous carbon,[253] carbon aerogel,[254] carbon NPs,[255, 256] and even carbon nanotubes[257] can catalyse the growth of CNTs *via* the

self-assembling route. For example, Song *et al.*[252] discerned that carbon self-assembly plays a key role in CNT evolution by conducting CNT growth experiments on both lanthanide metal oxides and activated carbons. They pointed out that the self-function of carbon species originates from the anisotropic properties of sp^2-hybrid carbon structures (such as CNTs, layered carbons).

3.4.3 Growth Mechanisms of Coiled CNT/Fs

Coiled CNTs are helical carbon nanostructures, created when carbon pentagon (C_5) and heptagon (C_7) rings are incorporated into carbon hexagonal networks of the graphene layers of normal 'straight' nanotubes. The existence of coiled CNTs was theoretically predicted in the early 1990s[80] and they were first experimentally synthesised in 1994.[258] However, the large-scale and structural-selective production of coiled CNTs remains problematic, and one of the plausible reasons lies in the lack of fundamental understanding of the architecture and growth mechanism of coiled CNTs.[259] The growth mechanisms proposed so far for coiled CNTs have always been relating to the C_5 and C_7 atomic rings, however, there have been disagreements regarding the distributions of these carbon rings within the atomic structures of coiled CNTs, as to whether the C_5 and C_7 rings were decorated defects and formed periodical pairs to induce the coiling (Figure 3.12 (a)),[28, 260] or if they were intrinsic building blocks, as stated in the Haeckelite model,[261] where the C_5 and C_7 rings constituted a large portion of the helical structures.

On the other hand, to rationalise the formation of coiled CNFs (referring to the dense helical nanostructures with no inner hollow), several growth models (as shown in Figure 3.12b-d) have been proposed in the previous literature, but none of them addresses the growth of coiled CNFs universally. The prevailing growth models are based on anisotropic extrusion of carbon from different facets of catalyst particles, which has been attributed to catalyst topography,[115, 178, 262-264] localised orientations,[79] and inhomogeneity of chemical composition within a catalyst particle[175, 176, 265] (Figure 3.12 (b)).

It is generally recognised that the morphology and yield of the grown carbon nanostructures are influenced by the type of catalyst used. Bandaru *et al.*[174] proposed that the repulsive interactions at the interface between the growing graphitic structure and the non-wetting catalyst materials can promote nonlinear growths (Figure 3.12 (c)). Such non-wetting catalysts, as In, Sn, *etc.*, have been widely proven experimentally to lead to the production of coiled CNT/Fs. Jian *et al.*[111] revealed that the use of Cu enabled an enhanced process of C_2H_2 adsorption and polymerisation, which would facilitate the formation of helical CNFs. Very recently, Chiu and his co-workers[18] used an efficient, cooperative catalytic system of coupling K and Ag to achieve successful synthesis of CNCs *via* C_2H_2-CVD. Based on the observed results, they proposed a 'cooperative catalyst enhanced VLS' growth model (Figure 3.12 (d))[18], which stated that the liquid phase K helped with C_2H_2 decomposition in a recycling manner, while Ag NPs assisted the extension of 1-D carbon nanowires (NWs), and the curled effect of the NWs was induced by the adhesive force between

the K liquid and the carbon. From my point of view, it is reasonable to have particular growth mechanisms for specific growth routes and conditions, given that there stays a variety of synthetic strategies as well as resulting materials in the field of coiled CNT/F growth, differing from case to case.

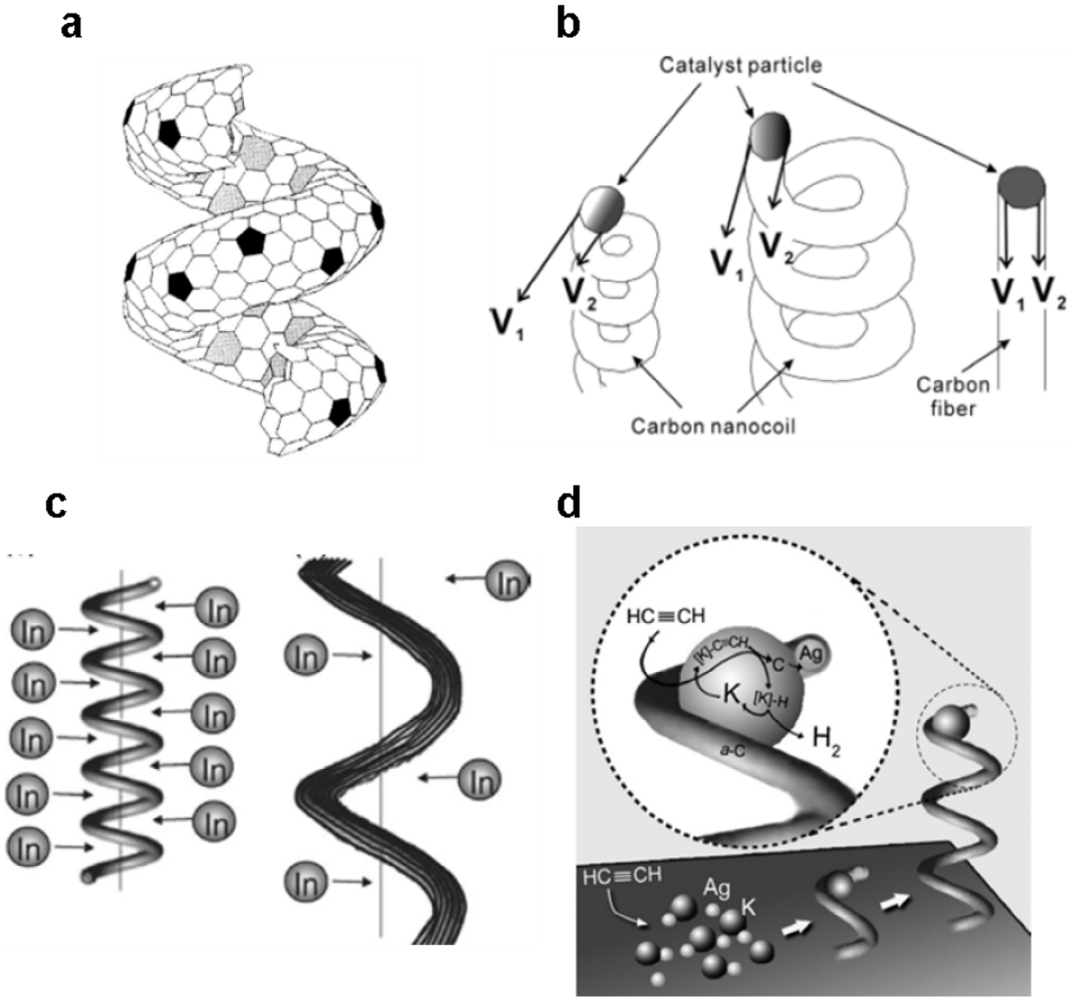

Figure 3.12: A collection of growth models of coiled CNT/Fs. (a) Regular insertion of C_5-C_7 pairs as defects causes the positive and negative curvatures on tubular structures.[28] (b) CNC/Fs grown from various Sn compositions, illustrating that the large gradient of Sn composition induced the coiling.[175] (c) Non-wetting behaviour of In plays an important role in coil formation.[174] (d) Cooperative effects of Ag and K on the formation of coiling structures.[18]

3.4.4 Short Summary

In this section, the role of catalysts in the growth of carbon nanostructures by surface-bound CVD has been studied. There appears to be a variety of models for the growth mechanisms of carbon nanostructure formation, and none of them completely explains the growth scenario, which is partially due to the fact that specific mechanisms are needed for particular synthetic methodologies and reaction conditions.[4, 92] However, huge progress has been made, including the discovery of new catalysts and the improvement of existing models.

3.5 Overview

This chapter has provided an overview of the field in the growth of carbon nanostructures by surface-bound CVD techniques, with special focus on the roles and effects of catalysts on CNT growth. This constitutes the background and fundamental understanding for the work presented in this thesis. A brief description of surface-bound CVD technique is also provided to relate the review to the experimental methodologies developed in this thesis. In Chapter 4, the growth of CNTs on the oxide substrate ($SrTiO_3$) by CVD (Section 3.2.3) *via* metal-catalyst-involved route will be discussed, with investigations on the influences of growth-control aspects (Section 3.3). In Chapters 5 and 6, the growths of CNTs by metal-catalyst-free CVD on both single crystal $SrTiO_3$ (001) substrates and

poly-crystalline BST surfaces (Section 3.3.4.1) will then be described; the growth mechanisms are also probed (Section 3.4.2). Finally, in Chapter 7, the fabrication of coiled CNT/Fs will be featured, in relation to the content mentioned in this chapter (Sections 3.1.1, 3.3.2, 3.3.4, and 3.4.3).

Chapter 4：

Metal-Catalyst-Involved Growth of Carbon Nanotubes (CNTs) on $SrTiO_3$ (001) Substrate

4.1 Background

Numerous studies of metal catalysed CNT growth on oxide substrates *via* CVD have been reported. The main aim of these investigations was to fabricate novel CNT-based nanodevices and understand the CNT growth mechanisms.[4] In typical metal-catalyst-involved CVD processes, the design of a catalyst system is essential to the growth of CNTs (especially on substrates), as the chemical and geometrical aspects of catalysts (size, shape, composition, lifetime, activity *etc.*) are controlled by the catalyst design (choice of catalyst/substrate material, synthetic methods *etc.*), and can greatly affect the morphologies and properties of grown CNTs.

Transition metals (such as Fe, Ni) are the most popular choice for CNT growth catalysts. A myriad of approaches (wet chemistry, physical metal deposition, *etc.*) have been developed to tailor these metals on oxide substrates for generating catalysts in a controlled manner. In this investigation, Fe and Ni were selected as catalysts for the surface-bound growth of CNTs. The catalyst fabrication was carried out in a UHV system. The reason for using the UHV kit to make the catalysts was based on the fact that it has been an established technique within the research group to grow metal nanocrystals on $SrTiO_3$ (001) supports, where a selection of metals (such as Fe[23], Co[22], Ag[24], Au[26], Pd[25], and Cu[27]) were successfully synthesised and characterised.

Apart from metal catalysts, the catalyst substrate plays an active role in the CVD process thus the choice of substrate is also of particular importance.[266] Although promising CNT growth have been attained on various types of oxide supports, such

as SiO_2, Al_2O_3, and MgO, limited investigation has been reported on the growth of CNTs on $SrTiO_3$ substrates.[214] Interest in the $SrTiO_3$ (001) surface emanates from its remarkable ability to support distinct nanosized metal shapes,[23-27] the combination of $SrTiO_3$ and CNT may spur novel properties and lead to the next generation of nanoelectronic devices, as $SrTiO_3$ has already stimulated intense interests in using it in the fields of oxygen sensors,[267] fuel cells,[268] and oxide-based electronic components[269] due to its photocatalytic and dielectric properties.

In this chapter, the growth of CNTs on $SrTiO_3$ (001) substrates with the aid of metal catalysts is investigated. Starting with the STM study of metal nanocrystal grown on $SrTiO_3$ (001) surface, it is shown that the metal catalyst particles can be fabricated in a controlled manner and characterised prior to the CVD reaction. This is followed by a detailed investigation on an array of CNT growth parameters (carbon feedstock, catalyst design, growth temperature, and carrier gas flow rate), where the optimised conditions for growing vertically aligned CNTs has been sought. Further design of the catalyst has also been performed, leading to encouraging CNT growth under unconventional growth conditions (fast heating, catalyst pretreatment under oxidising environment).

4.2 Experimental Details

Epipolished $SrTiO_3$ (001) (STO (001) for short) single crystals (PI-KEM Ltd, UK)

were employed as the substrates for the deposition of metal catalysts and growth of CNTs. The catalyst particles were fabricated using a JSTM-4500XT UHV system, which mainly incorporates a treatment chamber, an Ar^+ ion-sputtering source, a metal deposition kit and an STM, enabling the designing and characterisation of the substrates prior to the CVD process. To create desired substrates for subsequent growth of CNTs, the STO (001) samples were first introduced to the vacuum system without any pretreatment, and were degassed by resistance heating at 600˚C for up to one hour, then the samples were Ar^+ ion-sputtered for 10 min with an ion flux of 100 $\mu A/cm^2$, followed by selective annealing at UHV at approx. 1200˚C for 15 min. The preparation method led to a *c*(4×2) reconstructed STO (001) surface (with annealing), or a sputtered one (without annealing). Fe or Ni was deposited onto the prepared STO surfaces in UHV from an e-beam evaporator using 99.99% pure Fe or Ni rods (Goodfellow Cambridge Ltd, UK). The samples could then be annealed in UHV at approx. 400˚C for 15 min to form shaped nanocrystals, which were probed by STM. Atmospheric CVD was used to perform the growth of CNTs, details of which can be found in Chapter 2.

As for product characterisation, the as-engineered STO samples were imaged by STM prior to the CVD process. STM images were captured in constant current mode, using an electrochemically etched W tip, and then processed with WSxM software. The as-produced CNTs were characterised by SEM (JEOL JSM 840F, 5 kV & JSM 840A, 10 kV), Raman spectrometer (JY Horiba Labram Aramis imaging confocal Raman microscope, 532 nm laser), and were further analysed by TEM (JEOL

JEM-2010, 80-200 kV, and JEM-4000HR, 80 kV). TEM characterisations in this study were conducted by Dr Antal Koos from the Grobert's research group.

4.3 Results

In this section, the growth of CNTs on $SrTiO_3$ (001) substrates by metal-catalyst-involved CVD is reported. Firstly, an STM study of STO supported metal nanocrystal growth is presented, which provides information on the metal/STO (001) system for the design of a CNT growth catalyst. The growth of CNTs on STO (001) substrates is then detailed in terms of first attempts of using different carbon feedstocks, growth parameter investigations, and key achievements on growing CNT carpets. Unusual growth conditions are also explored, indicating that STO can function as a suitable substrate for CNT synthesis.

4.3.1 STM Study of Metal Nanocrystal Grown on $SrTiO_3$ (001) Substrate

Ni was selected as the metal representative (instead of Fe) for this STM study, although there were also some STM data of Fe produced by the author. The reason for presenting Ni data lies in: i) that there has been limited investigation on the STM of Ni/STO (001) system, researching in this system would be helpful to gain

knowledge on the structures and properties of STO supported Ni nanoparticles (NPs), which was therefore expected to benefit the design of Ni catalyst for the growth of CNTs. As for Fe, there was already a publication[23] on the same topic which can be referred to; ii) that the Ni was the only metal within the UHV metal deposition kit available for CNT growth (short of Fe) during the period of carrying out the STM studies. .

4.3.1.1 Time-Dependent Particle Size Change (at Constant T)

To explore the effect of the annealing period on the size change of STO supported Ni NPs, elevated-temperature STM imaging[270] (at 350˚C) was performed on the sample to acquire images at different times. The representative STM images (Figures 4.1a-4.1c) show the evolution of STO supported Ni nanocrystals at constant annealing temperature (350˚C) with increasing annealing time. The Ni (1 monolayer (ML) thickness) was deposited onto a room-temperature, $SrTiO_3$ (001)-*c*(4×2) substrate followed by UHV annealing at 350˚C. It is observed that both Ni-depleted areas and Ni particle sizes enlarge, as the annealing time is increased, indicating that Ostwald ripening occurs at elevated temperatures. Hence the annealing period plays a leading role in causing the nanocrystals to ripen at a given temperature. Original data plot (Figure 4.1d) and fitted curve (Figure 4.1e) shows the relationship between the radius of Ni (R) nanocrystals against the annealing duration (t) applied to the sample, where the mathematical expression can be interpreted as:

$$R = 0.42 + 0.34t^{0.55}$$

This is consistent with the exploitation of the Gibbs-Thomson effect on grain growth, where the particle radius (R) is expected to increase with the annealing period (t) as $t^{0.5}$.

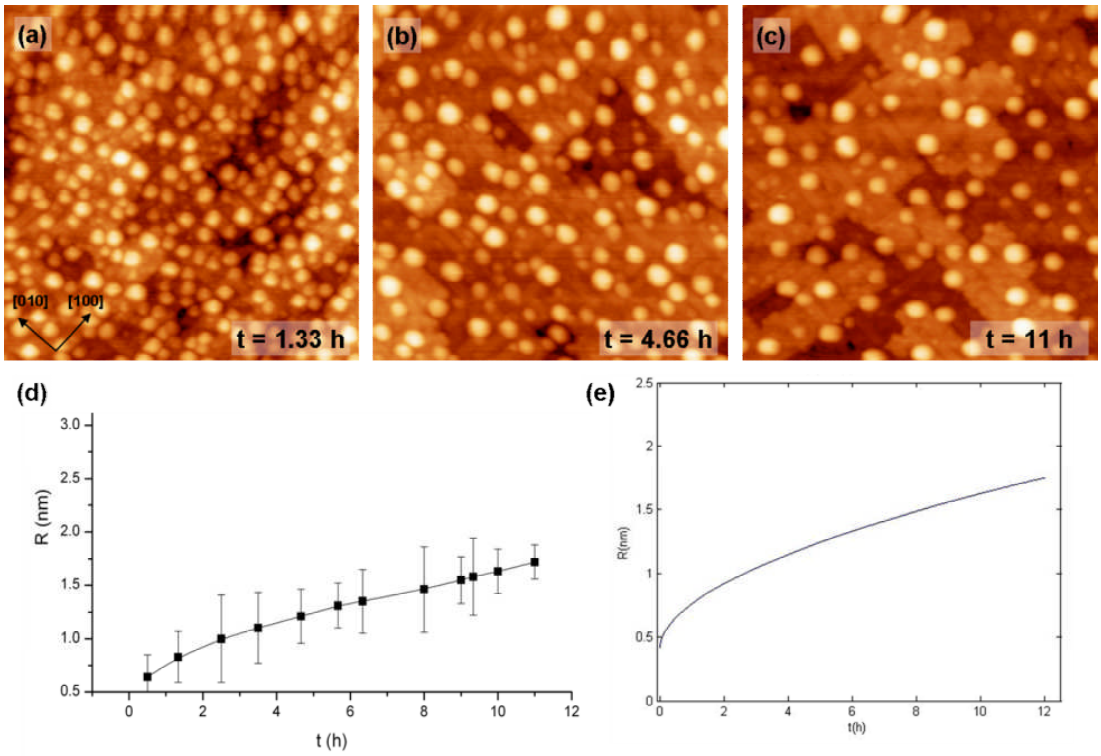

Figure 4.1: Hot-STM study of $SrTiO_3$ supported Ni nanocrystals at constant annealing temperature (350°C) with increasing annealing time. The Ni (1 ML) was deposited onto a room-temperature, $SrTiO_3$ (001)-c(4×2) substrate followed by UHV annealing at 350°C. Representative STM images (a-c) were taken at different annealing times, as marked on the images. (For images (a-c): Image size: 50 × 50 nm^2, V_s = 1.1 V, I_t = 0.1 nA). (d) Original data plot showing the radius of Ni NPs against the annealing durations applied to the sample. (e) Fitted curve showing radius of Ni NPs against the annealing durations applied to the sample.

4.3.1.2 $SrTiO_3$ Supported Ni Nanocrystal Shape Formation

Depositing Ni (3 ML) onto a room-temperature, $SrTiO_3$ (001)-*c*(4×2) substrate, followed by a UHV annealing at 390˚C for 15 min gives rise to the shape formation of Ni nanocrystals, as shown in Figure 4.2a. The grown Ni nanocrystals are randomly distributed, without preferential nucleation along the terrace edges of the substrate, and tend to form similar sized, square-like shapes on the STO surface. Further annealing induced ripening and allowed the nanocrystals to attain their equilibrium shapes.

No.	Height (*h*) (nm)	Length of Top Square (*l*) (nm)	Length of Bottom Square (*b*) (nm)	*l*/*h* ratio	Volume (nm^3) $V=\frac{1}{3}(a^2+ab+b^2)h$
1	2.04	1.8	4.7	0.88	23
2	1.86	1.65	4.3	0.89	20.4
3	1.83	1.6	4.2	0.87	16.4
4	1.72	1.5	3.9	0.87	13.4
5	1.56	1.31	3.5	0.84	9.6
6	1.55	1.3	3.5	0.84	9.55
7	1.55	1.3	3.5	0.84	9.55
8	1.54	1.3	3.49	0.84	9.45
9	1.54	1.27	3.45	0.82	9.18
10	1.54	1.25	3.43	0.82	9.04
11	1.39	1.15	3.12	0.83	6.79
12	1.39	1.1	3.07	0.83	6.44
13	1.38	1.1	3.05	0.84	6.38
14	1.22	1.07	2.8	0.88	4.87
15	1.21	1.05	2.6	0.87	4.27
16	1.04	0.9	2.38	0.86	3
17	1.03	0.85	2.31	0.83	2.75

Table 4.1: The dimensional information of $SrTiO_3$ supported Ni nanocrystals gathered from the STM image of Figure 4.2b.

Figure 4.2b shows an STM image of the same sample treated by further annealing at 320˚C for 13 hours. The prolonged annealing leads to the phenomenon that the Ni shaped nanocrystals grown on the STO substrate have achieved their equilibrium states.[23, 25] The arrow marked as 'i' denotes the line profile shown in Figure 4.2c, which indicates the height and shape of the measured nanocrystal. The Ni nanocrystals adopt truncated pyramid shapes on a $SrTiO_3$ (001)-*c*(4×2) surface; detailed information gained from image analysis for Figure 4.2b is presented in Table 4.1. It is worth mentioning that the tip convolution effects would result in particle size enlargement, but have no influence on the heights of the nanocrystals.

The height information on the nanocrystals was gathered as shown in Table 4.1. It is interesting to note that the nanocrystal heights are quantised into height steps of 1.8 Å, which could lead us to conjecture that the truncated pyramid shaped Ni have a face-centred-cubic (fcc) structure ($a_{fcc\text{-}Ni}$ = 3.52 Å; $a_{bcc\text{-}Ni}$ = 2.77 Å). The ratio of the length (*l*) of the top square to the height (*h*) of these truncated pyramids as a function of volume is shown in Figure 4.2d. The constant ratio of $l/h = 0.85 \pm 0.03$ implies that these pyramidal nanocrystals have reached their equilibrium shape. Figure 4.2e shows a 3D scheme of the equilibrium truncated pyramid-shaped Ni with fcc structure, which possess (001) top facets and four (111) side facets.

These studies on the crystallographic structures of metal particles grown on STO substrates would be helpful for designing catalysts for controllable growth of CNTs. Recent investigation by Chiang *et al.*[17] demonstrated that SWNTs with desired structures can be obtained by tuning the elemental composition of Fe-Ni binary

catalysts. They conjectured that the change of crystallographic structure within the catalyst particles between fcc (as for pure Ni) and bcc (as for pure Fe) can greatly influence the metal-carbon binding during the CNT nucleation.[17] Herein, the identification of the crystal structure of STO supported metal NPs (truncated pyramid shaped-fcc Ni and -bcc Fe[23] on STO surfaces) might also lead to future design in catalysis, *i.e.* Fe-Ni core-shell catalyst NPs.

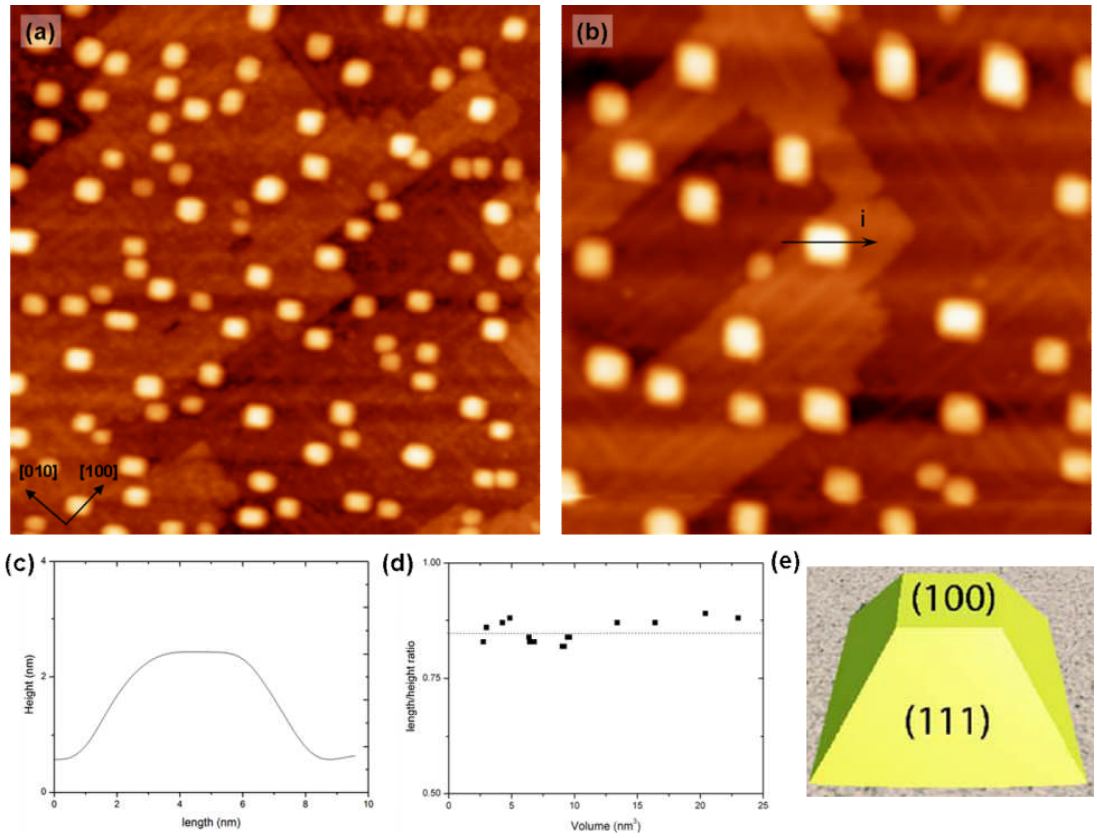

Figure 4.2: (a) STM image of $SrTiO_3$ (001)-c(4×2) supported Ni nanocrystals (Image size: 100 × 100 nm^2, V_s = 1.0 V, I_t = 0.4 nA). (b) STM image of the same sample, having undergone further annealing at 320°C for 13 hours (Image size: 70 × 70 nm^2, V_s = 1.0 V, I_t = 0.4 nA). (c) A line profile indicates the height and shape of a nanocrystal. (d) The l/h ratio of the nanocrystals is constant with volume at l/h = 0.85±0.03. (e) A 3D scheme of an fcc truncated pyramid-shaped Ni.

4.3.2 Growth of Carbon Nanotubes (CNTs) on $SrTiO_3$ (001) Substrate

4.3.2.1 First Attempts at Growing CNTs by Using Different Carbon Precursors

Since there has been no scientific report on employing $SrTiO_3$ substrates as a catalyst support for the growth of CNTs, it became necessary at the initial stage of the project to test the feasibility of this type of material with regard to functioning as a CNT growth substrate. The laboratory set-up for CNT growth relied on a set of aerosol CVD equipments (such as ultrasonic generator, plastic tubing), and hence carbon precursors in liquid forms (toluene and ethanol) were selected to serve this 'first attempt' purpose. The reason for using toluene was on a basis of inspirations drawn from the past practical experience within the group, where good results of CNT synthesis had been achieved *via* aerosol CVD by employing toluene as the carbon feedstock;[55, 69] whilst selecting ethanol was due to the fact that there had been a plethora of reports on the promising growth of CNTs by using ethanol as the carbon source. Indeed, several advantages of using ethanol in CVD reactions for CNT growth were already identified: low cost, practical ease in handling, easy to undergo thermal decomposition, non-hazardous and environmentally friendly.[118, 162] It was also proposed that ethanol could benefit to the CNT synthesis because its molecule contains oxygen. For the catalyst substrate preparation, Fe and Ni were used as catalyst metals. Fe (or Ni) (3 ML) was deposited onto a 390˚C $SrTiO_3$ (001)-*c*(4×2)

surface and then treated by UHV annealing at 390˚C for 2 hours; truncated pyramid-shaped Fe[23] (or Ni) nanocrystals were formed on the STO support, verified by STM imaging.

4.3.2.1.1 Toluene as a carbon feedstock

The SEM images in Figure 4.3 show the results of CVD experiments conducted at a growth temperature of 800˚C using Ni (Figure 4.3a) and Fe (Figure 4.3b) as catalysts, with toluene as the carbon feedstock. The carrier gas during growth was a mixture of Ar (550 sccm) and H_2 (50 sccm) and growth period was 30 min. The substrate surface is free of carbon tubular structures, indicating that toluene induces poor growth of CNTs on $SrTiO_3$ substrates. In view of the fact that toluene decomposition needs fairly high temperatures, higher growth temperature (800˚C) should have been provided; however, the coarsening process of catalyst particles also becomes severe when high growth temperature was applied (as can be seen in Figures 4.3a and 4.3b), which leads to the formation of large clusters and causes the deactivation of the catalysts.[102]

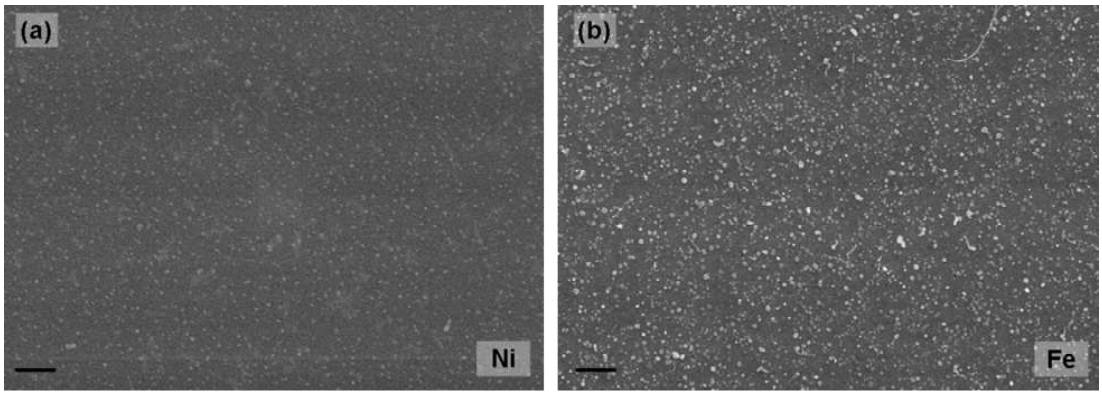

Figure 4.3: SEM images of Ni/STO (a) and Fe/STO (b) sample surfaces after CVD growth using toluene as the carbon feedstock. Scale bars: 1 μm.

4.3.2.1.2 Ethanol as a carbon feedstock

The STM images in Figures 4.4a and 4.4b show the catalyst morphology prior to the CVD process. Ni and Fe adopt fcc and bcc[23] truncated pyramid shapes on the $SrTiO_3$ (001)-*c*(4×2) substrates, respectively. This type of shape formation ought to be able to generate expected catalytic activity. Figures 4.4c and 4.4d show the SEM observations of growth of CNTs on the Ni/STO (Figure 4.4c) and Fe/STO (Figure 4.4d), using ethanol as the carbon source at a growth temperature of 650˚C. The growth conditions for both types of substrates were set to be identical: The gas flow was a mixture of Ar (550 sccm) and H_2 (50 sccm) and growth period was 30 min. Under these CVD conditions, both of the substrate surfaces are covered with networks of tubular structures. Raman spectra, as shown in Figures 4.4e and 4.4f, confirm that these architectures are CNTs. Moreover, by comparing the two spectra, it is interesting to note that a clear 2D peak only shows up in Figure 4.4f, indicating that the Fe catalyst leads to CNT production with better crystallinity and fewer defects.

The successful growth of CNTs on $SrTiO_3$ (001) substrates by using ethanol at relatively low growth temperatures not only expands the current category of CNT substrates reported in the research literature, but also opens up new avenues in CNT synthesis *via* surface-bound CVD. Further investigation centered on the attempt to find the optimum growth conditions by performing parameter studies.

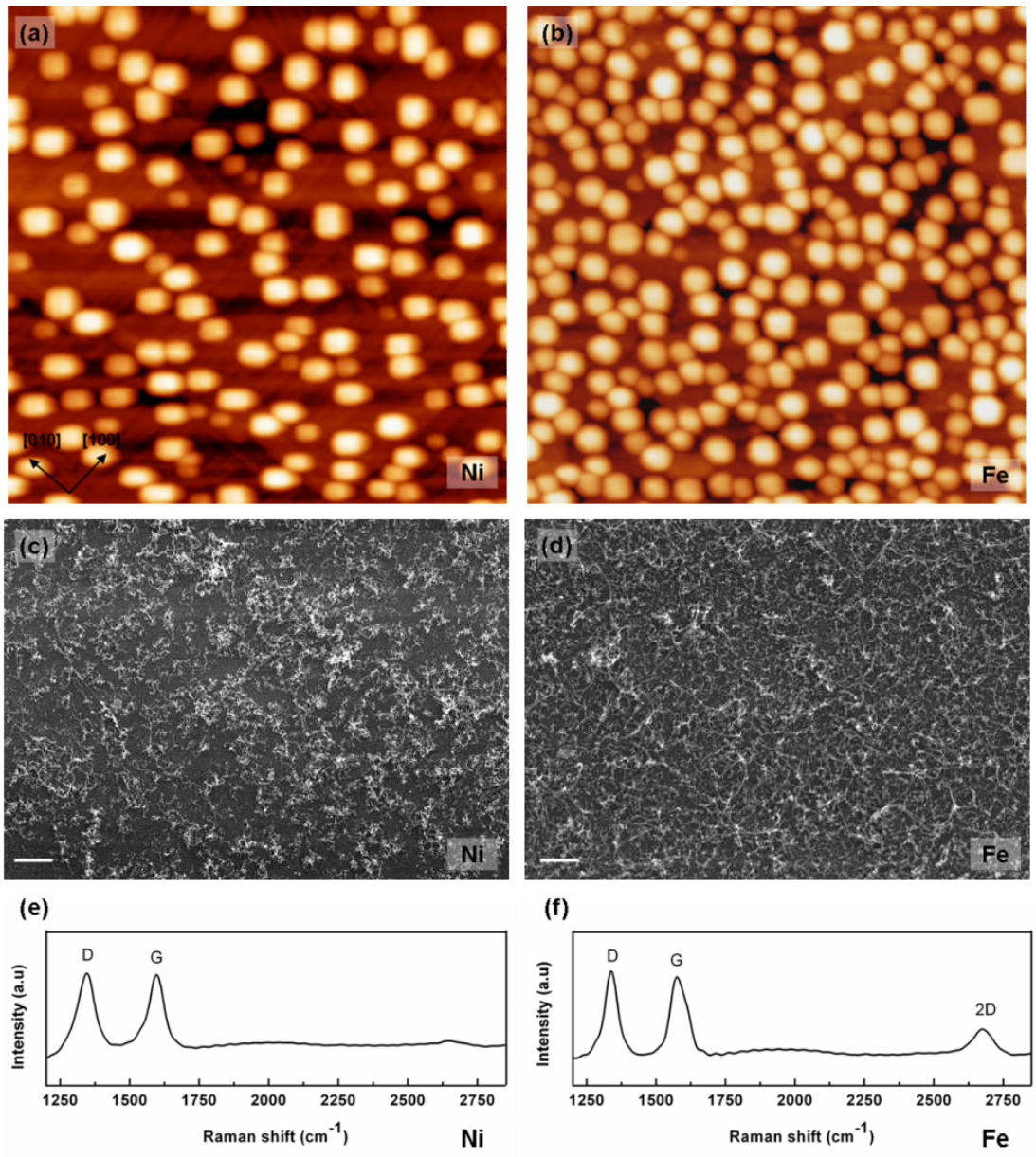

Figure 4.4: Successful growth of CNTs on $SrTiO_3$ (001) substrate, using ethanol as the carbon feedstock. STM images of Ni/STO (a) and Fe/STO (b) taken prior to the CVD process ((a): Image size: 100 × 100 nm^2, V_s = 1.0 V, I_t = 0.3 nA; (b): Image size: 100 × 100 nm^2, V_s = 1.0 V, I_t = 0.08 nA). SEM images of Ni/STO (c) and Fe/STO (d) samples after CVD show nanotube networks. Scale bars: 1 μm. Raman spectra (e and f) confirm the CNT formation on STO substrates.

4.3.2.2 SEM of CNT Growth on $SrTiO_3$ (001) Substrate: Parameter Investigations

As mentioned in Chapter 3, a large array of parameters, such as catalyst morphologies, choices of carrier gases, synthesis temperatures, and reactor technology can in practice influence the outcome of the CNT synthesis. To investigate the trends induced by key parameters and identify the optimum growth conditions for CNT synthesis on $SrTiO_3$ (001) surfaces by ethanol-CVD (EtOH-CVD), case studies were performed using Fe catalysts with the aid of SEM observations. The key reasons for using Fe for the parameter study lies in: i) that Fe was shown to lead to better CNT growth when using ethanol as a carbon feedstock (Section 4.3.2.1.2); ii) that it could facilitate the data comparison in a broader context, as Fe was mainly employed as the catalyst material within the research group.

4.3.2.2.1 Effect of Catalyst Fabrication

Three different Fe/STO catalyst substrates were engineered with an identical Fe dose (3 ML), which are designated as *NP@r-STO* (Truncated pyramid-shaped Fe nanoparticles grown on the $SrTiO_3$ (001)-*c*(4×2) surface), *TF@r-STO* (As-deposited Fe thin films grown on the $SrTiO_3$ (001)-*c*(4×2) surface), and *TF@s-STO* (As-deposited Fe thin films grown on the Ar^+ ion-sputtered $SrTiO_3$ (001) surface), in accordance with their fabrication routes. STM images in Figures 4.5a and 4.5b show morphological information of *NP@r-STO* and *TF@r-STO*, respectively. In Figure 4.5a, perfect shapes of Fe nanocrystals form on the STO surface, accompanied by

notable Fe-depleting surface areas, whereas for the *TF@r-STO* substrate, higher surface coverage of Fe NPs with smaller particle sizes is exhibited, following a room-temperature Fe deposition without further annealing, as shown in Figure 4.5b. It is worth mentioning that several attempts at imaging *TF@s-STO* substrates failed and ended up with STM tip damage or other problems, owing to the rough textures of the sputtered surfaces.

Figures 4.5c-4.5e show a series of SEM images of grown CNT networks on the three distinct substrates, with the corresponding Raman spectra shown in Figures 4.5c*-4.5e*. The growth experiment was performed by EtOH-CVD at a growth temperature of 700˚C for 30 min, with carrier gas flow of Ar (550 sccm) and H_2 (50 sccm). It is observed that the areal density of attained CNT networks on the *TF@s-STO* is the highest (Figure 4.5c), although CNTs were obtained on all three types of substrates. A likely hypothesis is that the sputtering procedure introduces a certain degree of roughness to the surface, hindering the surface diffusion/mass transportation of Fe catalyst species and, therefore, keeping the catalyst NPs relatively small during the CVD process, thus leading to the dense growth of tubes.

Moreover, it is worth noticing that the CNT production on *TF@r-STO* was larger (Figure 4.5e) in comparison with that on *NP@r-STO* (Figure 4.5d), which indicates that supported catalyst NPs without pre-annealing are more efficient in promoting CNT growth. As mentioned in Section 4.3.1.1, Ostwald ripening leads to particle agglomeration while annealing, and the particle sizes increase with the duration of heating. It may happen that some specific, already-formed NPs on *NP@r-STO* are

prone to further ripening during the CVD process and eventually become too large to support the growth of CNTs (which can be observed in Figure 4.5d), resulting in a reduction of the CNT yield.

Raman spectra (Figures 4.5c*-4.5e*) confirm that these grown nanomaterials are CNTs, since D and G peaks are exhibited for all the samples. The calculated G/D ratio for the CNTs grown on the *TF@s-STO* is approx. 1.3, indicating the CNTs are of fairly good quality, compared to those produced on the *NP@r-STO* (Figure 4.5d*, G/D ratio~0.96) and on the *TF@r-STO* (Figure 4.5e*, G/D ratio~1.05).

4.3.2.2.2 Effect of Growth Temperature

Figure 4.6 shows an SEM image library of the growth temperature effect on CNT production. EtOH-CVD was performed on the *TF@r-STO* substrates at a range of temperatures from 650-800°C. The gas flow was a mixture of Ar (550 sccm) and H_2 (50 sccm) with a growth period of 30 min. Both 0.5 ML and 5 ML Fe doses were used to check the feasibility of each growth temperature. From SEM observation, 700°C was found to be the most promising temperature for CNT growth on a $SrTiO_3$ (001) surface (as shown in Figures 4.6b and 4.6e). Lower T (650°C) was proven to be suitable for a small Fe dose (0.5 ML) (Figure 4.6a), but detrimental to high Fe concentration (5 ML), owing to the underfeeding of catalyst particles during CVD (Figure 4.6d). Both Figures 4.6c and 4.6f indicate poor growth when the catalyst system was exposed to 800°C, possibly the catalyst aggregation at high temperatures (800°C) becomes too severe to accommodate the nucleation of CNTs.

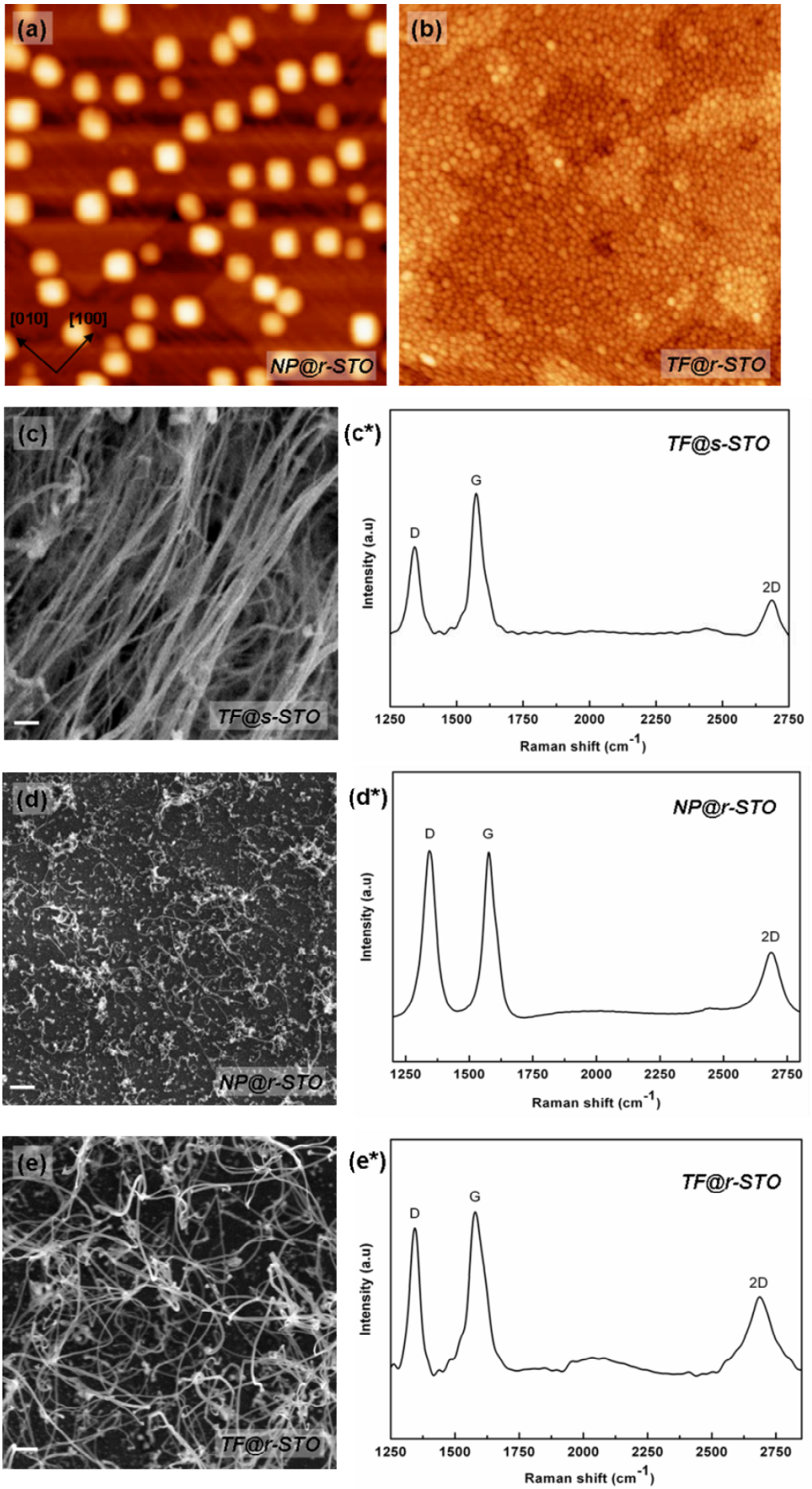
(a)
[010]
[100]
NP@r-STO
(b)
TF@r-STO
(c)
TF@s-STO
(c*)
TF@s-STO
G
D
2D
Intensity (a.u)
1250
1500
1750
2000
2250
2500
2750
Raman shift (cm-1)
(d)
NP@r-STO
(d*)
NP@r-STO
D
G
2D
Intensity (a.u)
1250
1500
1750
2000
2250
2500
2750
Raman shift (cm-1)
(e)
TF@r-STO
(e*)
TF@r-STO
G
D
2D
Intensity (a.u)
1250
1500
1750
2000
2250
2500
2750
Raman shift (cm-1)

Figure 4.5: STM images of catalyst morphologies of *NP@r-STO* (a) and *TF@r-STO* (b) substrates ((a): Image size: 100 × 100 nm^2, V_s = 1.0 V, I_t = 0.3 nA; (b): Image size: 100 × 100 nm^2, V_s = 1.0 V, I_t = 0.2 nA). The images were taken prior to the CVD process. SEM images of grown CNT networks on the three types of substrates, *TF@s-STO* (c), *NP@r-STO* (d), and *TF@r-STO* (e), highlighting that different catalyst fabrication routes give rise to distinct growth results. Scale bars: 1 μm. Corresponding Raman spectra of grown materials on three types of substrates, *TF@s-STO* (c*), *NP@r-STO* (d*), and *TF@r-STO* (e*), confirming the CNT formation and indicating the quality of produced CNTs.

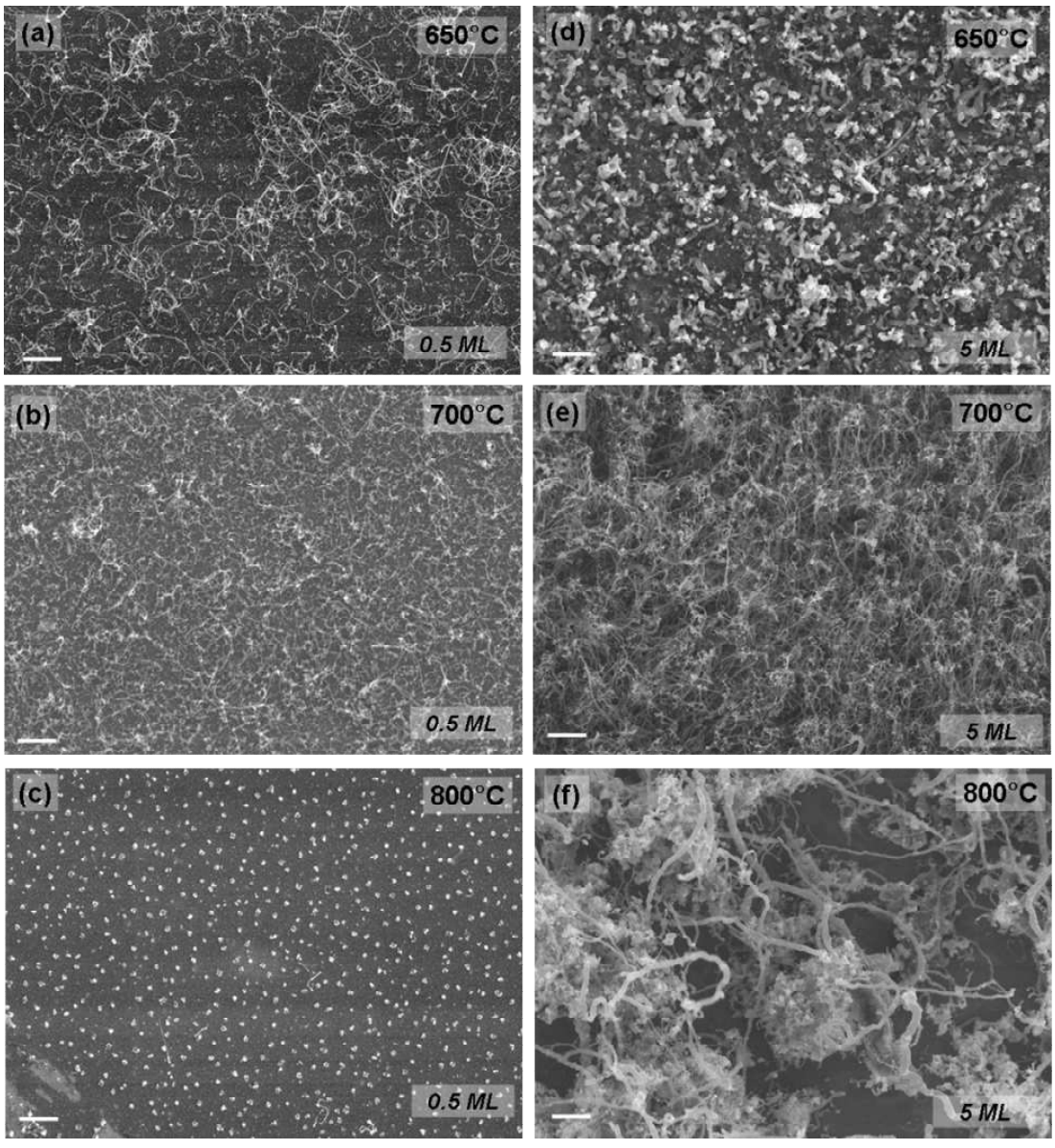

Figure 4.6: SEM investigation of growth temperature effect on *TF@r-STO* substrates. The Fe catalyst doses and applied growth temperatures are marked on each image. Scale bars: 1 μm.

4.3.2.2.3 Effect of Carrier Gas Flow Rate (H_2)

Here the H_2 gas flow rate is examined in detail. The EtOH-CVD experiments were conducted on *TF@s-STO* substrates (5 ML Fe) at a growth temperature of 700°C for 30 min, with a total gas flow rate of 600 sccm. All the growth parameters were kept identical, except that varied H_2 gas flow rates were used. It is observed that the amount of H_2 used as the carrier gas in the CVD process leads to huge differences of product morphologies, characterised by SEM (Figures 4.7a-4.7c) and Raman spectroscopy (Figures 4.7a*-4.7c*). Figure 4.7a shows the CNT growth subject to small H_2 gas flow rate (50 sccm), where the quality of grown materials is reflected by the corresponding Raman spectra shown in Figure 4.7a*, with a calculated G/D ratio of 1.3, indicating that maintaining a small H_2 flow rate (50 sccm) is beneficial to CNT growth; increasing the H_2 flow rate to 200 sccm surprisingly generates vertical-aligned CNT forests on STO substrates (as shown in Figure 4.7b) with fairly good quality (the G/D ratio is calculated ~1.8 from the corresponding Raman spectrum in Figure 4.7b*), which is detailed in section 4.3.2.3. It is well known that the H_2 as the carrier gas has an effect on the pyrolysis of precursors by suppressing the cracking rate of hydrocarbon molecules; it can also effectively etch amorphous carbon away and help to enable/sustain the activity of catalysts.[124, 125] However,

further increasing the flow rate to 400 sccm leads to undesired by-products (Figure 4.7c), Raman spectrum in Figure 4.7c* also shows a stronger D peak (compared to the G peak) with no sign of 2D peak, indicating that a high H_2 gas flow rate is detrimental to the quality of produced CNTs. Recent studies have suggested that high exposure of H_2 during the CVD process can cause the formation of oversized catalyst particles,[123] or directly damage the grown CNT structures.[130] The experimental findings presented here are consistent with these studies.

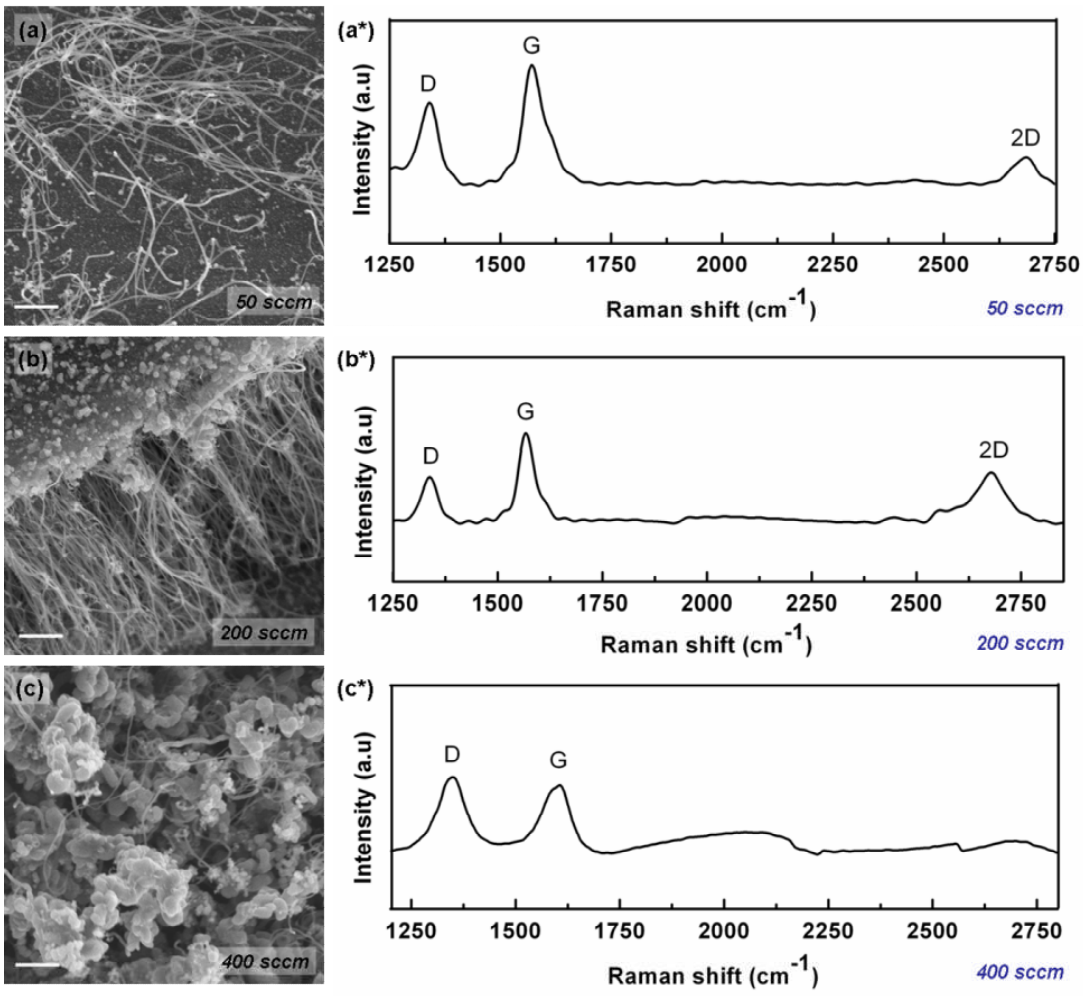

Figure 4.7: Investigations of H_2 gas flow effect on *TF@s-STO* substrates. The applied H_2 gas flow rate during growth is marked on each image. At play the carrier gas of a mixture of Ar and H_2 with a total flow rate of 600 sccm was maintained for a growth period of 30 min for all the samples. Scale bars: (a-c) 1 μm.

4.3.2.3 Realisation of Vertically-Aligned Growth of CNTs on $SrTiO_3$ (001) substrates

The parameter studies documented in the previous section are instructive in defining the optimum experimental conditions for CNT growth on STO (001) surfaces with Fe. The optimum protocols applying to current laboratory set-ups are defined and shown in Table 4.2.

CVD Parameters	*Settings*
Catalyst substrate	TF@s-STO
Catalyst metal dose	5 ML
Growth temperature	700°C
Carrier gas (during CVD)	Ar, H_2
Carrier Gas flow rate (in total)	600 sccm
Ar flow rate	400 sccm
H2 flow rate	200 sccm
Growth period	30 min
CVD type	EtOH-CVD

Table 4.2: The optimum growth conditions for the synthesis of CNTs on $SrTiO_3$ (001) substrates *via* Fe-involved EtOH-CVD.

As with Fe, the growth of vertically-aligned CNTs was realised on STO surfaces for the first time. The representative SEM images with different magnifications in Figures 4.8a-4.8c show the morphologies of a vertically-aligned CNT carpet, produced on a sputtered STO surface. The carpet grows in a uniform manner and covers the whole surface area of the substrate. Close cross-sectional SEM inspection shows that these tubes wave and stick to each other by van der Waals interactions[125]

(Figure 4.8c). Figures 4.8d and 4.8e show the TEM images of individual CNTs from the carpet. It can be observed that the grown tubular structures are MWNTs. The outer diameter of the tube in Figure 4.8e is measured at approx. 27 nm. The Raman spectrum of the grown carpet (Figure 4.8f) displays several characteristic peaks of CNT at the D band (~1350 cm^{-1}), G band (~1580 cm^{-1}), and 2D band (~2690 cm^{-1}); the calculated Raman G/D ratio is 1.6, indicating that the grown tubes are of fairly good quality.

For comparison, Ni was tested using an identical experimental set-up, although this growth protocol might not be the optimum conditions when employing Ni as a metal catalyst. The growth results are gathered in Figure 4.9. The SEM images in Figure 4.9a and 4.9b show that dense CNT networks are forming on the sputtered STO surfaces. As expected, the grown CNTs interweave with each other, growing without any preferential directions or alignments. The TEM image in Figure 4.9c shows the morphological observation of two entangled CNTs, partially covered by amorphous carbon species or by-products. Raman spectrum of obtained CNT networks (Figure 4.9d) exhibits D and G peaks, with a G/D ratio of 0.96, indicating that the CNT sample contains a relatively high density of defects. Moreover, the 2D peak can barely be detected in the spectrum, indicating the product lacks graphitic crystallisation to some extent, compared to that catalysed by Fe.

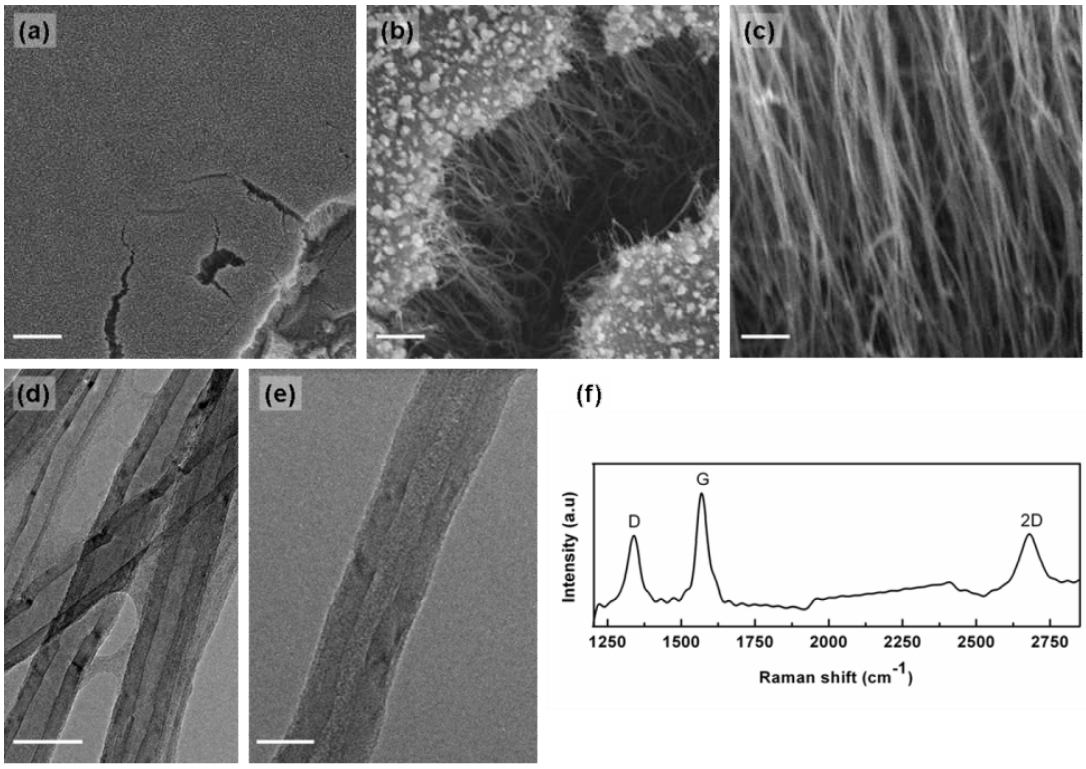

Figure 4.8: Realisation of vertically-aligned growth of CNTs on *TF@s-STO* substrates under practically refined CVD growth conditions, using Fe as metal catalyst. (a) SEM image of general view of CNT carpets grown on STO substrates. Scale bar: 10 μm. (b) SEM image of local areas of carpets, showing voids formed at the topmost surface of the CNT arrays. Scale bar:1 μm. (c) Close SEM observation of morphology and alignment of grown CNTs. Scale bar: 300 nm. (d-e) TEM images of grown CNTs from the carpets. Scale bars: (d) 50 nm. (e) 20 nm. (f) Raman spectrum of grown product. The characteristic peaks of CNTs (D, G, and 2D) are labelled on the spectrum.

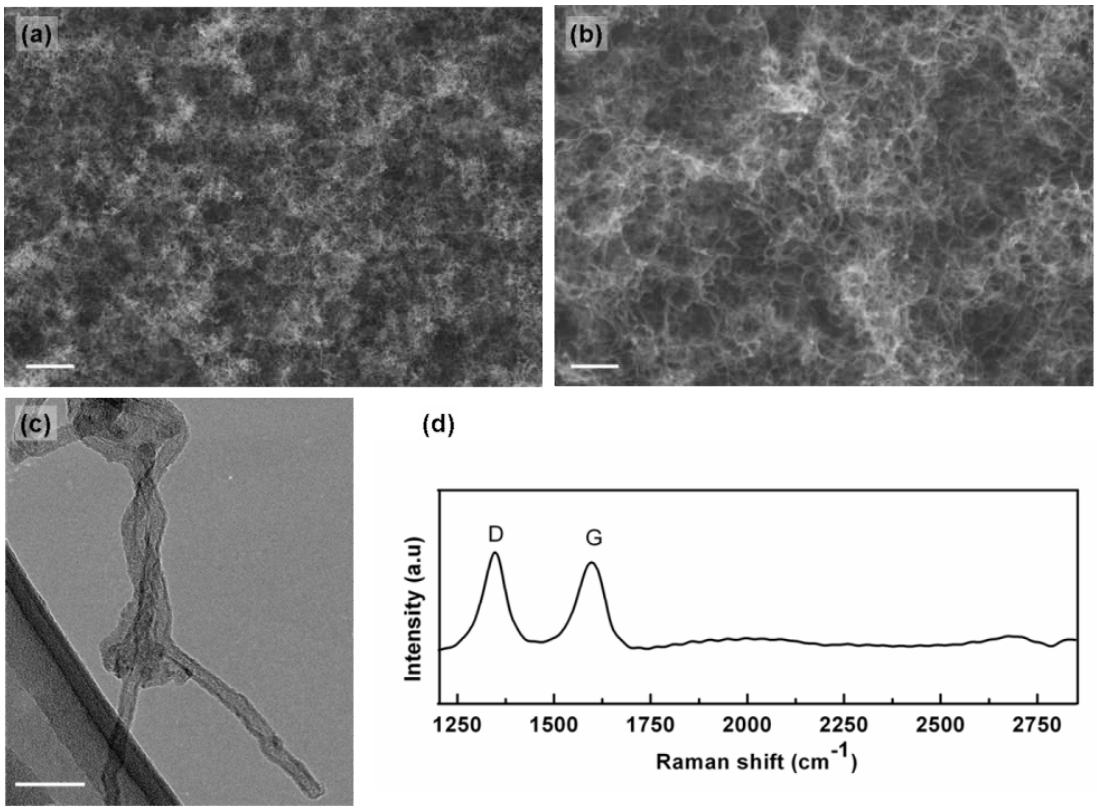

Figure 4.9: Growth of CNT networks on *TF@s-STO* substrates by adopting the growth protocols refined for Fe, using Ni as metal catalyst for comparison. (a-b) SEM images of grown CNT networks on STO substrates. Scale bars: (a) 1 μm. (b) 300 nm. (c) Corresponding low-magnification TEM image of these grown CNTs. Scale bar: 50 nm. (d) Raman spectrum of the grown sample. The characteristic peaks of CNTs (D, G) are marked on the spectrum.

4.3.3 Growth of CNTs under Unusual Growth Conditions on $SrTiO_3$ (001) Substrate

4.3.3.1 Fast Heating

As shown in Section 4.3.1.1, the sizes of STO supported catalyst particles increase with annealing times at elevated temperatures, giving rise to larger NPs, which are not able to support the nucleation and growth of CNTs. In a conventional CVD process, the catalyst substrate has been placed inside the furnace prior to turning on the heating, and hence the NPs on the substrate may agglomerate whilst the furnace is heating to the required temperature, e.g. 800°C. This causes catalyst coarsening before the introduction of carbon feedstock, owing to the pre-heat (approx. 30 min) on the catalyst substrate.

A fast heating method was introduced in an attempt to shorten the thermal history of catalyst NPs and broaden the growth temperature window of STO supported CNT growth. It can be easily implemented by sliding a long quartz tube, in which the substrate can be placed into the furnace when the required temperature is reached. Both Fe and Ni were employed in the investigation. In a typical trial, EtOH-CVD was performed on a *TF@s-STO* sample at a growth temperature of 800°C, using a mixture of Ar (400 sccm) and H_2 (200 sccm) in flow.

The SEM images in Figures 4.10a and 4.10b display morphological differences of STO surfaces obtained from traditional heating (Figure 4.10a) and fast heating (Figure 4.10b) CVD. Catalyst substrate subject to redundant annealing through the

regular heating route tends to form oversized Fe NPs, which are not suitable for CNT nucleation; thus no growth of CNTs is observed in Figure 4.10a. In contrast, massive production of CNT is achieved by fast heating CVD (Figure 4.10b), suggesting that the fast heating of substrate samples advances catalyst patterning and promotes the growth of CNTs, even when the temperature is considered to be relatively high for STO supported CNT synthesis. Figure 4.10c shows low magnification TEM observation of these grown CNTs. A closer view of the nanotube arrowed in Figure 4.10c is shown in Figure 4.10d. Raman spectrum of the grown product in Figure 4.10b confirms that the obtained nanomaterials are CNTs.

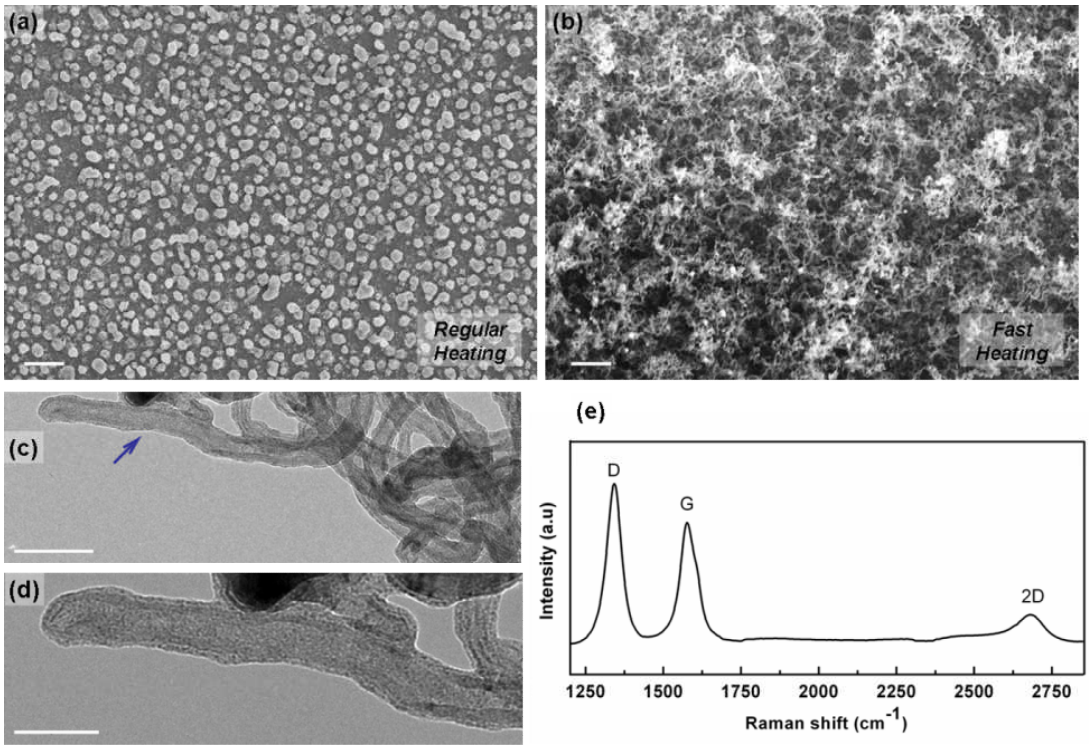

Figure 4.10: SEM images of growth results on *TF@s-STO* substrates by EtOH-CVD subject to regular heating (a) and fast heating (b) treatments of Fe catalyst at a growth temperature of 800°C. Scale bars: 1 μm. (c-d) Corresponding TEM images of grown CNTs shown in (b). The nanotube marked by the blue arrow is further inspected in (d). Scale bars: (c) 100 nm. (d) 50 nm. (e) Raman spectrum of the product generated by fast heating.

Similar results were achieved when switching the catalyst metal to Ni. Regular heating CVD, conducted at 800°C, results in severe aggregation of catalyst particles, which are not able to mediate CNT growth (Figure 4.11a). The SEM image in Figure 4.11b shows how CNT networks are formed on the substrate after fast heating CVD. The TEM images of grown CNT networks are presented in Figure 4.11c and 4.11d, showing that the obtained tubular nanostructures possess a clear view of inner channels and are free of catalyst particles. The corresponding Raman spectrum is displayed in Figure 4.11e, confirming the grown product are CNTs.

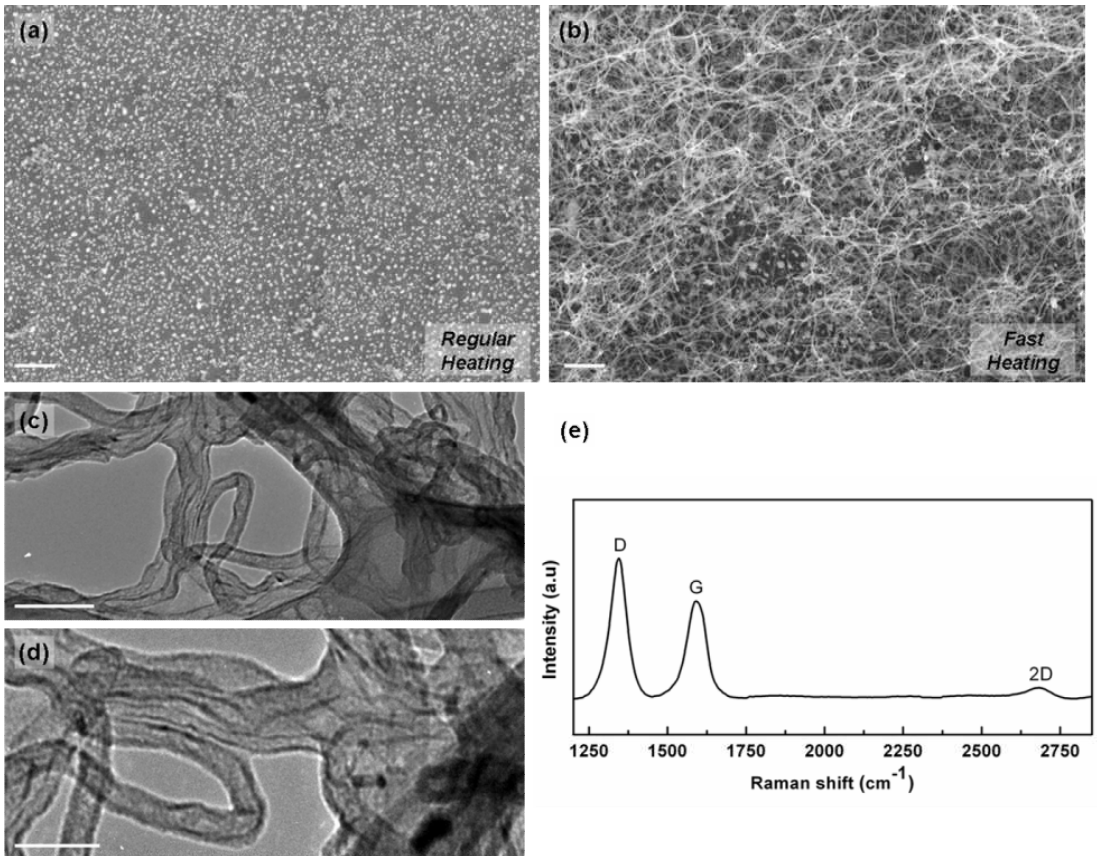

Figure 4.11: SEM images of growth results on *TF@s-STO* substrates by EtOH-CVD subject to regular heating (a) and fast heating (b) treatments of Ni metal catalyst at a growth temperature of 800°C. Scale bars: 500 nm. (c-d) Corresponding TEM observations of grown CNTs shown in (b). Scale bars: (c) 100 nm. (d) 50 nm. (e) Raman spectrum of the product generated by fast heating.

4.3.3.2 Catalyst Pretreatment Design

As discussed in Chapter 3, the structure and yield of grown CNTs can be manipulated through catalyst pretreatment. To optimise our current CNT growth recipe and improve the quality of the grown product, catalyst pretreatment was changed by altering the oxidising/reducing environment during catalyst formation. Here only Ni was tested and C_2H_2-CVD was performed to facilitate the comparison between our growth observations and results reported in the research literature.[127]

TF@s-STO samples were used as substrates with 5 ML Ni deposition. Subsequently, the substates received heating inside the furnace in a flow of Ar (500 sccm). When the temperature ramped to 500°C, the inert environment maintained by the Ar flow swiftly changed to reducing (pure H_2: 500 sccm) or oxidising pretreatments (open air), until the growth temperature (700°C) was reached. The CNT growth was carried out by C_2H_2-CVD, using $Ar/H_2/C_2H_2$ (500/500/10 sccm) for a period of 15 min.

The effect of these pretreatment designs on CNT growth is showed in Figure 4.12. The reducing pretreatment (RP) gives rise to sparse production of CNTs, indicating loss of catalyst activity (Figure 4.12a). In contrast, dramatic changes in product morphology and yield are observed in Figure 4.12b, where the sample is subject to oxidising pretreatment (OP) and shows massive production of CNTs. Raman spectra of grown samples from both RP and OP indicate differences in the quality of produced CNTs. In particular the prominent 2D peak in Figure 4.12d highlights a new feature for Ni-involved growth of CNTs on STO surfaces, as in normal cases it

does not show up in the spectrum. These findings demonstrate that pretreatment design can dictate the yield and quality of grown CNTs; and specifically OP proves to be an efficient approach for promoting tube synthesis.

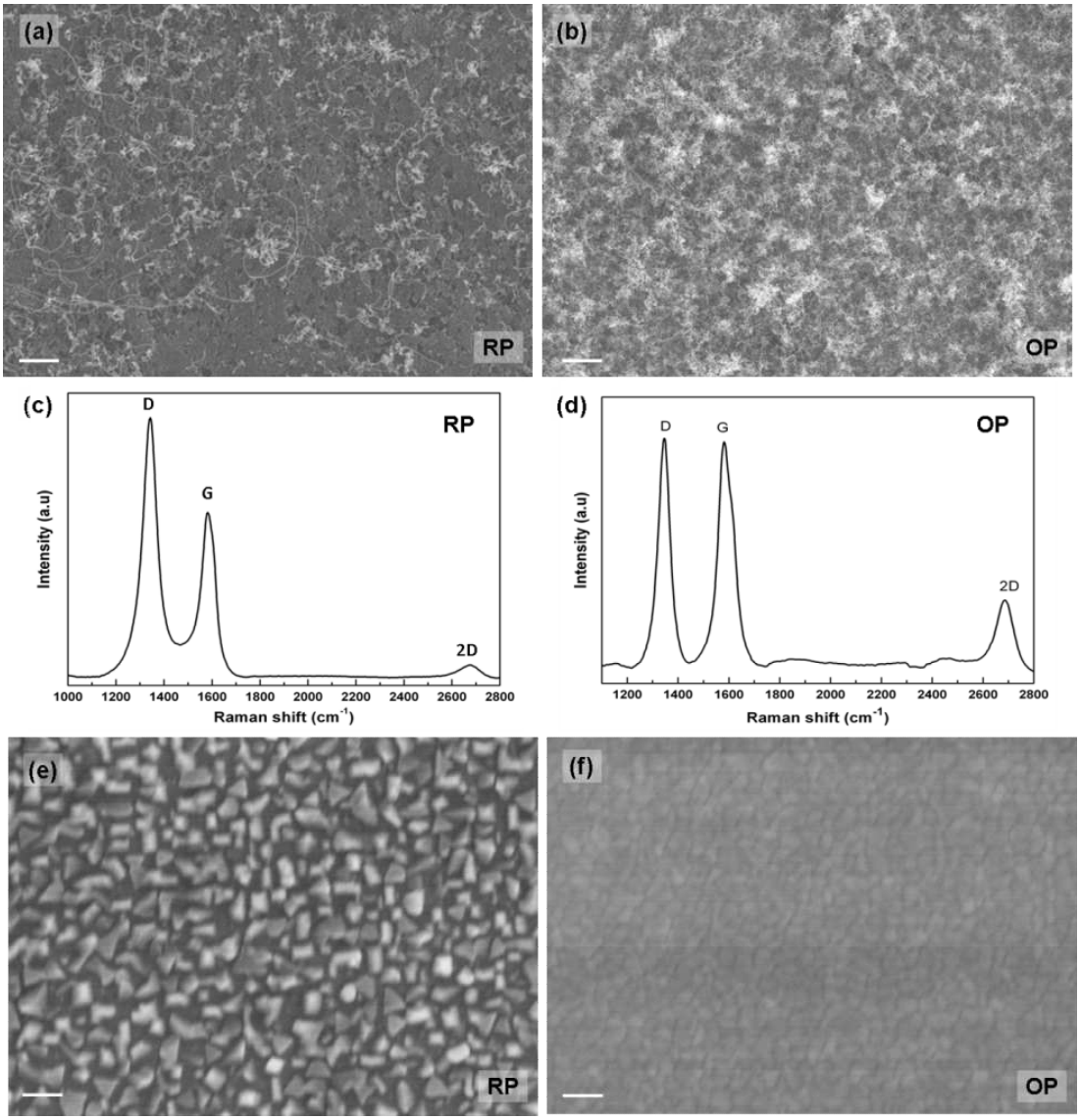

Figure 4.12: Investigation of the effect of pretreatment design on the growth of CNTs on *TF@s-STO* substrates using Ni metal catalyst at a growth temperature of 700°C. (a-b) SEM observations of grown CNTs on RP (a) and OP (b) catalyst substrates. Scale bars: 1 μm. (c-d) Corresponding Raman spectra of obtained CNTs (e-f) SEM images of morphologies of Ni catalysts on STO (001) surfaces subject to RP (e) and OP (f) from a blank-CVD process. Scale bars: 200 nm.

To seek possible explanations of the distinct growth behaviour of CNTs induced by catalyst pretreatments, blank-CVD (CVD process in absence of carbon feedstock) was performed on the pretreated substrates (both OP and RP), without the presence of C_2H_2 at the growth stage. Figures 4.12e and 4.12f summarise the results for both pretreatments. Figure 4.12e shows the SEM image of catalyst patterns having received RP in a blank-CVD process. The restructured NPs, as seen in the image, have a wider range of size distributions and larger particle sizes, whilst the substrate sample subject to OP leads to the formation of smaller, uniformly-distributed NPs (Figure 4.12f). These results are in agreement with previous findings reported in the research literature.[122, 127]

4.4 Discussion

Interest in the $SrTiO_3$ (001) surface has emerged because of its remarkable ability to support distinct metal nanocrystal growth, which can be expected to function as a catalyst for the growth of CNTs. Here encouraging results regarding the growth of CNTs on $SrTiO_3$ (001) substrates *via* atmospheric, catalytic CVD are achieved, proving that $SrTiO_3$ support can be functioned as a substrate for CNT growth, and this would certainly boost the types of CNT substrates currently used. It is also instructive to compare observed CNT growth behaviour with that reported on other substrates. For instance, sub-millimeter range, dense VACNTs have been extensively

synthesised on alumina supports, owing to the advanced abilities of Al_2O_3 surfaces in catalyst restructuring.[196] Our findings also document the realisation of VACNTs on $SrTiO_3$ substrates, but with limited carpet length (~5 μm) and loose-packed configurations, suggesting that further control over catalyst patterning on STO surfaces might be needed. The formation of VACNT on STO surfaces is of particular importance for potential applications such as CNT-based nanoelectronic devices, because the CMOS industry often requires direct electrical contact between VACNTs and the supports, and the STO could become conductive after proper doping (e.g. Nb-doped). In recent times, the growth of VACNTs on metallic substrates (such as Ta, Cu, W *etc.*) has proven to be challenging;[95, 105, 199] hence the realisation of growths of VACNTs on doped $SrTiO_3$ substrates, especially at low growth temperatures, will pave the way for nanoelectronic processing and related applications.

There is a vast literature on the significance of catalyst support on catalyst morphology and subsequent CNT growth. Amama *et al.*[198] studied the effects of different type of alumina supports on the activity, lifetime, and evolution of supported Fe catalysts in terms of SWNT carpet growth. Magrez and his colleagues indicated that distinct CNT growth behaviour can be dictated by tuning the acid-base properties of catalyst supports.[241] In this study, it has been shown that the sputtered STO substrate is able to support CNT growth, in respect of the quality and yield of production, compared to the reconstructed one, for the reason that the texture of the sputtered surface is rougher and thus can hinder catalyst ripening to some extent at elevated temperatures. It is also worth mentioning that the $SrTiO_3$ (001) surfaces tend

to aid the process of catalyst coarsening, leading to the presence of oversized catalyst NPs and poor growth of CNTs at higher growth temperatures, *i.e.* 800°C. The strategy of tackling this problem is to lower the CNT growth temperatures to suppress ripening or to try out unusual growth recipes, e.g. fast heating, as mentioned above. Moreover, another feature is that the shape-forming of various types of metals on STO (001) surfaces could lead to catalytic properties; for instance, it can be expected that the different shapes of STO supported metals will dictate the structures of CNTs. However, this has not been observed in our investigation, which is probably due to the evolution/reconstruction of catalyst NPs caused by ambient gas annealing (Ar, H_2, O_2, C feeding gas *etc.*),[2, 115] or the NP distortion/deformation caused by internal pressures exerted by surrounding CNT walls during the growth stage,[222] resulting in the damaging of these metal shapes in CVD processes. Future work would lie in seeking methods (e.g. cold-wall, hot-filament CVD) of 'freezing' the STO supported metal shapes to perform studies on whether the shaped catalyst could dictate the structures and hence properties of grown CNTs. Moreover, monitoring these catalyst particles prior to/during/after the CVD process with the aid of *in situ* TEM would also be helpful to gain information about the geometrical states of the catalytic NPs.

Our results showed that oxygen species play prominent roles in CNT growth in a variety of ways. Firstly, as a perovskite oxide, the $SrTiO_3$ contains oxygen and has low surface energies compared with those of metals, thus the Volmer-Weber (VW) growth mode (3D islands) of metals predominates, when deposited onto the STO

substrate, leading to the forming of a thin film of NPs, which function as catalysts. Furthermore, recent studies have claimed that oxide support is beneficial to CNT growth.[216, 218] Secondly, the use of ethanol (C_2H_5OH) as the carbon feedstock in our investigation brought about promising growth results, compared to those obtained by using hydrocarbons, such as toluene (C_7H_8), which is consistent with the findings from previous studies, indicating that an oxygen-containing carbon precursor is able to enhance the growth of CNTs. Lastly, oxygen can be introduced by manipulating the pretreatment gas to tune the catalyst morphology and catalyst-substrate interactions. The results shown in Section 4.3.3.2 demonstrate that oxidising pretreatment surprisingly produces catalyst NPs of small size, high density and reduced mobility, which show great promise for CNT production with high yields and quality. Our work for the next-step is to probe the chemical aspects of the catalyst systems by means of XPS, XRD *etc.*

In surface-bound CVD processing, the growth mode of CNTs greatly depends on the interactions between catalysts and supports. In our case, the experimental observations suggest that the growth of CNTs on $SrTiO_3$ (001) substrate with the aid of Fe follows a base growth mode, as shown in the TEM images of Figure 4.13. Figure 4.13a displays the general morphologies of CNTs grown on Fe/s-STO substrate-the outer diameters of CNTs are ~20-25 nm, whereas Figure 4.13b shows a specific region of the tip of an individual CNT. The arrows in both images indicate the tip of the CNTs without encapsulated catalyst particles, which suggests a base growth mode.

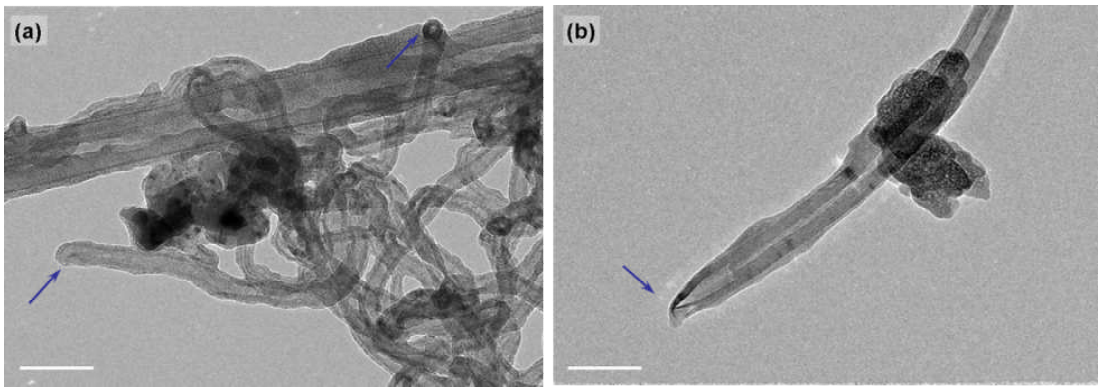

Figure 4.13: TEM images of CNTs grown on $SrTiO_3$ (001) surfaces with the aid of Fe. The arrows in figures indicate the tips of CNTs, highlighting that the CNT tips are free of catalyst particles. Scale bars: 100 nm.

As mentioned above, Fe adopts 3D islands when deposited onto oxide surfaces. The formation of bcc Fe islands has been observed in the past and the contact angle (θ) between the Fe nanoislands and oxide support (STO (001)) can be obtained as 45°.[23] Therefore the adhesion energy of STO supported Fe catalyst NPs can be deduced, which is significant for understanding the growth mode of grown CNTs. The adhesion energy (E_{ad}) can be calculated from Young-Dupre equation[271]:

$$E_{ad} = \gamma(1+\cos\theta) \tag{4.1}$$

where γ is the surface energy of the nanoislands. Specifically, the catalyst particles have been annealed at the CNT growth temperature (T) of 700°C, and γ_T can be obtained from:

$$\gamma_T = \gamma_{Tm} + (T - T_m)\frac{\delta\gamma}{\delta T}\Big|_{Tm} \tag{4.2}$$

where T_m is the melting temperature. For Fe, the T_m is 1515°C, the γ_{Tm} and $(\delta\gamma_T/\delta T)|_{Tm}$ are 1.88 J/m^2 and -4.3×10^{-4} J/m^2°C, respectively.[201] Combining Equations 4.1 and 4.2 with the obtained contact angle 45° for $SrTiO_3$ (001) support, a value of the adhesion

energy of 3.807 J/m^2 is calculated for Fe/STO. Taken in comparison with Wang's study, where the deduced E_{ad} was 2.24-3.95 J/m^2 for the Fe/Ta system and CNTs followed a base growth mode,[201] our calculated result is broadly consistent and thus points to a base growth mode as well, further confirming the experimental observations shown above.

Lastly, it is worth-noting that in our case the catalytic performance of Fe seems superior to those of Ni under identical CNT growth conditions. $SrTiO_3$ supported Fe NPs, rather than Ni ones, assist in catalysing the growth of VACNTs on the oxide surface, with encouraging yields and qualities of tube production. This is consistent with the results from comparative studies of (Fe, Ni) catalytic performances conducted by some other groups, which reveal that Fe leads to the CNT production with higher yield and better crystallinity than Ni does.[90, 152, 272] However, a few investigations have concluded that Ni catalysts possess greater ability to support CNT growth compared to Fe, especially with respect to the CNT growth rate.[151, 273] At present, a solid understanding of the discrepancy of catalytic performances in the cases of Fe and Ni is still lacking. However, experimental observations combined with theoretical calculations have been conducted to seek possible explanations, based on the structural and chemical characteristics of the catalyst particles. Jacob *et al.*[272] investigated the effect of Fe and Ni catalysts on the synthesis of MWNT on Si (111) substrate under identical conditions and found that the sizes and shapes of Fe NPs are more suitable than those of Ni NPs for CNT growth. They also revealed that the catalyst material responsible for the CNT growth stayed in a pure metal state,

without any trace of metal carbide formation. Page and his colleagues conducted a detailed simulation to study the SWNT nucleation on Fe- and Ni-carbide NPs.[274] In their study, a three-stage process in terms of SWNT nucleation has been invoked, indicating that the interplay between the strength of metal-carbon interaction and the phase of the catalyst NP plays a crucial role in governing the formation and the stability of bulk/surface/sub-surface metal carbide. They revealed that SWNT nucleation from the Ni carbide is preferable to nucleation from Fe carbide.[274] Veering away from these published findings, future work of this investigation will aim at revealing the reason for the difference in the catalytic activities of STO supported Fe and Ni NPs with regard to CNT growth, by looking into the crystallographic characteristics of catalyst NPs and gathering information on the possibility of the formation and evolution of metal carbide species, with the aid of HRTEM, XPS, and XRD *etc.*

4.5 Conclusions

In summary, metal-catalyst-involved CVD growth of CNTs has been achieved on $SrTiO_3$ (001) substrates for the first time. In this study, STO has been proven as a suitable substrate to support the growth of CNTs, and controls over designing the CNT growth catalyst onto STO surfaces have also been gained to some extent. Two types of metals (Fe and Ni) have been used as catalyst materials and ethanol has been

the main carbon feedstock. Through STM investigation of the growth of STO supported metal nanocrystals and SEM study of the effects of various CVD parameters, the growth conditions have been optimised and the synthesis of vertically-aligned CNTs has then been realised on the $SrTiO_3$ (001) surface, with the aid of Fe. In addition, the growth of CNTs under unusual conditions (fast-heating, pretreatment design) has been investigated, with some interesting results. Finally, several topics such as substrate effects, oxygen influences, growth mode, and the catalytic performance of Fe and Ni have been discussed. Future studies are necessary to better understand the metal/STO catalytic systems and detailed catalyst behaviour during the STO-surface-bound CVD process.

Chapter 5：

Metal-Catalyst-Free Growth of Carbon Nanotubes (CNTs) on $SrTiO_3$ (001) Surfaces

5.1 Background

The growth of CNTs on oxide substrates by CVD is technologically important for the development of novel devices and composites.[1, 4, 66] In a typical CVD process, consensus had previously been reached that the involvement of various metals[161-164, 166] as catalysts is required for the formation of CNTs. However, recent studies have indicated that even oxide materials (SiO_2[19-21, 181, 245-247], ZrO_2[249], ZnO[248] *etc.*) can catalyse the growth of CNTs, without the presence of any metals. The latest findings bear further witness to the development of this metal-catalyst-free route, leading to the CVD production of various other carbon nanostructures, e.g. few-layer nanographene grown on MgO crystals[217, 275] and carbon nanocoils (CNCs) generated from SiO_2.[276] The synthesis of carbon nanostructures by metal-catalyst-free CVD has not only opened up new avenues in nano-research[64] but also benefited novel applications such as electromagnetic devices, field emission displays, and energy storage.[19, 250] The growth of carbon nanostructures by oxides with the aid of metal-catalyst-free CVD is summarised in Table 5.1.

Regarding surface-bound, metal-catalyst-free CVD for CNT growth, engineering the oxide substrates for catalyst preparation is essential.[19, 21] Different approaches have been attempted for this purpose: depositing a SiO_2 film (30 nm thickness) onto a Si wafer[19], synthesising ZrO_2 nanoparticles (NPs) *via* a solution-based route onto inert supports[249], or simply conducting high temperature annealing of SiO_2 substrates in a H_2 ambient[246], all of which would in turn create a rough surface compatible for the subsequent initiation of tubular structures. In this chapter, a systematic

investigation of metal-catalyst-free growth of CNTs, using engineered $SrTiO_3$ (001) substrates is presented. The impetus for utilising STO (001) surfaces emanates from their remarkable ability to provide various surface morphologies and practical ease of surface handling[277-279], which leads to the growth of CNTs on substrates in a controllable manner, compared to other oxide materials (*i.e.*, SiO_2, ZrO_2). This work will pave the way for investigating the relationship between the structure of STO surfaces and the related catalytic activities.

Catalyst	*Methodology*	*Carbon form (s)*	*Year published*	*Ref.*
MgO, Al_2O_3, Ga_2O_3 *etc.*	Using nanopowdered oxides	Graphitic layers	**2007**	**217**
SiO_2	Diamond blade scratching on SiO_2 layers	SWNT/MWNT/CNFs	**2009**	**21**
SiO_2	Depositing a rough thin film of SiO_2 on Si or Si/SiO_2	SWNTs	**2009**	**19**
SiO_2/SiC	Using commercially quartz substrate	Graphitic nanostructures	**2009**	**247**
ZrO_2	Using nanoparticulate ZrO_2 for various experimental purposes	SWNT/MWNTs	**2009**	**249**
Lanthanide metal oxides	Detonation induced reaction on oxide particles	MWNTs	**2009**	**252**
Eu_2O_3	Using nanoparticulate Eu_2O_3	SWNTs	**2010**	**250**
ZnO	Generating ZnO NPs by a diblock copolymer templating method	SWNTs	**2010**	**248**
SiO_2	Thermally grown SiO_2 layer on Si; Using H_2 as pretreatment agent	SWNTs	**2010**	**246**
MgO	Using MgO powders	Few-layer nanographene	**2010**	**275**
SiO_2	Simulation work indicated a VSS mechanism responsible for SWNT growth on SiO_2 NPs	SWNTs	**2011**	**245**
SiO_2	*In situ* TEM study in combination with theoretical modelling	SWNTs	**2011**	**20**
SiO_2	H_2 induced growth of carbon helical nanostructures over SiO_2 catalysts	Carbon nanohelics/CNFs	**2011**	**276**
$SrTiO_3$	Surface engineering; Scratching the surface; Particulate STO powders	Various carbon nanostructures	**This work**	**Manuscript in preparation**

Table 5.1: Summary of growth of carbon nanostructures by oxide materials with the aid of metal-catalyst-free CVD.

5.2 Experimental Details

5.2.1 Engineering $SrTiO_3$ (001) Surfaces

In this study, epi-polished $SrTiO_3$ (001) samples with 0.5 wt% Nb-dopant (PI-KEM Ltd, UK) were used as substrates. A UHV system, incorporating a treatment chamber, an Ar^+ ion sputtering source, and an STM, enables the engineering and characterisation of the substrates prior to the CVD process. In terms of catalyst substrate preparation, a series of $SrTiO_3$ (001) surfaces were created *via* different treatments described as follows:

BHF etched (disordered): The as-received STO sample was etched for 10 min in a buffered HF (NH_4F-HF) solution (pH = 4.5), in accordance with the recipe described by Kawasaki *et al.*[56] It has been proved that the surface SrO layers could be removed after etching, resulting in a rough surface with TiO_2 termination.

Degassed (disordered): The as-received STO sample was introduced into a JEOL JSTM 4500XT ultra-high vacuum (UHV) system and annealed by resistive heating at 600°C for up to 1 hour. This degassing process produces a relatively rough surface on the STO sample and also removes possible contamination.

Sputtered (disordered): The as-received STO sample was first degassed, followed by Ar^+ ion bombardment with an ion energy of 0.75 keV and an ion flux at 1.28 A/m^2 for 20 min (0.75 keV, 1.28 A/m^2, 20 min). This procedure leads to the highest surface roughness amongst these engineered substrate surfaces.

(2×1)-reconstructed (semi-ordered): The STO (001) (2×1)-reconstructed surface

was prepared by annealing the sample in UHV at 800°C for 30 min. The resulting surface is more defective and rougher in comparison with the *c*(4×2)-reconstructed surface.

Nanostructured (semi-ordered): The nanostructured substrate was produced by relatively light sputtering (0.75 keV; 1 A/m^2; 10 min) and subsequently annealing in UHV at 900°C for 30 min.

c(4×2)-reconstructed (ordered): The STO (001) *c*(4×2)-reconstructed surface was produced through sputtering (0.75 keV; 1 A/m^2; 10 min), followed by annealing at an elevated temperature (1200°C) for 15 min.

Methods involved in the image analysis: Surface roughness reveals the vertical deviations of a real surface from its ideal form. Herein the *root-mean-square (rms) areal surface roughness* (R_{rms}) of STO surfaces was measured to evaluate the obtained surface texture of sampling areas. For performing this measurement, The STM images (Figure 5.3A-5.3F) were processed with a scanning probe image processor (SPIP, version 6.0.2, Image Metrology) and the R_{rms} of selected area can be calculated by this software. To obtain the value of density of CNTs grown on a series of STO substrates (Figure 5.4), high magnification SEM images (Mag: ×50,000) were used. The method involved was to simply count the numbers of CNTs within selected areas on clear printing forms of SEM images. Specifically, it should be noted that the nucleation point (tiny white dot) at one end of a CNT could be very helpful for carrying out this counting, as it could help determine the exact number of tubes in specific sites where several CNTs were intertwined with each other.

5.2.2 Preparing Particulate $SrTiO_3$ Powders

The STO powders were created using as-received STO samples (non-doping of Nb). The production method involved putting the STO sample between two pieces of clean printing paper, milling it with a pestle (interleaved by paper) and collecting the product. Then the obtained powders were either placed onto a piece of cleansing Si wafer (inert substrate) or directly deposited onto a TEM grid (Cu), for subsequent CVD reactions.

5.2.3 Creating Scratched $SrTiO_3$ Substrates

To create the scratched STO substrates, as-received STO samples were firstly etched within the BHF solution for 5 min, the surfaces of these etched samples were then scratched, using a diamond blade instead of a stainless steel one, in order to avoid any metal contamination. The surface morphologies of the scratched samples were observed by SEM, prior to the CVD process, as shown in Figure 5.1. Figure 5.1a presents a general view of the original scratched surface; the scratching marks can be clearly seen. A closer view of the surface morphology (Figure 5.1b) shows that microsized and nanosized particles are generated in the areas of the scratching marks.

5.2.4 Performing Metal-Free CVD

For CNT growth, both EtOH- and C_2H_2-CVD were carried out on the prepared STO

samples. To ensure that a completely metal-catalyst-free process takes place, a brand new quartz tube was employed in each CVD run, and plastic tools were used instead of metallic ones for the sample transfer, collection and handling. Moreover, the samples (especially the sputtered ones) were subject to XPS characterisation before and after the CVD reaction, which was performed with the assistance of Mr. Clive Downing (BegbrokeNano). The XPS measurements were carried out on a G Clam X-ray photoelectron spectrometer at the OCMS Begbroke Science Park, using X-ray radiation from the Mg Kα band (hυ = 1253 eV), and recorded using an analyzer energy of 100 eV for survey scans with a take-off angle of 90°. Representative XPS analysis was performed on the sputtered samples (Figure 5.2), indicating that there is no trace of conventional types of metal catalysts (Fe, Co, Ni *etc.*)

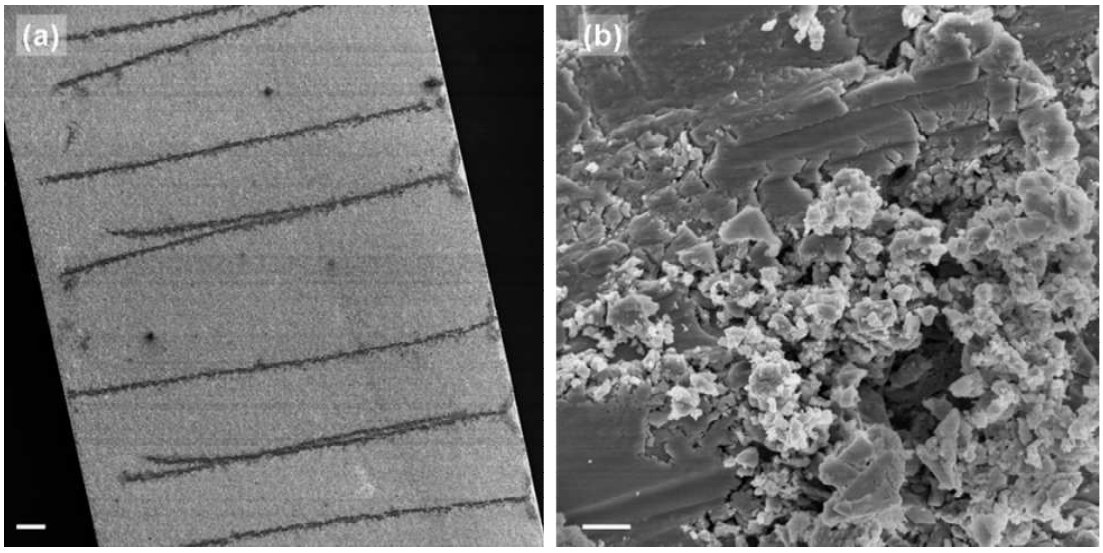

Figure 5.1: SEM observations of scratched STO surfaces prior to CVD reactions. (a) A low magnification image shows the scratching marks on the surface. Scale bar: 100 μm. (b) A close view of the surface morphology in the area of one of these scratches, indicating that microsized and nanosized particles are presented. Scale bar: 1 μm.

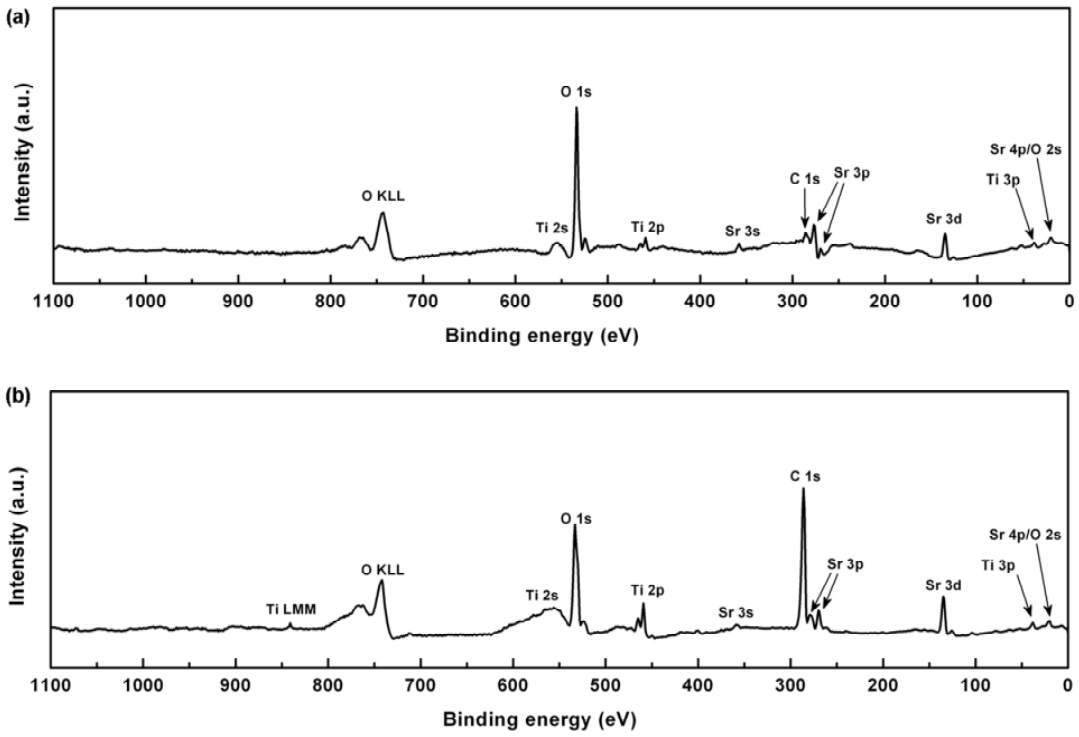

Figure 5.2: XPS measurements of sputtered STO sample surface prior to (a) and after (b) a CVD reaction, revealing that the substrate is free of metallic contaminations (Fe, Co, Ni *etc.*).

5.3 Results

In this study, a series of engineered STO substrates with distinct surface structures is produced. A correlation between the surface roughness/morphology of substrates and relevant catalytic activity/CNT yield has been successfully revealed. Complementary investigations using other forms of STO samples (powders, scratched surfaces) are performed to confirm the catalytic capability of STO.

5.3.1 Growth of CNTs on Engineered $SrTiO_3$ (001) Surfaces

5.3.1.1 Surface-Roughness-Tailored Growth of CNTs

Figure 5.3 presents an image library of surface-roughness-tailored growth of CNTs on a series of engineered $SrTiO_3$ (001) substrates by metal-catalyst-free CVD. Figures 5.3A-5.3F show the STM characterisation of a series of engineered STO (001) substrates, namely, sputtered (A), BHF-etched (B), degassed (C), (2×1)-reconstructed (D), nanostructured (E), and *c*(4×2)-reconstructed (F). The differences in surface features/structures of these substrates are attributed to the distinct surface-engineering approaches applied. The corresponding 3D views of the surfaces (Figures 5.3A*-5.3F*) provide clearer impressions of the surface morphologies of these substrates. CNTs were grown on these STO substrates by EtOH-CVD in an Ar/H_2 (400/200 sccm) atmosphere at a growth temperature of

700°C for 30 min. It is worth mentioning that all these substrates have experienced a H_2 anneal (800 sccm) for 5 min at the growth temperature of 700°C, prior to the introduction of carbon feedstock.

The distinct surface-engineering methodologies give rise to a series of STO substrates presenting various surface structures/roughness, which can dictate the subsequent growth of CNTs. The SEM observations in Figures 5.3a-5.3f show the CNT production grown on these STO substrates under identical experimental conditions. The formation of CNTs occurs on the disordered surfaces with a certain degree of roughness (Figures 5.3a-5.3c). It is specifically worth-noting that dense CNT networks are grown on the 'sputtered' substrate (Figure 5.3a), indicating that Ar^+ ion bombardment is an efficient method for achieving high yield of CNTs on substrates (CNT growth with an areal count of CNTs of ~$3.4\times10^9/cm^2$). However, for the more ordered (flatter) surfaces, such as '(2×1)-reconstructed' and 'nanostructured' substrates, only a limited amount of CNTs was observed (Figures 5.3d and 5.3e). Moreover, Figure 5.3f demonstrates that no CNT could be produced utilising the well-ordered '*c*(4×2)-reconstructed' substrates, probably because the surface is too flat to provide any nucleation centres or high-energy sites for forming the tubular structures. These results reveal that rougher STO surfaces possess enhanced capacities to support the growth of CNTs.

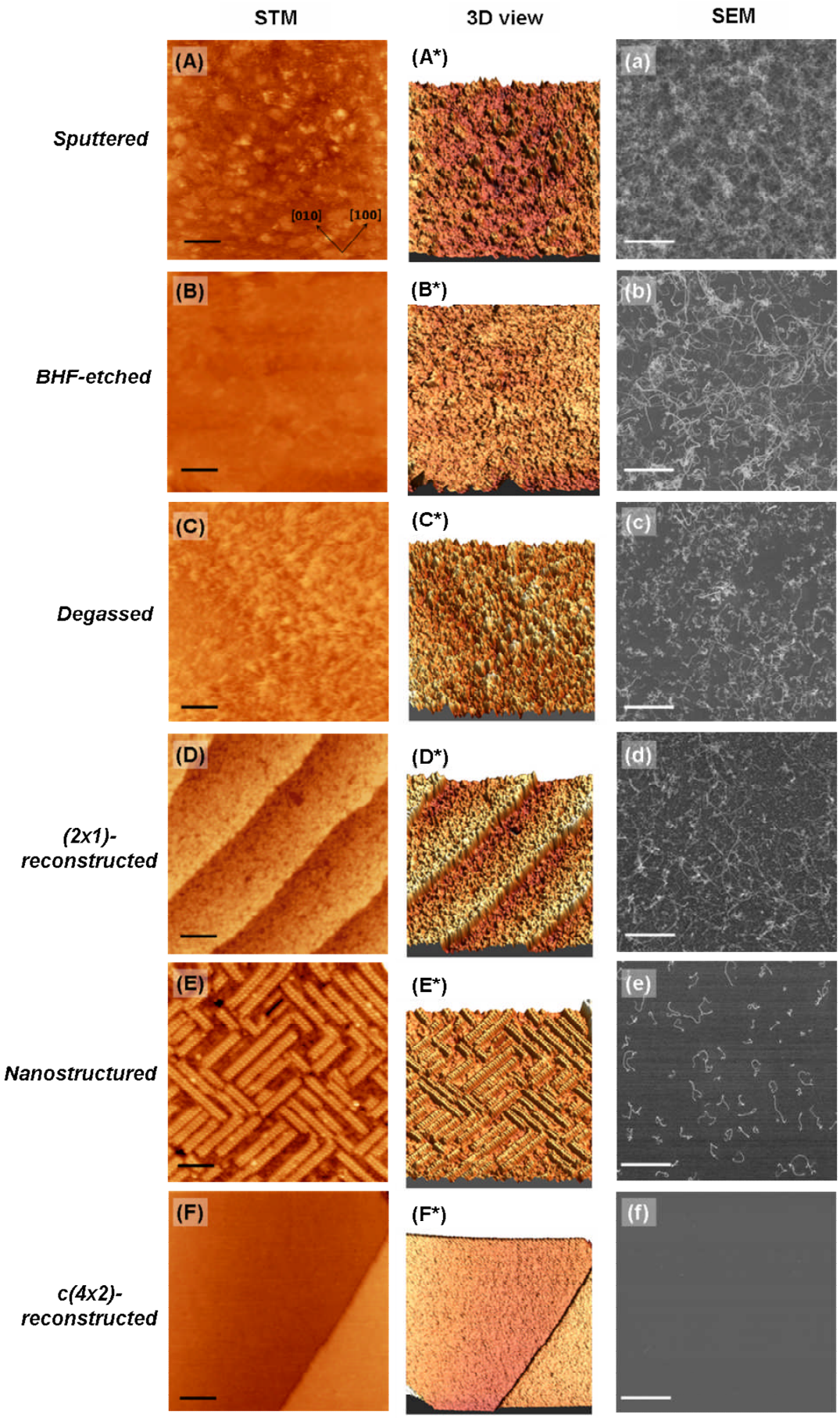
STM
3D view
SEM
Sputtered
BHF-etched
Degassed
(2x1)-reconstructed
Nanostructured
c(4x2)-reconstructed
(A)
(A*)
(a)
[010]
[100]
(B)
(B*)
(b)
(C)
(C*)
(c)
(D)
(D*)
(d)
(E)
(E*)
(e)
(F)
(F*)
(f)

Figure 5.3: Image library of surface-roughness-tailored growth of CNTs on a series of engineered $SrTiO_3$ (001) substrates by metal-catalyst-free CVD. (A-F) STM images of (A) sputtered, (B) BHF-etched, (C) degassed, (D) (2×1)-reconstructed, (E) nanostructured, and (F) *c*(4×2)-reconstructed substrates. Scale bars: 20 nm. (A*-F*) 3D views of the imaged surfaces. (a-f) SEM observations of CNTs grown on corresponding STO substates by EtOH-CVD. Scale bars: 1 μm.

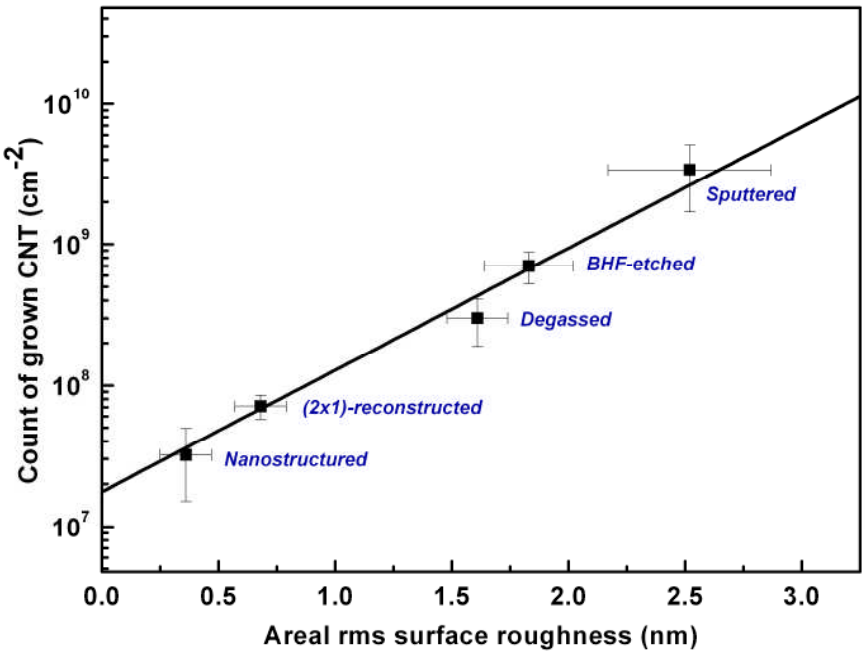

Figure 5.4: The graph of the areal rms surface roughness of the engineered STO substrates *versus* the areal count of CNTs grown on them. The case of *c*(4×2)-reconstructed sample has not been shown, for the reason that there was no CNT production on such substrate surfaces.

The most striking point conveyed here is that the growth trend of CNTs, even the CNT yield on the whole range of engineered STO substrates, strongly correlates with the roughness of the STO surfaces. The relationship between the areal surface roughness of STO substrate surfaces and the corresponding CNT yield (areal count of CNTs) is plotted in Figure 5.4. The data of areal rms surface roughness (R_{rms}) of each imaged substrate were measured with the aid of SPIP software, with a typical measurement of 20 times for each image. The values of the density of grown CNTs were obtained by analysing the SEM micrographs. The error (shown as error bars along both the *x* and *y* axes in Figure 5.4) represents the standard deviation of the measured sampling statistic.

This investigation encompasses several simple, flexible methods for the induction of atomic surface roughness to achieve metal-catalyst-free growth of CNTs on STO (001) substrates. In particular, the approach of Ar^+ ion bombardment on STO surfaces is specially highlighted, owing to its assurance of a high yield of CNT production. A detailed study of the Ar^+ ion-sputtered samples is presented in the following Section 5.3.1.2.

5.3.1.2 Special Focus on the Ar^+ Ion-Sputtered Sample

To further verify that surface roughness is responsible for CNT growth, the Ar^+ ion-sputtered STO substrates were selected as a representative for scrutinized investigation. The designed growth experiment was conducted at identical growth conditions as stated before, followed by detailed sample characterisation.

Figure 5.5 presents the growth results (identical experimental conditions as stated in Section 5.3.1.1) from the sputtered samples, characterised by SEM, TEM, and Raman spectroscopy. The CNT network grown at 700°C on bare sputtered STO substrate is observed by SEM in Figures 5.5a and 5.5b. Figure 5.5a is a general view of part of the sample, showing how uniformly the layers of CNT production grow on the substrate. A high magnified image is presented in Figure 5.5b, which exhibits dense CNT films covering the sample surface. TEM observation of grown CNTs (Figure 5.5c) shows regular nanotube structures with no catalyst particles presented. The quality of the obtained CNTs was further evaluated by Raman spectroscopy. The Raman spectra of the CNT films (Figure 5.5d) displays several characteristic peaks of CNTs at the D band (~1350 cm^{-1}), G band (~1580 cm^{-1}), and 2D band (~2690 cm^{-1}); the calculated Raman G/D ratio is 2.2, which indicates that the grown tubes are of good quality even at a relatively low growth temperature (700°C).

The encouraging production of CNTs grown on a sputtered STO surface may confirm that the atomic surface roughness is responsible for generating CNTs. However, in a metal-catalyst-free CVD process, the scientific challenge is to reveal what would actually act as a ‘catalyst’ for the growth of CNTs, instead of metal nanoparticles[64, 77, 280]. STM (Figure 5.6a), combined with AFM (Figure 5.6b) measurements on the sputtered STO surface, shows the appearance of nanosized bumps after blank CVD experiments in the absence of carbon feedstock (Figures 5.6c and 5.6d). Here the AFM measurement was performed by the tapping mode. An STM image of the same sample was obtained, using the constant current mode. Moreover,

the *base* growth mode of CNTs grown on sputtered substrates was identified with the aid of SEM and TEM (Figure 5.7). Based on these experimental observations, It is speculated that the formed $SrTiO_3$ nanometer scale bumps/asperities on the surfaces (which were induced by Ar^+ ion bombardment and are reflected in the form of atomic surface fluctuations/roughness) acted as the nucleation sites of CNTs. To test this hypothesis, complementary investigations were carried out to further confirm the catalytic ability of STO NPs in respect of CNT growth, by using particulated STO powders and scratched STO substrates.

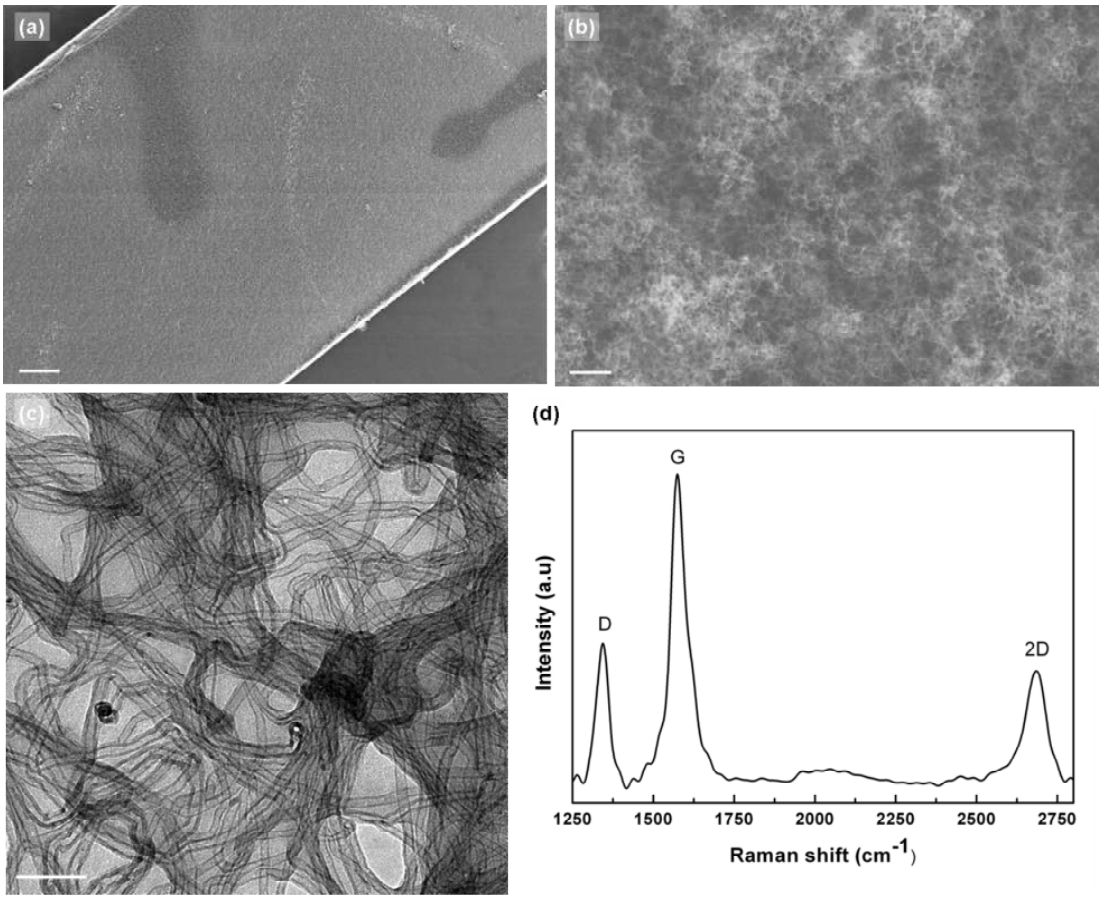

Figure 5.5: Analysis of the growth scenario of Ar^+ ion-sputtered samples. (a-b) SEM, (c) TEM observations, and (d) Raman spectrum of CNTs grown on bare sputtered STO surfaces by EtOH-CVD at 700°C. Scale bars: (a) 200 μm. (b) 500 nm. (c) 100 nm.

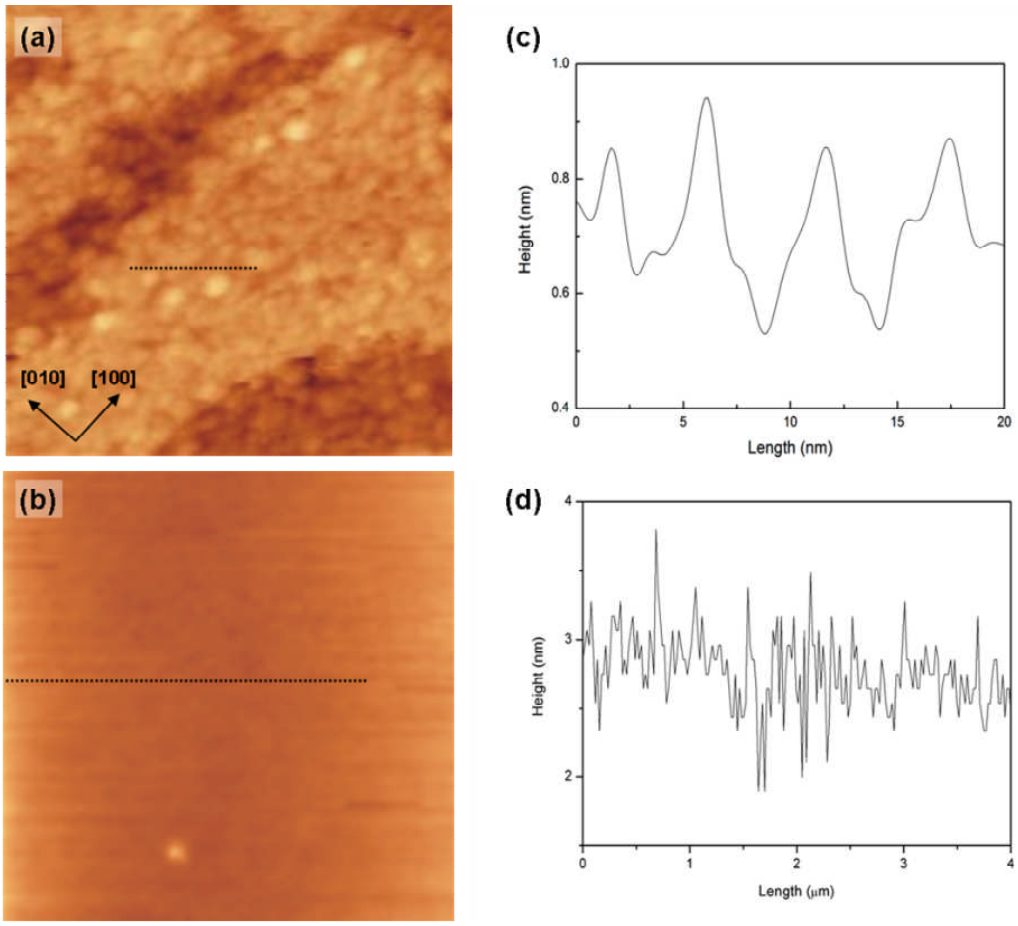

Figure 5.6: (a) STM and (b) AFM images of the sputtered STO surface after a blank metal-catalyst-free experiment. ((a): Image size: 70 × 70 nm^2, V_s = 2.0 V, I_t = 0.06 nA. (b): Image size: 5 × 5 μm^2). Survey height traces, marked as black-dashed lines on (a) and (b), are shown in (c) and (d), respectively, indicating the formation of nanosized bumps on the sputtered surface by CVD conditions.

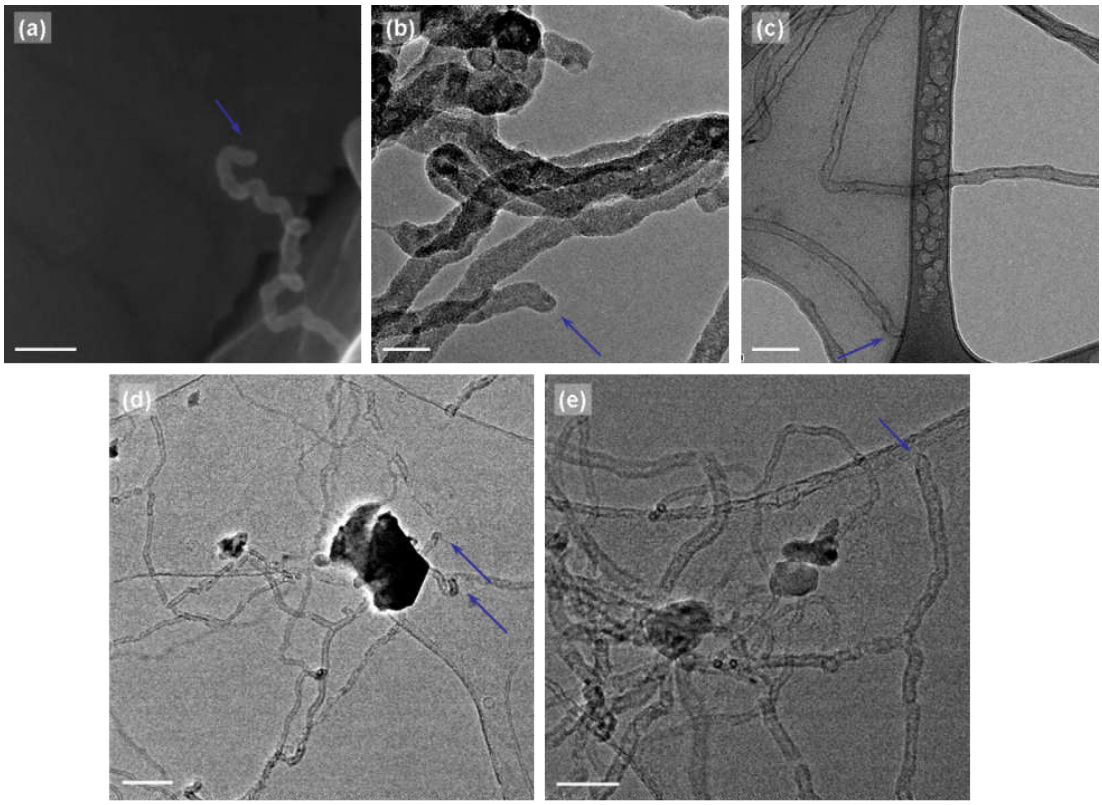

Figure 5.7: Investigation of the growth mode of CNTs grown on sputtered $SrTiO_3$ (001) samples. (a) HRSEM observation of the tip of an individual tube grown on the sputtered surface. Clearly no distinguishable contrast could be detected; thus no NPs are trapped inside the tip, as indicated by the blue arrow. (b-c) TEM images of the CNTs grown on the sputtered surfaces by C_2H_2-CVD (b) and EtOH-CVD (c) show that the tips of CNTs are free of catalyst particles (highlighted by blue arrows). (d-e) TEM observations of CNTs generated on Cu-grid-supported STO microsized particles with miniature surfaces presented. The images of two different sites show that the CNTs are generated from the STO surface with the tips free of catalyst particles (as indicated by blue arrows). These EM observations confirm that the growth of CNTs on sputtered STO (001) substrates follows a base growth mode. Scale bars: (a-e) 50 nm.

5.3.2 Growth of CNTs by Particulated $SrTiO_3$ Powders

The STO powders employed here were made from as-received, non-doped STO samples, details of which can be found in Section 5.2.2. For the subsequent CNT growth experiments, both EtOH- and C_2H_2-CVD were carried out at a growth temperature of 700°C.

5.3.2.1 Metal-Free EtOH-CVD

The growth results of CNTs, grown by STO powder with the aid of metal-free EtOH-CVD, are gathered in Figure 5.8. The growth experiments were carried out in the identical experimental conditions (gas flow rate, growth time, growth temperature) as stated in Section 5.3.3.1. The SEM images in Figures 5.8a and 5.8b display the formation of CNT/Fs from the STO particles after the CVD process. Representative TEM observations (Figures 5.8c and 5.8d) of the same sample reveal morphologies of carbon filaments grown by STO particulates, some of which are trapped within the tips of tubes, as indicated by the blue arrow in Figure 5.8c. Figure 5.8d captures a scene in which graphitic layers (as marked by red arrows on the image) form and wrap a nanoparticle, which has a diameter of ~10 nm. This NP, trapped within the graphitic ring, was probed by point-localised energy-dispersive X-ray spectroscopy (EDX), as marked by the blue circle. The EDX analysis (Figure 5.8d*) displays the presence of Sr, Ti, O, C, and Cu (attributed by the TEM grid). It also indicates the absence of any other metal elements (such as Fe, Co, and Ni).

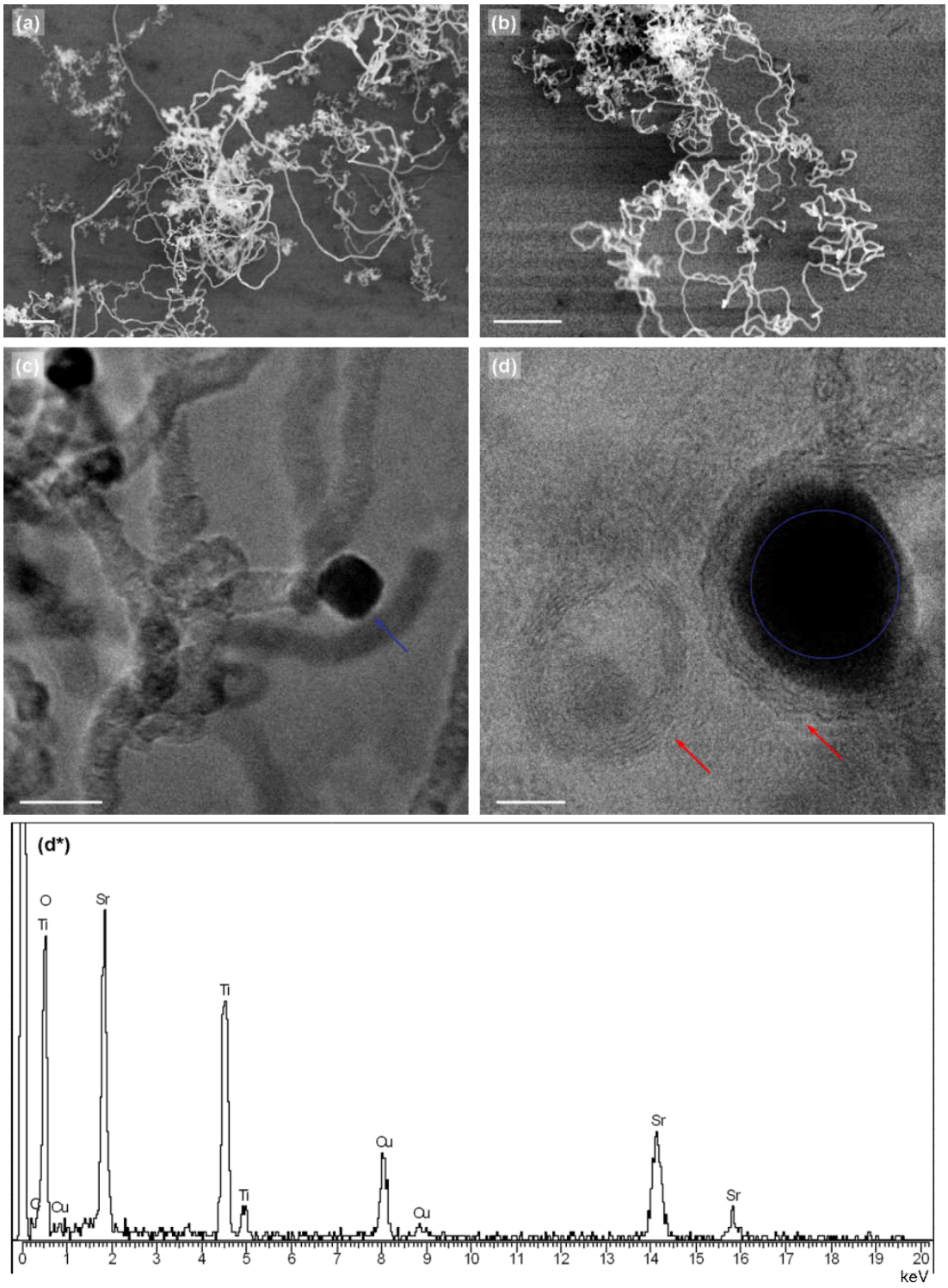

Figure 5.8: Characterisation of carbon nanotube/fibres produced on pure particulate STO powders by EtOH-CVD. (a-b) SEM observations of the grown sample. Scale bars: (a-b) 1 μm. (c-d) TEM observations of the CNT/Fs grown from the same sample. The blue arrow marked on (c) highlights a trapped NP. The red arrows marked on (d) indicate the presence of graphitic layers generated around the NPs. Scale bars: (c) 20 nm. (d) 5 nm. (d*) EDX from the blue-circled region of the trapped NP in (d).

5.3.2.2 Metal-Free C_2H_2-CVD

In a similar manner, metal-free C_2H_2-CVD was conducted on the particulated STO samples. The SEM images of grown samples (Figures 5.9a and 5.9b) display prolific production of CNT/Fs, sprouted from the powders. The TEM image (Figure 5.9c) reveals the typical filamentous structure grown from STO particles, when using C_2H_2 as the carbon feedstock ($Ar/H_2/C_2H_2$ here at 400/200/40 sccm), with a close view of an individual tube indicating the formation of CNFs (Figure 5.9d). The nanoparticle trapped inside a CNF was characterised by point-localised EDX, and the obtained EDX spectrum in Figure 5.9c* indicates the presence of STO.

5.3.3 Growth of CNTs on Scratched $SrTiO_3$ Substrates

The scratched STO substrates employed here were made with the aid of a diamond blade (in order to avoid any possible metal contamination), details of which can be found in Section 5.2.3. In addition, the surface morphologies of scratched samples were probed by SEM imaging, which are shown in Figure 5.1. For the subsequent CNT growth experiments, both EtOH- and C_2H_2-CVD were carried out. For EtOH-CVD, the reaction occurred at a growth temperature of 700°C. For C_2H_2-CVD, a particular investigation of the effect of growth temperatures was conducted, where various forms of carbon nanostructures (CNTs, CNFs, CNC/CMCs) were produced, corresponding with the temperature windows applied.

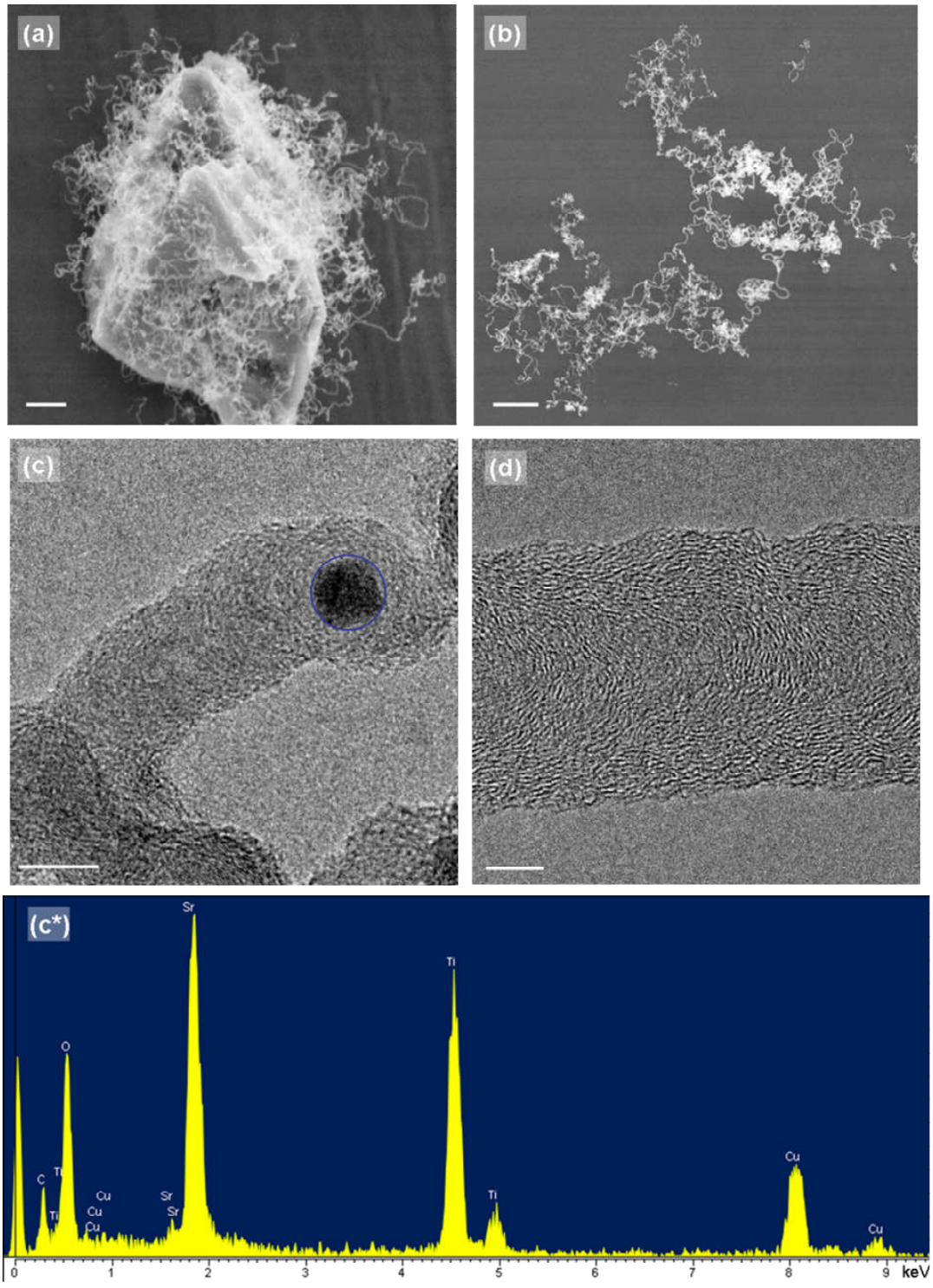

Figure 5.9: Characterisation of CNF/Ts produced on pure particulate STO powders by C_2H_2-CVD. (a-b) SEM and (c-d) TEM observations of the grown sample. (c*) EDX from the blue-circled region of the trapped NP in (c). The signal of Cu in the spectrum were from the TEM grid. Scale bars: (a) 300 nm. (b) 1 μm. (c) 10 nm. (d) 5 nm.

5.3.3.1 Metal-Free EtOH-CVD

The SEM image in Figure 5.10a exhibits the growth of CNTs alongside the scratched mark on the STO sample. The Raman spectrum taken from the grown sample is shown in Figure 5.10b, which displays G, D, and 2D peaks. The EDX spectrum collected from the red rectangular area marked on Figure 5.10a is presented in Figure 5.10c, showing the presence of elements such as C, O, Ti, and Sr and the lack of any other metals. Moreover, the sample after the CVD reaction was subject to an XPS measurement, which also indicates that there was no trace of any other metallic species on the sample surface, as shown in the spectrum in 5.10d, confirming that the CNT were grown from metal-free processes.

5.3.3.2 Metal-Free C_2H_2-CVD

5.3.3.2.1 TEM Combined with Point-Localised EDX Investigations

In this case, the growth experiment was conducted at a growth temperature of 700°C. The sample was subject to H_2 (800 sccm for 5 min) pretreatment before the introduction of C_2H_2. The gas flow recipe used here was $Ar/H_2/C_2H_2$ at 400/200/40 sccm. The growth results are shown in Figure 5.11. The SEM (Figure 5.11a) and TEM (Figure 5.11b) images of the grown sample reveal the morphologies of the attained carbon nanomaterials. It is believed that scratching the STO surface with the aid of a diamond blade leads to the generation of nanosized and microsized STO particles on the surface, which in turn function as catalysts for the growth of CNT/Fs. Figure 5.11b shows that the formation of CNTs occurs at the periphery of the

blue-circled particle. The EDX measurements on the catalyst particle and the sample stage background (Figures 5.11b* and 5.11b**) verify the presence of STO.

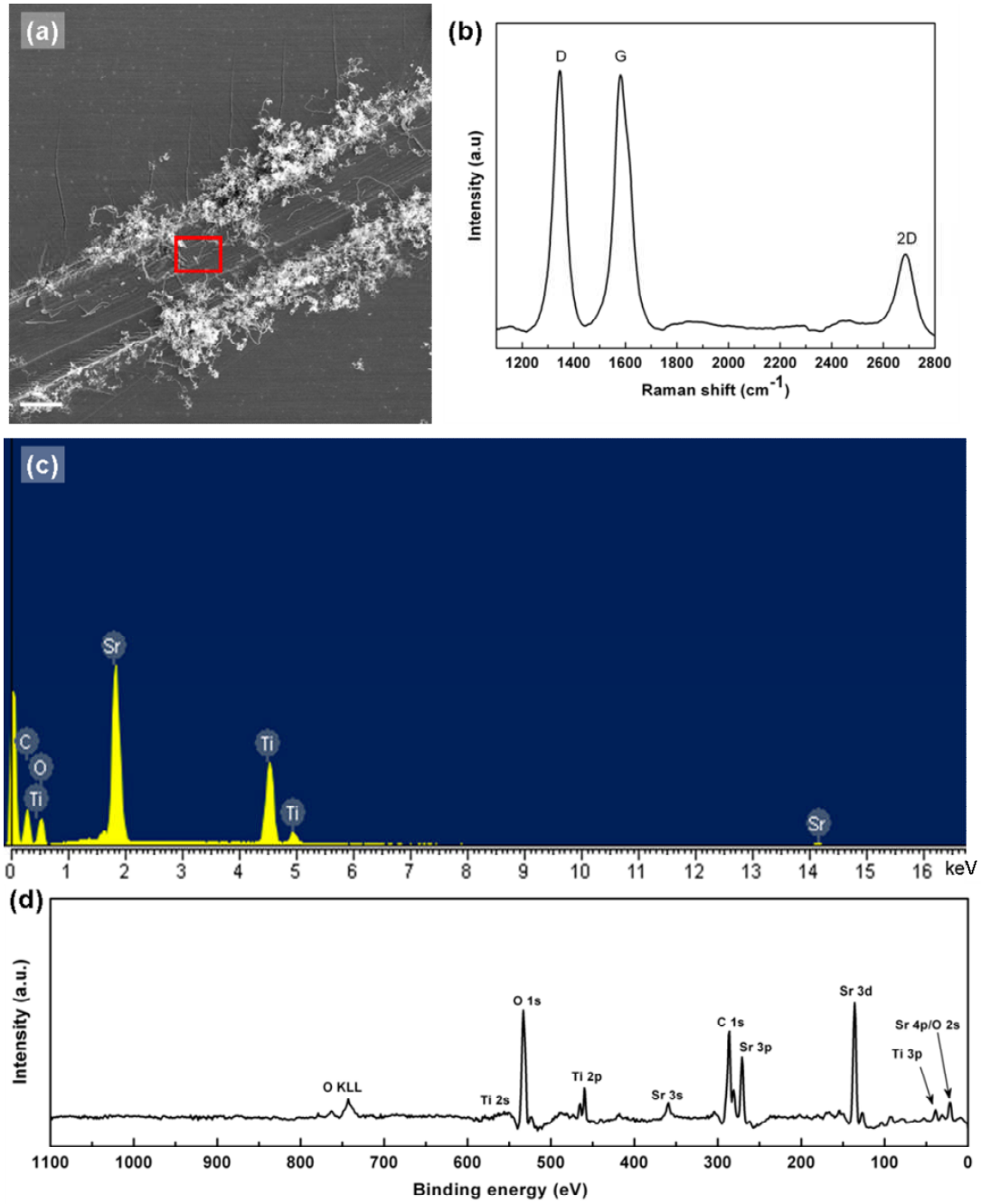

Figure 5.10: Characterisation of CNTs grown on scratched STO surfaces by EtOH-CVD at a growth temperature of 700°C. (a) SEM observation showing the appearance of CNTs generated alongside the scratching mark. Scale bar: 3 μm. (b) Raman spectrum of the CNTs shown in (a). (c) EDX data generated from the red box on (a). (d) Survey XPS spectrum of the substrate after growth experiment.

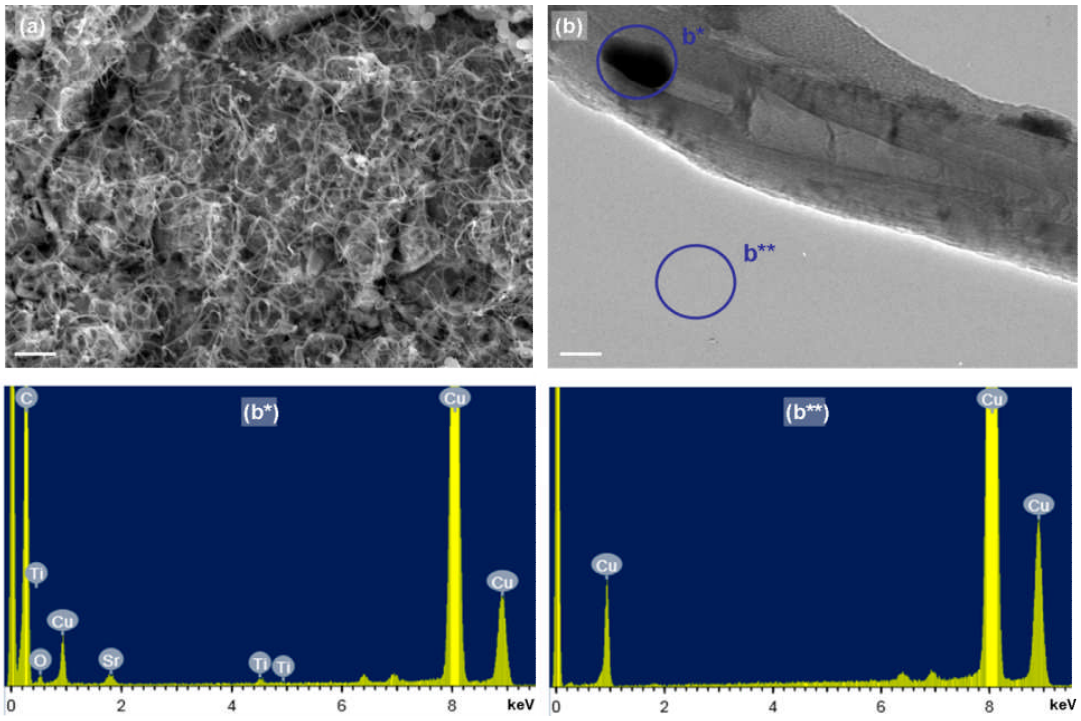

Figure 5.11: Characterisation of CNT/Fs grown on scratched STO surfaces by C_2H_2-CVD at a growth temperature of 700°C. (a) SEM and (b) TEM observations of the grown sample. (b*-b**) EDX spectra of the blue-circled regions in (b). The EDX spectrum (b*) of the catalytic NP trapped within the tube proves the existence of STO. The EDX spectrum (b**) of sample stage background shows bare Cu signal. Scale bars: (a) 500 nm. (b) 20 nm.

5.3.3.2.2 Effect of Growth Temperatures on the Forms of Carbon Nanostructures

A parameter investigation regarding growth temperatures was performed by C_2H_2-CVD on scratched STO substrates. Here the experiments were conducted at various growth temperatures (450, 575, 650, 700, 750°C). All other growth conditions were kept identical. The samples were subject to H_2 (800 sccm for 5 min) pretreatment before the introduction of C_2H_2. The gas flow recipe used here was $Ar/H_2/C_2H_2$ at 200/400/40 sccm. Surprisingly, diverse forms of carbon products were attained, as shown in Figure 5.12.

The SEM image in Figure 5.12a exhibits the growth products at 450°C. The formation of carbon NPs and 'spaghetti-like' carbons can be observed. Figure 5.12b documents the production of carbon nanostructures at 575°C, with the network of CNT/Fs found on the STO surface. At a growth temperature of 650°C, similar CNT/F structures were produced, but with higher yield, as shown in Figure 5.12c. The CVD reaction at 700°C produced carbon helical structures (Figure 5.12d), whereas normal CNTs were produced, along with the formation of some by-products, when the growth temperature was set at 750°C (Figure 5.12e). Representative Raman spectra of obtained products are presented in Figure 5.12f.

The production of assorted types of carbon nanostructures here indicates the capacity of C_2H_2 to boost the diversity of carbon forms. It is interesting that the carbon nanocoils/microcoils were formed at a specific temperature of 700°C, the reproducibility of which has also been confirmed by repeated trials in this study. The detailed investigations are shown in Chapter 7.

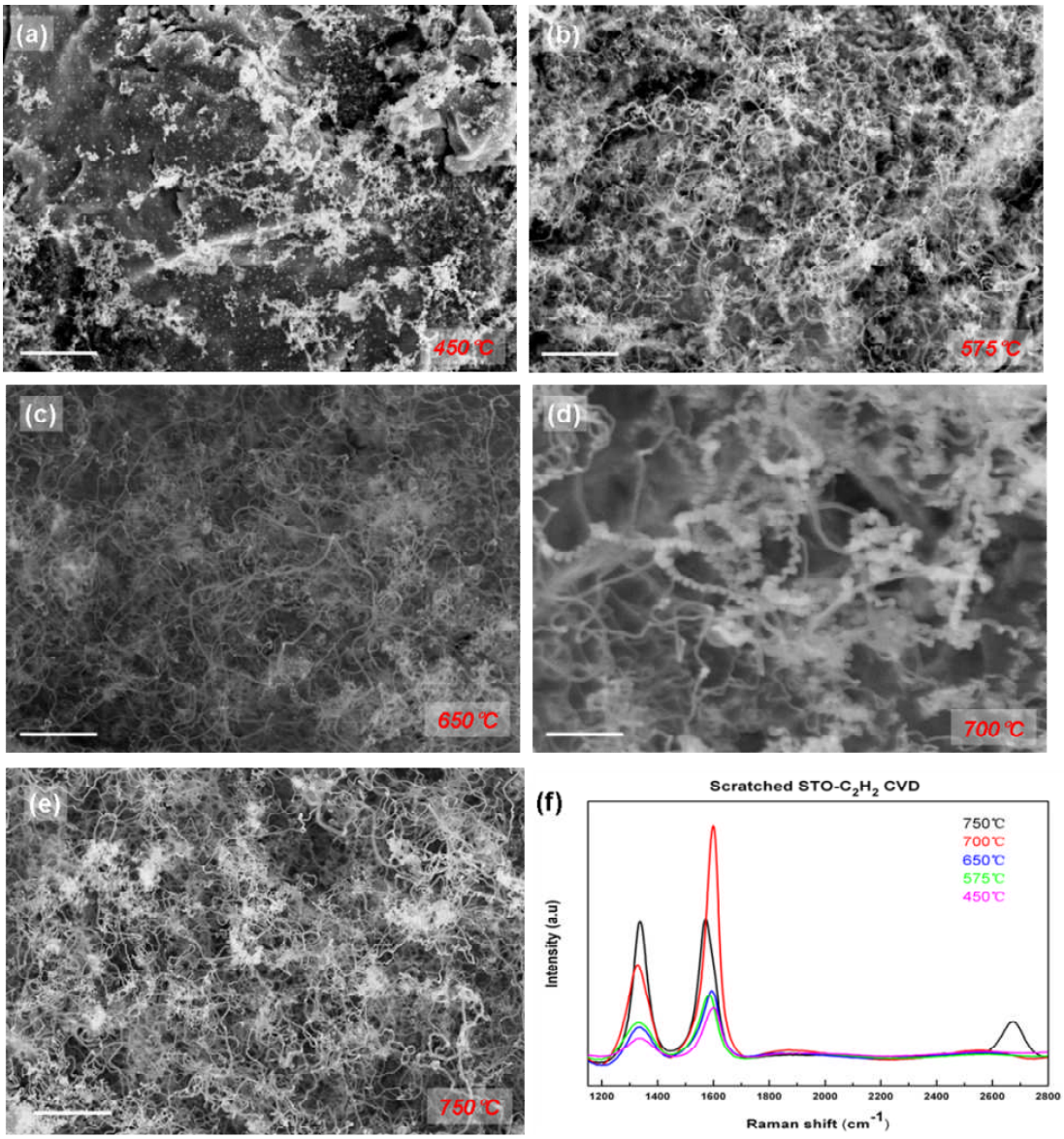

Figure 5.12: Effects of the growth temperatures on the forms of carbon nanostructures grown on scratched STO substrates by C_2H_2-CVD. SEM images (a-e) and Raman spectra (f) of obtained products are documented. The samples were grown under various temperatures with other growth parameters set identically. The growth temperatures applied are marked on each SEM image. Scale bars: (a-e) 1 μm.

5.4 Discussion

5.4.1 Metal-Catalyst-Free CVD Process

Metal-catalyst-free CVD process can be described as using non-metal species (normally oxides) as catalysts/templates for the production of carbon nanomaterials by CVD reaction. For the synthesis of CNTs, various types of oxides have been tried, giving rise to promising results (Table 1), which indicate that oxides are a feasible material for catalysing the growth of CNTs; moreover, the fabrication of graphene and carbon helices by oxide materials reported in recent publications certainly demonstrates the versatility of this method.

For performing a metal-free CVD, it is important to establish beforehand that there are neither metallic species nor other sources of contamination within the reaction. In this study, several measurements were taken to ensure that a completely metal-free CVD process took place in each experimental trial. Firstly, several measures were put in place to create a clean reaction zone, free of any metal contamination. For example, new quartz tube was used for every CVD run, plastic tools were used instead of stainless steel ones for sample handling and transfer, and a diamond blade was employed for scratching the STO substrates. Secondly, in the case of the Ar^+ ion-sputtered STO sample, XPS measurements were performed prior to and after the CVD process, which show the absence of metal elements, such as Fe, Co, and Ni, indicating that the growth of CNTs is not related to these conventional types of CNT catalysts. Lastly, controlled experiments were conducted with the aid of

c(4×2)-reconstructed samples, which were positioned in the quartz tubes, along with other STO samples in the CVD processes, to detect whether the reaction zone (gas ambients, carbon feedstocks, reactors, connectors, quartz tubes *etc.*) was free of metallic species. For each experimental run, there should be nothing grown on the *c*(4×2)-reconstructed substrate surface, if the CVD process is not contaminated by metals.

5.4.2 Effect of Nb Dopants

For the investigations depicted in Section 5.3.1 and Section 5.3.3, the STO single crystals used were doped with 0.5 wt% Nb. It is reasonable to assume that the Nb can function as a catalyst for the growth of CNTs. However, evidence is provided in the following text to rule out this possibility. For the sputtered samples, it is very unlikely that the observed asperities on the sputtered substrates (Figure 5.6) are composed of Nb, since no Nb surface segregation was observed on the substrate surfaces[277, 278]. For the scratched samples, point-localised EDX spectra clearly show that no Nb peak (locates approx. at 2.2~2.3 keV) can be detected, indicating that the scratch-induced catalyst NPs are free of Nb. In addition, to the best of my knowledge, there is no report whatsoever in the research literature to claim the catalytic ability of Nb in terms of generating/assisting CNT growth.

5.4.3 Speculation on the Formation of CNTs

The latest findings regarding the metal-catalyst-free growth of CNTs by oxides prove to be encouraging; however, there appears to be no universal explanation for the growth mechanisms involved. For example, there has been a wealth of studies focusing on the growth of CNTs on SiO_2 substrates *via* metal-free CVD, with large disagreements over the growth mechanisms. Huang and his colleagues[21] revealed, after careful XPS measurements, that the presence of silica NPs was responsible for the growth of SWNTs at high temperatures. They suggested that only a nanoscale curvature was needed to generate SWNTs, and the defects and distortions created within the quasi-liquid SiO_2 NPs during elevated temperature CVD conditions could enhance the decomposition of hydrocarbons. This result is consistent with the findings of Liu and Cheng[20], where the importance of oxygen-containing SiO_x NPs was highlighted through *in situ* TEM experiments and DFT calculations. Furthermore, Page *et al.*[245] employed quantum-chemical molecular dynamics simulations to investigate the SWNT nucleation on SiO_2 NPs. In their study, a vapour-solid-solid (VSS) mechanism, rather than a VLS mechanism, was suggested to explain SWNT generation on SiO_2. However, Bachmatiuk *et al.*[247] observed that the SiO_2 NPs were carbothermally reduced to SiC during the synthesis of CNFs and stated that the VLS mechanism was applicable in this sense; whilst another route of mechanisms has been argued by Liu *et al.*[246], who proposed that the SiO_2 substrate subjected to high-temperature H_2 annealing would present defects on its surface, which provided stack-up sites for facilitating the deposited carbons to self-assemble

into SWNTs.

In this study, the surface-roughness-tailored growth of CNTs on engineered $SrTiO_3$ (001) single crystals by metal-catalyst-free CVD is of great interest. This investigation encompasses several simple, flexible methods for engineering the STO (001) substrates to achieve metal-free growth of CNTs on them, where the induction of atomic surface roughness is responsible for the catalytic performances of substrate samples. Here a special focus is put on the sputtered samples. It is observed that nanosized bumps appear on the surface after a blank CVD experiment (Figure 5.6); furthermore, the base growth mode of CNTs grown on sputtered substrates was identified (Figure 5.7). Based on these experimental investigations, it is speculated that those surface engineering methods lead to the creation of $SrTiO_3$ asperities with nanometer scale on the surfaces and these acted as the catalysts for the formation of CNTs. This argument is supported by the previous study by Bowker *et al.*,[281] which indicated that $SrTiO_3$ nanosized particles possessed catalytic capacities to absorb and decompose hydrocarbons, especially alcohols, such as methanol.

The complementary studies using STO powders and scratched STO substrates further verify this theory. Direct evidence have been found that the growth of CNTs occurs right on the STO NPs (Figures 5.8c, 5.9c, and 5.11b), indicating that the STO NPs function as catalysts for the generation of CNTs. Additionally, the observation of graphitic rings around the oxide NPs (Figure 5.8d) demonstrates the catalytic ability of oxides to boost the formation of graphene layers. The point-localised EDX spectrum of the NP (Figure 5.8d*) shows the existence of oxygen, with no peaks of

Fe, Co, and Ni; moreover, it has been shown that nanoparticulate $SrTiO_3$ or TiO_2 appears to be stable against carbothermic reduction at extremely high temperatures (>1000°C),[282] therefore it can be deduced that the chemical constitution of the catalyst NP is neither metallic nor carbide.

Despite considerable efforts to prove the catalytic ability of STO NPs, it is still arguable that the CNTs grown on engineered STO (001) substrates are formed *via* a self-assembling route, where the STO surface assists the decomposition and transportation of carbon feedstocks and provides stacking-up sites for deposited carbon to assemble into tubes. While the author cannot rule out this possibility, there has not been sufficient evidence so far to substantiate the explanation in this investigation; for example, bamboo-shaped CNT/Fs have not been observed in this case, which is regarded as a 'sign' for this self-assembling route[252, 256]. Here the engineered STO surfaces with atomic surface roughness automatically possess asperities with nanoscale curvatures, which will then function as templates, rather than provide carbon stacking-up stages, for generating CNTs on them during CVD reactions, as indicated below.

In view of the experimental observations and evidences gathered above, the surface-roughness-tailored CNT formation on the engineered STO (001) surfaces by metal-free CVD can be explained: Engineering the STO surfaces through various treatments gives rise to the formation of STO asperities with nanoscale curvatures on the surfaces, which will function as templates for generating CNTs. A rougher surface (within atomic surface roughness), such as an ion-sputtered one, provides

more nucleation sites for the induction of CNTs, whilst an atomically flat surface, such as a *c*(4×2)-reconstructed one cannot support the growth of CNTs, owing to the lack of suitable curvatured asperities. Thus, the growth mechanism of CNTs can be suggested as follows: The growth of CNTs on engineered STO surfaces *via* metal-catalyst-free CVD adopts a base-growth mode. The STO bumps/asperities with nanoscale curvatures on the substrate surface function as catalysts to provide nucleation sites for carbons and assist to form the hemispherical carbon cap, where the defects/distortions over the STO asperities, which were created by the elevated-temperature H_2 pretreatment in CVD conditionings, could enhance the adsorption and decomposition of hydrocarbons. The growth of carbon tubular structures over these STO asperities was then through the lift-off process of the formed carbon cap, where the supply of carbon atoms/species generated from the thermal/catalytic pyrolysis were continuously added through the bottom of the tube, allowing the CNT to keep growing. During the whole process, the STO catalyst stays in its oxidising form, and the oxygen contained within STO lattices might benefit the growth of CNTs from them[20].

5.5 Conclusions

In summary, surface-roughness-tailored growth of carbon nanotubes (CNTs) by metal-catalyst-free CVD on $SrTiO_3$ (001) substrates has been achieved. An ultra-high

vacuum (UHV) system, equipped with an STM, allowed us to engineer and characterize the substrates prior to the CVD process. Ethanol-CVD was carried out at a growth temperature of 700°C. In this study, a series of engineered STO substrates with distinct surface structures was produced. A correlation between the surface roughness/morphology of substrate and relevant catalytic activity/CNT yield has been successfully revealed. Complementary studies were performed with the aid of EtOH- and C_2H_2-CVD to confirm the catalytic capability of STO nanoparticulates/nanoasperities. Ultimately the growth mechanism of CNTs is suggested, based on the experimental findings and related discussions.

Chapter 6：

Metal-Catalyst-Free Growth of Carbon Nanotubes (CNTs) on Polycrystalline $BaSrTiO_3$ Surfaces

6.1 Background

The metal-catalyst-free growth of CNTs by oxides is a major breakthrough in carbon nanomaterials research.[64, 92] As discussed earlier, the growth of SWNTs has been achieved on various oxide materials, SiO_2[19-21, 246], ZrO_2[249], MgO[217, 275], a very recent study has even revealed that carbon nanohelices can be generated from SiO_2 without any involvement of metals using CVD.[276] In this thesis, the surface-roughness-tailored growth of CNTs on $SrTiO_3$ (001) single crystals is also demonstrated in Chapter 5. One further issue that would be interesting is to investigate to see which perovskite facet(s) is (are) the most catalytically active for the growth of CNTs. The way to answer that is to use a polycrystalline sample with a flat surface for CNT growth *via* a metal-free CVD, which is the investigation presented in this chapter. This work is of great importance because it not only leads to the realisation of controllable synthesis of CNTs directly on oxides throughout careful selection of oxide faceted surface, but also provides insights into the usage of perovskite oxides in catalysis.

In this chapter, the facet-selective growth of CNTs on polycrystalline $BaSrTiO_3$ surfaces by metal-catalyst-free CVD is discussed. It is well known that $BaSrTiO_3$ can serve as a good candidate for numerous applications, e.g. high-sensitivity sensors and tunable microwave systems, due to the benefits of its low costs and well-known ferroelectric properties.[29-32] Moreover, the combination of the CNTs with $BaSrTiO_3$ may spur novel properties and lead to the fabrication of future DRAM devices and MEMS-based sensors.[31] Here, the effect of facet orientation on the growth of CNTs

is explored, along with the influence of surface roughness. Although detailed studies have been carried out on the impact of substrate orientations, with regard to the metal nanoparticle patterning and corresponding CNT growth behaviour *via* metal-catalyst-involved CVD,[214] the growth of CNTs on polycrystalline oxide surfaces without the aid of metal catalysts has never been attempted.

6.2 Experimental Details

Epi-polished polycrystalline $Ba_{0.6}Sr_{0.4}TiO_3$ (BST for short) surfaces (PI-KEM Ltd, UK) were employed for the growth of CNTs. In this work, the BST samples were typically etched for 10 min in the prepared BHF solution. This etching treatment removes the polishing damage/carbon layers/metal contamination on the substrate, giving rise to a clean (free of metal contamination) polycrystalline BST surface with various facets clearly exposed. The detailed procedure of BHF etching is described in Chapter 2. The experiments on CNT growth were performed with the aid of atmospheric CVD apparatus in the Department of Materials at the Begbroke Science Park, details of which can be found in Chapter 2. For CNT growth, both EtOH- and C_2H_2-CVD were conducted on the prepared BHF-BST samples. An identical set-up to the one used for the growth of CNTs on the bare $SrTiO_3$ (001) single crystals described in Chapter 5, ensures that the CVD process taking place is metal-catalyst-free.

6.3 Results

To conduct CNT growth on bare BST substrates, the surface itself is firstly characterised prior to the CVD process. The successful growth of CNTs on BST substrates by metal-catalyst-free CVD is then documented with the aid of SEM, TEM, and Raman investigations. Furthermore, detailed investigations on the phenomenon of facet-selective growth of CNTs are carried out through SEM, EBSD, and Micro-XAM co-observations.

6.3.1 Probing the Polycrystalline BHF-BST Surface Prior to the CVD Process

6.3.1.1 SEM, EDX, XPS, and AFM of the BHF-BST Surface

To acquire information on the surface morphology and chemistry of the BHF-BST surface, prior to the growth of CNTs, SEM, EDX, XPS, and AFM have been carried out on the samples. The SEM image in Figure 6.1a shows the morphological features of the BHF-etched BST sample surface. The distinct crystal facets can be clearly observed, with varied grain sizes. Figure 6.1b displays a representative EDX spectrum, generated from the red rectangular area marked in Figure 6.1a. This chemical analysis shows the presence of Sr, Ba, Ti, and O, which is consistent with the elemental composition of the detected sample. The EDX pattern also indicates

the absence of carbon and any other metal contamination (such as Fe, Co, and Ni) on the surface. The sample was further analysed with XPS characterisation, which was performed by Mr. Clive Downing. The representative XPS spectrum shown in Figure 6.1c indicates that the sample surface is free of any metal contaminations. The surface texture of the polycrystalline BHF-BST is probed with the aid of AFM, as shown in Figure 6.1d. Additionally, the areal root-mean-square (rms) surface roughness (R_{rms}) of different crystal facets can be accessed by SPIP Image software. The values obtained of areal R_{rms} of the facets marked (i), (ii), and (iii) in Figure 6.1d are 6 nm, 11 nm, and 5 nm, respectively. The AFM observation of the BHF-BST polycrystalline substrate reveals that BHF etching gives rise to different crystal facets, which possess distinct surface roughness and grain heights.

6.3.1.2 Micro-XAM of the BHF-BST Surface

To facilitate the investigation of the surface texture and ease the process of acquiring information on the surface roughness of BHF-BST samples, a Micro-XAM was employed, instead of an AFM. Figure 6.2 shows two Micro-XAM images of the same area on the BHF-BST sample surface, prior to (a) and after (b) a blank-CVD process. The blank-CVD was carried out at 750˚C for a period of 5 min in a maintained carrier gas flow of Ar (500 sccm) and H_2 (500 sccm), which is identical to the CVD conditions for CNT growth discussed in Section 6.3.2, but without the presence of carbon feedstocks. Image analyses on these two micrographs reveal that there is no drastic change in the surface textures/roughness of the sample surface

when exposed to the applied CVD conditions.

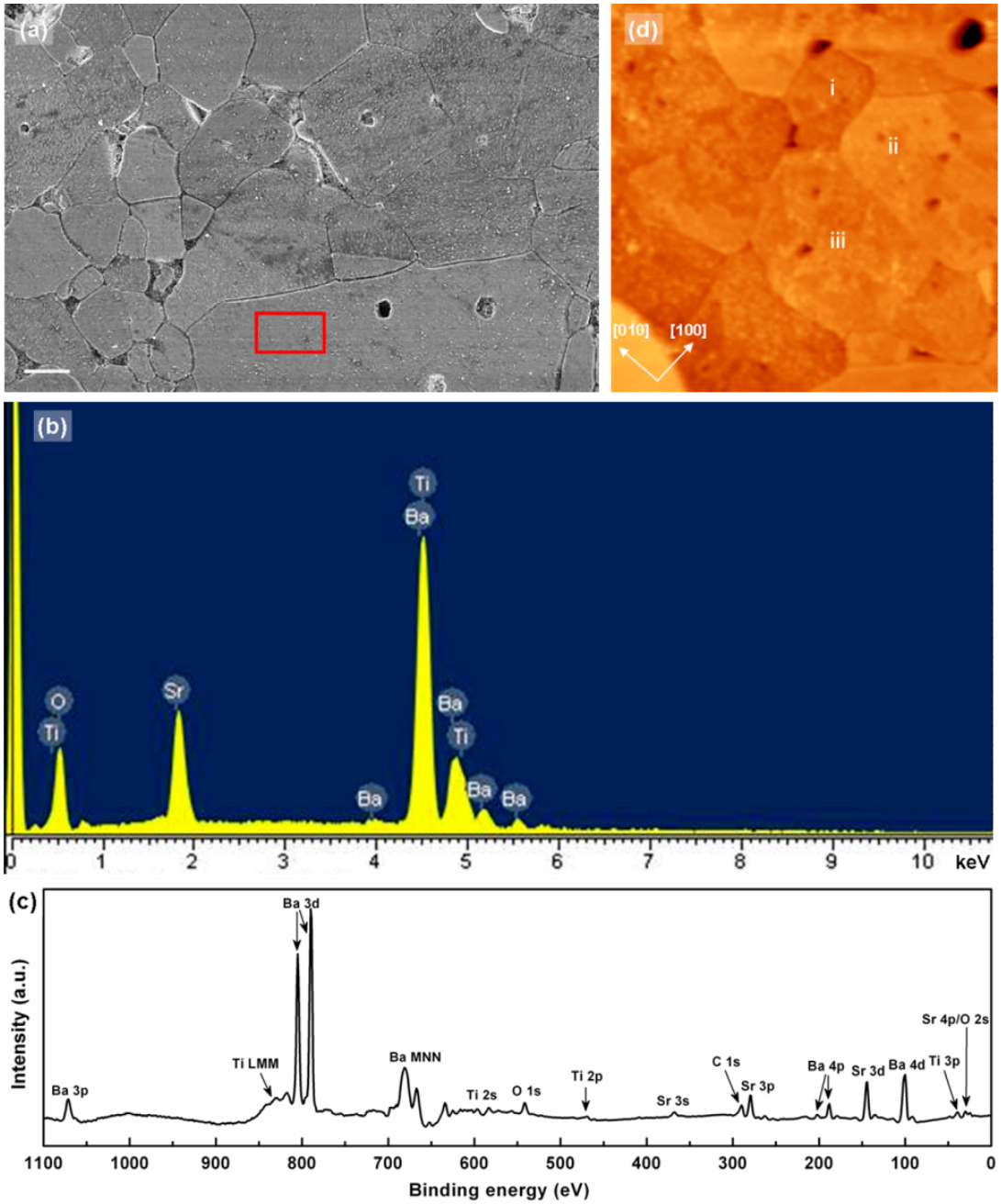

Figure 6.1: (a) SEM observation of BHF-etched BST surface prior to the CVD process. The different crystal facets, along with the phenomenon of grain grooving, can be clearly observed. Scale bar: 1 μm. (b) EDX spectrum formed from the red region marked in (a). (c) XPS spectrum of the same sample surface prior to the CVD reaction. (d) AFM image of the etched BST surface prior to the CVD process. The various crystal facets are shown in the image. (Image size: 30 × 30 μm^2).

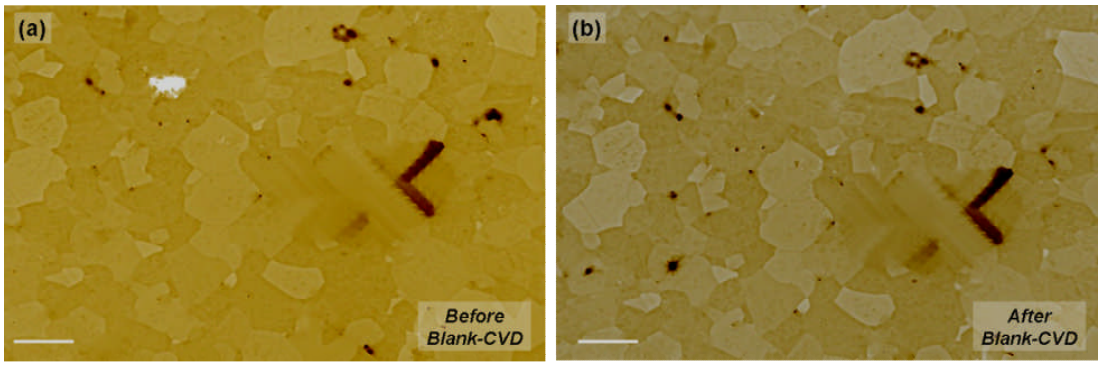

Figure 6.2: Micro-XAM imaging of the same area of the BHF-etched BST surface prior to (a) and after (b) the blank-CVD process. It is observed that there is no apparent change in the surface structures/features, when this treatment is applied to the sample. Measurements of the surface roughness, performed before and after the CVD process, also show no variation in the values. Scale bar: 30 μm.

6.3.2 Metal-Catalyst-Free Growth of CNTs on Polycrystalline $BaSrTiO_3$ Surfaces

6.3.2.1 Realisation of Metal-Catalyst-Free Growth of CNTs

The growth of CNTs on the BHF-etched BST surface was firstly realised with the aid of metal-free EtOH-CVD. The CVD experiment was performed at a growth temperature of 750˚C for a period of 5 min (To choose 750˚C (not 700˚C as used in the experiments presented in Chapter 5) for this work is because there was no CNT formation at 700˚C herein). A mixture of Ar and H_2 was used as the carrier gas. The grown sample was collected after the CVD process and subsequently characterised by SEM, TEM, and Raman spectroscopy.

Figure 6.3 shows a gathering of growth results of CNTs generated from the BHF-BST surface by metal-free CVD. The SEM images in Figures 6.3a and 6.3b display tubular structures covered on the BST surface. Surprisingly, Figure 6.3a exhibits apparent distinction in product distribution in terms of crystal facets where the tubes are generated. This interesting feature of facet-selective growth of nanostructures on polycrystalline BST surfaces is detailed in Section 6.3.3. Low-magnification TEM observation in Figure 6.3c provides a general view of the tubular nanostructures produced, with a closer look into the morphologies of the tubes shown in Figure 6.3d. It is clearly observed that hollow compartments occur regularly inside the tubes, revealing the formation of bamboo-shaped nanotubes. The Raman spectrum in Figure 6.3e indicates that the produced nanostructures are indeed

CNTs, and the notable 2D peak reveals that the grown CNTs are quite graphitic.

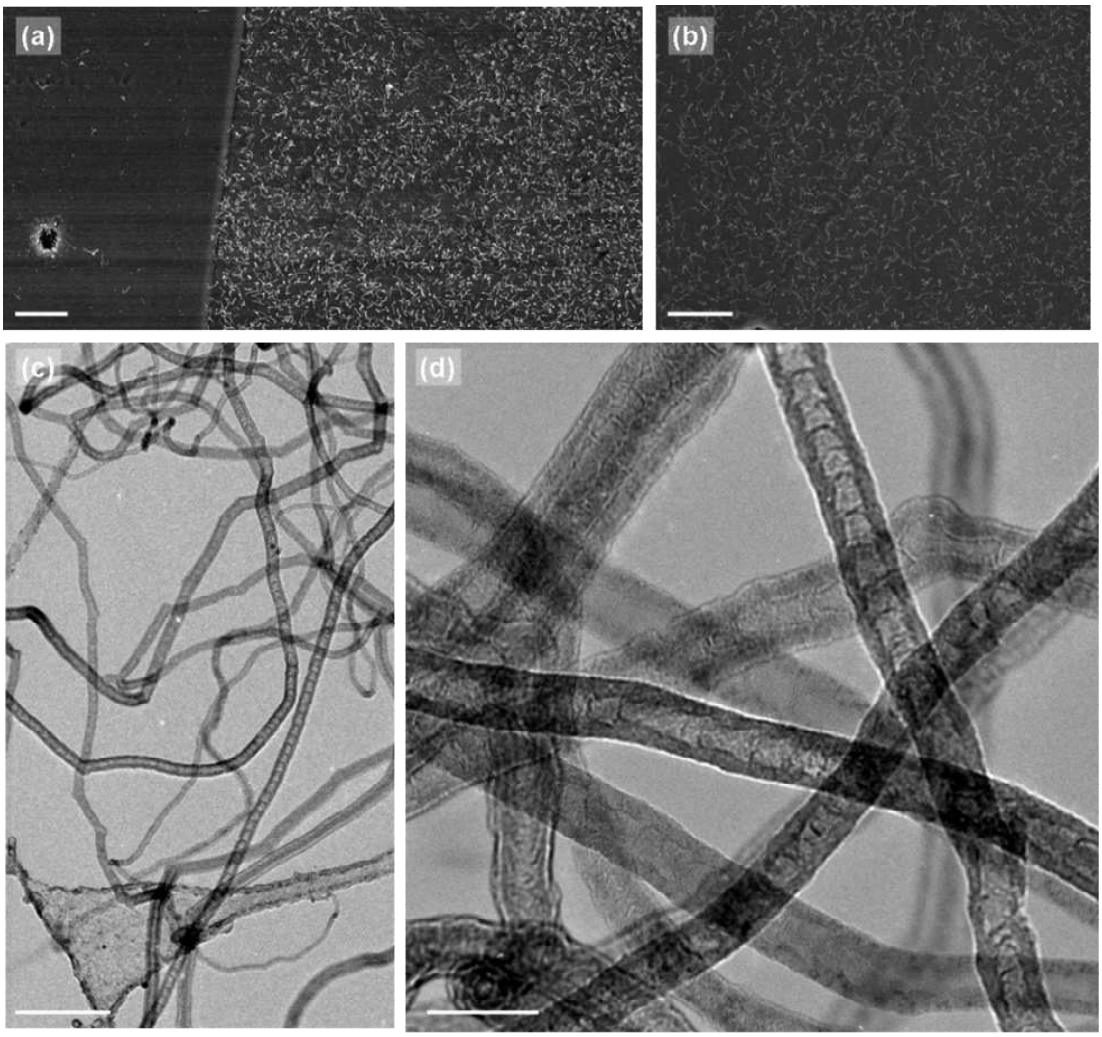

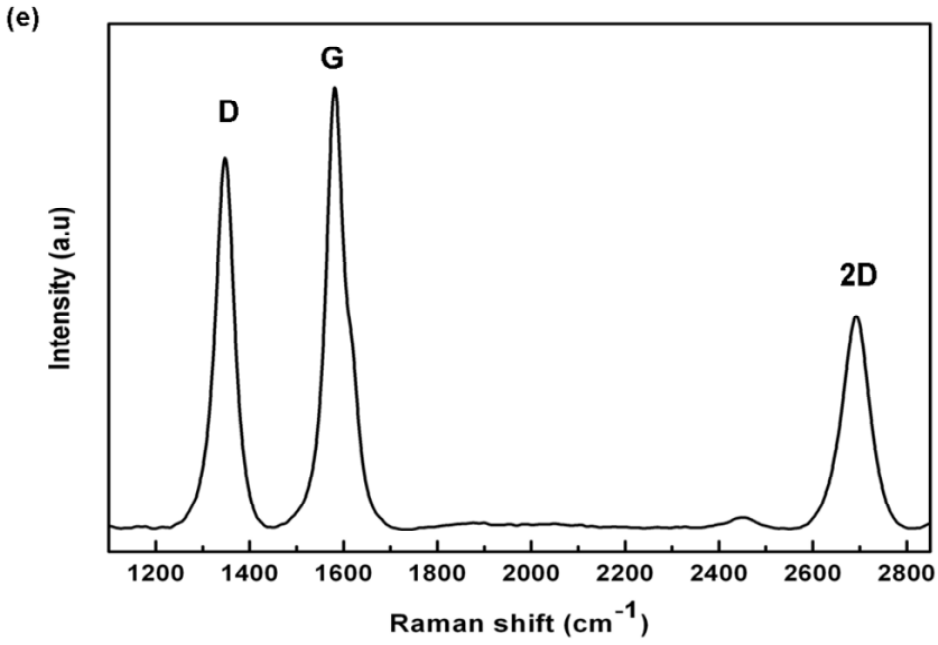

Figure 6.3: Metal-catalyst-free growth of CNTs on the BHF-BST surface by EtOH-CVD. (a) SEM image of grown sample, showing two adjacent facets, on which the facet-selective growth of CNTs occurs. Scale bar: 1 μm. (b) SEM observation of morphologies of the generated CNTs. Scale bar: 1 μm. (c-d) Low (c) and high (d) magnification TEM images of grown CNTs collected from BST surfaces, revealing the formation of bamboo-like CNTs, free of trapped catalyst particles. Scale bars: (c) 200 nm and (d) 50 nm. (e) Representative Raman spectrum of the obtained CNT production. A notable 2D peak can be clearly observed.

6.3.2.2 TEM of Growth of CNTs on Particulate BST

The successful growth of CNTs on the BHF-BST surface by metal-catalyst-free CVD has been achieved for the first time; this prompts the idea that the BST possesses catalytic abilities to catalyse the growth of CNTs, or at least offers a possible stage to assist the tube formation. The same type of experimental investigation described in Section 5.3.2 (CVD on particulate STO powders) is carried out here to confirm the capability of BST in terms of CNT growth. In this study, BST microsized particles (made from the BHF-etched BST sample) were directly deposited onto a TEM grid in order to facilitate post-TEM imaging, and EtOH-CVD was subsequently performed on the loaded TEM grid at 750°C.

TEM observations of CNTs grown on the TEM-grid-supported $BaSrTiO_3$ microsized clusters (Figure 6.4) confirm the previous experimental findings. Figure 6.4a shows that the CNTs are generated from a BST cluster, with blue arrows indicating that the roots of the tubes anchor onto the surfaces of the cluster. Figure

6.4b shows a higher magnified image of an individual nanotube generated from a BST cluster. Moreover, the CVD reaction leads to a possible carbon layer encapsulation of BST nano-bumps and a thin cover of carbon layers on the BST surface, as marked by the red arrow in the image of Figure 6.4b.

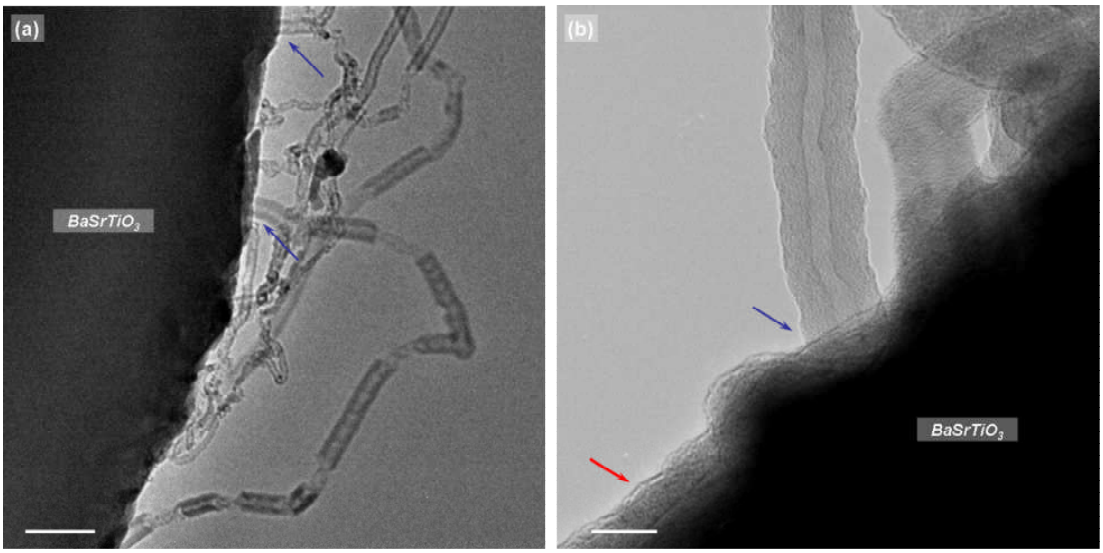

Figure 6.4: TEM observations of CNTs generated on Cu-grid-supported BST microsized clusters. (a) TEM image of grown sample, showing produced tubular structures are generated from the surface of a BST cluster, as marked by the blue arrows. Scale bar: 100 nm. (b) TEM image of an individual nanotube generating from a BST cluster (indicated by the blue arrow), along with the formation of carbon layer-wrapped NPs and carbon layer-covered surfaces (indicated by the red arrow). Scale bar: 20 nm.

6.3.3 Facet-Selective Growth of CNTs via Metal-Free CVD: SEM, EBSD, and Micro-XAM co-Investigations

6.3.3.1 Facet-Selective Growth of CNTs on BHF-BST Surfaces

The phenomenon of facet-selective growth of CNTs on polycrystalline BST surfaces has been observed, where metal-free EtOH-CVD and C_2H_2-CVD were applied, as shown in SEM image library in Figure 6.5. Figures 6.5a and 6.5b are SEM observations with different magnifications, which document the growth of CNTs on the BHF-BST surface by EtOH-CVD. The EtOH-CVD was conducted at a growth temperature of 750˚C for a period of 5 min, with mixed carrier gas (Ar: 500 sccm; H_2: 500 sccm) flowing during the CVD reaction. The facet-selective growth behaviour can be clearly seen, as some facets support prolific production of CNTs, whilst other facets have nothing to grow at all. The same growth trend was observed when C_2H_2-CVD was used (Figures 6.5c and 6.5d). The C_2H_2-CVD was performed at a growth temperature of 750˚C for a period of 5 min. The gas flow recipe during the growth stage was $Ar/H_2/C_2H_2$ at 500/500/20 sccm. Moreover, an experiment was designed to monitor the initial stage of CNT growth on the polycrystalline BST surfaces, by running the C_2H_2-CVD for just 30 sec. The obtained results shown in Figures 6.5e and 6.5f reveal that carbon depositions are facet-selectively condensed, indicating that the nucleation of CNTs favours certain crystal facets.

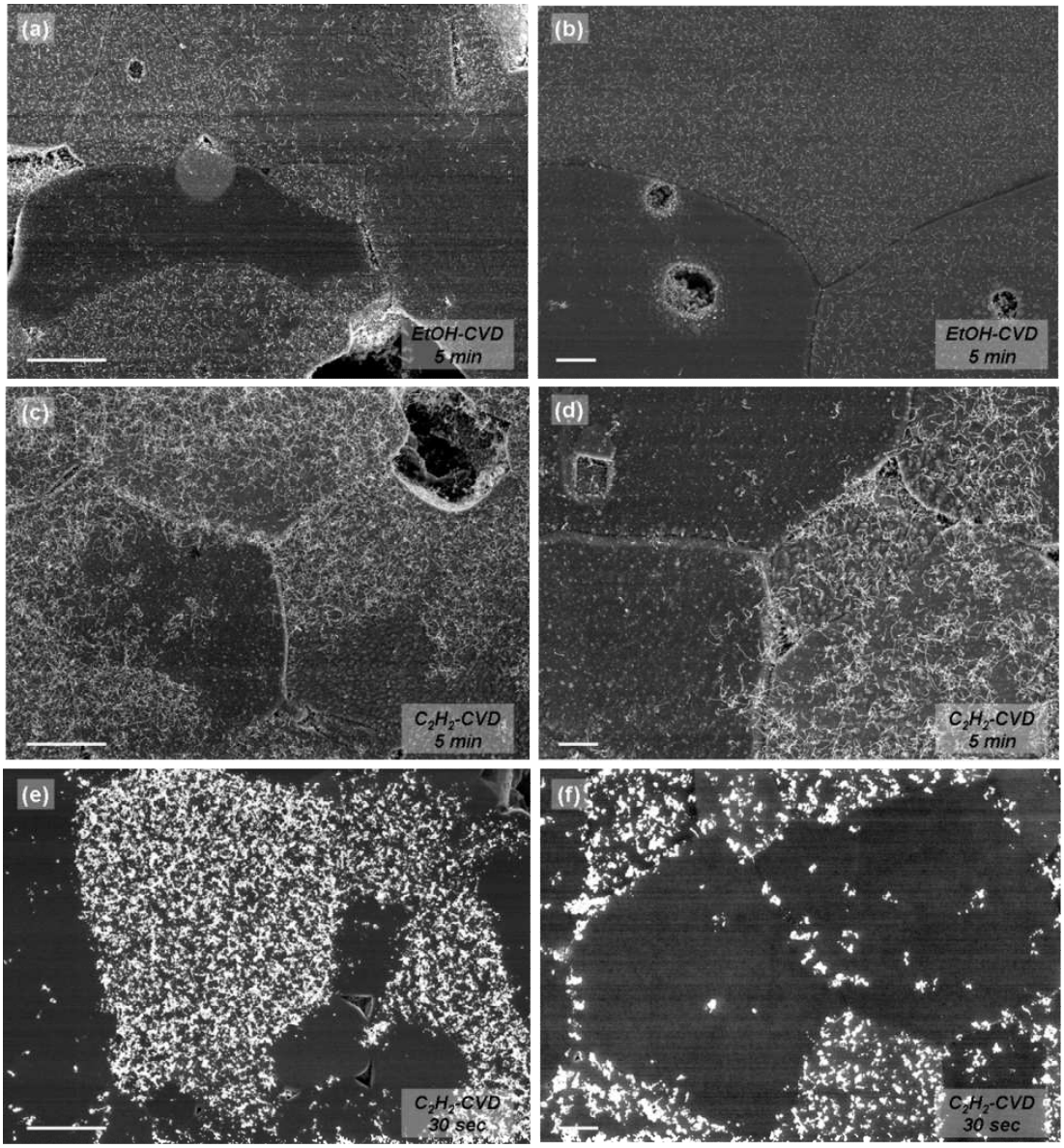

Figure 6.5:. The SEM image library shows the facet-selective growth behaviour of CNTs grown on the polycrystalline BHF etched BST surfaces. EtOH-CVD (a-b) and C_2H_2-CVD (c-d) were conducted for a growth period of 5 min. A specific investigation was designed to tentatively observe the nucleation stage of CNT formation (e-f). Scale bars: (a), (c), and (e): 3 μm. (b), (d), and (f): 1 μm.

6.3.3.2 SEM, EBSD, and Micro-XAM co-Investigations

The surprising finding of facet-selective growth behaviour of CNTs leads to further investigations. Considering the fact that the CNTs were grown without the presence of any metal catalyst, it is speculated that the $BaSrTiO_3$ surface itself, and in particular its surface roughness/lattice arrangements/crystal features, play a crucial role in the nucleation and growth of CNTs. To understand the reason behind the observed phenomenon, SEM, EBSD, and Micro-XAM are manipulated to co-investigate the same sites of interest on the grown sample, where SEM and Micro-XAM provide morphological and textural information on the sites of interest, and EBSD identifies the grain orientations of each facet at the same place.

A representative position of interest from the grown sample was co-characterised by SEM, EBSD, and Micro-XAM, as shown in Figure 6.6. The SEM image in Figure 6.6a clearly presents facet-selective growth of CNTs on three distinct crystal facets, where Facets 1 and 3 display promising production of CNTs, whilst Facet 2 does not support CNT growth. Moreover, it seems that the CNT production on Facet 1 possesses a larger density and more uniform distribution, compared to that on Facet 3. Figure 6.6b shows the EBSD patterns of the three different facets: Facet 1, 2, and 3, as marked on the image, correspond to (110), (001), and (111) crystal planes, respectively. The Micro-XAM image taken from the same place is shown in Figure 6.6c, where the areal surface roughness of each facet can be obtained through image analysis. For Facets 1, 2, and 3, the measured areal R_{rms} are approx. 6 nm, 5 nm, and 5 nm, respectively.

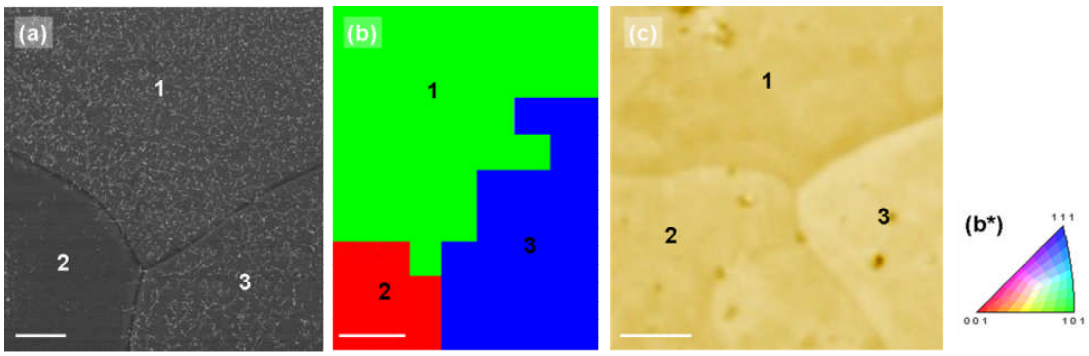

Figure 6.6:. SEM (a), EBSD (b) and Micro-XAM (c) co-investigation of facet-selective growth of CNTs on BHF-etched BST surfaces. The images were taken from the same place on the grown sample. The numbers marked on each image indicate the three different crystal facets. A Miller index, presented in a colourful triangle, is shown in (b*). Scale bars: (a) 1 μm. (b) 5 μm. (c) 5 μm.

The realisation of co-investigation in a technical sense is decisive in revealing the trend of facet-selective growth of CNTs on polycrystalline BST surfaces. It can be deduced from Figure 6.6 that the (110) facet is the most active plane for aiding CNT growth; next is the (111) facet; least is the (001) facet. It is interesting to note that all the three facets presented in Figure 6.6 possess almost the same values of areal R_{rms}, which is deemed to be one of the paramount factors for producing CNTs; thus it is reasonable to assume that the BST facet orientations and/or surface lattice arrangements have a critical effect on the facet-selective growth behaviour of CNTs. To verify these experimental findings, more co-investigations have been carried out.

Figure 6.7 presents a group of results from the SEM, EBSD, and Micro-XAM co-investigations on three different positions on the grown samples, with three images in each row taken from the same site on the sample surfaces. In general, (001) facets (red colour) are not able to support CNT growth on them, no matter how suitable the areal R_{rms} are. For instance, there is no tube growth on Facet 2 in Figure 6.7A, a, and a*, which is a (001) facet with a value of areal R_{rms} approx. 10 nm. Facet 3 in Figure 6.7B, b, and b* (areal R_{rms} ~11 nm), and Facet 4 in Figure 6.7C, c, and c* (areal R_{rms} ~8 nm) confirm this. In contrast, all the (110) facets (green colour) are promising crystal planes for CNT formation, even when the surfaces are slightly rougher. In this case, there is good evidence for Facet 3 in Figure 6.7A, a, and a*, which is a (110) plane with a larger value of areal R_{rms} (~19 nm), but it still sustains good growth of CNTs. As for the (111) crystal planes (blue colour), compromises between the surface roughness and surface orientation/lattice arrangements exert

influences on the generation of CNTs. It is observed that (111) facets with a value of areal R_{rms} (<15 nm) are able to accommodate CNT growth, such as Facet 5 in Figure 6.7A, a, and a*. However, rougher (111) facets cannot support CNT growth, such as Facet 3 in Figure 6.7C, c, and c*, which has an areal R_{rms} value of ~27 nm. Meanwhile, Facet 2 ((111) facet) in Figure 6.7B, b, and b* shows the phenomenon that grown CNTs always appear on the facet areas with small values of surface roughness (6~11 nm).

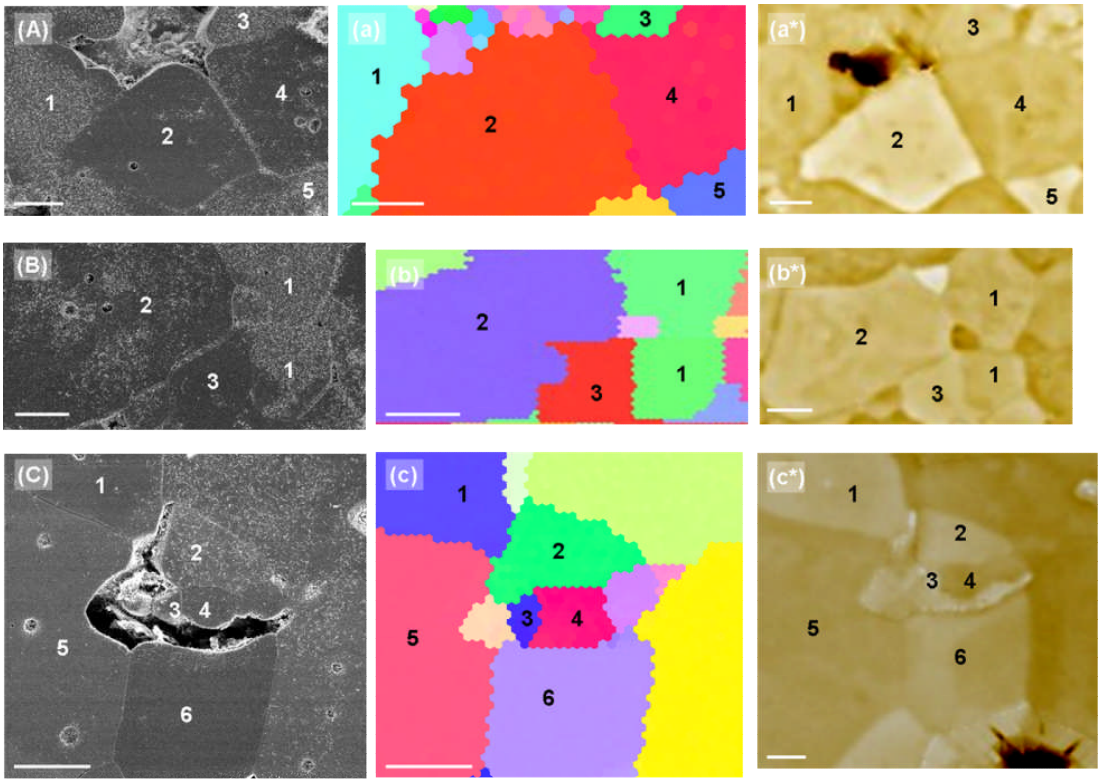

Figure 6.7:. SEM (A-C), EBSD (a-c) and Micro-XAM (a*-c*) co-investigation of facet-selective growth of CNTs on BHF-etched BST surfaces, with each row corresponding to one site of interest. The numbers marked on the images indicate the different crystal facets for each position. Scale bars: (A-C) 5 μm. (a-c) 5 μm. (a*-c*) 10 μm.

6.4 Discussion

The facet-selective growth of CNTs on BHF-etched polycrystalline $BaSrTiO_3$ surfaces by metal-catalyst-free CVD is of great interest. To the best of my knowledge, there have not been any studies reported on the facet-selective growth of CNTs on oxide surfaces *via* metal-free CVD, although the oxide facet-tailored CNT synthesis by metal-catalyst-involved CVD has been a focus of research. Ren *et al.*[214] achieved the growth of millimeter-long VACNT arrays on all MgO single crystals with orientations of (001), (110), and (111), using Fe as a metal catalyst. Surprisingly they found that the orientation of MgO substrates had an influence on the length of grown CNT arrays, where (110) plane led to the longest length but (111) plane produced one 55% shorter in length. What they have speculated is that the different interactions between Fe and faceted MgO crystals give rise to the distinct nucleation durations of CNTs[214]. Another good example is that Ago and his colleagues[207] have demonstrated that the horizontally aligned growth of CNTs can only be realised on the A-plane and R-plane sapphire but not on the C-plane with the aid of Co catalyst. These findings suggest that, by means of metal-catalyst-involved CVD, the crystal facets of oxide substrates can strongly affect the catalyst patterning and subsequent CNT growth on them. However, what accounts for the facet-selective growth of CNTs where the metal-catalyst-free CVD is applied needs further identification.

The technique of SEM, EBSD, and Micro-XAM co-imaging serves as a powerful tool in this study for investigating the interesting phenomenon of facet-selective growth of CNTs. As mentioned in Section 6.3.1.2, at the beginning of the

investigation, AFM was attempted to provide topological images of the sites of interest on the surface but, unfortunately, was unsuccessful in obtaining clear images of the key areas in most cases. To overcome this technical limitation, the Micro-XAM was employed instead to image the surface, which can offer accurate *z*-information on characterised surfaces, with easy means of manipulation and high measuring stability. Thanks to the technical realisation of SEM, EBSD, and Micro-XAM co-investigation, it becomes apparent in this study that the BST (110) facets lead to promising growth of CNTs on them, whereas the (001) facets result in no growth at all. Notably, the CVD reactions were conducted without the aid of any metals; thus the BST oxide surface itself should be responsible for the catalysis occurring. Different crystal facets on the polycrystalline BST adopt distinct lattice arrangements and differ in surface nanostructures, which could result in discrepancy in catalytic performances. Therefore, the interplay between the surface roughness and surface orientations/energies is suggested to make contribution to the facet-selective growth behaviour of grown CNTs on the polycrystalline BST surfaces.

Although the facet-selectivity of CNT growth on the polycrystalline $BaSrTiO_3$ surfaces is a focus of discussion, the ‘metal-catalyst-free’ route, which has been used, leading to CVD growth of CNTs on BST substrates also raises great interest. Figure 6.4 shows the presence of layered carbon-covered BST surfaces and layered carbon-wrapped NPs, along with the formation of CNTs after CVD reaction, indicating that the BST benefits the process of graphitisation. A similar observation has been reported using Al_2O_3[218], MgO[217, 275]. While the catalytic activities of oxide

surfaces have not been clearly understood, certain aspects are nevertheless well documented. For example, a wealth of studies has reported the importance of oxides in the field of CNT synthesis[20, 216-218, 280, 283], such as enhancing the capture of carbon species, advancing graphitisation, catalytically activating the formation of CNTs, and promoting the performance of CNT metal catalysts. Specifically for this study, it has already been mentioned in Chapter 5 that SrO, TiO_2, and $SrTiO_3$ surfaces possess catalytic capacities to absorb and decompose hydrocarbons. Meanwhile, BaO is more catalytically active than SrO[284, 285], and since the formation of BST can be regarded as the partial substitution of Sr by Ba in the STO lattice, the BST surface is expected to be superior to the STO surface in catalysis.

The $BaSrTiO_3$ surface-bound CVD reaction gives rise to the bamboo-shaped CNTs, where there are no catalyst particles trapped within the tubes (Figure 6.3). Very recent studies show that similar carbon nanostructure has been found, when conducting CNT growth experiments on lanthanide metal oxide NPs[252] and on Au surfaces[256] *via* metal-catalyst-free routes. Akin to the conclusions drawn from those investigations, it is proposed here that the as-grown CNTs on BST surfaces are formed *via* self-assembling, *i.e.* self-function/reconstruction of certain carbon species (meta-stable graphite layers, activated carbon NPs/atoms, branched aromatic segments, *etc.*), which originate from the anisotropic properties of sp^2-hybrid carbon structures[255, 286]. This proposal conceptually contrasts with the VSS model, which has been advocated by Liu *et al.*[20] and Page *et al.*[245] with regard to highlighting the importance of oxide NPs in catalysis for explaining the growth of SWNTs by

metal-free CVD. While it is unlikely to be the case here, as no direct evidence has been found in this study that the CNTs are grown right on the surface-bumped NPs, the possible explanation that the BST surface-bumped oxide NPs with nanoscale curvatures could function as templates for generating CNTs on them cannot be ruled out. It would therefore be useful to perform *in situ* TEM investigations to seek evidence of the CNT formation on the nano-bumps on BST surfaces.

It is known that the adsorption of a carbon precursor onto the catalyst surface and the diffusion of carbon species generated from thermal/catalytic pyrolysis are the crucial steps towards the formation of CNTs on any catalyst sites[20]. Here, a wealth of crystal facets on the BST surface offer locations to guide the above-mentioned steps directly, but only the low-index facets ((001), (110), and (111)) have been considered in this study, owing to their high crystal symmetry and facet stability[287, 288]. The major difference among the (001), (110), and (111) facets is the surface atom arrangements (it is assumed that all the facets possess identical values of surface roughness), a DFT calculation was made to study the adsorption and diffusion of carbon species (C_2H_2 molecules and C atoms) on these low-index BST surfaces, in order to understand the facet-selective growth of CNTs better, and in order to further evaluate the experimental findings. It should be mentioned that this calculation was performed by the group research collaborators, Assistant Prof. Christina Lekka (University of Ioannina, Greece) and Prof. Yilin Cao (Henan Normal University, China). Briefly, the adsorption energies (E_{ads}= $E_{adsorbate/surface}$ - ($E_{surface}$ + $E_{adsorbate}$)) are used in this calculation to characterise the levels of difficulty in the adsorption

and diffusion of carbon species on the three distinct facets, with negative values indicating that such adsorptions are preferable. Here the scenario of the adsorption of a carbon atom on BST (001) facet is shown as a representative of this calculation. Firstly, by considering and comparing the total energies of the modeled system, the most stable surface can be determined, as shown in Figure 6.8a (Note that the BST (001) surface has a TiO_2 termination because of the BHF-etching). When a C atom adsorbs on this BST (001) surface, three possible adsorption sites are considered: i) on top of an O atom; ii) on top of a Ti atom and iii) on a 4-fold hollow site formed by O atoms. The adsorption energies for the ii) (-0.35 eV) and iii) (-1.96 eV) are much lower than that for the i) (-3.32 eV), at least by 1.36 eV. Therefore, only the configuration based on C-O bonding structures is presented here, as shown in Figures 6.8b (top view) and 6.8c (side view).

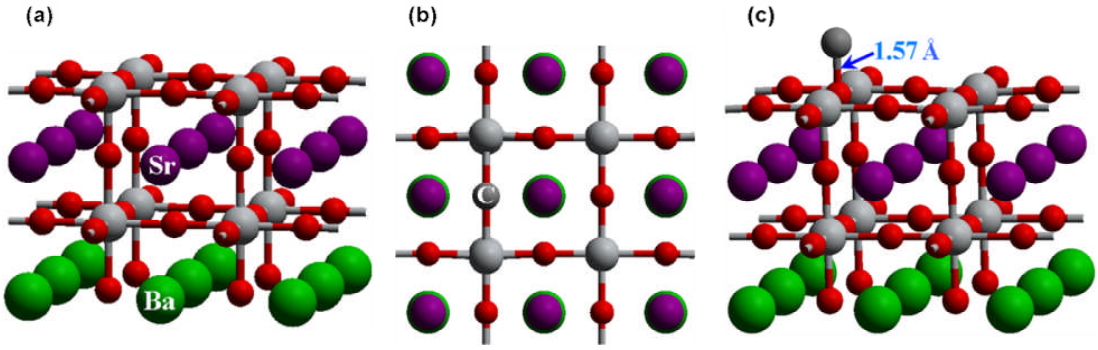

Figure 6.8: Geometry of a carbon atom adsorbed on a BHF-etched BST (001) facet. Sr, Ba, Ti, O, and C are indicated as purple, green, light grey, red, and dark grey spheres, respectively. (a) The most stable surface which can be used for this modeling work. (b) Top view of the adsorption of a carbon atom on an oxygen atom. (c) Side view of the same geometry as in (b), with an indication that the distance between carbon and oxygen atoms is 1.56 Å.

Likewise, by considering possible adsorption sites and diffusion paths in each case, values of the adsorption of a C_2H_2 molecule ($(C_2H_2)_{ad}$), adsorption of a carbon atom (C_{ad}), and the diffusion of a carbon atom (C_{diff}) on the surface of each facet can be obtained, respectively; moreover, the most possible scenarios of carbon adsorption and diffusion (*i.e.* the most stable adsorption and preferable diffusion of carbon species) on each facet can be determined, as shown below:

For BST (100) facet, C_{ad} = -3.32 eV. $(C_2H_2)_{ad}$ = 0.09 eV. C_{diff} = 1.35 eV.

For BST (110) facet, C_{ad} = -9.31 eV. $(C_2H_2)_{ad}$ = -5.32 eV. C_{diff} = 0.17 eV.

For BST (111) facet, C_{ad} = -4.15 eV. $(C_2H_2)_{ad}$ = -0.23 eV. C_{diff} = 0.58 eV.

It can be deduced from the values that, among the (100), (110), and (111) crystal planes, the (110) facet promotes the capture of carbons (especially C_2H_2) and facilitates the transportation of carbon species, thus enhancing the formation of CNTs, whilst the (100) facet retards the adsorption and diffusion of carbons, such that it is not able to benefit the growth of CNTs. Compared to the (110) facet, a (111) facet displays intermediate values of $(C_2H_2)_{ad}$ and C_{ad}, but has a larger diffusion barrier for carbon transportation (considering the fact that the CNTs are formed *via* a catalyst-free route driven by assembling carbon segments), which is in accord with the observation shown in Figure 6.6, where the CNT production on the (110) facet possesses larger density and more uniform distribution than that on the (111) facet. In conclusion, the theoretical work shown here is consistent with the experimental results and speculations, confirming that the surface orientations/surface lattice arrangements remain responsible for the facet-selective growth behaviour of

produced CNTs on the polycrystalline BST surfaces.

In view of the experimental findings and detailed discussions presented above, a two-fold function of the BST surfaces in this case can be suggested as follows: i) to provide a possible stage for producing carbon segments needed for CNT growth; ii) to act as a platform for transporting carbon segments to self-assemble into CNTs. Correspondingly, the mechanism of the CNT formation on the polycrystalline BST surfaces by metal-free CVD can be surmised. At the initial stage of CVD reaction, the BST textured surface assists the catalytic adsorption and decomposition of carbon feedstocks (such as C_2H_2, C_2H_5OH) into carbon fragments (carbon NPs, carbon layers) and aids the transportation/diffusion of these carbon species. In this respect, the interplay between the surface roughness and surface lattice arrangements of crystal facets on the polycrystalline BST surface plays a key role in the adsorption of the carbon source and the diffusion of carbon species, leading to the phenomenon of facet-selective growth of CNTs on such surface. The produced carbon species then assemble into tubular nanostructures as a consequence of particle coalescence and structural reorganisation, while the distorted sites on the BST surfaces, such as defects, nano-bumps, and tiny pits, provide the stack-up sites for the carbon species to make the assembly happen. It is worth mentioning that BST facets with large surface roughness are not able to support the growth of CNTs on them, for the reason that the rougher surface hinders the transportation process of the produced carbon species desired for the consequent self-assembly of CNTs.

6.5 Conclusions

In this chapter, the facet-selective growth of CNTs on polycrystalline $BaSrTiO_3$ surfaces has been achieved *via* metal-catalyst-free CVD. The detailed SEM, EBSD, and Micro-XAM co-investigations reveal that the facet orientations/lattice arrangements, along with the surface roughness of the $BaSrTiO_3$ substrate, have a critical effect on the facet-selective growth behaviour of CNTs. The mechanism of CNT formation seems to depend upon the assembly of carbon segments, which are produced with the aid of distinct BST facets.

Chapter 7：

Growth of Carbon Nanocoils (CNCs) on $BaSrTiO_3/SrTiO_3$ Substrates without/with Sn

7.1 Background

Research in the field of helical carbon nanostructures has grown rapidly in the past decade, owing to the unique morphologies and attractive properties of these materials.[78, 79, 259, 289] These structures have generally been referred to as carbon nanocoils (CNCs) although this is the wrong geometrical description. A coil is a 2D object which refers to a series of loops, whilst a helix is a 3D object which describes a type of space curve. Although I realise that the use of 'coil' is not accurate, it has become so commonplace in this field that I have decided to adopt this term. Helical carbon nanostructures (referred to as CNCs) are expected to have numerous applications, for example in structural cushions (nanosprings)[290], field emission displays[18], electrical circuits[291], tactile sensors[292], magnetic components[293], and energy storage devices[294]. Various approaches to fabricating CNCs are reported in the research literature. The major route towards forming CNCs has been the catalytic decomposition of hydrocarbons, such as C_2H_2 and CO, *via* CVD.[259] The essential aspect for the production of CNCs by CVD is the catalyst employed. To date, assorted types of elements have been investigated to induce the formation of helical structures, such as Ni, Cu, Co, Ti; moreover, recent reports have indicated that the modification of a transition metal catalyst is required for the synthesis of CNCs.[33, 174, 177] The ways of modifying metal catalysts mainly lie in: i) the addition of elements of S[292, 295, 296], P[297], and Si[104] during growth, and ii) the employment of binary and ternary metal alloys.[18, 112, 175] Apart from metals, the latest study has revealed that carbon nanohelices can be generated from oxide materials (SiO_2) by CVD without

the aid of any metals, although the product yield was tuned by concentrations of hydrogen gas and the formation of these helical structures was claimed to be *via* a metal-catalyst-free route driven by assembling carbon fragments.[276]

In this chapter the growth of CMC/CNCs on STO and BST substrates by CVD is presented. Firstly, the growth of helical carbon nanostructures on scratched STO and BST substrates *via* a metal-free route is explored, followed by the investigation of Sn-assisted fabrication of CMC/CNCs on BST substrates *via* metal-involved CVD; furthermore, some discussion of the speculation about growth mechanisms and of future work is presented.

7.2 Experimental Details

Epi-polished $SrTiO_3$ (001) crystals and polycrystalline $Ba_{0.6}Sr_{0.4}TiO_3$ substrates (PI-KEM Ltd, UK) were employed to serve the experimental purposes. It should be noted here that the STO crystals are single crystals without pores/pits on the surface, whilst in the BST samples the existing pores/pits can trap impurities, such as Sn in this case. In this work, several routes were tried to prepare the substrates, aiming to perform a complete investigation of the growth of CNC/CMCs on perovskite oxides.

7.2.1 Preparing Scratched STO and BST Substrates (For Metal-Catalyst-Free CVD)

The procedure for preparing scratched STO substrates is stated in detail in Chapter 5. In brief, as-received STO samples were etched within the BHF solution for 5 min, followed by surface scratching with the aid of a diamond blade. It has been observed that STO particles (generated by scratching) with nano/micro sizes are presented on the substrate surfaces. The identical procedures were applied to BST samples to obtain scratched BST substrates. This type of substrates was involved in the investigations without the presence of Sn, which is detailed in Section 7.3.1.

7.2.2 Preparing Sn-Modified BST Substrates (For Metal-Catalyst-Involved CVD)

It should be noted that the as-received BST substrates originally contain Sn; specifically the pits/holes on the surface of as-received samples are traced with the presence of Sn, which is detailed in Section 7.3.2.1. Basically, I am aware, after communicating with the material supplier, that the Sn trapped inside the pits might come from the polishing stage in the manufacturing process of products, where the samples were polished on a tin plate.

To further modify the BST substrates with Sn for achieving the growth of CNCs on a larger scale, $SnCl_2$ powders (Sigma-Aldrich Co. LLC, UK) were employed and mixed with ethanol to prepare a Sn^{2+} solution. The concentration of Sn^{2+} ($c(Sn^{2+})$)

was tuned by the amount of $SnCl_2$ used. The BST samples used in this case were the ones treated by BHF-etching (for an etching period of 5 min). The samples were coated with Sn^{2+} by dipping the processed BHF-BST substrates into a Sn^{2+} solution. There have been numerous reports on using Fe-Sn binary compounds as effective catalysts for CNC growth,[33,175,179] in this study the Sn-coated samples were then dipped into a ferrocene-ethanol solution (c(Fe^{2+}) ~ 0.02 mol/L) for 5 sec, in order to get coated with an Fe layer as well. Here these two types of substrates were involved in the investigations with the presence of Sn, which is detailed in Section 7.3.2.2.

7.2.3 Growth of Carbon Nano/Microcoils by CVD

The experiments on CNC/CMC growth were performed with the aid of atmospheric CVD apparatus, details of which can be found in Chapter 2. For the synthesis of carbon helical nanostructures, C_2H_2-CVD was conducted on the prepared STO and BST samples. A mixture of Ar and H_2 was used as the carrier gas during the growth stage, with a H_2 pretreatment (800 sccm; for a period of 5 min at a growth temperature), applied to all the samples.

7.3 Results

The growth of CNC/CMCs is achieved on the scratched STO and BST substrates by metal-catalyst-free CVD, though with low yield. Introducing Sn into the catalysts

brings about high yield and diversified morphologies of the CNC product on the BST substrates, where the chemical and geometrical aspects of the CVD reactions are investigated.

7.3.1 Metal-Free Growth of Carbon Nanocoils on Scratched $SrTiO_3$ and $BaSrTiO_3$ Substrates

7.3.1.1 The STO Case

As discussed in Section 5.3.3.2, the use of C_2H_2 as a carbon feedstock gave rise to a wealth of grown carbon shapes at different growth temperatures; in particular at 700˚C it was found that CNCs occur. Here a separate investigation, under identical growth conditions to those used previously, was performed to check the reproducibility of the product, with the results presented in Figure 7.1. The SEM images in Figures 7.1a-7.1d show the morphologies of the grown coiled carbon structures on the STO substrate. The shapes of these displayed coils differ from each other, forming nanosprings with tight (Figure 7.1a) and loose (Figure 7.1b) pitches, CNC-CNF hybrid structures (Figure 7.1c), and CNCs with twisted forms (Figure 7.1d). It should be noted that these CNCs were grown with low yield and detected by random observations. Figure 7.1e displays a representative XPS spectrum of the sample surface. This chemical analysis shows the presence of Sr, Ti, O, and C, which is consistent with the elemental composition of the employed sample, experienced through a metal-free C_2H_2-CVD reaction. The XPS spectrum also indicates the

deficiency of any other metal contamination (such as Fe, Co, and Ni) on the surface. Moreover, the EDX pattern (Figure 7.1f) generated from the red rectangular area marked in Figure 7.1b shows the similar results. In addition, these grown coiled nanostructures were inspected by Raman spectra analysis, as shown in Figure 7.1g. Two main peaks are observed in the spectrum; one is G-band originated from graphite structures, and the other is D-band originated from structural defects or disorders in carbon nanomaterials.

The characterisation protocol designed here involving the SEM, XPS, EDX, and Raman spectroscopy demonstrated an interesting growth scenario of CNCs occurring on the scratched STO surfaces. However, it is worth mentioning that TEM investigation of these grown structures has not been realised, owing to the low yield of the desired product. It would be helpful to figure out possible approaches to perform TEM study on these nanomaterials, as it could provide further information on the morphologies of CNCs and related catalyst particles, in order to deepen the understanding of the growth behaviour of CNCs.

7.3.1.2 The BST Case

The growth of CNC on scratched BST surfaces was also carried out, at a growth temperature of 750˚C. The SEM image library in Figures 7.2a-7.2d shows the features of interest of the grown samples. Figures 7.2a and 7.2b present the structures of carbon solenoids, which were occasionally observed on the substrate surface. A higher magnified SEM micrograph as an inset is shown in Figure 7.2a*, where the

blue arrow marked on the image points to a catalyst particle. The EDX spectrum generated from the red rectangular area (where the particle is sitting) is displayed in Figure 7.2f, showing the presence of Ba, Sr, Ti, O and C. The grown samples were also subject to XPS characterisation. The representative XPS spectrum in Figure 7.2e indicates that the grown sample surface is free of metals. It can be deduced from the XPS analysis and the EDX pattern that there is no conventional, metallic CNC catalyst (such as Fe, Co, and Ni *etc.*) responsible for the growth of CNCs; thus it is likely that the catalyst particle marked by the blue arrow is mainly composed of Ba, Sr, Ti, and O, as it was induced by the treatment of surface-scratching. Figures 7.2c and 7.2d display the observations of carbon helices with twisted forms, the morphologies of which are considerably different from the solenoids shown in Figures 7.2a and 7.2b. A higher magnified SEM image as an inset shows a close view of these twisted carbon helices (Figure 7.2d*).

It is known that controlling the shapes of nanomaterials plays a crucial role in nanotechnology. In this case, the fact that two distinct types of helical nanostructures were obtained from the same, metal-free experimental run is of great interest. Apparently, the solenoid-like CNCs possess larger diameters, compared to the twisted CNCs. It is possible that the growth of these shaped carbon nanostructures are strongly correlated with the geometry and chemistry of the catalysts. Here the scratch-induced BST particles, with differing sizes and configurations, and the chemical constitutions, especially the Ti elements[265, 298] within these particles, lead to the formation of CNCs.

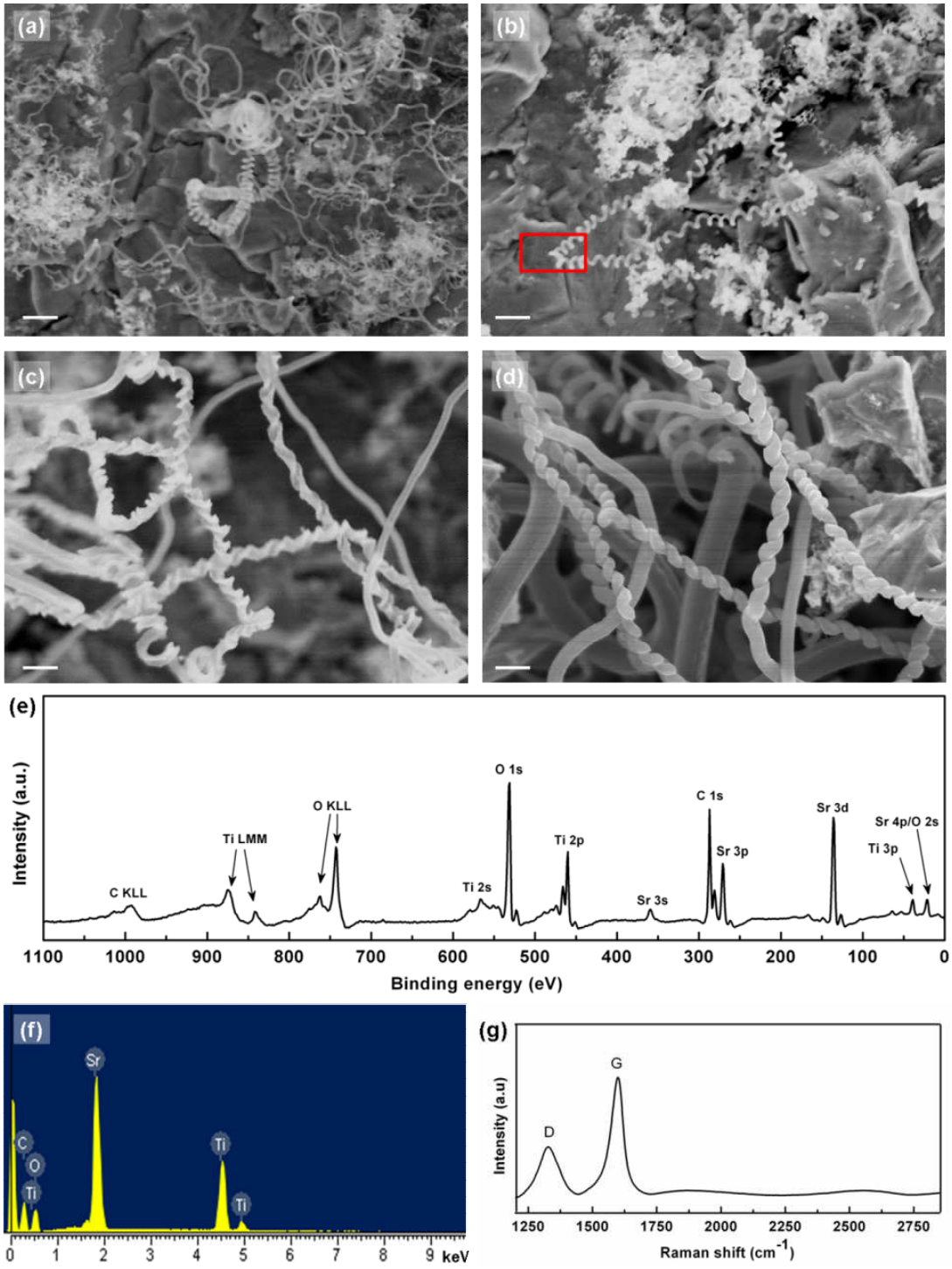

Figure 7.1: (a-d) SEM observations of carbon coiled nanostructures grown on scratched STO substrates by C_2H_2-CVD. Various shapes of CNCs were generated as (a-b) nanosprings, (c) CNC-CNF hybrid structures, and (d) twisted CNCs. Scale bars: 500 nm. (e) Representative XPS spectrum of grown sample shows that the surface is free of metal species. (f) EDX spectrum formed from the red region marked in (b). (g) A representative Raman spectrum of obtained CNC production.

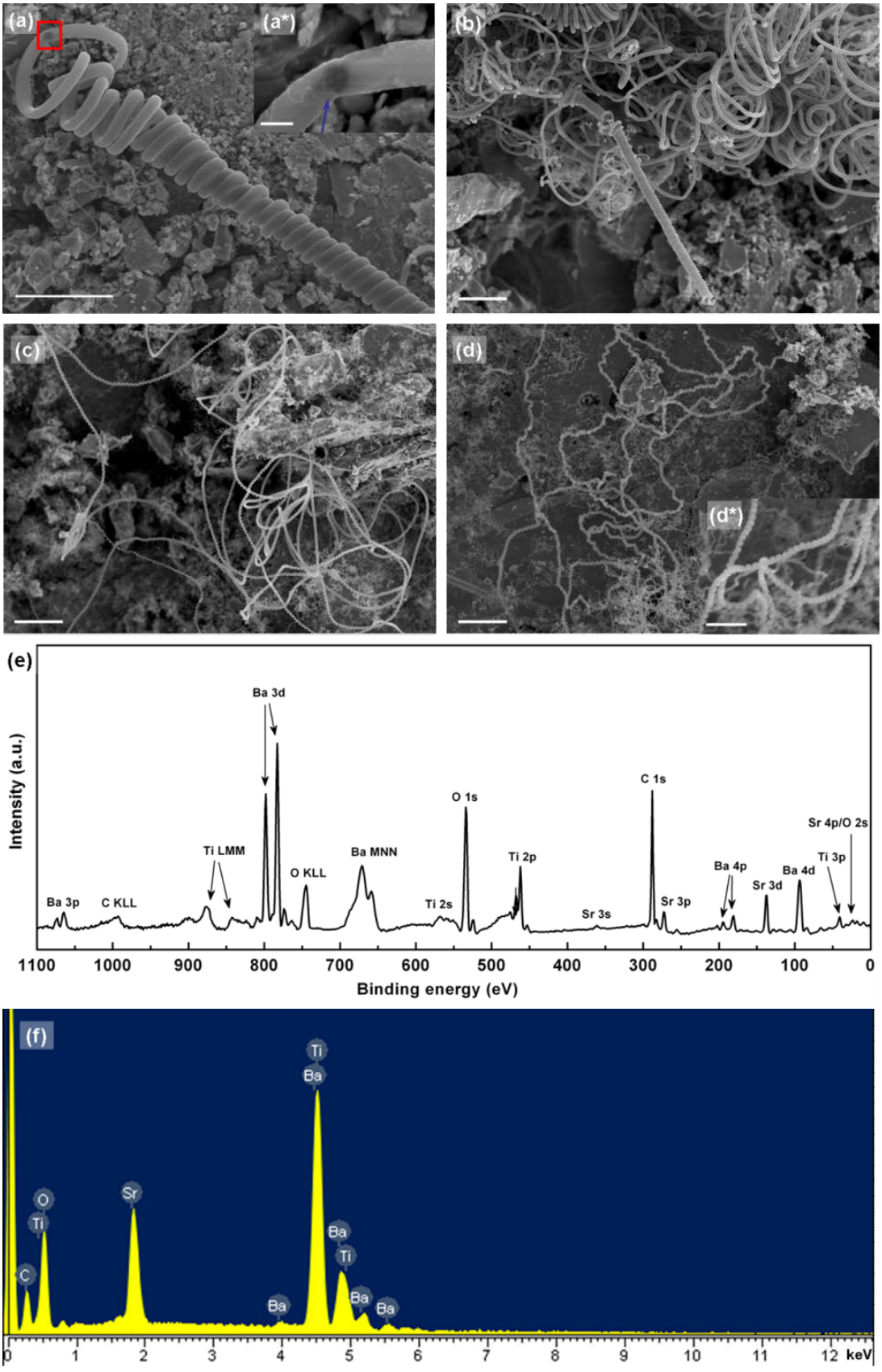
(a)
(a*)
(b)
(c)
(d)
(d*)
(e)
Intensity (a.u.)
Ba 3d
Ti LMM
O KLL
Ba MNN
O 1s
Ti 2p
C 1s
Sr 4p/O 2s
Ti 3p
Ba 4p
Sr 3d
Ba 4d
Ba 3p
C KLL
Ti 2s
Sr 3s
Sr 3p
1100
1000
900
800
700
600
500
400
300
200
100
0
Binding energy (eV)
(f)
Ti
Ba
O
Ti
Sr
C
Ba
Ba
Ti
Ba
Ba
0
1
2
3
4
5
6
7
8
9
10
11
12
keV

Figure 7.2: (a-d) SEM observations of carbon non-linear growth on scratched BST substrates by C_2H_2-CVD, with distinct shapes in (a-b) solenoid-like CNCs and (c-d) twisted CNCs. Scale bars: 3 μm. The inset shown in (a*) indicates the presence of a catalyst particle (blue arrow). The inset shown in (d*) shows a close view of twisted CNCs. Scale bar: 1 μm. (e) XPS spectrum and (f) EDX pattern (the red region marked in (a)) indicate the grown samples are free of metallic species.

7.3.2 Sn-Involved Growth of Carbon Nanocoils on $BaSrTiO_3$ Substrates

7.3.2.1 For the As-received BST Samples

The trials of fabrication of CNCs on the as-received BST samples came up with surprising results, as shown in the SEM image library in Figure 7.3. The growth experiment was carried out using C_2H_2 (40 sccm for 15 min) as a carbon feedstock, at a growth temperature of 750˚C. It can be observed that clusters of CNCs sprout from the pits on the sample surface, with large quantities and diversified morphologies. The images taken at low magnifications in Figures 7.3a and 7.3b show general views of the BST substrate surface after the CVD reaction. It is interesting to note that the pits/cracks on the surfaces function as the cultivating centres for nurturing the growth of CNC clusters, as indicated by the blue arrows marked on the images. Figures 7.3c-7.3f show closer views of these CNC clusters, within which are contained branches of CNCs with different coil diameters and pitches. The catalyst particles are found at the tips of grown CNCs, suggesting a tip growth mode, which

is consistent with that reported in most of the research articles[33, 175, 178, 179, 263, 299].

To examine the morphologies of these CNCs, high-resolution SEM (HRSEM) was performed on the grown sample. The SEM image library obtained in Figure 7.4 displays the diversity of the shapes of the produced CNCs. Figures 7.4a-7.4i show the morphologies of CNCs with loose pitches, whilst Figures 7.4j-7.4r centre on the tightly-pitched coiled architectures. Close views of the catalyst particles are particularly shown in Figures 7.4q and 7.4r.

The obtained structures were further investigated by TEM and Raman spectroscopy. Similar sizes and shapes of grown CNCs are shown in the SEM images (Figures 7.5a-7.5c) and in the TEM micrographs (Figures 7.5d-7.5f), respectively. The TEM observation reveals that the grown CNCs differ from each other in coil diameters (range: 200~900 nm) and lengths of pitches (range: 200~600 nm), which probably originates from the inhomogeneous size and shape distributions of catalyst particles, for the reason that the sizes and geometries of catalyst particles can dictate the morphologies and scales of resultant carbon nanostructures. Moreover, it can be seen from the TEM images that these obtained CNCs barely possess hollow channels along the axis of the tubules, from which the coiled structures are formed. Thus the structures of these CNCs are similar to CNFs. The representative Raman spectrum of grown CNCs (Figure 7.5g) exhibits the characteristic D and G peaks, with a G/D ratio at approx. 2.2, indicating a fairly high graphitisation of produced CNCs.

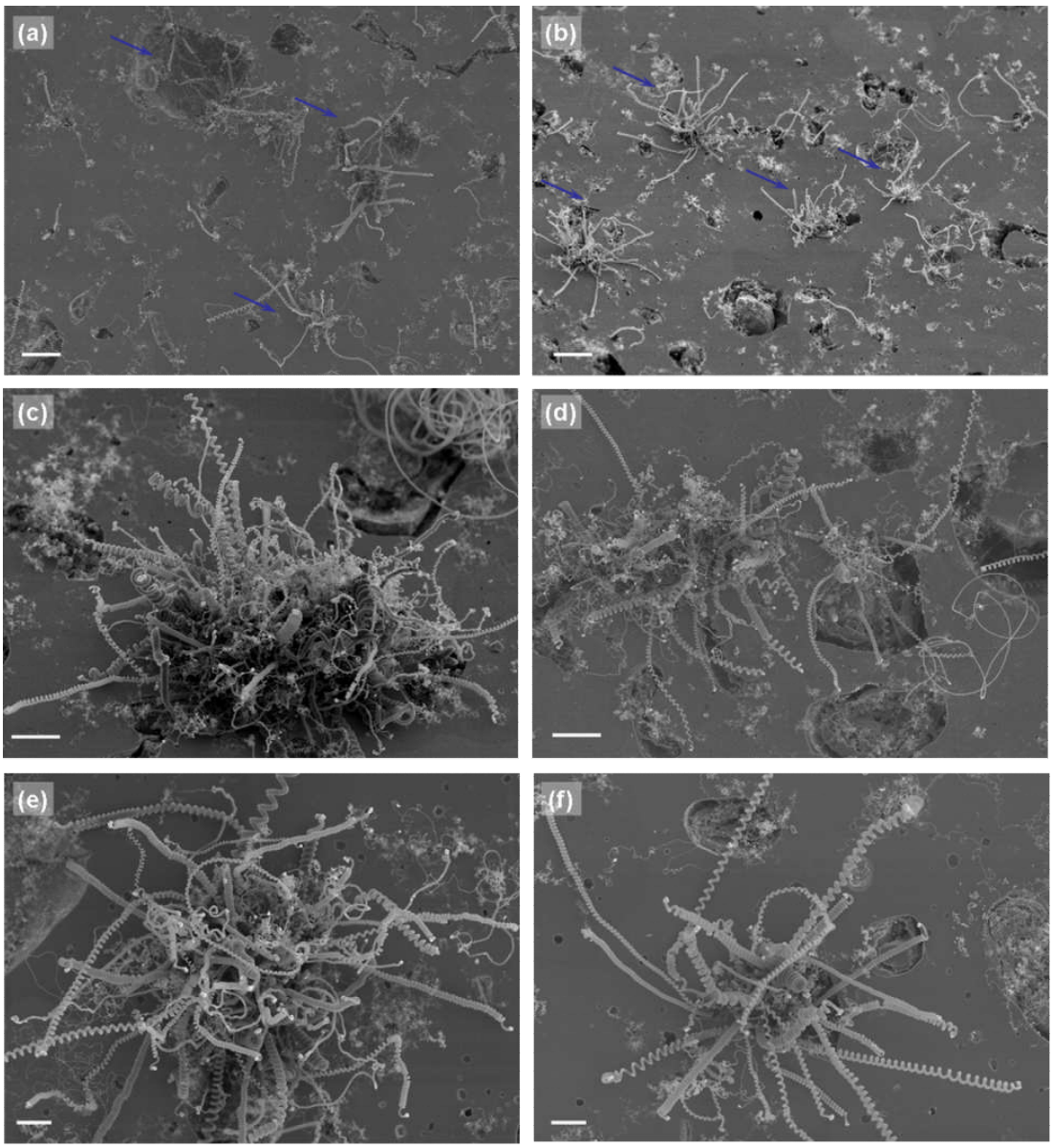

Figure 7.3: SEM observations of carbon coiled nanostructures grown on as-received BST substrates by C_2H_2-CVD. The blue arrows marked in (a) and (b) indicate that the clusters of CNCs are generated from the pits/cracks along the BST surface. Scale bars: (a-b) 10 μm. (c-d) 5 μm. (e-f) 3 μm.

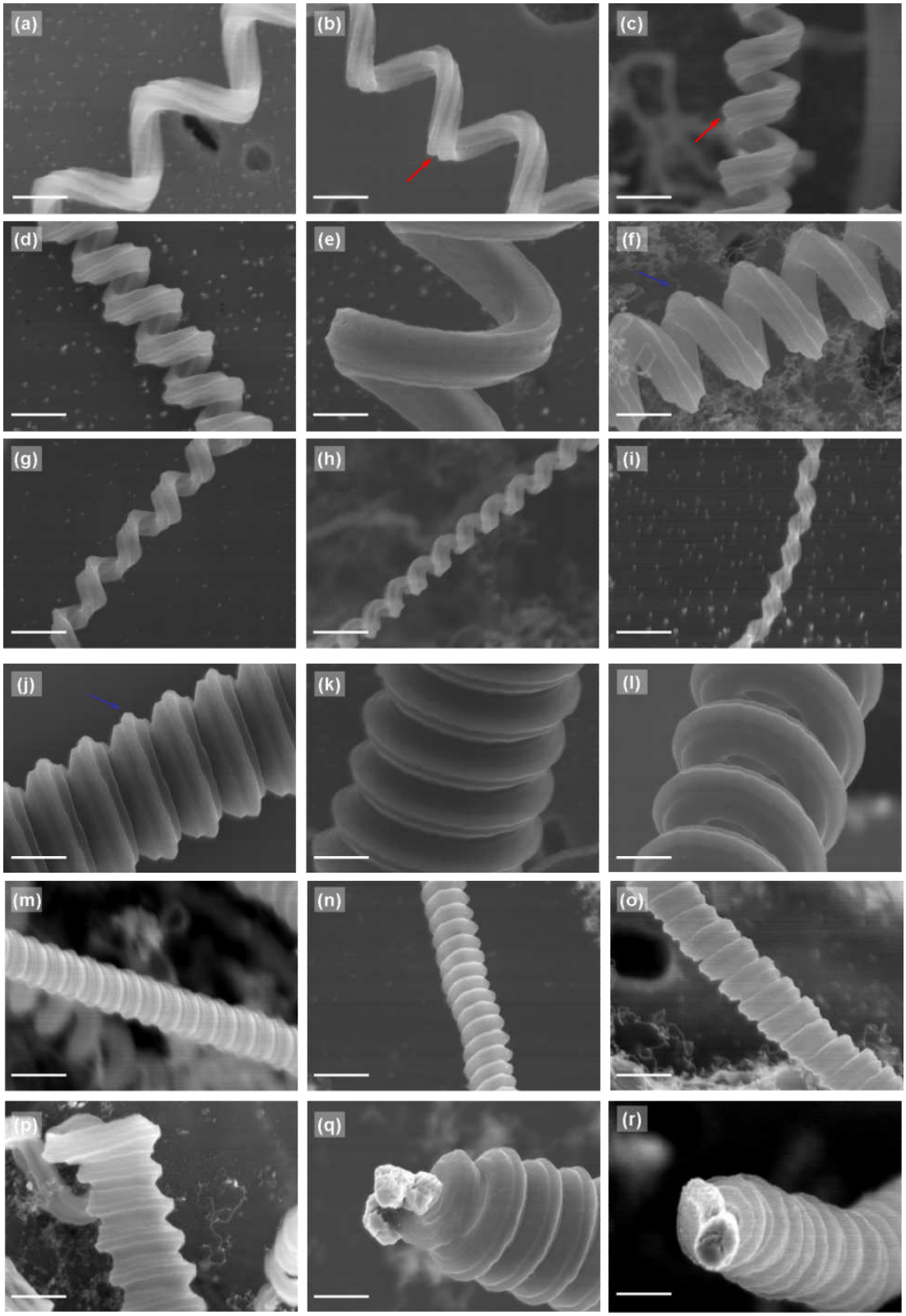
(a)
(b)
(c)
(d)
(e)
(f)
(g)
(h)
(i)
(j)
(k)
(l)
(m)
(n)
(o)
(p)
(q)
(r)

Figure 7.4: HRSEM image library of the diversified morphologies of CNC/CMCs grown on as-received BST substrates, showing (a-i) produced CNC/CMCs with loose coil pitches; (j-r) produced CNC/CMCs with tight coil pitches. Scale bars: 500 nm. It is interesting to note that the walls of most of the grown CNC/CMCs are characterised with either protrusions (as indicated by the blue arrows in (f) and (j)) or depressions (as indicated by the red arrows in (b) and (c)) that are uniformly patterned.

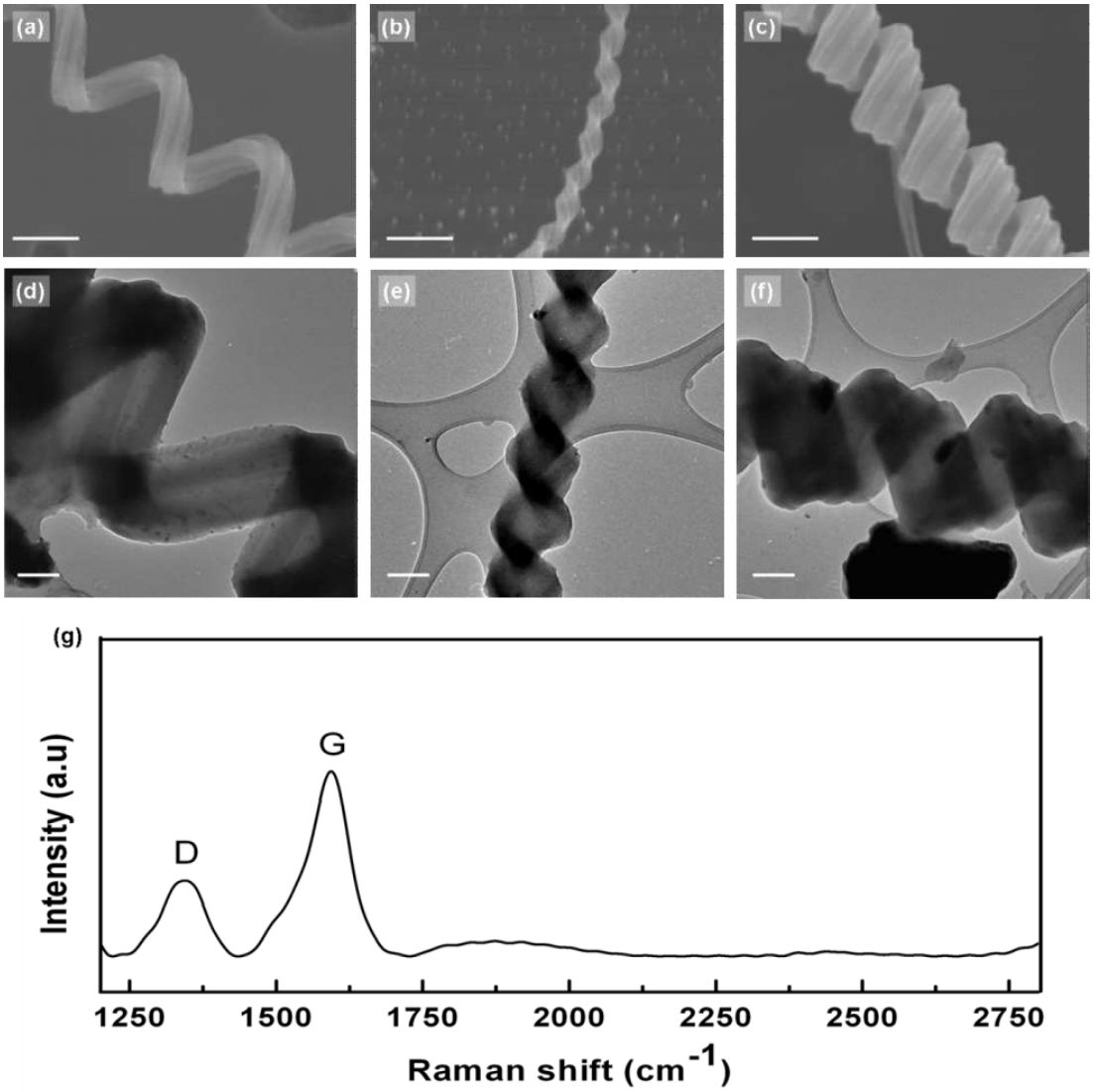

Figure 7.5: Detailed characterisation of CNC/CMCs grown on as-received BST substrates. (a-c) SEM observations of distinct shaped-CNCs. Scale bars: 500 nm. (d-f) TEM observations of CNCs in similar sizes and shapes as shown in SEM images (a-c), respectively. Scale bars: 200 nm. (g) A representative Raman spectrum of grown CNCs showing the characteristic D and G peaks.

During the SEM study, EDX measurements were performed to estimate roughly the catalytic species within the catalyst particles staying at the tips of the grown CNCs. Figure 7.6a presents a cross-section SEM viewing of CNCs grown from a specific crack on the substrate. The two conspicuous coiled structures were selected as features of interest, where EDX analyses were carried out on the catalyst particles, as marked by the blue circles on the image. Surprisingly, the element of tin was detected in the EDX spectra (Figures 7.6a* and 7.6a**) for the catalyst particles. It is widely reported that Sn possesses the ability to induce the helical growth of carbons[33, 175, 178, 179, 299]. Here the tin is regarded as being critical for the most efficient synthesis of CNCs on the as-received BST substrates. More specific characterisation of the grown sample was performed with the aid of point-localised EDX equipped within a TEM, which reveals the detailed chemical constitutions of catalyst particles. Figure 7.6b shows a representative TEM micrograph of the obtained coiled structure, with a catalyst particle staying at the tip. This inspected nanocoil possesses a diameter of approx. 600 nm and a pitch length of approx. 200 nm. The catalyst particle trapped at the tip of the nanocoil appears to have an irregular polyhedral structure, the size of which is approx. 550 nm. Figure 7.6b* shows a point-localised EDX spectrum of the catalyst particle. It can be discovered that the TEM-EDX signal from the catalyst particle mainly consists of Sn, Sr, Ba, Ti, and O, the chemical composition of which is entirely consistent with the SEM-EDX study (Figures 7.6a* and a**). It is highlighted that Sn has significant peaks in the spectrum; however, the origin/source of this specific element necessitates further study.

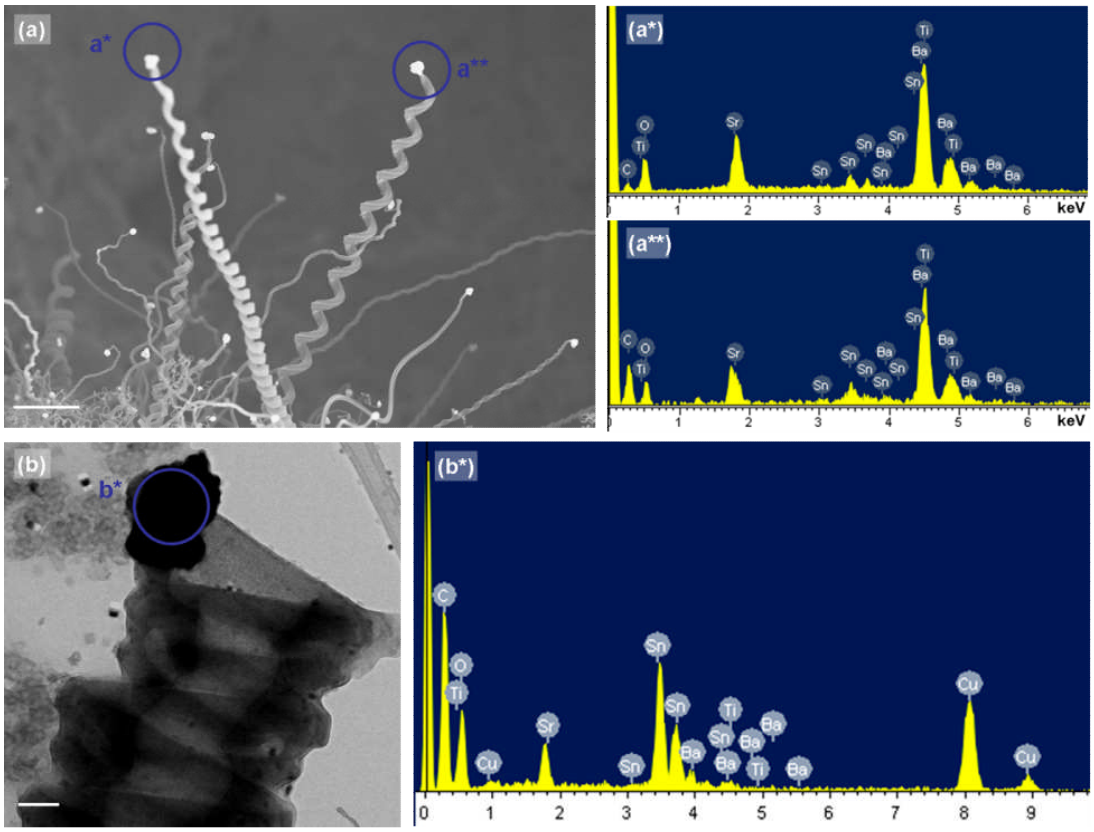

Figure 7.6: (a) Cross-section SEM view of CNC/CMCs grown on as-received BST substrates. Two nanocoils were selected for the subsequent EDX measurements. Scale bar: 3 μm. (a*-a**) EDX spectra taken from the blue-circled regions in (a), showing the presence of Sn, apart from the existence of Ba, Sr, Ti, O, and C. (b) TEM observation of an individual nanocoil, with a catalyst particle trapped at the tip. Scale bar: 100 nm. (b*) Point-localised EDX spectrum of the catalyst particle, suggesting that the chemical composition of the catalyst is ~BST with Sn decoration. The signal of Cu is attributed to the TEM grid.

As discussed above, the formation of CNCs only occurs at the pits/cracks on the as-received BST surfaces, but not at the polished, flat surfaces of the substrate. To investigate the reason for this position-determined behaviour of CNC growth, a comparative investigation between the polished surface and the pit of as-received samples was performed by EDX measurements, as shown in Figure 7.7. It was found that Sn is detected inside the pit on the substrate, whereas there is no trace of Sn at the polished surfaces of the substrate. Moreover, there were no other metals found either within the pit or at the substrate surface. Considering the fact that the pits/cracks, being the defects on the surface, provide non-uniformly geometrical sites to facilitate the creation of catalyst particles with anisotropic properties, compared to the polished, flat surface of the substrate, it is reasonable to suggest that the position determination of carbon nonlinear growth can be attributed to the geometrical and chemical inhomogeneity of catalyst particles formed inside the pits.

Furthermore, in order to track the origin of Sn, the material supplier, PI-KEM Ltd. was consulted. According to the information drawn from the correspondences, the Sn comes from the polishing stage in the manufacturing process of BST products, where the samples positioned on a tin plate were polished. The samples are processed *via* water-based, chemical-mechanical planarisation (CMP) steps afterwards; thus it is likely that the Sn can be completely removed from the sample surfaces, but trapped inside the pits as residues to some extent.

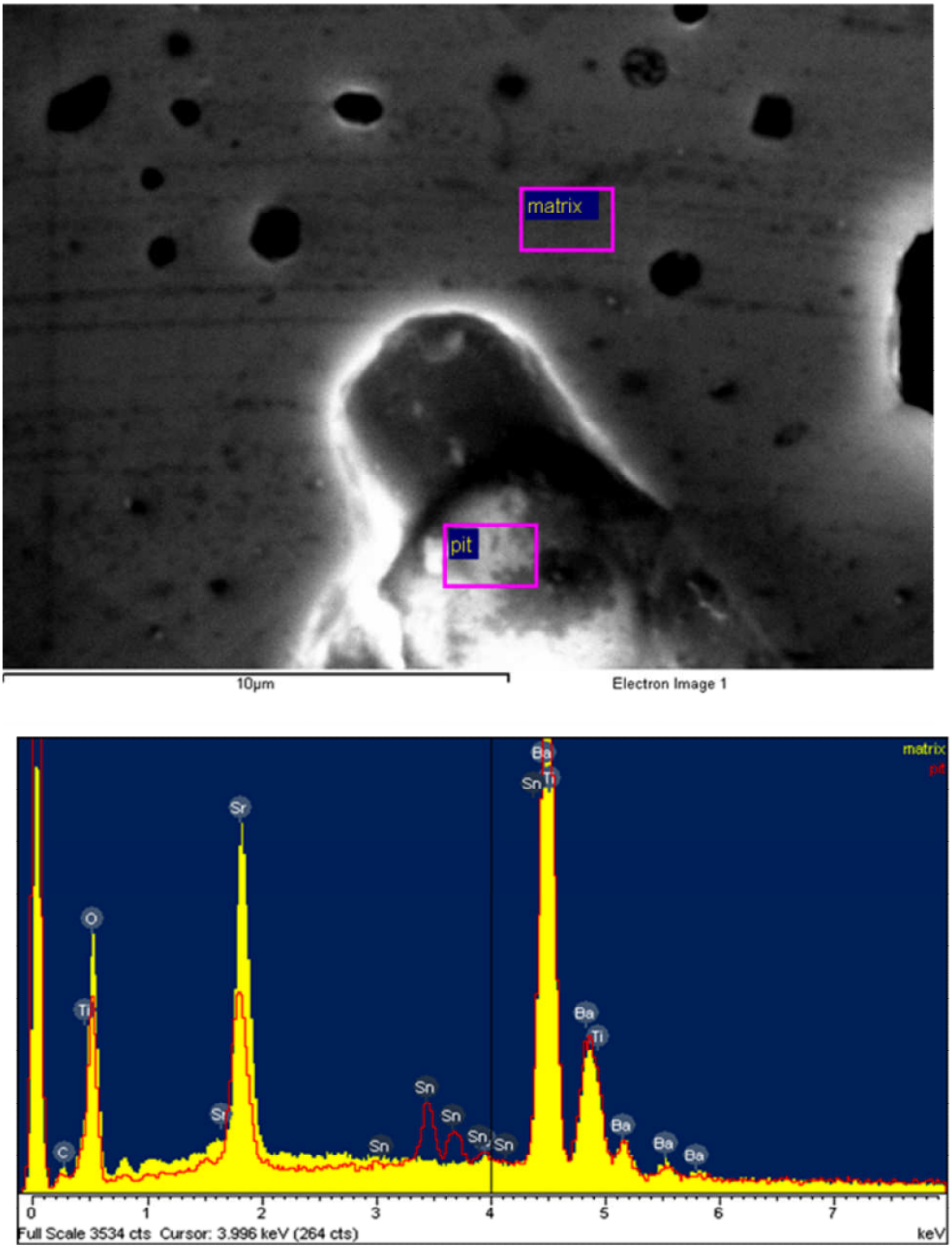

Figure 7.7: Comparison between the EDX spectra of the pits and the polished, flat surface (matrix) of the as-received BST substrate. The red curve on the spectra clearly indicates the presence of Sn inside the pits, whereas the yellow curve shows the regular composition of BST, without any sign of Sn appearing.

7.3.2.2 For the Sn-Modified BHF-BST Samples

7.3.2.2.1 High-Yield Production of CNCs on BHF-BST Samples

Using Fe and Sn to modify the BHF-BST samples ($c(Sn^{2+})$ = 0.01 mol/L; $c(Fe^{2+})$ = 0.02 mol/L) is a step further towards the catalyst design, which leads to promising growth of CNCs. Here the growth of CNCs not only occurs at the pits on the surface (similar to as-received samples), but also arises on the edges of the substrates. The synthesis is of such great efficiency that CNC forests have been obtained. Figure 7.8a displays the side-view SEM image of the grown CNC forests on the substrate edge. It reveals that the overall thickness of the forest is about 30 μm. Figure 7.8b provides a closer view of the CNC forest. It can be seen that the catalyst particles are found at the tips of the coils, suggesting that the grown CNCs follow a tip growth mechanism. Apart from CNC forests, CNC bouquets also formed on the sample edges, as shown by the side-view SEM images in Figures 7.8c and 7.8d. The SEM top-views shown in Figures 7.8e and 7.8f present the growth of CNC clusters generated from the pits on the sample surface, where various shapes of NCs (twisted forms, solenoids, spring-like forms, waved fibres, NC-NF hybrid forms) can be observed.

The EDX measurement on an individual grown coiled structure positioned on a Si wafer confirms that the synthesised NCs are a carbon-based material (Figures 7.9a and 7.9a*). Moreover, Raman spectroscopy was employed to characterise the obtained product. The presence of G and D peaks in Figure 7.9b further verifies the production of carbon nanostructures.

TEM, combined with point-localised EDX measurements, was conducted to further examine the morphological structure of grown nanocoils and detect chemical constitution of the catalyst particles responsible for the coil growth, as presented in Figure 7.10. The TEM images in Figures 7.10a-7.10d* show low (Figures 7.10a and 7.10c) and high (Figures 7.10b, 7.10d and 7.10d*) magnified views of grown CNCs with twisted forms. The coil diameter and pitch of the same CNC inspected in Figures 7.10a and 7.10b is 130 nm and 160 nm, and there is no hollow channel inside the carbon tubule which has been twisted to form the CNC. Another helical structure displayed in Figures 7.10c-7.10d shows larger coiling size, with a coil diameter of 160 nm and a coil pitch of 210 nm. A closer view in Figure 7.10d* shows that the examined structure is completely dense without a pore presented within the carbon tubule. Figure 7.10e presents a spring-like CNC with a catalyst particle staying at the tip. Point-localised EDX measurement (Figure 7.10e*) of the catalyst particle reveals that the catalyst NP contains Fe and Sn, with an estimated composition ratio (Fe/Sn) of 5:2, consistent with the atomic ratio of elements used in the experiment.

7.3.2.2.2 Effect of Amount of Sn Used on the Morphologies of the Grown Product

An investigation into the effect of Sn concentration used on the morphologies of grown carbons has been conducted. Surprisingly, tuning the amount of Sn leads to the production of distinct-shaped carbon structures. Briefly, a series of Sn^{2+}-containing solutions with different concentrations of Sn^{2+} ($c(Sn^{2+})$: 0.1, 0.06,

0.03, and 0.01 mol/L, respectively) and a Fe^{2+}-containing solution ($c(Fe^{2+})$: 0.02 mol/L) were prepared. BHF-BST substrates were modified by Sn and Fe within these solutions. The C_2H_2-CVD was conducted at growth temperatures of 750˚C for 15 min. The gas flow recipe was kept with $Ar/H_2/C_2H_2$ at 900/100/40 sccm in all these experiments, unless otherwise stated.

Figure 7.11 displays the SEM image library of various shapes of grown carbon nanostructures, dictated by the Sn^{2+} concentrations used. Figures 7.11a and 7.11b show the formation of flower-like carbon structures, constituted by straight CNFs, where the substrate was coated with a solution of 0.1 mol/L Sn^{2+} in ethanol, and there is no helical growth of carbon observed in this situation. Once the concentration of the chemical modifier Sn^{2+} is reduced to 0.06 mol/L, beaded CNFs start to dominate the morphologies of grown products (Figures 7.11c and 7.11d). Further reducing the amount of Sn triggers carbon helical growth. Figures 7.11e and 7.11f present the formation of CNC/CMCs on the edge as well as on the flat surface of the substrate, when the concentration of Sn^{2+} is approx. at 0.03 mol/L. Furthermore, a coating of Sn^{2+} solution with concentration at 0.01 mol/L for sample treatments witnesses encouraging production of CNC/CMCs, as shown in Figures 7.11g and 7.11h. However, the morphologies of carbon helical structures can be slightly changed from carbon spirals to CNC-CNF hybrid structures or twisted carbon tubules (Figures 7.11i and 7.11j), when the C_2H_2 gas flow rate is decreased to 20 sccm at growth.

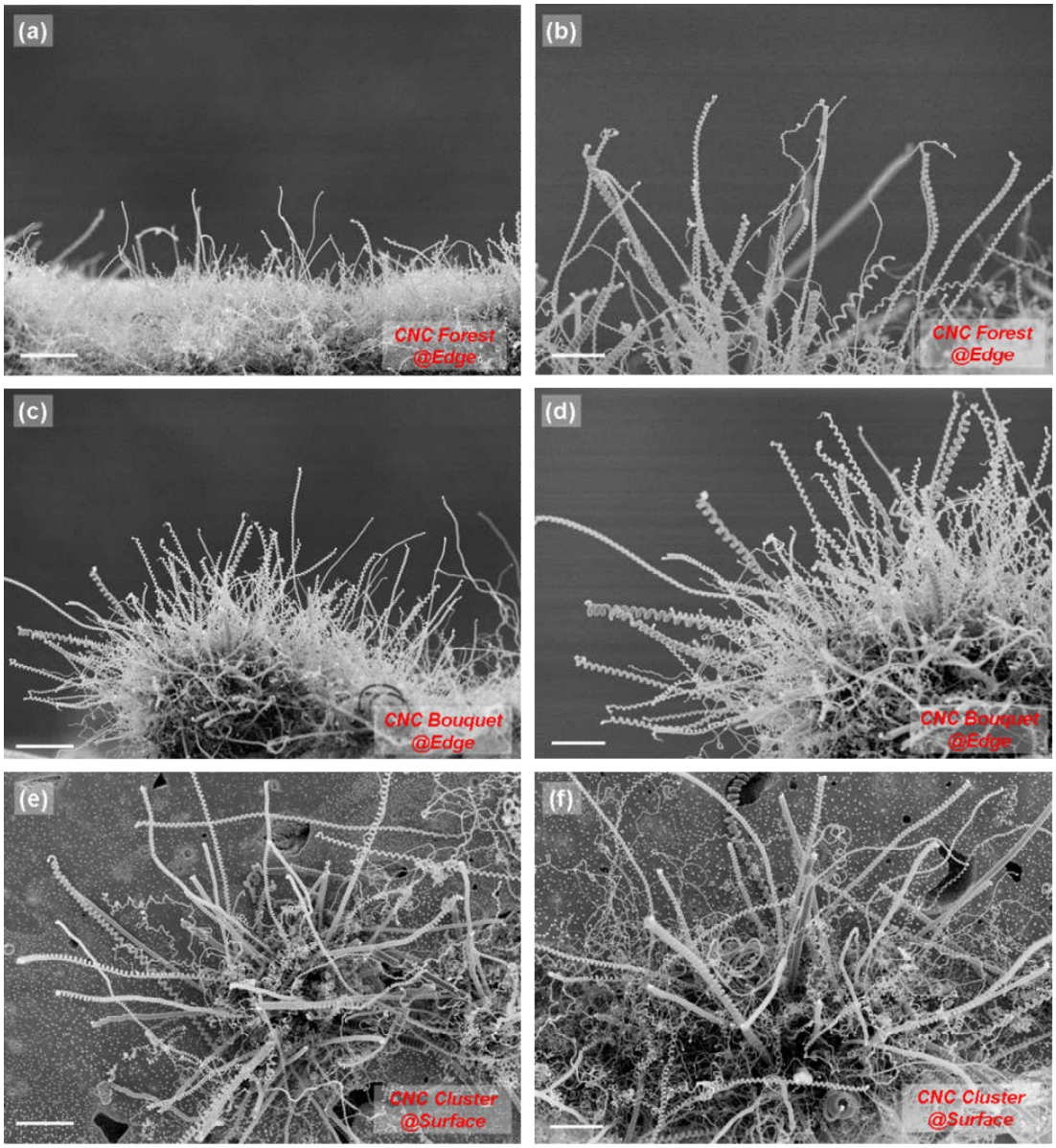

Figure 7.8: SEM image library of CNC/CMCs grown on Sn-modified BHF-BST substrates. (a-b) Side-views of CNC/CMC forests grown on the edge of the substrate. (c-d) Side-views of CNC/CMC bouquets formed on the edge. (e-f) Top-views of CNC/CMC clusters sprouted from the pits on the substrate surface. Scale bars: (a), (c), (e) 10 μm. (b), (d), (f) 5 μm.

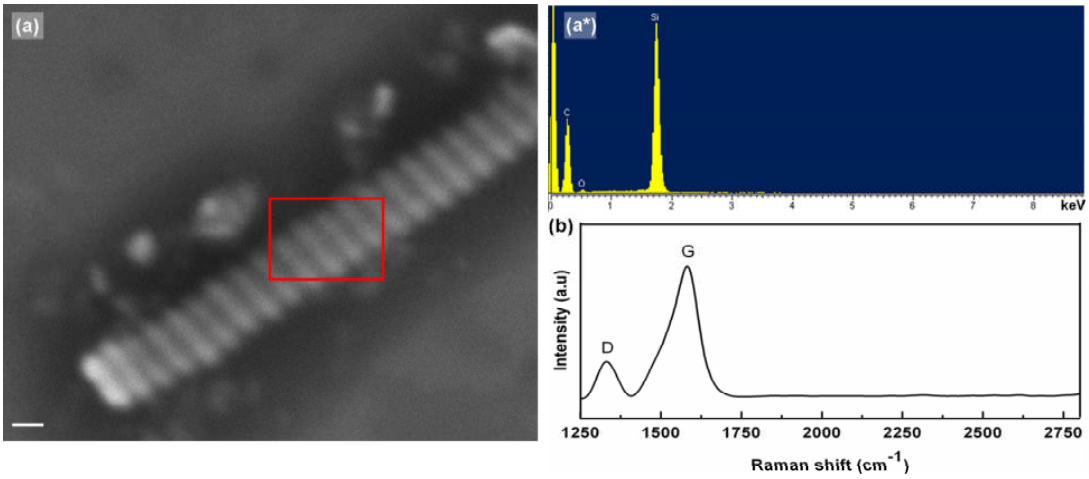

Figure 7.9: (a) SEM observation of an individual coiled structure positioned on Si wafer for further characterisation. Scale bar: 500 nm. (a*) EDX spectrum taken from the red-rectangular region marked on (a), showing the presence of C, Si, and O, indicating that C is the major constituent in the coil. (b) Representative Raman spectrum of grown sample: a remarkable G/D ratio indicates a high graphitisation of obtained coils.

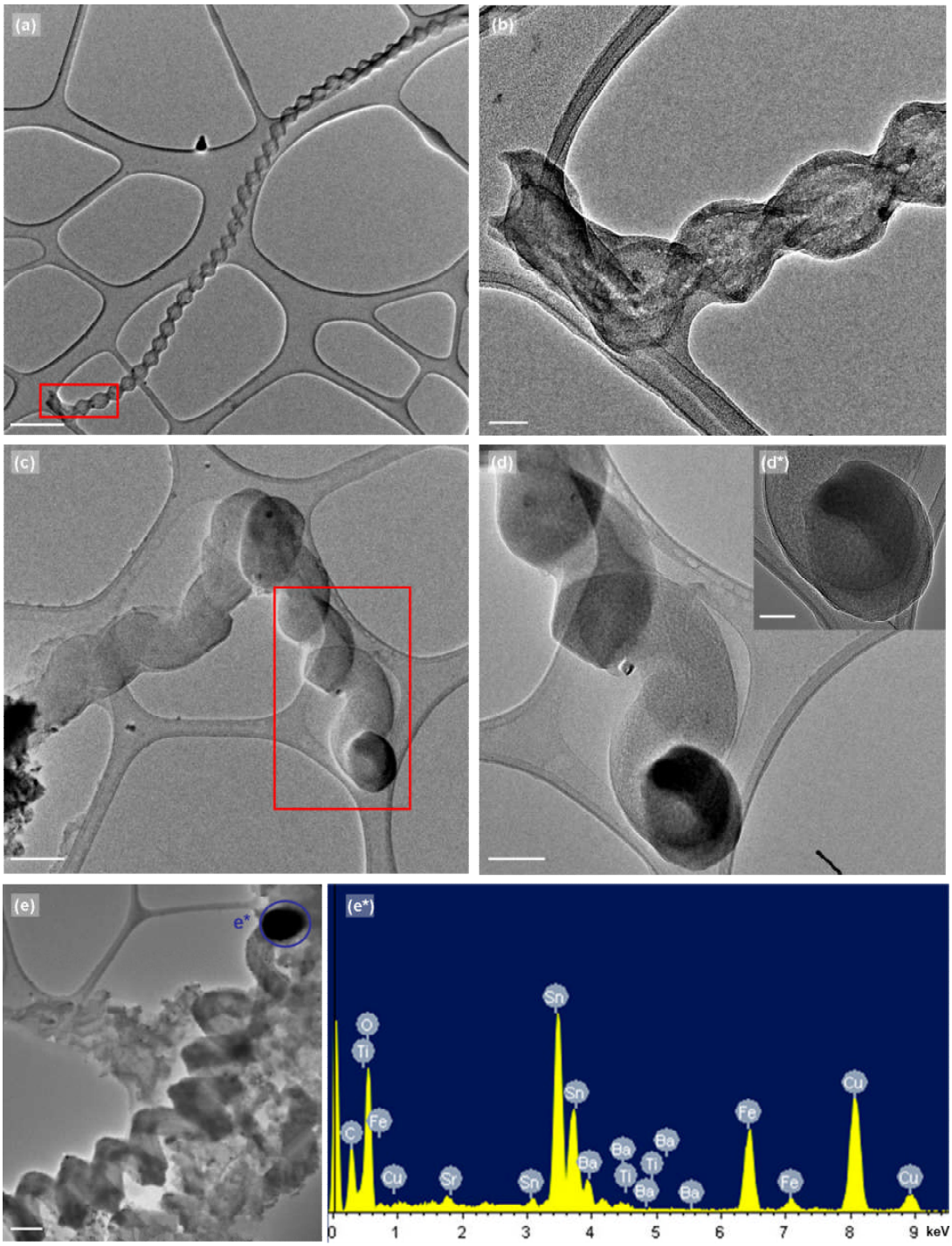

Figure 7.10: (a-d) TEM observations of grown CNCs. (d*) HRTEM view of the CNCs shown in (c) and (d). Scale bars: (a) 500 nm. (b) 50 nm. (c) 200 nm. (d) 100 nm. (d*) 50 nm. (e) TEM image of an individual CNC with a catalyst particle staying at the tip. Scale bar: 100 nm. (e*) Point-localised EDX spectrum of the catalyst particle, indicating the presence of Sn and Fe. The signal of Cu is attributed to the TEM grid.

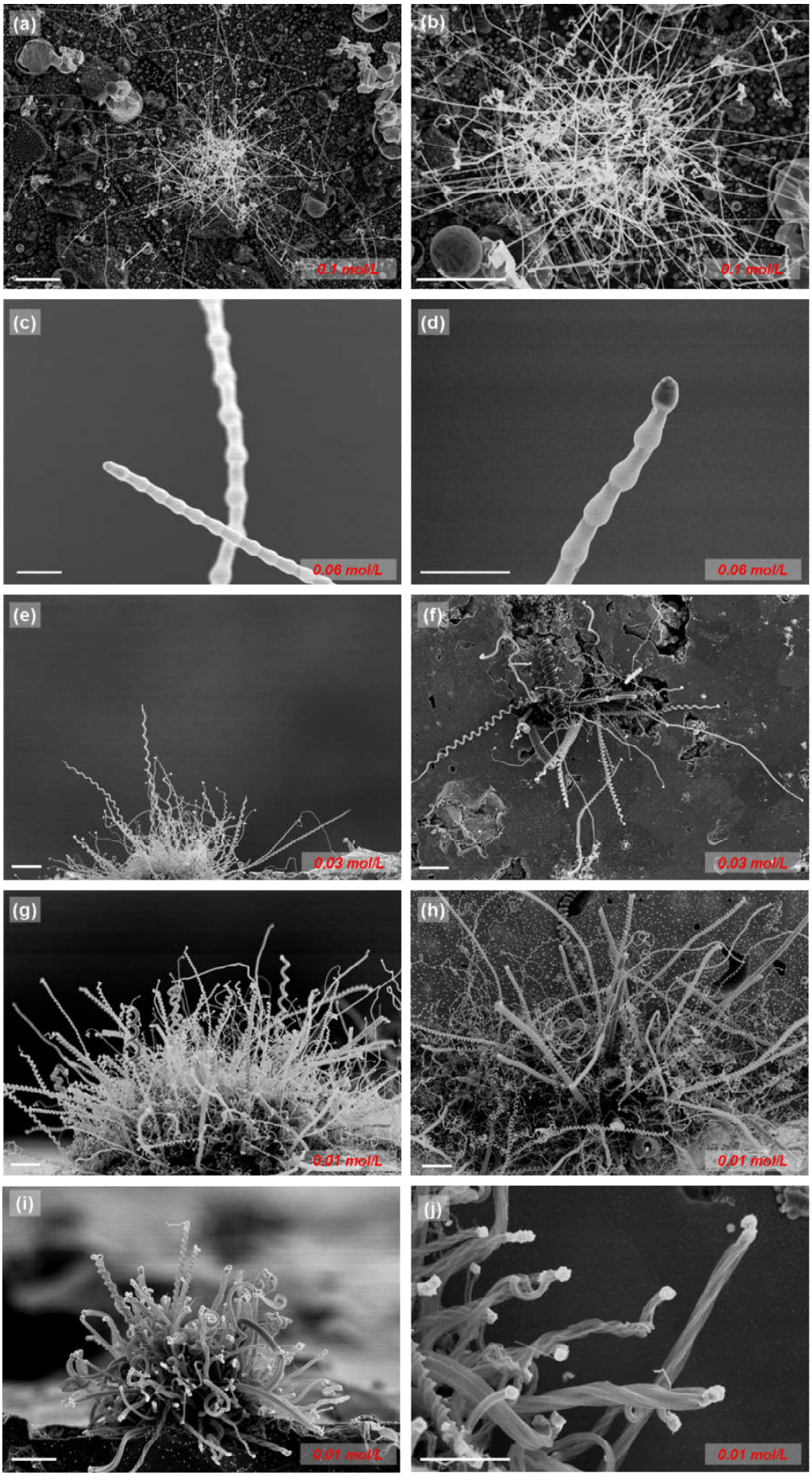
(a)
0.1 mol/L
(b)
0.1 mol/L
(c)
0.06 mol/L
(d)
0.06 mol/L
(e)
0.03 mol/L
(f)
0.03 mol/L
(g)
0.01 mol/L
(h)
0.01 mol/L
(i)
0.01 mol/L
(j)
0.01 mol/L

Figure 7.11: SEM image library of the effect of Sn concentration used on the morphologies of the grown product, showing distinctly-shaped carbon nanostructures: (a-b) flower-like structures constituted by straight CNFs, (c-d) beaded CNFs, (e-f) CNC/CMCs, (g-h) CNC/CMCs (with higher yield), and (i-j) twisted tubules. Scale bars: 3 μm. The amount of Sn used in each case during substrate preparation is marked on each image.

7.4 Discussion

It is instructive to compare the growth results that have been achieved here with those grown on other catalyst systems, as there is no study on the helical growth of carbons on $SrTiO_3$ and $BaSrTiO_3$ substrates. For metal-catalyst-free cases, comparable growth scenarios similar to those presented here were investigated by other researchers employing TiC, Ti_2O_3, and Ti compounds, although chemical modifications on the CVD process by a small addition of S are noticed in all these studies[265, 298]. For Sn-involved cases, there were quite a few reports revealing that Sn is an efficient catalyst for inducing carbon helical growth, normally co-functioning with transition metals such as Fe[33, 175, 178, 179], Ni[180, 299], and Cr[180, 299]. For example, Rao *et al.*[33] demonstrated a promising synthesis of helical carbon nanowires with the aid of a Fe and Sn binary catalyst. A specific model based on the mutual solubility of Fe and Sn, along with metallic catalyst-carbon product interactions, has been proposed in their study to elucidate the role of the Sn catalyst[33]. Similarly, the yield

and quality of carbon helices synthesised in this study have been greatly enhanced by the involvement of Sn.

It is well known that specific types of catalysts need to be used for promoting the formation of carbon coils[259]. To date, a wealth of catalysts (mainly metal elements, binary metals, and metal carbides) have been tested by various research groups in respect of synthesising coiled carbon nanostructures, such as Cu[111, 113-116, 262], Fe[260, 293, 300, 301], Ni[104, 264, 292, 302], Fe-Sn[33, 177, 303], Fe-In[33, 174, 175], Fe-Ni[304, 305], Fe/ITO[306], Co/SiO_2[307], Ni/Al_2O_3[296, 308], TiC[265, 298], Mo[180], Cr[299, 309], and Ag-K[18]. Moreover, a small addition of S- or P-containing compounds into ambient gases during CVD reactions has been proven to be successful in aiding carbon helical growth. By way of contrast, this study employs pure perovskite oxides (in metal-free scenarios) or Sn/Sn-Fe dosed, perovskite oxides (in metal-involved scenarios) as catalysts for achieving the growth of CNC/CMCs. Thus it would be helpful to explore the roles played by these new catalysts within the course of carbon coil synthesis.

Among the metal catalysts used in the growth of CNC/CMCs up to now, Sn has attracted most attention, owing to its capacity to lead to high-yield, good-quality production of carbon helices at low cost. Unlike traditional metal catalysts (*i.e.* Fe, Ni, Co), Sn has a special interaction with graphite surfaces, where the small degree of wettability (non-wetting) of graphite nanostructure surfaces by Sn induces a repulsive interaction, thus promotes non-linear growth of carbon.[33] Sn was extensively reported as cooperating with Fe and/or Fe-In in synthesising coiled CNTs and CNFs. Earlier study conducted by Pan *et al.*[176] suggests that In contributes to the

formation of coiling structures, whilst the use of Sn is only to enhance the growth rate, since limited yield of the CNC product was obtained when using Fe-Sn or Fe-SnO_2 as catalysts. However, recent investigations have shown that Fe-Sn can act as an efficient catalyst without the dose of In[33, 179, 303]. The work herein confirms the catalytic capacity of Sn in promoting carbon coil growth. Moreover, an interesting growth scenario has been observed by varying the concentrations of Sn^{2+}-coating towards the BHF-BST substrates (with the concentration of Fe^{2+} remaining constant). It can be clearly observed that large Sn doses lead to the formation of straight CNFs, whilst small concentrations of Sn additive give rise to non-linear growth of carbons. This tendency is consistent with the one noted in a previous report regarding the synthesis of CNCs using Fe-Sn-O NPs as catalysts[175]. The reason for this is believed to be the inhomogeneous distributions of Fe and Sn elements within the catalyst particles leading to the difference in carbon precipitation/extrusion speeds in different parts of the catalyst.

As outlined in Chapter 3, to elucidate the growth mechanisms of helical carbon nanostructures, several models have been proposed in previous research articles, but none of them addresses the growth of coiled CNTs universally. In this study of metal-free growth and metal-involved growth of CNC/CMCs, different types of samples, growth conditions, reaction routes *etc*. have been applied; hence different formation mechanisms of grown structures need to be considered. With regard to the metal-free scenario presented in Section 7.3.1, random observations of CNC/CMCs were gained on the scratched STO and BST substrates. It is believed that the

scratching treatment on the surface induces the formation of nanosized and microsized NPs. It is possible that some of the NPs are in proper sizes and shapes, which are suitable for the generation of helical structures from them. This speculation is entirely consistent with the experimental observations (Figures 7.1 and 7.2), where limited amounts of carbon coils were produced in the restricted conditions (narrow growth temperature windows). On the basis of this, a growth mechanism in terms of CNC formation on the scratched perovskites is conjectured. Generally, the formation of CNCs from the scratch-induced NPs (Figure 7.2a) on the scratched perovskite substrate is attributed to the synergetic effects of geometry (particle shapes, facet orientations) and chemistry (localised compositions) of the NPs. The scratch-induced NPs expose distinct crystal facets during the growth process, the C_2H_2 gas is supplied to the catalytically active facets and decomposed to carbon segments (atoms, branches), as it is already posited in Chapter 6 that the distinct BST/STO facets differ in the adsorption and diffusion of carbon species. These formed carbon segments are then diffused to the precipitation facets. It is reasonable to suggest that surface diffusion would dominate here rather than bulk diffusion, considering the fact that C has limited solubility in STO/BST at applied temperatures, and even the rates of surface diffusion *via* distinct crystal facets are of different values; therefore a gradient of carbon precipitation rate is established alongside the planes of precipitation facets, giving rise to the non-linear growth of carbons[178, 263]. On the other hand, the presence of Ti within the NPs could also play an important role in inducing the bending, since quite a few reports indicated that the

Ti, especially in the forms of TiC, Ti_2O_3 *etc.*, tends to catalyse the growth of CNCs[265, 298, 310]. The scratch procedure might produce nanosized NPs with distinct facet exposed, where different facets possess different Ti compositions and hence chemistry, which would result in the anisotropic precipitation of carbons throughout these regions. It is also likely that the H_2 pretreatment used at elevated temperatures prior to the CVD reaction assists the conversion from Ti^{4+} (TiO_2) to Ti^{3+} (Ti_2O_3) within the surface lattices, thus partially modifying the chemical constitutions of NPs. Moreover, the localised formation of TiC on the NPs is also suggested, which is unlikely to be the case, as it is claimed that the carbothermal reduction of TiO_2 occurs at extremely high temperatures (>1000˚C)[282]; however, this possibility cannot be ruled out until solid evidence in terms of localised chemical information about the catalyst NPs is provided. Lastly, I cannot also rule out the possibility, at the current stage, that the grown helical structures were formed *via* a route driven by carbon fragment assembling (without the aid of catalyst NPs), as revealed recently by Bachmatiuk *et al.*[276] in preparing helical carbon nanostructures over pure SiO_2, although a catalyst particle trapped inside the coils has been observed here in this case (Figure 7.2a).

In respect of the metal-involved scenario presented in Section 7.3.2, various shapes of CNC/CMCs can be obtained in high yield with the assistance of Sn (Figures 7.4 and 7.5; Figure 7.8). The grown CNC/CMCs follow a tip growth mode, where the catalyst particles are found at the tips of the nanostructures. Here two types of BST samples have been employed for investigating the growth of CNC/CMCs on

them: as-received samples (containing Sn) and processed BHF-BST samples (containing Fe and Sn). The growth mechanisms of CNC/CMCs in these two types of catalyst systems differ one from the other, but both of them contrast with the one proposed for the CNC/scratched BST case aforementioned. For the as-received BST sample (Section 7.3.2.1), the NPs inside the pits/cracks of the BST substrate act as reservoirs for the Sn dispersion. The uniformity of Sn composition is greatly dependent upon the configuration and position of a NP and the distribution of the Sn itself. Judging from the sample preparing/processing method described by the material supplier, it is highly unlikely that a uniform Sn distribution can be established, thus giving rise to the inhomogeneity of Sn composition on/in a catalyst particle. Under this circumstance, the carbon deposition/extrusion rates on different parts of the particle should be different, since they are dictated by this non-uniform distribution of Sn, or by the localised formation of special compounds (titanium-tin carbides[311]). The non-linear growth of carbons is therefore achieved (Figures 7.3-7.5). It is also worth noticing that both the morphological structure and the chemical constitution of a catalyst particle trapped within a grown CNC have been detected (Figures 7.6b and b*), suggesting that the carbon helical growth was induced by an irregularly-shaped polyhedral BST nanoparticle, modified by Sn, without the aid of any other transition metal elements (Fe, Co, Ni *etc.*). However, the fashion in which the Sn decoration onto the BST nanoparticle remains unknown, it would be helpful to perform EDX elemental mapping towards the catalyst particles to see the morphology of Sn distributions.

As for the processed BHF-BST samples (Section 7.3.2.2), the growth of helical carbons occurred on the sample surfaces as well as at the substrate edges (Figure 7.8), where the deposited Fe- and Sn-containing NPs aided the formation of CNCs. The point-localised EDX study performed within a TEM has verified that the elements of Fe and Sn are responsible for catalysing the growth of CNCs (Figures 7.10e and 7.10e*), which is consistent with quite a few investigations claiming that Fe-Sn is catalytically active for inducing carbon helical structures. Moreover, the Fe and Sn ratio in the catalyst composition is also an important factor for inducing non-linear growth. Wang *et al.*[33] observed that an Fe/Sn ratio of 4:1 can lead to a promising growth of coiled carbon nanowires. Chang *et al.*[299] suggested that a composition ratio of Fe and Sn (19:1) was critical to yield carbon helical structures, by conducting CNC synthesis on stainless steel plates. Li and his colleagues[178] considered a Fe/Sn ratio of 15:6 optimal for the growth of coiled carbon nanostructures. Herein the EDX analysis of a catalyst particle staying at the CNC tip shows the presence of Fe and Sn with a Fe/Sn ratio of approx. 5:2, which has been shown to be suitable for the growth of CNCs[177]. The growth mechanism for the formation of CNCs is proposed owing to the difference between the carbon deposition/diffusion and extrusion rates in different regions of catalyst particle, which possesses inhomogeneous distribution of the elements of Fe and Sn. There might be Fe and Sn carbides forming within a catalyst particle during the CVD process, such as $Fe_3Sn_xC_y$ and Fe_3C, which could cause the difference in the extrusion speeds of carbon network among different parts of the catalyst, as reported by Okazaki *et al.*[175]

Lastly, the carbon non-linear growth in this investigation requires careful thermodynamic and kinetic control. For example, the temperature window applied for CVD reactions can greatly influence the products (for metal-free route using STO, the only temperature for generating CNCs is 700°C); the amount of Sn-coating used in the catalyst preparation process can also dictate the morphologies of grown CNCs, as observed in Figures 7.11. Moreover, the formation of catalyst particles is affected by the C_2H_2 gas (concentration, pressure *etc.*), which have been observed recently by using Cu as a CNC growth catalyst[115]. This point sheds some light on the interesting observations shown in Figures 7.11g-7.11j.

7.5 Future Work

The work presented in this chapter centers on the growth of carbon helical structures on STO and BST substrates without/with the aid of Sn, which are regarded as new catalyst systems for fabrication of carbon helices. It would be helpful to determine possible synthetic routes to achieve larger scale production (at industrial levels) of CNCs at low costs on such substrates. Moreover, the properties of these grown coiled nanostructures need to be investigated, for example, *via* mechanical strength testing, field emission experiments *etc.*

Chapter 8：

Conclusions

8.1 Overview

This thesis presents original work on the growth of carbon nanostructures (mainly CNTs) on perovskite oxide surfaces *via* CVD technique. The results in Chapters 4-7 advance the understanding of the growth mechanisms of CNTs and the role of catalysts played during CVD reactions. Two types of perovskite oxide, single crystal $SrTiO_3$ (001) and polycrystalline $BaSrTiO_3$, have been used for experimental purposes: they can function as catalyst supports (in metal-catalyst-involved CVD routes) or as catalysts (*via* metal-catalyst-free CVD routes) for the growth of carbon nanostructures. In this study, grown carbon nanomaterials with various morphologies have been observed as a result of employing different types of catalysts and catalyst design methods. The experimental results will be summarised in Sections 8.2 and 8.3 according to the catalytic routes used, followed by an outlook for future work.

8.2 The Metal-Catalyst-Involved Route

The study presented in Chapter 4 demonstrates that the $SrTiO_3$ (001) surface can function as a suitable substrate for the growth of CNTs, and that the $SrTiO_3$ supported metal catalysts can be designed and fabricated in a controllable way, prior to CNT growth. Key progress achieved here is concerned with the realisation of vertically-aligned growth of CNTs on $SrTiO_3$ (001) surfaces by Fe catalyst, but only with limited CNT carpet length (~5 μm). This finding provides a clear indication that

it is feasible to build up future perovskite-based CNT devices (in the field of nanoelectronics *etc.*) at the nanoscale, although more delicate design on catalysts needs to be implemented. Indeed, further steps in catalyst fabrication have been attempted by using catalysts subject to unconventional methods (fast-heating, oxidising pretreatment), giving rise to promising CNT growth. It can be inferred from these results that the $SrTiO_3$ substrate has unexpected potentials in forming fine catalytic NPs (with controllable sizes and shapes) for CNT synthesis compared to commonly-used oxide substrates (SiO_2, Al_2O_3), which have been heavily investigated to date.

Bringing the element of Sn into the catalyst system induces the non-linear growth of CNTs, which is discussed in detail in Chapter 7. It is found that both Sn-decorated oxide ($BaSrTiO_3$) nanoclusters and Sn-modified metal (Fe) nanopowders can lead to the formation of carbon nanocoils (CNCs). The non-linear growth behaviour of carbons is due to the difference between the carbon deposition/diffusion and extrusion rates in different regions of the catalyst particles. This finding is important because it stimulate a general question: Can nanopowders of any material covered by Sn cause the helical growth of carbons? It is well known that Sn has a non-wetting interaction with graphite thus could promote non-linear growth of carbons. With regard to metals (Fe, Cr, Mn, Ni *etc.*), the formation of bimetallic phases (e.g. Fe-Sn mixtures) or complex alloys (e.g. Fe-Ni-Cr-Sn) results in inhomogeneous distributions of Sn within the catalyst particles, which can lead to the uneven deposition/extrusion of carbons to establish the helical growth. With regard to oxides

(in this case, $BaSrTiO_3$), it is expected that Sn would wet the $BaSrTiO_3$ surface, owing to a lower surface energy of Sn (approx. 0.5~0.7 J/m^2) in comparison with $BaSrTiO_3$ (approx. 1.5~2 J/m^2). During CVD process, Sn (in molten state) would cover the $BaSrTiO_3$ nanoclusters in a non-uniform manner (speculatively described as 'partially wrap the $BaSrTiO_3$ particle'), this effect would synergistically function along with the distinct $BaSrTiO_3$ facet effect to dictate the carbon helical growth. For future reference, it should be interesting to try using SiO_2 instead of $BaSrTiO_3$ under this circumstance, for the reason that Sn will de-wet the SiO_2 surface by forming 3D nanocrystals. It might not be possible to generate helical growth of carbons in such Sn-decorated SiO_2 nanoclusters.

8.3 The Metal-Catalyst-Free Route

The growth of metal-free CNTs is of significant importance, because many potential applications nowadays require CNT production free of metal catalyst residues, which are detrimental to the magnetic properties of CNTs and also incompatible with CNT-based nanodevices.[166, 312-314] It is the metal-catalyst-free CVD that makes it possible to synthesise CNTs by using non-metallic species as catalysts. The work presented in this thesis reveals that the perovskite oxides ($SrTiO_3$ and $BaSrTiO_3$) can serve as catalysts for the growth of CNTs. Interesting results are achieved by using single crystal $SrTiO_3$ (001) and polycrystalline $BaSrTiO_3$ surfaces *via*

metal-catalyst-free CVD routes.

The study shown in Chapter 5 focuses on catalyst designs in engineering $SrTiO_3$ (001) single crystals to realise surface-roughness-tailored growth of CNTs *via* metal-catalyst-free CVD. The investigation includes several simple, flexible methods for engineering the $SrTiO_3$ (001) substrates, giving rise to the $SrTiO_3$ asperities with nanoscale curvatures, which are responsible for the catalytic performances of substrate surfaces in the formation of CNTs. Interestingly, the growth trend of CNTs, even the CNT yield on the whole range of engineered STO substrates, strongly correlates with the roughness of the STO surfaces. The growth mechanism is suggested in the content of the formation of hemispherical carbon caps over the $SrTiO_3$ asperities *via* a lift-off process, where the defects/distortions on the asperities could enhance the adsorption and decomposition of hydrocarbons. Complementary studies are performed by using scratched and powdered $SrTiO_3$ samples to confirm the catalytic capability of $SrTiO_3$ nanoscale roughness. These results could be extended to a broader context as to 'Is the roughness of any oxide surface related to its catalytic activity or is this particularly the case for perovskites'? To the best of my knowledge, current findings in CNT research indicate that the growth of CNTs requires nano-dimensional particles as catalysts, which are not limited in chemical compositions. Hence, it could be expected that any oxide surface with roughness at the nanoscale can aid the growth of CNTs without the presence of any metallic catalysts, however, the specific advantage of $SrTiO_3$ lies in the fact that its surface roughness can be tailored *via* various types of surface treatments, which could

subsequently support the metal-free growth of CNTs on it in a controllable manner.

The investigation, presented in Chapter 6, on the metal-catalyst-free production of CNTs on polycrystalline $BaSrTiO_3$ surfaces is even more interesting, as the phenomenon of facet-selective growth of CNTs has been observed. The used sample has been treated by buffered HF etching, which helps remove the polishing damage/carbon layers/metal contamination on the substrate surface, resulting in a clean (free of metal contamination) polycrystalline $BaSrTiO_3$ surface with various facets clearly exposed. Thanks to SEM, EBSD, and Micro-XAM co-investigation, it becomes apparent in this investigation that the $BaSrTiO_3$ (110) facets lead to promising growth of CNTs on them, whereas the (001) facets result in no growth at all. A complementary DFT calculation on studying the adsorption and diffusion of carbon species (C_2H_2 molecules and C atoms) on these low-index $BaSrTiO_3$ surfaces is performed, revealing that the (110) facet promotes the capture of carbons (especially C_2H_2) and facilitates the transportation of carbon species, thus enhancing the formation of CNTs, whilst the (100) facet retards the adsorption and diffusion of carbons, to such a degree that it is not able to benefit the growth of CNTs. This theoretical work is consistent with the experimental results, confirming that the surface orientations/surface lattice arrangements remain responsible for the facet-selective growth behaviour of CNTs on polycrystalline $BaSrTiO_3$ surfaces. This is followed by some speculation on the mechanism of CNT formation, which seems to depend upon the assembly of carbon segments, produced with the aid of distinct $BaSrTiO_3$ facets.

In summary, the perovskite oxides ($SrTiO_3$ and $BaSrTiO_3$ in this case) can be directly used as catalysts for the growth of CNTs, as well as serving as suitable catalyst supports for the surface-bound synthesis of carbon nanostructures. The results generated *via* the metal-catalyst-free CVD route provide insights into the usage of perovskite oxides in catalysis.

8.4 Future Works

This project could be furthered by a range of future works, in which the two types of CVD route for catalyst usage could come into play. In respect of the metal-catalyst-involved route, firstly, further control over catalyst design on oxide substrates will substantially enhance the quality and yield of resulting carbon nanomaterials and influence their structures. For instance, attempts could be made to fabricate $SrTiO_3$ supported Fe/Ni binary catalysts. The combination of bcc Fe and fcc Ni nanosized particles, which possess unique crystal shapes (truncated pyramids) with uniform size distributions on $SrTiO_3$ (001) supports, shows great promise for catalysis, *i.e.* catalysing the growth of SWNTs with narrow chriality distributions. Also, the method of tailoring the catalyst patterning on $SrTiO_3$ (001) surfaces needs to be developed, for the purpose of improving the VACNT synthesis on substrates, which could have huge implications for key applications, such as integrated circuits and thermal interface materials. The principle at stake here is to try to increase the

areal density of metal catalyst NPs (e.g., up to 10^{11}-10^{13} cm^{-2}) on $SrTiO_3$ substrates during catalyst fabrication. A method reported by Hofmann *et al.*[315] on cyclic deposition might be helpful in this quest.

Secondly, the experimental protocols in terms of synthesising carbon nanomaterials on perovskite substrates will continue to improve. For those $SrTiO_3$ supported metal shaped catalyst particles, a recipe could be sought for freezing the metal shapes during the CVD reaction, for example, by using cold wall CVD technique, as mentioned in Chapter 4. Moreover, designing a possible apparatus to monitor *in situ* the growth of CNTs from these shaped metal catalysts, to witness how the structures of grown materials are tailored by the catalysts (e.g. using Au, Cu, and Ag), if the catalyst shape can be preserved, or to observe how the catalyst particle evolves/restructures itself during the CVD process, if the catalyst shape is jeopardized, would help better understand the role of $SrTiO_3$ supported metal catalysts during CNT growth.

Thirdly, the growth of CNTs will benefit from further characterisations and analysis through relatively developed techniques, such as *in situ* TEM and XPS. Although this will definitely involve more sophisticated sample preparation procedures, it can unequivocally provide more information on the circumstances of CNT growth. For example, *in situ* TEM and XPS/XRD could offer valuable information on both catalyst geometry/dynamics and chemical constitution during CNT growth.

The metal-catalyst-free growth of CNTs has been considered as a major

breakthrough in CNT research. In this thesis, perovskite oxides are used as catalysts for growing CNTs, and future works on the metal-free route lies in the following aspects: firstly, the role played by perovskites during metal-free CVD reactions needs further clarification; the relevant CNT growth mechanisms also need further investigations before a relatively convincing model can be proposed. Secondly, the scaling-up and quality of metal-free CNTs could be improved by designing the oxide catalysts more smartly. There has been no report so far on the growth of CNTs in a vertically aligned manner *via* a metal-free CVD approach, thus seeking possible methods of densely patterning oxide catalyst NPs on substrates, in order to achieve the growth of VACNTs. This could be of paramount importance for various applications such as energy storage, nanoelectronics, and magnetic nanodevices. Thirdly, it is possible to use $SrTiO_3$ substrates to grow graphene on them *via* a metal-catalyst-free CVD route, as shown by several studies on the CVD of graphene on oxide (silicon oxide,[316] sapphire[317] *etc.*) surfaces. $SrTiO_3$ has the advantages of presenting numerous surface reconstructions, subject to different surface treatments. Graphene films are expected to grow on these tailored $SrTiO_3$ surfaces (for example, on a reconstructed $SrTiO_3$ (111) surface) *via* metal-free CVD. This novel study might pave the way for the full use of perovskite oxides in catalysis and for the direct fabrication of metal-free graphene into field effect transistor devices capable of high performances.

References

1. Baughman, R. H.; Zakhidov, A. A.; de Heer, W. A., Carbon Nanotubes - the Route toward Applications. *Science* 2002, 297, 787-792.
2. Harutyunyan, A. R.; Chen, G. G.; Paronyan, T. M.; Pigos, E. M.; Kuznetsov, O. A.; Hewaparakrama, K.; Kim, S. M.; Zakharov, D.; Stach, E. A.; Sumanasekera, G. U., Preferential Growth of Single-Walled Carbon Nanotubes with Metallic Conductivity. *Science* 2009, 326, 116-120.
3. Wang, Y.; Shi, Z. X.; Yin, J., Unzipped Multiwalled Carbon Nanotubes for Mechanical Reinforcement of Polymer Composites. *J. Phys. Chem. C* 2010, 114, 19621-19628.
4. Tessonnier, J. P.; Su, D. S., Recent Progress on the Growth Mechanism of Carbon Nanotubes: A Review. *ChemSusChem* 2011, 4, 824-847.
5. Lu, F. S.; Gu, L. R.; Meziani, M. J.; Wang, X.; Luo, P. G.; Veca, L. M.; Cao, L.; Sun, Y. P., Advances in Bioapplications of Carbon Nanotubes. *Adv. Mater.* 2009, 21, 139-152.
6. Landi, B. J.; Ganter, M. J.; Cress, C. D.; DiLeo, R. A.; Raffaelle, R. P., Carbon Nanotubes for Lithium Ion Batteries. *Energy Environ. Sci.* 2009, 2, 638-654.
7. Lee, S. W.; Yabuuchi, N.; Gallant, B. M.; Chen, S.; Kim, B. S.; Hammond, P. T.; Shao-Horn, Y., High-Power Lithium Batteries from Functionalized Carbon-Nanotube Electrodes. *Nature Nanotechnol.* 2010, 5, 531-537.
8. Shaikjee, A.; Coville, N. J., The Synthesis, Properties and Uses of Carbon Materials with Helical Morphology. *J. Adv. Res.* 2011, Article in Press.
9. Futaba, D. N.; Hata, K.; Yamada, T.; Hiraoka, T.; Hayamizu, Y.; Kakudate, Y.; Tanaike, O.; Hatori, H.; Yumura, M.; Iijima, S., Shape-Engineerable and Highly Densely Packed Single-Walled Carbon Nanotubes and Their Application as Super-Capacitor Electrodes. *Nature Mater.* 2006, 5, 987-994.
10. Hu, L. B.; Choi, J. W.; Yang, Y.; Jeong, S.; La Mantia, F.; Cui, L. F.; Cui, Y., Highly Conductive Paper for Energy-Storage Devices. *Proc. Natl. Acad. Sci. U. S. A.* 2009, 106, 21490-21494.
11. Zhang, J.; Hu, Y.-S.; Tessonnier, J.-P.; Weinberg, G.; Maier, J.; Schlögl, R.; Su, D. S., Carbon Nanofibers@Carbon Nanotubes: Superior Carbon for Electrochemical Energy Storage. *Adv. Mater.* 2008, 20, 1450-1455.
12. Wildoer, J. W. G.; Venema, L. C.; Rinzler, A. G.; Smalley, R. E.; Dekker, C., Electronic Structure of Atomically Resolved Carbon Nanotubes. *Nature* 1998, 391, 59-62.
13. Cantoro, M.; Hofmann, S.; Pisana, S.; Scardaci, V.; Parvez, A.; Ducati, C.; Ferrari, A. C.; Blackburn, A. M.; Wang, K. Y.; Robertson, J., Catalytic Chemical Vapor Deposition of Single-Wall Carbon Nanotubes at Low Temperatures. *Nano Lett.* 2006, 6, 1107-1112.
14. Hofmann, S.; Sharma, R.; Ducati, C.; Du, G.; Mattevi, C.; Cepek, C.; Cantoro, M.; Pisana, S.; Parvez, A.; Cervantes-Sodi, F.; Ferrari, A. C.; Dunin-Borkowski, R.; Lizzit, S.; Petaccia, L.; Goldoni, A.; Robertson, J., In Situ Observations of

Catalyst Dynamics During Surface-Bound Carbon Nanotube Nucleation. *Nano Lett.* 2007, 7, 602-608.
15. Hata, K.; Futaba, D. N.; Mizuno, K.; Namai, T.; Yumura, M.; Iijima, S., Water-Assisted Highly Efficient Synthesis of Impurity-Free Single-Waited Carbon Nanotubes. *Science* 2004, 306, 1362-1364.
16. Yamada, T.; Namai, T.; Hata, K.; Futaba, D. N.; Mizuno, K.; Fan, J.; Yudasaka, M.; Yumura, M.; Iijima, S., Size-Selective Growth of Double-Walled Carbon Nanotube Forests from Engineered Iron Catalysts. *Nature Nanotechnol.* 2006, 1, 131-136.
17. Chiang, W. H.; Sankaran, R. M., Linking Catalyst Composition to Chirality Distributions of as-Grown Single-Walled Carbon Nanotubes by Tuning Ni/Fe Nanoparticles. *Nature Mater.* 2009, 8, 882-886.
18. Liu, W. C.; Lin, H. K.; Chen, Y. L.; Lee, C. Y.; Chiu, H. T., Growth of Carbon Nanocoils from K and Ag Cooperative Bicatalyst Assisted Thermal Decomposition of Acetylene. *Acs Nano* 2010, 4, 4149-4157.
19. Liu, B. L.; Ren, W. C.; Gao, L. B.; Li, S. S.; Pei, S. F.; Liu, C.; Jiang, C. B.; Cheng, H. M., Metal-Catalyst-Free Growth of Single-Walled Carbon Nanotubes. *J. Am. Chem. Soc.* 2009, 131, 2082-2083.
20. Liu, B. L.; Tang, D. M.; Sun, C. H.; Liu, C.; Ren, W. C.; Li, F.; Yu, W. J.; Yin, L. C.; Zhang, L. L.; Jiang, C. B.; Cheng, H. M., Importance of Oxygen in the Metal-Free Catalytic Growth of Single-Walled Carbon Nanotubes from Silicon Oxide by a Vapor-Solid-Solid Mechanism. *J. Am. Chem. Soc.* 2011, 133, 197-199.
21. Huang, S. M.; Cai, Q. R.; Chen, J. Y.; Qian, Y.; Zhang, L. J., Metal-Catalyst-Free Growth of Single-Walled Carbon Nanotubes on Substrates. *J. Am. Chem. Soc.* 2009, 131, 2094-2095.
22. Silly, F.; Castell, M. R., Self-Assembled Supported Co Nanocrystals: The Adhesion Energy of Face-Centered-Cubic Co on Strontium Titanate (001). *Appl. Phys. Lett.* 2005, 87, 053106.
23. Silly, F.; Castell, M. R., Fe Nanocrystal Growth on Strontium Titanate (001). *Appl. Phys. Lett.* 2005, 87, 063106.
24. Silly, F.; Castell, M. R., Growth of Ag Icosahedral Nanocrystals on a Strontium Titanate (001) Support. *Appl. Phys. Lett.* 2005, 87, 213107.
25. Silly, F.; Castell, M. R., Selecting the Shape of Supported Metal Nanocrystals: Pd Huts, Hexagons, or Pyramids on Strontium Titanate (001). *Phys. Rev. Lett.* 2005, 94, 046103.
26. Silly, F.; Castell, M. R., Bimodal Growth of Au on Strontium Titanate (001). *Phys. Rev. Lett.* 2006, 96, 086104.
27. Silly, F.; Castell, M. R., Temperature-Dependent Stability of Supported Five-Fold Twinned Copper Nanocrystals. *Acs Nano* 2009, 3, 901-906.
28. Ihara, S.; Itoh, S.; Kitakami, J., Helically Coiled Cage Forms of Graphitic Carbon. *Phys. Rev. B* 1993, 48, 5643-5647.
29. Im, J.; Auciello, O.; Streiffer, S. K., Layered Barium Strontium Titanate Thin Films for High Frequency Tunable Devices. *Thin Solid Films* 2002, 413,

243-247.
30. Kirchoefer, S. W.; Cukauskas, E. J.; Barker, N. S.; Newman, H. S.; Chang, W., Barium Strontium Titanate Thin Films for Application in Radio-Frequency-Microelectromechanical Capacitive Switches. *Appl. Phys. Lett.* 2002, 80, 1255-1257.
31. Mendoza, F.; Kumar, A.; Martinez, R.; Scott, J. F.; Weiner, B.; Katiyar, R. S.; Morell, G., Conformal Coating of Ferroelectric Oxides on Carbon Nanotubes. *Europhys. Lett.* 2012, 97, 27001
32. Scott, J. F.; Dearaujo, C. A. P., Ferroelectric Memories. *Science* 1989, 246, 1400-1405.
33. Wang, W.; Yang, K.; Gaillard, J.; Bandaru, P. R.; Rao, A. M., Rational Synthesis of Helically Coiled Carbon Nanowires and Nanotubes through the Use of Tin and Indium Catalysts. *Adv. Mater.* 2008, 20, 179-182.
34. Zhong, D. Y.; Liu, S.; Wang, E. G., Patterned Growth of Coiled Carbon Nanotubes by a Template-Assisted Technique. *Appl. Phys. Lett.* 2003, 83, 4423-4425.
35. Bronikowski, M. J., Chemical Vapour Deposition Growth of Carbon Nanotube Bundle Arrays. *Carbon* 2006, 44, 2822-2832.
36. Binnig, G.; Rohrer, H.; Gerber, C.; Weibel, E., Tunneling through a Controllable Vacuum Gap. *Appl. Phys. Lett.* 1982, 40, 178-180.
37. Binnig, G.; Rohrer, H.; Gerber, C.; Weibel, E., 7x7 Reconstruction on Si(111) Resolved in Real Space. *Phys. Rev. Lett.* 1983, 50, 120-123.
38. Vickerman, J. C.; Gilmore, I. S.; Gilmore, I., *Surface Analysis: The Principal Techniques*. Wiley: 2009.
39. Castell, M., Scanning Tunneling Microscopy of Surfaces and Nanostructures. In *Nanocharacterisation*, Royal Society of Chemistry: 2007; pp 66-93
40. Gerber, C.; Lang, H. P., How the Doors to the Nanoworld Were Opened. *Nature Nanotechnol.* 2006, 1, 3-5.
41. Diebold, U.; Anderson, J. F.; Ng, K. O.; Vanderbilt, D., Evidence for the Tunneling Site on Transition-Metal Oxides: Tio2(110). *Phys. Rev. Lett.* 1996, 77, 1322-1325.
42. Goodhew, P. J.; Humphreys, F. J.; Beanland, R., *Electron Microscopy and Analysis*. Taylor & Francis: 2001.
43. Dresselhaus, M. S.; Dresselhaus, G.; Saito, R.; Jorio, A., Raman Spectroscopy of Carbon Nanotubes. *Phys. Rep.* 2005, 409, 47-99.
44. Dresselhaus, M. S.; Dresselhaus, G.; Jorio, A.; Souza, A. G.; Saito, R., Raman Spectroscopy on Isolated Single Wall Carbon Nanotubes. *Carbon* 2002, 40, 2043-2061.
45. Kasuya, A.; Sasaki, Y.; Saito, Y.; Tohji, K.; Nishina, Y., Evidence for Size-Dependent Discrete Dispersions in Single-Wall Nanotubes. *Phys. Rev. Lett.* 1997, 78, 4434-4437.
46. Conroy, M.; Mansfield, D., Scanning Interferometry Measuring Microscale Devices. *Nat. Photonics* 2008, 2, 661-663.
47. *Instructions: Omniscan Microxam 5000b 3d Ade Phase Shift Interference*

Contrast Optical Profiler Olympus Ltd 2006.
48. Dupuis, A. C., The Catalyst in the Catalytic Chemical Vapour Deposition of Carbon Nanotubes - a Review. *Prog. Mater. Sci.* 2005, 50, 929-961.
49. Grobert, N., Carbon Nanotubes - Becoming Clean. *Mater. Today* 2007, 10, 28-35.
50. Binnig, G.; Quate, C. F.; Gerber, C., Atomic Force Microscope. *Phys. Rev. Lett.* 1986, 56, 930-933.
51. Wu, C. *Elemental Growth of Oxide Thin Films*. D. Phil. Thesis, University of Oxford, Oxford, 2010.
52. Russell, B. C. *The Polar Surfaces of Strontium Titanate* D. Phil. Thesis, University of Oxford, Oxford, 2008.
53. Newell, D. T. *The Surface Structure and Reconstructions of Strontium Titanate (001)*. D. Phil. Thesis, University of Oxford, Oxford, 2007.
54. *Instructions: Jspm-4500xt Ultrahigh Vacuum Scanning Tunneling Microscope*. JEOL Ltd.: 1991.
55. Koos, A. A.; Dowling, M.; Jurkschat, K.; Crossley, A.; Grobert, N., Effect of the Experimental Parameters on the Structure of Nitrogen-Doped Carbon Nanotubes Produced by Aerosol Chemical Vapour Deposition. *Carbon* 2009, 47, 30-37.
56. Kawasaki, M.; Takahashi, K.; Maeda, T.; Tsuchiya, R.; Shinohara, M.; Ishiyama, O.; Yonezawa, T.; Yoshimoto, M.; Koinuma, H., Atomic Control of the Strontium Titanate Crystal Surface. *Science* 1994, 266, 1540-1542.
57. Jorio, A.; Dresselhaus, G.; Dresselhaus, M. S., *Carbon Nanotubes. Advanced Topics in the Synthesis, Structure, Properties and Applications*. Springer: 2008.
58. Ajayan, P. M., Nanotubes from Carbon. *Chem. Rev.* 1999, 99, 1787-1800.
59. Dai, H., Carbon Nanotubes: Synthesis, Integration, and Properties. *Acc. Chem. Res.* 2002, 35, 1035-1044.
60. Dai, H. J.; Kong, J.; Zhou, C. W.; Franklin, N.; Tombler, T.; Cassell, A.; Fan, S. S.; Chapline, M., Controlled Chemical Routes to Nanotube Architectures, Physics, and Devices. *J. Phys. Chem. B* 1999, 103, 11246-11255.
61. Vairavapandian, D.; Vichchulada, P.; Lay, M. D., Preparation and Modification of Carbon Nanotubes: Review of Recent Advances and Applications in Catalysis and Sensing. *Anal. Chim. Acta* 2008, 626, 119-129.
62. Zhou, O.; Shimoda, H.; Gao, B.; Oh, S.; Fleming, L.; Yue, G., Materials Science of Carbon Nanotubes: Fabrication, Integration, and Properties of Macroscopic Structures of Carbon Nanotubes. *Acc. Chem. Res.* 2002, 35, 1045-1053.
63. Zhang, Q.; Huang, J.-Q.; Zhao, M.-Q.; Qian, W.-Z.; Wei, F., Carbon Nanotube Mass Production: Principles and Processes. *ChemSusChem* 2011, 4, 864-889.
64. Kumar, M.; Ando, Y., Chemical Vapor Deposition of Carbon Nanotubes: A Review on Growth Mechanism and Mass Production. *J. Nanosci. Nanotechnol.* 2010, 10, 3739-3758.
65. Hayamizu, Y.; Yamada, T.; Mizuno, K.; Davis, R. C.; Futaba, D. N.; Yumura, M.; Hata, K., Integrated Three-Dimensional Microelectromechanical Devices

from Processable Carbon Nanotube Wafers. *Nature Nanotechnol.* 2008, 3, 289-294.

66. Qu, L. T.; Du, F.; Dai, L. M., Preferential Syntheses of Semiconducting Vertically Aligned Single-Walled Carbon Nanotubes for Direct Use in Field Effect Transistors. *Nano Lett.* 2008, 8, 2682-2687.
67. Fan, S.; Chapline, M. G.; Franklin, N. R.; Tombler, T. W.; Cassell, A. M.; Dai, H., Self-Oriented Regular Arrays of Carbon Nanotubes and Their Field Emission Properties. *Science* 1999, 283, 512-514.
68. Cheng, Q. F.; Wang, J. P.; Wen, J. J.; Liu, C. H.; Jiang, K. L.; Li, Q. Q.; Fan, S. S., Carbon Nanotube/Epoxy Composites Fabricated by Resin Transfer Molding. *Carbon* 2010, 48, 260-266.
69. Otieno, G.; Koos, A. A.; Dillon, F.; Wallwork, A.; Grobert, N.; Todd, R. I., Processing and Properties of Aligned Multi-Walled Carbon Nanotube/Aluminoborosilicate Glass Composites Made by Sol-Gel Processing. *Carbon* 2010, 48, 2212-2217.
70. Dai, H. J.; Hafner, J. H.; Rinzler, A. G.; Colbert, D. T.; Smalley, R. E., Nanotubes as Nanoprobes in Scanning Probe Microscopy. *Nature* 1996, 384, 147-150.
71. Hafner, J. H.; Cheung, C.-L.; Oosterkamp, T. H.; Lieber, C. M., High-Yield Assembly of Individual Single-Walled Carbon Nanotube Tips for Scanning Probe Microscopies. *J. Phys. Chem. B* 2001, 105, 743-746.
72. Ye, Q.; Cassell, A. M.; Liu, H. B.; Chao, K. J.; Han, J.; Meyyappan, M., Large-Scale Fabrication of Carbon Nanotube Probe Tips for Atomic Force Microscopy Critical Dimension Imaging Applications. *Nano Lett.* 2004, 4, 1301-1308.
73. Kong, J.; Franklin, N. R.; Zhou, C.; Chapline, M. G.; Peng, S.; Cho, K.; Dai, H., Nanotube Molecular Wires as Chemical Sensors. *Science* 2000, 287, 622-625.
74. Stampfer, C.; Helbling, T.; Obergfell, D.; Schoberle, B.; Tripp, M. K.; Jungen, A.; Roth, S.; Bright, V. M.; Hierold, C., Fabrication of Single-Walled Carbon-Nanotube-Based Pressure Sensors. *Nano Lett.* 2006, 6, 233-237.
75. Graham, A. P.; Duesberg, G. S.; Hoenlein, W.; Kreupl, F.; Liebau, M.; Martin, R.; Rajasekharan, B.; Pamler, W.; Seidel, R.; Steinhoegl, W.; Unger, E., How Do Carbon Nanotubes Fit into the Semiconductor Roadmap? *Appl. Phys. A-Mater. Sci. Process.* 2005, 80, 1141-1151.
76. Iijima, S.; Ichihashi, T., Single-Shell Carbon Nanotubes of 1-Nm Diameter. *Nature* 1993, 363, 603-605.
77. Nessim, G. D., Properties, Synthesis, and Growth Mechanisms of Carbon Nanotubes with Special Focus on Thermal Chemical Vapor Deposition. *Nanoscale* 2010, 2, 1306-1323.
78. Zhang, M.; Li, J., Carbon Nanotube in Different Shapes. *Mater. Today* 2009, 12, 12-18.
79. Amelinckx, S.; Zhang, X. B.; Bernaerts, D.; Zhang, X. F.; Ivanov, V.; Nagy, J. B., A Formation Mechanism for Catalytically Grown Helix-Shaped Graphite Nanotubes. *Science* 1994, 265, 635-637.

80. Dunlap, B. I., Connecting Carbon Tubules. *Phys. Rev. B* 1992, 46, 1933-1936.
81. Dunlap, B. I., Relating Carbon Tubules. *Phys. Rev. B* 1994, 49, 5643-5650.
82. Ihara, S.; Itoh, S., Helically Coiled and Toroidal Cage Forms of Graphitic Carbon. *Carbon* 1995, 33, 931-939.
83. Ebbesen, T. W.; Ajayan, P. M., Large-Scale Synthesis of Carbon Nanotubes. *Nature* 1992, 358, 220-222.
84. Guo, T.; Nikolaev, P.; Thess, A.; Colbert, D. T.; Smalley, R. E., Catalytic Growth of Single-Walled Nanotubes by Laser Vaporization. *Chem. Phys. Lett.* 1995, 243, 49-54.
85. Endo, M.; Takeuchi, K.; Igarashi, S.; Kobori, K.; Shiraishi, M.; Kroto, H. W., The Production and Structure of Pyrolytic Carbon Nanotubes. *J. Phys. Chem. Solids* 1993, 54, 1841-1848.
86. Meyyappan, M.; Delzeit, L.; Cassell, A.; Hash, D., Carbon Nanotube Growth by Pecvd: A Review. *Plasma Sources Sci. Technol.* 2003, 12, 205-216.
87. Lee, S.; Choi, S.; Park, K. H.; Chae, K. W.; Cho, J. B.; Ahn, Y.; Park, J.-Y.; Koh, K. H., Hot-Filament Cvd Synthesis and Application of Carbon Nanostructures. *Thin Solid Films* 2008, 516, 700-705.
88. Choi, H. C.; Kim, W.; Wang, D. W.; Dai, H. J., Delivery of Catalytic Metal Species onto Surfaces with Dendrimer Carriers for the Synthesis of Carbon Nanotubes with Narrow Diameter Distribution. *J. Phys. Chem. B* 2002, 106, 12361-12365.
89. Kong, J.; Cassell, A. M.; Dai, H., Chemical Vapor Deposition of Methane for Single-Walled Carbon Nanotubes. *Chem. Phys. Lett.* 1998, 292, 567-574.
90. Lee, C. J.; Park, J.; Yu, J. A., Catalyst Effect on Carbon Nanotubes Synthesized by Thermal Chemical Vapor Deposition. *Chem. Phys. Lett.* 2002, 360, 250-255.
91. Li, Y. M.; Kim, W.; Zhang, Y. G.; Rolandi, M.; Wang, D. W.; Dai, H. J., Growth of Single-Walled Carbon Nanotubes from Discrete Catalytic Nanoparticles of Various Sizes. *J. Phys. Chem. B* 2001, 105, 11424-11431.
92. Rümmeli, M. H.; Bachmatiuk, A.; Bo̎rrnert, F.; Schäffel, F.; Ibrahim, I.; Cendrowski, K.; Simha-Martynkova, G.; Placha, D.; Borowiak-Palen, E.; Cuniberti, G.; Büchner, B., Synthesis of Carbon Nanotubes with and without Catalyst Particles. *Nanoscale Res. Lett* 2011, 6, 303.
93. Murakami, Y.; Chiashi, S.; Miyauchi, Y.; Hu, M. H.; Ogura, M.; Okubo, T.; Maruyama, S., Growth of Vertically Aligned Single-Walled Carbon Nanotube Films on Quartz Substrates and Their Optical Anisotropy. *Chem. Phys. Lett.* 2004, 385, 298-303.
94. Wirth, C. T.; Zhang, C.; Zhong, G. F.; Hofmann, S.; Robertson, J., Diffusion- and Reaction-Limited Growth of Carbon Nanotube Forests. *Acs Nano* 2009, 3, 3560-3566.
95. Bayer, B. C.; Hofmann, S.; Castellarin-Cudia, C.; Blume, R.; Baehtz, C.; Esconjauregui, S.; Wirth, C. T.; Oliver, R. A.; Ducati, C.; Knop-Gericke, A.; Schlogl, R.; Goldoni, A.; Cepek, C.; Robertson, J., Support-Catalyst-Gas Interactions During Carbon Nanotube Growth on Metallic Ta Films. *J. Phys. Chem. C* 2011, 115, 4359-4369.

96. Plata, D. L.; Meshot, E. R.; Reddy, C. M.; Hart, A. J.; Gschwend, P. M., Multiple Alkynes React with Ethylene to Enhance Carbon Nanotube Synthesis, Suggesting a Polymerization-Like Formation Mechanism. *Acs Nano* 2010, 4, 7185-7192.
97. Nessim, G. D.; Seita, M.; Plata, D. L.; O'Brien, K. P.; Hart, A. J.; Meshot, E. R.; Reddy, C. M.; Gschwend, P. M.; Thompson, C. V., Precursor Gas Chemistry Determines the Crystallinity of Carbon Nanotubes Synthesized at Low Temperature. *Carbon* 2011, 49, 804-810.
98. Siegal, M. P.; Overmyer, D. L.; Provencio, P. P.; Tallant, D. R., Linear Behavior of Carbon Nanotube Diameters with Growth Temperature. *J. Phys. Chem. C* 2010, 114, 14864-14867.
99. Zhao, Y. L.; Huang, D. X.; Saito, Y., A Temperature Window for Ethanol Chemical Vapor Deposition of a Carbon Nanotube Array Catalyzed by Co Particles. *Nanotechnology* 2007, 18, 445608.
100. Lacerda, R. G.; Teo, K. B. K.; Teh, A. S.; Yang, M. H.; Dalal, S. H.; Jefferson, D. A.; Durrell, J. H.; Rupesinghe, N. L.; Roy, D.; Amaratunga, G. A. J.; Milne, W. I.; Wyczisk, F.; Legagneux, P.; Chhowalla, M., Thin-Film Metal Catalyst for the Production of Multi-Wall and Single-Wall Carbon Nanotubes. *J. Appl. Phys.* 2004, 96, 4456-4462.
101. Homma, Y.; Kobayashi, Y.; Ogino, T.; Takagi, D.; Ito, R.; Jung, Y. J.; Ajayan, P. M., Role of Transition Metal Catalysts in Single-Walled Carbon Nanotube Growth in Chemical Vapor Deposition. *J. Phys. Chem. B* 2003, 107, 12161-12164.
102. Seidel, R.; Duesberg, G. S.; Unger, E.; Graham, A. P.; Liebau, M.; Kreupl, F., Chemical Vapor Deposition Growth of Single-Walled Carbon Nanotubes at 600°C and a Simple Growth Model. *J. Phys. Chem. B* 2004, 108, 1888-1893.
103. Kayastha, V. K.; Yap, Y. K.; Pan, Z.; Ivanov, I. N.; Puretzky, A. A.; Geohegan, D. B., High-Density Vertically Aligned Multiwalled Carbon Nanotubes with Tubular Structures. *Appl. Phys. Lett.* 2005, 86, 253105.
104. Liu, Q.; Cui, Z.-M.; Ma, Z.; Bian, S.-W.; Song, W.-G., Carbon Materials with Unusual Morphologies and Their Formation Mechanism. *J. Phys. Chem. C* 2007, 111, 12420-12424.
105. Nessim, G. D.; Seita, M.; O'Brien, K. P.; Hart, A. J.; Bonaparte, R. K.; Mitchell, R. R.; Thompson, C. V., Low Temperature Synthesis of Vertically Aligned Carbon Nanotubes with Electrical Contact to Metallic Substrates Enabled by Thermal Decomposition of the Carbon Feedstock. *Nano Lett.* 2009, 9, 3398-3405.
106. Mora, E.; Pigos, J. M.; Ding, F.; Yakobson, B. I.; Harutyunyan, A. R., Low-Temperature Single-Wall Carbon Nanotubes Synthesis: Feedstock Decomposition Limited Growth. *J. Am. Chem. Soc.* 2008, 130, 11840-11841.
107. Bae, E. J.; Min, Y. S.; Kang, D.; Ko, J. H.; Park, W., Low-Temperature Growth of Single-Walled Carbon Nanotubes by Plasma Enhanced Chemical Vapor Deposition. *Chem. Mater.* 2005, 17, 5141-5145.
108. Kong, J.; Soh, H. T.; Cassell, A. M.; Quate, C. F.; Dai, H., Synthesis of

Individual Single-Walled Carbon Nanotubes on Patterned Silicon Wafers. *Nature* 1998, 395, 878-881.
109. Mizuno, K.; Hata, K.; Saito, T.; Ohshima, S.; Yumura, M.; Iijima, S., Selective Matching of Catalyst Element and Carbon Source in Single-Walled Carbon Nanotube Synthesis on Silicon Substrates. *J. Phys. Chem. B* 2005, 109, 2632-2637.
110. Meshot, E. R.; Plata, D. L.; Tawfick, S.; Zhang, Y.; Verploegen, E. A.; Hart, A. J., Engineering Vertically Aligned Carbon Nanotube Growth by Decoupled Thermal Treatment of Precursor and Catalyst. *Acs Nano* 2009, 3, 2477-2486.
111. Jian, X. A.; Jiang, M.; Zhou, Z. W.; Yang, M. L.; Lu, J.; Hu, S. C.; Wang, Y.; Hui, D., Preparation of High Purity Helical Carbon Nanofibers by the Catalytic Decomposition of Acetylene and Their Growth Mechanism. *Carbon* 2010, 48, 4535-4541.
112. Qi, X. S.; Zhong, W.; Deng, Y.; Au, C. T.; Du, Y. W., Characterization and Magnetic Properties of Helical Carbon Nanotubes and Carbon Nanobelts Synthesized in Acetylene Decomposition over Fe-Cu Nanoparticles at 450 Degrees C. *J. Phys. Chem. C* 2009, 113, 15934-15940.
113. Qin, Y.; Jiang, X.; Cui, Z. L., Low-Temperature Synthesis of Amorphous Carbon Nanocoils Via Acetylene Coupling on Copper Nanocrystal Surfaces at 468 K: A Reaction Mechanism Analysis. *J. Phys. Chem. B* 2005, 109, 21749-21754.
114. Qin, Y.; Li, H.; Zhang, Z. K.; Cui, Z. L., Symmetric and Helical Growth of Polyacetylene Fibers over a Single Copper Crystal Derived from Copper Tartrate Decomposition. *Org. Lett.* 2002, 4, 3123-3125.
115. Shaikjee, A.; Franklyn, P. J.; Coville, N. J., The Use of Transmission Electron Microscopy Tomography to Correlate Copper Catalyst Particle Morphology with Carbon Fiber Morphology. *Carbon* 2011, 49, 2950-2959.
116. Yu, L. Y.; Qin, Y.; Sui, L.; Zhang, Q.; Cui, Z. L., Two Opposite Growth Modes of Carbon Nanofibers Prepared by Catalytic Decomposition of Acetylene at Low Temperature. *J. Mater. Sci.* 2008, 43, 883-886.
117. Zhang, Q.; Yu, L.; Cui, Z., Effects of the Size of Nano-Copper Catalysts and Reaction Temperature on the Morphology of Carbon Fibers. *Mater. Res. Bull.* 2008, 43, 735-742.
118. Maruyama, S.; Kojima, R.; Miyauchi, Y.; Chiashi, S.; Kohno, M., Low-Temperature Synthesis of High-Purity Single-Walled Carbon Nanotubes from Alcohol. *Chem. Phys. Lett.* 2002, 360, 229-234.
119. Zhan, Z.-Y.; Zhang, Y.-N.; Sun, G.-Z.; Zheng, L.-X.; Liao, K., The Effects of Catalyst Treatment on Fast Growth of Millimeter-Long Multi-Walled Carbon Nanotube Arrays. *Appl. Surf. Sci.* 2011, 257, 7704-7708.
120. de los Arcos, T.; Oelhafen, P.; Thommen, V.; Mathys, D., The Influence of Catalyst's Oxidation Degree on Carbon Nanotube Growth as a Substrate-Independent Parameter. *J. Phys. Chem. C* 2007, 111, 16392-16396.
121. Dijon, J.; Szkutnik, P. D.; Fournier, A.; de Monsabert, T. G.; Okuno, H.; Quesnel, E.; Muffato, V.; De Vito, E.; Bendiab, N.; Bogner, A.; Bernier, N.,

How to Switch from a Tip to Base Growth Mechanism in Carbon Nanotube Growth by Catalytic Chemical Vapour Deposition. *Carbon* 2010, 48, 3953-3963.

122. Esconjauregui, S.; Fouquet, M.; Bayer, B. C.; Eslava, S.; Khachadorian, S.; Hofmann, S.; Robertson, J., Manipulation of the Catalyst-Support Interactions for Inducing Nanotube Forest Growth. *J. Appl. Phys.* 2011, 109, 044303.
123. Geissler, A.; He, M. S. A.; Benoit, J. M.; Petit, P., Effect of Hydrogen Pressure on the Size of Nickel Nanoparticles Formed During Dewetting and Reduction of Thin Nickel Films. *J. Phys. Chem. C* 2010, 114, 89-92.
124. Joshi, R.; Schneider, J. J.; Yilmazoglu, O.; Pavlidis, D., Patterned Growth of Ultra Long Carbon Nanotubes. Properties and Systematic Investigation into Their Growth Process. *J. Mater. Chem.* 2010, 20, 1717-1721.
125. Nessim, G. D.; Hart, A. J.; Kim, J. S.; Acquaviva, D.; Oh, J. H.; Morgan, C. D.; Seita, M.; Leib, J. S.; Thompson, C. V., Tuning of Vertically-Aligned Carbon Nanotube Diameter and Areal Density through Catalyst Pre-Treatment. *Nano Lett.* 2008, 8, 3587-3593.
126. Nishiyama, Y.; Tamai, Y., Effect of Hydrogen on Carbon Deposition Catalyzed by Copper-Nickel-Alloys. *J. Catal.* 1976, 45, 1-5.
127. Esconjauregui, S.; Fouquet, M.; Bayer, B.; Robertson, J., Carbon Nanotubes Growth: From Entanglement to Vertical Alignment. *Phys. Status Solidi B* 2010, 247, 2656-2659.
128. He, M.; Chernov, A. I.; Obraztsova, E. D.; Sainio, J.; Rikkinen, E.; Jiang, H.; Zhu, Z.; Kaskela, A.; Nasibulin, A. G.; Kauppinen, E. I.; Niemela, M.; Krause, O., Low Temperature Growth of Swnts on a Nickel Catalyst by Thermal Chemical Vapor Deposition. *Nano Res.* 2011, 4, 334-342.
129. Zhang, Y.; Gregoire, J. M.; van Dover, R. B.; Hart, A. J., Ethanol-Promoted High-Yield Growth of Few-Walled Carbon Nanotubes. *J. Phys. Chem. C* 2010, 114, 6389-6395.
130. Zhang, G. Y.; Mann, D.; Zhang, L.; Javey, A.; Li, Y. M.; Yenilmez, E.; Wang, Q.; McVittie, J. P.; Nishi, Y.; Gibbons, J.; Dai, H. J., Ultra-High-Yield Growth of Vertical Single-Walled Carbon Nanotubes: Hidden Roles of Hydrogen and Oxygen. *Proc. Natl. Acad. Sci. U. S. A.* 2005, 102, 16141-16145.
131. Wen, Q.; Qian, W. Z.; Wei, F.; Ning, G. Q., Oxygen-Assisted Synthesis of Swnts from Methane Decomposition. *Nanotechnology* 2007, 18, 7.
132. Zhao, B.; Futaba, D. N.; Yasuda, S.; Akoshima, M.; Yamada, T.; Hata, K., Exploring Advantages of Diverse Carbon Nanotube Forests with Tailored Structures Synthesized by Supergrowth from Engineered Catalysts. *Acs Nano* 2009, 3, 108-114.
133. Nishino, H.; Yasuda, S.; Namai, T.; Futaba, D. N.; Yamada, T.; Yumura, M.; Iijima, S.; Hata, K., Water-Assisted Highly Efficient Synthesis of Single-Walled Carbon Nanotubes Forests from Colloidal Nanoparticle Catalysts. *J. Phys. Chem. C* 2007, 111, 17961-17965.
134. Futaba, D. N.; Hata, K.; Yamada, T.; Mizuno, K.; Yumura, M.; Iijima, S., Kinetics of Water-Assisted Single-Walled Carbon Nanotube Synthesis

Revealed by a Time-Evolution Analysis. *Phys. Rev. Lett.* 2005, 95, 4.
135. Futaba, D. N.; Hata, K.; Namai, T.; Yamada, T.; Mizuno, K.; Hayamizu, Y.; Yumura, M.; Iijima, S., 84% Catalyst Activity of Water-Assisted Growth of Single Walled Carbon Nanotube Forest Characterization by a Statistical and Macroscopic Approach. *J. Phys. Chem. B* 2006, 110, 8035-8038.
136. Yun, Y. H.; Shanov, V.; Tu, Y.; Subramaniam, S.; Schulz, M. J., Growth Mechanism of Long Aligned Multiwall Carbon Nanotube Arrays by Water-Assisted Chemical Vapor Deposition. *J. Phys. Chem. B* 2006, 110, 23920-23925.
137. Yamada, T.; Maigne, A.; Yudasaka, M.; Mizuno, K.; Futaba, D. N.; Yumura, M.; Iijima, S.; Hata, K., Revealing the Secret of Water-Assisted Carbon Nanotube Synthesis by Microscopic Observation of the Interaction of Water on the Catalysts. *Nano Lett.* 2008, 8, 4288-4292.
138. Hasegawa, K.; Noda, S., Millimeter-Tall Single-Walled Carbon Nanotubes Rapidly Grown with and without Water. *Acs Nano* 2011, 5, 975-984.
139. Amama, P. B.; Pint, C. L.; McJilton, L.; Kim, S. M.; Stach, E. A.; Murray, P. T.; Hauge, R. H.; Maruyama, B., Role of Water in Super Growth of Single-Walled Carbon Nanotube Carpets. *Nano Lett.* 2009, 9, 44-49.
140. Nasibulin, A. G.; Brown, D. P.; Queipo, P.; Gonzalez, D.; Jiang, H.; Kauppinen, E. I., An Essential Role of Co2 and H2o During Single-Walled Cnt Synthesis from Carbon Monoxide. *Chem. Phys. Lett.* 2006, 417, 179-184.
141. Magrez, A.; Seo, J. W.; Smajda, R.; Korbely, B.; Andresen, J. C.; Mionic, M.; Casimirius, S.; Forro, L., Low-Temperature, Highly Efficient Growth of Carbon Nanotubes on Functional Materials by an Oxidative Dehydrogenation Reaction. *Acs Nano* 2010, 4, 3702-3708.
142. Magrez, A.; Seo, J. W.; Kuznetsov, V. L.; Forro, L., Evidence of an Equimolar C2h2-Co2 Reaction in the Synthesis of Carbon Nanotubes. *Angew. Chem. Int. Edit.* 2007, 46, 441-444.
143. Huang, J.; Zhang, Q.; Zhao, M.; Wei, F., Process Intensification by Co(2) for High Quality Carbon Nanotube Forest Growth: Double-Walled Carbon Nanotube Convexity or Single-Walled Carbon Nanotube Bowls? *Nano Res.* 2009, 2, 872-881.
144. Futaba, D. N.; Goto, J.; Yasuda, S.; Yamada, T.; Yumura, M.; Hata, K., General Rules Governing the Highly Efficient Growth of Carbon Nanotubes. *Adv. Mater.* 2009, 21, 1-5.
145. Futaba, D. N.; Goto, J.; Yasuda, S.; Yamada, T.; Yumura, M.; Hata, K., A Background Level of Oxygen-Containing Aromatics for Synthetic Control of Carbon Nanotube Structure. *J. Am. Chem. Soc.* 2009, 131, 15992-3.
146. Zhou, W. W.; Ding, L.; Liu, J., Role of Catalysts in the Surface Synthesis of Single-Walled Carbon Nanotubes. *Nano Res.* 2009, 2, 593-598.
147. Ding, F.; Larsson, P.; Larsson, J. A.; Ahuja, R.; Duan, H. M.; Rosen, A.; Bolton, K., The Importance of Strong Carbon-Metal Adhesion for Catalytic Nucleation of Single-Walled Carbon Nanotubes. *Nano Lett.* 2008, 8, 463-468.
148. Moisala, A.; Nasibulin, A. G.; Kauppinen, E. I., The Role of Metal

Nanoparticles in the Catalytic Production of Single-Walled Carbon Nanotubes - a Review. *J. Phys.-Condes. Matter* 2003, 15, S3011-S3035.
149. Laurent, C.; Flahaut, E.; Peigney, A.; Rousset, A., Metal Nanoparticles for the Catalytic Synthesis of Carbon Nanotubes. *New. J. Chem.* 1998, 22, 1229-1237.
150. Ayre, G. N.; Uchino, T.; Mazumder, B.; Hector, A. L.; Hutchison, J. L.; Smith, D. C.; Ashburn, P.; de Groot, C. H., On the Mechanism of Carbon Nanotube Formation: The Role of the Catalyst. *J. Phys.-Condes. Matter* 2011, 23, 394201.
151. Huang, Z. P.; Wang, D. Z.; Wen, J. G.; Sennett, M.; Gibson, H.; Ren, Z. F., Effect of Nickel, Iron and Cobalt on Growth of Aligned Carbon Nanotubes. *Appl. Phys. A-Mater. Sci. Process.* 2002, 74, 387-391.
152. Crouse, C. A.; Maruyama, B.; Colorado Jr, R.; Back, T.; Barron, A. R., Growth, New Growth, and Amplification of Carbon Nanotubes as a Function of Catalyst Composition. *J. Am. Chem. Soc.* 2008, 130, 7946-7954.
153. Huang, S.; Woodson, M.; Smalley, R.; Liu, J., Growth Mechanism of Oriented Long Single Walled Carbon Nanotubes Using 'Fast-Heating' Chemical Vapor Deposition Process. *Nano Lett.* 2004, 4, 1025-1028.
154. Schaffel, F.; Schunemann, C.; Rummeli, M. H.; Taschner, C.; Pohl, D.; Kramberger, C.; Gemming, T.; Leonhardt, A.; Pichler, T.; Rellinghaus, B.; Buchner, B.; Schultz, L., Comparative Study on Thermal and Plasma Enhanced Cvd Grown Carbon Nanotubes from Gas Phase Prepared Elemental and Binary Catalyst Particles. *Phys. Status Solidi B* 2008, 245, 1919-1922.
155. Schaffel, F.; Taschner, C.; Rummeli, M. H.; Neu, V.; Wolff, U.; Queitsch, U.; Pohl, D.; Kaltofen, R.; Leonhardt, A.; Rellinghaus, B.; Buchner, B.; Schultz, L., Carbon Nanotubes Terminated with Hard Magnetic Fept Nanomagnets. *Appl. Phys. Lett.* 2009, 94, 3.
156. Wang, X.; Yue, W. B.; He, M. S.; Liu, M. H.; Zhang, J.; Liu, Z. F., Bimetallic Catalysts for the Efficient Growth of Swnts on Surfaces. *Chem. Mater.* 2004, 16, 799-805.
157. Tang, S.; Zhong, Z.; Xiong, Z.; Sun, L.; Liu, L.; Lin, J.; Shen, Z. X.; Tan, K. L., Controlled Growth of Single-Walled Carbon Nanotubes by Catalytic Decomposition of Ch4 over Mo/Co/Mgo Catalysts. *Chem. Phys. Lett.* 2001, 350, 19-26.
158. Bachilo, S. M.; Balzano, L.; Herrera, J. E.; Pompeo, F.; Resasco, D. E.; Weisman, R. B., Narrow (N,M)-Distribution of Single-Walled Carbon Nanotubes Grown Using a Solid Supported Catalyst. *J. Am. Chem. Soc.* 2003, 125, 11186-11187.
159. Lolli, G.; Zhang, L. A.; Balzano, L.; Sakulchaicharoen, N.; Tan, Y. Q.; Resasco, D. E., Tailoring (N,M) Structure of Single-Walled Carbon Nanotubes by Modifying Reaction Conditions and the Nature of the Support of Como Catalysts. *J. Phys. Chem. B* 2006, 110, 2108-2115.
160. Wang, B.; Yang, Y.; Li, L. J.; Chen, Y., Effect of Different Catalyst Supports on the (N,M) Selective Growth of Single-Walled Carbon Nanotube from Co-Mo Catalyst. *J. Mater. Sci.* 2009, 44, 3285-3295.

161. Bhaviripudi, S.; Mile, E.; Steiner, S. A.; Zare, A. T.; Dresselhaus, M. S.; Belcher, A. M.; Kong, J., Chemical Vapour Deposition Synthesis of Single-Walled Carbon Nanotubes from Gold Nanoparticle Catalysts. *J. Am. Chem. Soc.* 2007, 129, 1516-1517.
162. Takagi, D.; Homma, Y.; Hibino, H.; Suzuki, S.; Kobayashi, Y., Single-Walled Carbon Nanotube Growth from Highly Activated Metal Nanoparticles. *Nano Lett.* 2006, 6, 2642-2645.
163. Takagi, D.; Kobayashi, Y.; Hlbirio, H.; Suzuki, S.; Homma, Y., Mechanism of Gold-Catalyzed Carbon Material Growth. *Nano Lett.* 2008, 8, 832-835.
164. Yuan, D. N.; Ding, L.; Chu, H. B.; Feng, Y. Y.; McNicholas, T. P.; Liu, J., Horizontally Aligned Single-Walled Carbon Nanotube on Quartz from a Large Variety of Metal Catalysts. *Nano Lett.* 2008, 8, 2576-2579.
165. Cui, R. L.; Zhang, Y.; Wang, J. Y.; Zhou, W. W.; Li, Y., Comparison between Copper and Iron as Catalyst for Chemical Vapor Deposition of Horizontally Aligned Ultralong Single-Walled Carbon Nanotubes on Silicon Substrates. *J. Phys. Chem. C* 2010, 114, 15547-15552.
166. Zhou, W. W.; Han, Z. Y.; Wang, J. Y.; Zhang, Y.; Jin, Z.; Sun, X.; Zhang, Y. W.; Yan, C. H.; Li, Y., Copper Catalyzing Growth of Single-Walled Carbon Nanotubes on Substrates. *Nano Lett.* 2006, 6, 2987-2990.
167. Wong, Y. M.; Wei, S.; Kang, W. P.; Davidson, J. L.; Hofmeister, W.; Huang, J. H.; Cui, Y., Carbon Nanotubes Field Emission Devices Grown by Thermal Cvd with Palladium as Catalysts. *Diamond Relat. Mater.* 2004, 13, 2105-2112.
168. Qian, Y.; Wang, C. Y.; Ren, G. Y.; Huang, B., Surface Growth of Single-Walled Carbon Nanotubes from Ruthenium Nanoparticles. *Appl. Surf. Sci.* 2010, 256, 4038-4041.
169. Zhang, Y.; Zhou, W. W.; Jin, Z.; Ding, L.; Zhang, Z. Y.; Liang, X. I.; Li, Y., Direct Growth of Single-Walled Carbon Nanotubes without Metallic Residues by Using Lead as a Catalyst. *Chem. Mater.* 2008, 20, 7521-7525.
170. Ritschel, M.; Leonhardt, A.; Elefant, D.; Oswald, S.; Buchner, B., Rhenium-Catalyzed Growth Carbon Nanotubes. *J. Phys. Chem. C* 2007, 111, 8414-8417.
171. Wu, H. C.; Huang, C. J.; Youh, M. J.; Tseng, C. L.; Chen, H. T.; Li, Y. Y.; Sakoda, A., Thin-Walled Carbon Nanotubes Grown Using a Zirconium Catalyst. *Carbon* 2010, 48, 1897-1901.
172. Deck, C. P.; Vecchio, K., Prediction of Carbon Nanotube Growth Success by the Analysis of Carbon-Catalyst Binary Phase Diagrams. *Carbon* 2006, 44, 267-275.
173. Yazyev, O. V.; Pasquarello, A., Effect of Metal Elements in Catalytic Growth of Carbon Nanotubes. *Phys. Rev. Lett.* 2008, 100, 156102.
174. Bandaru, P. R.; Daraio, C.; Yang, K.; Rao, A. M., A Plausible Mechanism for the Evolution of Helical Forms in Nanostructure Growth. *J. Appl. Phys.* 2007, 101, 094307.
175. Okazaki, N.; Hosokawa, S.; Goto, T.; Nakayama, Y., Synthesis of Carbon Tubule Nanocoils Using Fe-in-Sn-O Fine Particles as Catalysts. *J. Phys. Chem.*

B 2005, 109, 17366-17371.
176. Pan, L. J.; Zhang, M.; Nakayama, Y., Growth Mechanism of Carbon Nanocoils. *J. Appl. Phys.* 2002, 91, 10058-10061.
177. Kanada, R.; Pan, L.; Akita, S.; Okazaki, N.; Hirahara, K.; Nakayama, Y., Synthesis of Multiwalled Carbon Nanocoils Using Codeposited Thin Film of Fe-Sn as Catalyst. *Jpn. J. Appl. Phys.* 2008, 47, 1949-1951.
178. Li, D. W.; Pan, L. J.; Liu, D. P.; Yu, N. S., Relationship between Geometric Structures of Catalyst Particles and Growth of Carbon Nanocoils. *Chem. Vapor Depos.* 2010, 16, 166-169.
179. Li, D. W.; Pan, L. J.; Qian, J. J.; Liu, D. P., Highly Efficient Synthesis of Carbon Nanocoils by Catalyst Particles Prepared by a Sol-Gel Method. *Carbon* 2010, 48, 170-175.
180. Su, C. C.; Chang, S. H., Radial Growth of Carbon Nanocoils on Stainless Steel Wires Coated with Tin Particles Using Chemical Vapor Deposition from Acetylene. *Mater. Lett.* 2011, 65, 1114-1116.
181. Hirsch, A., Growth of Single-Walled Carbon Nanotubes without a Metal Catalyst-a Surprising Discovery. *Angew. Chem. Int. Edit.* 2009, 48, 5403-5404.
182. Gohier, A.; Ewels, C. P.; Minea, T. M.; Djouadi, M. A., Carbon Nanotube Growth Mechanism Switches from Tip- to Base-Growth with Decreasing Catalyst Particle Size. *Carbon* 2008, 46, 1331-1338.
183. Lu, C. G.; Liu, J., Controlling the Diameter of Carbon Nanotubes in Chemical Vapor Deposition Method by Carbon Feeding. *J. Phys. Chem. B* 2006, 110, 20254-20257.
184. Rummeli, M. H.; Kramberger, C.; Loffler, M.; Jost, O.; Bystrzejewski, M.; Gruneis, A.; Gemming, T.; Pompe, W.; Buchner, B.; Pichler, T., Catalyst Volume to Surface Area Constraints for Nucleating Carbon Nanotubes. *J. Phys. Chem. B* 2007, 111, 8234-8241.
185. Jeong, G. H.; Yamazaki, A.; Suzuki, S.; Yoshimura, H.; Kobayashi, Y.; Homma, Y., Cobalt-Filled Apoferritin for Suspended Single-Walled Carbon Nanotube Growth with Narrow Diameter Distribution. *J. Am. Chem. Soc.* 2005, 127, 8238-8239.
186. Schäffel, F.; Kramberger, C.; Rümmeli, M. H.; Grimm, D.; Mohn, E.; Gemming, T.; Pichler, T.; Rellinghaus, B.; Büchner, B.; Schultz, L., Nanoengineered Catalyst Particles as a Key for Tailor-Made Carbon Nanotubes. *Chem. Mater.* 2007, 19, 5006-5009.
187. Jeong, G.-H.; Yamazaki, A.; Suzuki, S.; Kobayashi, Y.; Homma, Y., Behavior of Catalytic Nanoparticles During Chemical Vapor Deposition for Carbon Nanotube Growth. *Chem. Phys. Lett.* 2006, 422, 83-88.
188. Gavillet, J.; Loiseau, A.; Ducastelle, F.; Thair, S.; Bernier, P.; Stephan, O.; Thibault, J.; Charlier, J. C., Microscopic Mechanisms for the Catalyst Assisted Growth of Single-Wall Carbon Nanotubes. *Carbon* 2002, 40, 1649-1663.
189. Zhou, D.; Seraphin, S.; Wang, S., Single-Walled Carbon Nanotubes Growing Radially from Yc2 Particles. *Appl. Phys. Lett.* 1994, 65, 1593-1595.
190. Saito, T.; Ohshima, S.; Xu, W. C.; Ago, H.; Yumura, M.; Iijima, S., Size

Control of Metal Nanoparticle Catalysts for the Gas-Phase Synthesis of Single-Walled Carbon Nanotubes. *J. Phys. Chem. B* 2005, 109, 10647-10652.
191. An, L.; Owens, J. M.; McNeil, L. E.; Liu, J., Synthesis of Nearly Uniform Single-Walled Carbon Nanotubes Using Identical Metal-Containing Molecular Nanoclusters as Catalysts. *J. Am. Chem. Soc.* 2002, 124, 13688-13689.
192. Dai, H.; Rinzler, A. G.; Nikolaev, P.; Thess, A.; Colbert, D. T.; Smalley, R. E., Single-Wall Nanotubes Produced by Metal-Catalyzed Disproportionation of Carbon Monoxide. *Chem. Phys. Lett.* 1996, 260, 471-475.
193. Adhikari, A. R.; Huang, M. B.; Wu, D.; Dovidenko, K.; Wei, B. Q.; Vajtai, R.; Ajayan, P. M., Ion-Implantation-Prepared Catalyst Nanoparticles for Growth of Carbon Nanotubes. *Appl. Phys. Lett.* 2005, 86, 1-3.
194. Xia, Y.; Xiong, Y. J.; Lim, B.; Skrabalak, S. E., Shape-Controlled Synthesis of Metal Nanocrystals: Simple Chemistry Meets Complex Physics? *Angew. Chem. Int. Edit.* 2009, 48, 60-103.
195. Rummeli, M. H.; Schaffel, F.; de los Arcos, T.; Haberer, D.; Bachmatiuk, A.; Kramberger, C.; Ayala, P.; Borowiak-Palen, E.; Adebimpe, D.; Gemming, T.; Leonhardt, A.; Rellinghaus, B.; Schultz, L.; Pichler, T.; Buchner, B., On the Graphitisation Role of Oxide Supports in Carbon Nanotube Chemical Vapour Deposition Synthesis. *Phys. Status Solidi B* 2008, 245, 1939-1942.
196. Noda, S.; Hasegawa, K.; Sugime, H.; Kakehi, K.; Zhang, Z. Y.; Maruyama, S.; Yamaguchi, Y., Millimeter-Thick Single-Walled Carbon Nanotube Forests: Hidden Role of Catalyst Support. *Jpn. J. Appl. Phys. Part 2 - Lett. Express Lett.* 2007, 46, L399-L401.
197. Mattevi, C.; Wirth, C. T.; Hofmann, S.; Blume, R.; Cantoro, M.; Ducati, C.; Cepek, C.; Knop-Gericke, A.; Milne, S.; Castellarin-Cudia, C.; Dolafi, S.; Goldoni, A.; Schloegl, R.; Robertson, J., In-Situ X-Ray Photoelectron Spectroscopy Study of Catalyst-Support Interactions and Growth of Carbon Nanotube Forests. *J. Phys. Chem. C* 2008, 112, 12207-12213.
198. Amama, P. B.; Pint, C. L.; Kim, S. M.; McJilton, L.; Eyink, K. G.; Stach, E. A.; Hauge, R. H.; Maruyama, B., Influence of Alumina Type on the Evolution and Activity of Alumina-Supported Fe Catalysts in Single-Walled Carbon Nanotube Carpet Growth. *Acs Nano* 2010, 4, 895-904.
199. Nessim, G. D.; Acquaviva, D.; Seita, M.; O'Brien, K. P.; Thompson, C. V., The Critical Role of the Underlayer Material and Thickness in Growing Vertically Aligned Carbon Nanotubes and Nanofibers on Metallic Substrates by Chemical Vapor Deposition. *Adv. Funct. Mater.* 2010, 20, 1306-1312.
200. Baker, R. T. K., Catalytic Growth of Carbon Filaments. *Carbon* 1989, 27, 315-323.
201. Wang, Y.; Luo, Z.; Li, B.; Ho, P. S.; Yao, Z.; Shi, L.; Bryan, E. N.; Nemanich, R. J., Comparison Study of Catalyst Nanoparticle Formation and Carbon Nanotube Growth: Support Effect. *J. Appl. Phys.* 2007, 101, 124310.
202. Esconjauregui, S.; Whelan, C. M.; Maex, K., Carbon Nanotube Catalysis by Metal Silicide: Resolving Inhibition Versus Growth. *Nanotechnology* 2007, 18, 015602.

203. Kocabas, C.; Hur, S. H.; Gaur, A.; Meitl, M. A.; Shim, M.; Rogers, J. A., Guided Growth of Large-Scale, Horizontally Aligned Arrays of Single-Walled Carbon Nanotubes and Their Use in Thin-Film Transistors. *Small* 2005, 1, 1110-1116.
204. Jeong, S.; Oshiyama, A., Selective Alignment of Carbon Nanotubes on Sapphire Surfaces: Bond Formation between Nanotubes and Substrates. *Phys. Rev. Lett.* 2011, 107, 065501.
205. Ismach, A.; Segev, L.; Wachtel, E.; Joselevich, E., Atomic-Step-Templated Formation of Single Wall Carbon Nanotube Patterns. *Angew. Chem. Int. Edit.* 2004, 43, 6140-6143.
206. Ishigami, N.; Ago, H.; Nishi, T.; Ikeda, K. I.; Tsuji, M.; Ikuta, T.; Takahashi, K., Unidirectional Growth of Single-Walled Carbon Nanotubes. *J. Am. Chem. Soc.* 2008, 130, 17264-17265.
207. Ishigami, N.; Ago, H.; Imamoto, K.; Tsuji, M.; Iakoubovskii, K.; Minami, N., Crystal Plane Dependent Growth of Aligned Single-Walled Carbon Nanotubes on Sapphire. *J. Am. Chem. Soc.* 2008, 130, 9918-9924.
208. Hongo, H.; Yudasaka, M.; Ichihashi, T.; Nihey, F.; Iijima, S., Chemical Vapor Deposition of Single-Wall Carbon Nanotubes on Iron-Film-Coated Sapphire Substrates. *Chem. Phys. Lett.* 2002, 361, 349-354.
209. Han, S.; Liu, X. L.; Zhou, C. W., Template-Free Directional Growth of Single-Walled Carbon Nanotubes on a- and R-Plane Sapphire. *J. Am. Chem. Soc.* 2005, 127, 5294-5295.
210. Ago, H.; Nakamura, K.; Ikeda, K. I.; Uehara, N.; Ishigami, N.; Tsuji, M., Aligned Growth of Isolated Single-Walled Carbon Nanotubes Programmed by Atomic Arrangement of Substrate Surface. *Chem. Phys. Lett.* 2005, 408, 433-438.
211. Huang, S. M.; Cai, X. Y.; Liu, J., Growth of Millimeter-Long and Horizontally Aligned Single-Walled Carbon Nanotubes on Flat Substrates. *J. Am. Chem. Soc.* 2003, 125, 5636-5637.
212. Su, M.; Li, Y.; Maynor, B.; Buldum, A.; Lu, J. P.; Liu, J., Lattice-Oriented Growth of Single-Walled Carbon Nanotubes. *J. Phys. Chem. B* 2000, 104, 6505-6508.
213. Orofeo, C. M.; Ago, H.; Ikuta, T.; Takahasi, K.; Tsuji, M., Growth of Horizontally Aligned Single-Walled Carbon Nanotubes on Anisotropically Etched Silicon Substrate. *Nanoscale* 2010, 2, 1708-1714.
214. Xiong, G. Y.; Wang, D. Z.; Ren, Z. F., Aligned Millimeter-Long Carbon Nanotube Arrays Grown on Single Crystal Magnesia. *Carbon* 2006, 44, 969-973.
215. Maret, M.; Saubat, B.; Flock, J.; Mantoux, A.; Charlot, F.; Makarov, D., Horizontal Single-Walled Carbon Nanotubes on Mgo(110) and Mgo(001) Substrates. *Chem. Phys. Lett.* 2010, 495, 96-101.
216. Rümmeli, M. H.; Schäffel, F.; Kramberger, C.; Gemming, T.; Bachmatiuk, A.; Kalenczuk, R. J.; Rellinghaus, B.; Büchner, B.; Pichler, T., Oxide-Driven Carbon Nanotube Growth in Supported Catalyst Chemical Vapour Deposition.

J. Am. Chem. Soc. 2007, 129, 15772-15773.
217. Rümmeli, M. H.; Kramberger, C.; Gruneis, A.; Ayala, P.; Gemming, T.; Büchner, B.; Pichler, T., On the Graphitization Nature of Oxides for the Formation of Carbon Nanostructures. *Chem. Mater.* 2007, 19, 4105-4107.
218. Rümmeli, M. H.; Schäffel, F.; Bachmatiuk, A.; Adebimpe, D.; Trotter, G.; Borrnert, F.; Scott, A.; Coric, E.; Sparing, M.; Rellinghaus, B.; McCormick, P. G.; Cuniberti, G.; Knupfer, M.; Schultz, L.; Büchner, B., Investigating the Outskirts of Fe and Co Catalyst Particles in Alumina-Supported Catalytic Chemical Vapour Deposition Carbon Nanotube Growth. *Acs Nano* 2010, 4, 1146-1152.
219. Wirth, C. T.; Hofmann, S.; Robertson, J., State of the Catalyst During Carbon Nanotube Growth. *Diamond Relat. Mater.* 2009, 18, 940-945.
220. Baker, R. T. K.; Alonzo, J. R.; Dumesic, J. A.; Yates, D. J. C., Effect of the Surface-State of Iron on Filamentous Carbon Formation. *J. Catal.* 1982, 77, 74-84.
221. Tibbetts, G. G.; Devour, M. G.; Rodda, E. J., An Adsorption-Diffusion Isotherm and Its Application to the Growth of Carbon Filaments on Iron Catalyst Particles. *Carbon* 1987, 25, 367-375.
222. Behr, M. J.; Mkhoyan, K. A.; Aydil, E. S., Orientation and Morphological Evolution of Catalyst Nanoparticles During Carbon Nanotube Growth. *Acs Nano* 2010, 4, 5087-5094.
223. Ducati, C.; Alexandrou, I.; Chhowalla, M.; Robertson, J.; Amaratunga, G. A. J., The Role of the Catalytic Particle in the Growth of Carbon Nanotubes by Plasma Enhanced Chemical Vapor Deposition. *J. Appl. Phys.* 2004, 95, 6387-6391.
224. Oberlin, A.; Endo, M.; Koyama, T., Filamentous Growth of Carbon through Benzene Decomposition. *J. Cryst. Growth* 1976, 32, 335-349.
225. Sharma, R.; Chee, S. W.; Herzing, A.; Miranda, R.; Rez, P., Evaluation of the Role of Au in Improving Catalytic Activity of Ni Nanoparticles for the Formation of One-Dimensional Carbon Nanostructures. *Nano Lett.* 2011, 11, 2464-2471.
226. Helveg, S.; Lopez-Cartes, C.; Sehested, J.; Hansen, P. L.; Clausen, B. S.; Rostrup-Nielsen, J. R.; Abild-Pedersen, F.; Norskov, J. K., Atomic-Scale Imaging of Carbon Nanofibre Growth. *Nature* 2004, 427, 426-429.
227. Lin, M.; Tan, J. P. Y.; Boothroyd, C.; Loh, K. P.; Tok, E. S.; Foo, Y. L., Direct Observation of Single-Walled Carbon Nanotube Growth at the Atomistic Scale. *Nano Lett.* 2006, 6, 449-452.
228. Hofmann, S.; Blume, R.; Wirth, C. T.; Cantoro, M.; Sharma, R.; Ducati, C.; Haevecker, M.; Zafeiratos, S.; Schnoerch, P.; Oestereich, A.; Teschner, D.; Albrecht, M.; Knop-Gericke, A.; Schloegl, R.; Robertson, J., State of Transition Metal Catalysts During Carbon Nanotube Growth. *J. Phys. Chem. C* 2009, 113, 1648-1656.
229. Yoshida, H.; Takeda, S.; Uchiyama, T.; Kohno, H.; Homma, Y., Atomic-Scale in-Situ Observation of Carbon Nanotube Growth from Solid State Iron Carbide

Nanoparticles. *Nano Lett.* 2008, 8, 2082-2086.
230. Sharma, R.; Moore, E.; Rez, P.; Treacy, M. M. J., Site-Specific Fabrication of Fe Particles for Carbon Nanotube Growth. *Nano Lett.* 2009, 9, 689-694.
231. Feng, X.; Chee, S. W.; Sharma, R.; Liu, K.; Xie, X.; Li, Q.; Fan, S.; Jiang, K., In Situ Tem Observation of the Gasification and Growth of Carbon Nanotubes Using Iron Catalysts. *Nano Res.* 2011, 4, 767-779.
232. Ding, F.; Bolton, K.; Rosen, A., Nucleation and Growth of Single-Walled Carbon Nanotubes: A Molecular Dynamics Study. *J. Phys. Chem. B* 2004, 108, 17369-17377.
233. Tibbetts, G. G., Why Are Carbon Filaments Tubular. *J. Cryst. Growth* 1984, 66, 632-638.
234. Behr, M. J.; Mkhoyan, K. A.; Aydil, E. S., Catalyst Rotation, Twisting, and Bending During Multiwall Carbon Nanotube Growth. *Carbon* 2010, 48, 3840-3845.
235. Baker, R. T. K.; Barber, M. A.; Harris, P. S.; Feates, F. S.; Waite, R. J., Nucleation and Growth of Carbon Deposits from the Nickel Catalyzed Decomposition of Acetylene. *J. Catal.* 1972, 26, 51-62.
236. Saito, Y., Nanoparticles and Filled Nanocapsules. *Carbon* 1995, 33, 979-988.
237. Gavillet, J.; Loiseau, A.; Journet, C.; Willaime, F.; Ducastelle, F.; Charlier, J. C., Root-Growth Mechanism for Single-Wall Carbon Nanotubes. *Phys. Rev. Lett.* 2001, 87, 4.
238. Hofmann, S.; Csanyi, G.; Ferrari, A. C.; Payne, M. C.; Robertson, J., Surface Diffusion: The Low Activation Energy Path for Nanotube Growth. *Phys. Rev. Lett.* 2005, 95, 4.
239. Bartsch, K.; Biedermann, K.; Gemming, T.; Leonhardt, A., On the Diffusion-Controlled Growth of Multiwalled Carbon Nanotubes. *J. Appl. Phys.* 2005, 97, 114301.
240. Wang, Y. Y.; Gupta, S.; Nemanich, R. J.; Liu, Z. J.; Qin, L. C., Hollow to Bamboolike Internal Structure Transition Observed in Carbon Nanotube Films. *J. Appl. Phys.* 2005, 98, 014312.
241. Magrez, A.; Smajda, R.; Seo, J. W.; Horvath, E.; Ribic, P. R.; Andresen, J. C.; Acquaviva, D.; Olariu, A.; Laurenczy, G.; Forro, L., Striking Influence of the Catalyst Support and Its Acid-Base Properties: New Insight into the Growth Mechanism of Carbon Nanotubes. *Acs Nano* 2011, 5, 3428-3437.
242. Feng, H.; Ma, J.; Hu, Z., Six-Membered-Ring-Based Radical Mechanism for Catalytic Growth of Carbon Nanotubes with Benzene Precursor. *J. Phys. Chem. C* 2009, 113, 16495-16502.
243. Reilly, P. T. A.; Whitten, W. B., The Role of Free Radical Condensates in the Production of Carbon Nanotubes During the Hydrocarbon Cvd Process. *Carbon* 2006, 44, 1653-1660.
244. Liu, H.; Takagi, D.; Ohno, H.; Chiashi, S.; Chokan, T.; Homma, Y., Growth of Single-Walled Carbon Nanotubes from Ceramic Particles by Alcohol Chemical Vapor Deposition. *Appl. Phys. Express* 2008, 1, 014001.
245. Page, A. J.; Chandrakumar, K. R. S.; Irle, S.; Morokuma, K., Single-Walled

Carbon Nanotube Nucleation from Carbon-Coated Silicon Oxide Nanoparticles Via a Vapor-Solid-Solid Mechanism. *J. Am. Chem. Soc.* 2011, 133, 621-628.
246. Liu, H. P.; Takagi, D.; Chiashi, S.; Homma, Y., The Growth of Single-Walled Carbon Nanotubes on a Silica Substrate without Using a Metal Catalyst. *Carbon* 2010, 48, 114-122.
247. Bachmatiuk, A.; Borrnert, F.; Grobosch, M.; Schaffel, F.; Wolff, U.; Scott, A.; Zaka, M.; Warner, J. H.; Klingeler, R.; Knupfer, M.; Buchner, B.; Rummeli, M. H., Investigating the Graphitization Mechanism of Silica Nanoparticles in Chemical Vapor Deposition. *Acs Nano* 2009, 3, 4098-4104.
248. Gao, F.; Zhang, L.; Huang, S., Zinc Oxide Catalyzed Growth of Single-Walled Carbon Nanotubes. *Appl. Surf. Sci.* 2010, 256, 2323-2326.
249. Steiner, S. A., III; Baumann, T. F.; Bayer, B. C.; Blume, R.; Worsley, M. A.; MoberlyChan, W. J.; Shaw, E. L.; Schloegl, R.; Hart, A. J.; Hofmann, S.; Wardle, B. L., Nanoscale Zirconia as a Nonmetallic Catalyst for Graphitization of Carbon and Growth of Single- and Multiwall Carbon Nanotubes. *J. Am. Chem. Soc.* 2009, 131, 12144-12154.
250. Qian, Y.; Huang, B.; Gao, F.; Wang, C.; Ren, G., Preferential Growth of Semiconducting Single-Walled Carbon Nanotubes on Substrate by Europium Oxide. *Nanoscale Res. Lett* 2010, 5, 1578-1584.
251. Takagi, D.; Kobayashi, Y.; Homma, Y., Carbon Nanotube Growth from Diamond. *J. Am. Chem. Soc.* 2009, 131, 6922-6923.
252. Song, J.; Du, G.; Song, C.; Zhao, J.; Feng, S.; Zheng, J.; Zhu, Z., Identification and Technical Accessibility of the Carbon Self-Assembly Concept Hidden in Catalytic Carbon Nanotube Evolution. *J. Mater. Chem.* 2009, 19, 7725-7729.
253. Lin, J.-H.; Chen, C.-S.; Ma, H.-L.; Chang, C.-W.; Hsu, C.-Y.; Chen, H.-W., Self-Assembling of Multi-Walled Carbon Nanotubes on a Porous Carbon Surface by Catalyst-Free Chemical Vapor Deposition. *Carbon* 2008, 46, 1619-1623.
254. Worsley, M. A.; Stadermann, M.; Wang, Y. M.; Satcher, J. H., Jr.; Baumann, T. F., High Surface Area Carbon Aerogels as Porous Substrates for Direct Growth of Carbon Nanotubes. *Chem. Commun.* 2010, 46, 9253-9255.
255. Du, G.; Song, C.; Zhao, J.; Feng, S.; Zhu, Z., Solid-Phase Transformtion of Glass-Like Carbon Nanoparticles into, Nanotubes and the Related Mechanism. *Carbon* 2008, 46, 92-98.
256. Lin, J.-H.; Chen, C.-S.; Ruemmeli, M. H.; Zeng, Z.-Y., Self-Assembly Formation of Multi-Walled Carbon Nanotubes on Gold Surfaces. *Nanoscale* 2010, 2, 2835-2840.
257. Zhu, Z. P.; Lu, Y.; Qiao, D. H.; Bai, S. L.; Hu, T. P.; Li, L.; Zheng, J. F., Self-Catalytic Behavior of Carbon Nenotubes. *J. Am. Chem. Soc.* 2005, 127, 15698-15699.
258. Zhang, X. B.; Zhang, X. F.; Bernaerts, D.; Vantendeloo, G. T.; Amelinckx, S.; Vanlanduyt, J.; Ivanov, V.; Nagy, J. B.; Lambin, P.; Lucas, A. A., The Texture of Catalytically Grown Coil-Shaped Carbon Nanotubules. *Europhys. Lett.* 1994, 27, 141-146.

259. Hanus, M. J.; Harris, A. I., Synthesis, Characterisation and Applications of Coiled Carbon Nanotubes. *J. Nanosci. Nanotechnol.* 2010, 10, 2261-2283.
260. Hou, H.; Jun, Z.; Weller, F.; Greiner, A., Large-Scale Synthesis and Characterization of Helically Coiled Carbon Nanotubes by Use of Iron Carbonyl as Floating Catalyst Precursor. *Chem. Mater.* 2003, 15, 3170-3175.
261. Biro, L. P.; Mark, G. I.; Koos, A. A.; Nagy, J. B.; Lambin, P., Coiled Carbon Nanotube Structures with Supraunitary Nonhexagonal to Hexagonal Ring Ratio. *Phys. Rev. B* 2002, 66, 165405.
262. Qin, Y.; Zhang, Z.; Cui, Z., Helical Carbon Nanofibers with a Symmetric Growth Mode. *Carbon* 2004, 42, 1917-1922.
263. Xia, J. H.; Jiang, X.; Jia, C. L.; Dong, C., Hexahedral Nanocementites Catalyzing the Growth of Carbon Nanohelices. *Appl. Phys. Lett.* 2008, 92, 063121.
264. Yang, S.; Chen, X.; Motojima, S., Morphology of the Growth Tip of Carbon Microcoils/Nanocoils. *Diamond Relat. Mater.* 2004, 13, 2152-2155.
265. Yang, S.; Chen, X.; Kikuchi, N.; Motojima, S., Catalytic Effects of Various Metal Carbides and Ti Compounds for the Growth of Carbon Nanocoils. *Mater. Lett.* 2008, 62, 1462-1465.
266. Amama, P. B.; Pint, C. L.; Mirri, F.; Pasquali, M.; Hauge, R. H.; Maruyama, B., Catalyst-Support Interactions and Their Influence in Water-Assisted Carbon Nanotube Carpet Growth. *Carbon* 2012, 50, 2396-2406.
267. Menesklou, W.; Schreiner, H. J.; Hardtl, K. H.; Ivers-Tiffee, E., High Temperature Oxygen Sensors Based on Doped Strontium Titanate. *Sens. Actuator B-Chem.* 1999, 59, 184-189.
268. Ruiz-Morales, J. C.; Canales-Vazquez, J.; Savaniu, C.; Marrero-Lopez, D.; Zhou, W. Z.; Irvine, J. T. S., Disruption of Extended Defects in Solid Oxide Fuel Cell Anodes for Methane Oxidation. *Nature* 2006, 439, 568-571.
269. Ohtomo, A.; Hwang, H. Y., A High-Mobility Electron Gas at the Lanthanum Aluminate/Strontium Titanate Heterointerface. *Nature* 2004, 427, 423-426.
270. Marsh, H. L.; Deak, D. S.; Silly, F.; Kirkland, A. I.; Castell, M. R., Hot Scanning Tunneling Microscopy of Nanostructure Dynamics on Strontium Titanate (001). *Nanotechnology* 2006, 17, 3543-3548.
271. Gadre, K. S.; Alford, T. L., Contact Angle Measurements for Adhesion Energy Evaluation of Silver and Copper Films on Parylene-N and Sio2 Substrates. *J. Appl. Phys.* 2003, 93, 919-923.
272. Sengupta, J.; Jacob, C., The Effect of Fe and Ni Catalysts on the Growth of Multiwalled Carbon Nanotubes Using Chemical Vapor Deposition. *J. Nanopart. Res.* 2010, 12, 457-465.
273. Page, A. J.; Minami, S.; Ohta, Y.; Irle, S.; Morokuma, K., Comparison of Single-Walled Carbon Nanotube Growth from Fe and Ni Nanoparticles Using Quantum Chemical Molecular Dynamics Methods. *Carbon* 2010, 48, 3014-3026.
274. Page, A. J.; Yamane, H.; Ohta, Y.; Irle, S.; Morokuma, K., Qm/Md Simulation of Swnt Nucleation on Transition-Metal Carbide Nanoparticles. *J. Am. Chem.*

Soc. 2010, 132, 15699-15707.
275. Rummeli, M. H.; Bachmatiuk, A.; Scott, A.; Borrnert, F.; Warner, J. H.; Hoffman, V.; Lin, J. H.; Cuniberti, G.; Buchner, B., Direct Low-Temperature Nanographene Chemical Vapour Deposition Synthesis over a Dielectric Insulator. *Acs Nano* 2010, 4, 4206-4210.
276. Bachmatiuk, A.; Borrnert, F.; Hoffmann, V.; Lindackers, D.; Lin, J. H.; Buchner, B.; Rummeli, M. H., Hydrogen-Induced Self-Assembly of Helical Carbon Nanostructures from Ethanol over Silica Catalysts. *J. Appl. Phys.* 2011, 109, 094317.
277. Castell, M. R., Nanostructures on the Strontium Titanate (001) Surface Studied by Scanning Tunneling Microscopy. *Surf. Sci.* 2002, 516, 33-42.
278. Castell, M. R., Scanning Tunneling Microscopy of Reconstructions on the Strontium Titanate (001) Surface. *Surf. Sci.* 2002, 505, 1-13.
279. Deak, D. S.; Silly, F.; Newell, D. T.; Castell, M. R., Ordering of Titatium Dioxide-Based Nanostructures on Strontium Titanate (001) Surfaces. *J. Phys. Chem. B* 2006, 110, 9246-9251.
280. Rummeli, M. H.; Bachmatiuk, A.; Borrnert, F.; Schaffel, F.; Ibrahim, I.; Cendrowski, K.; Simha-Martynkova, G.; Placha, D.; Borowiak-Palen, E.; Cuniberti, G.; Buchner, B., Synthesis of Carbon Nanotubes with and without Catalyst Particles. *Nanoscale Res. Lett* 2011, 6, 303.
281. Aas, N.; Pringle, T. J.; Bowker, M., Adsorption and Decomposition of Methanol on Titanium Oxide, Strontium Titanate and Strontium Oxide. *J. Chem. Soc.-Faraday Trans.* 1994, 90, 1015-1022.
282. Swift, G. A.; Koc, R., Formation Studies of Titanium Carbide from Carbon Coated Titanium Dioxide. *J. Mater. Sci.* 1999, 34, 3083-3093.
283. Qi, X. S.; Zhong, W.; Yao, X. J.; Zhang, H.; Ding, Q.; Wu, Q.; Deng, Y.; Au, C. T.; Du, Y. W., Controllable and Large-Scale Synthesis of Metal-Free Carbon Nanofibers and Carbon Nanocoils over Water-Soluble Na_x-K_y, Catalysts. *Carbon* 2012, 50, 646-658.
284. Tanabe, K.; Saito, K., The Conversion of Benzaldehyde into Benzyl Benzoate with Alkaline Earth Metal Oxide Catalysts. *J. Catal.* 1974, 35, 247-255.
285. Zhang, G.; Hattori, H.; Tanabe, K., Aldol Addition of Acetone, Catalyzed by Solid Base Catalysts: Magnesium Oxide, Calcium Oxide, Strontium Oxide, Barium Oxide, Lanthanum Oxide and Zirconium Oxide. *Appl. Catal.* 1988, 36, 189-197.
286. Du, G. X.; Feng, S. A.; Zhao, J. H.; Song, C.; Bai, S. L.; Zhu, Z. P., Particle-Wire-Tube Mechanism for Carbon Nanotube Evolution. *J. Am. Chem. Soc*. 2006, 128, 15405-15414.
287. Tian, N.; Zhou, Z. Y.; Sun, S. G.; Ding, Y.; Wang, Z. L., Synthesis of Tetrahexahedral Platinum Nanocrystals with High-Index Facets and High Electro-Oxidation Activity. *Science* 2007, 316, 732-735.
288. Geelhaar, L.; Temko, Y.; Marquez, J.; Kratzer, P.; Jacobi, K., Surface Structure of Gallium Arsenide (2511). *Phys. Rev. B* 2002, 65, 155308.
289. Terrones, H.; Terrones, M.; Hernandez, E.; Grobert, N.; Charlier, J. C.; Ajayan,

P. M., New Metallic Allotropes of Planar and Tubular Carbon. *Phys. Rev. Lett.* 2000, 84, 1716-1719.
290. Chen, X. Q.; Zhang, S. L.; Dikin, D. A.; Ding, W. Q.; Ruoff, R. S.; Pan, L. J.; Nakayama, Y., Mechanics of a Carbon Nanocoil. *Nano Lett.* 2003, 3, 1299-1304.
291. Castrucci, P.; Scarselli, M.; De Crescenzi, M.; El Khakani, M. A.; Rosei, F.; Braidy, N.; Yi, J. H., Effect of Coiling on the Electronic Properties Along Single-Wall Carbon Nanotubes. *Appl. Phys. Lett.* 2004, 85, 3857-3859.
292. Motojima, S.; Chen, X.; Yang, S.; Hasegawa, M., Properties and Potential Applications of Carbon Microcoils/Nanocoils. *Diamond Relat. Mater.* 2004, 13, 1989-1992.
293. Tang, N. J.; Wen, J. F.; Zhang, Y.; Liu, F. X.; Lin, K. J.; Du, Y. W., Helical Carbon Nanotubes: Catalytic Particle Size-Dependent Growth and Magnetic Properties. *Acs Nano* 2010, 4, 241-250.
294. Furuya, Y.; Hashishin, T.; Iwanaga, H.; Motojima, S.; Hishikawa, Y., Interaction of Hydrogen with Carbon Coils at Low Temperature. *Carbon* 2004, 42, 331-335.
295. Valles, C.; Perez-Mendoza, M.; Castell, P.; Martinez, M. T.; Maser, W. K.; Benito, A. M., Towards Helical and Y-Shaped Carbon Nanotubes: The Role of Sulfur in Cvd Processes. *Nanotechnology* 2006, 17, 4292-4299.
296. Hanus, M. J.; Harris, A. T., Synthesis of Twisted Carbon Fibres Comprised of Four Intertwined Helical Strands. *Carbon* 2010, 48, 2989-2992.
297. Motojima, S.; Hasegawa, I.; Kagiya, S.; Momiyama, M.; Kawaguchi, M.; Iwanaga, H., Preparation of Coiled Carbon-Fibers by Pyrolysis of Acetylene Using a Ni Catalyst and Sulfur or Phosphorus Compound Impurity. *Appl. Phys. Lett.* 1993, 62, 2322-2323.
298. Motojima, S.; Asakura, S.; Kasemura, T.; Takeuchi, S.; Iwanaga, H., Catalytic Effects of Metal Carbides, Oxides and Ni Single Crystal on the Vapor Growth of Micro-Coiled Carbon Fibers. *Carbon* 1996, 34, 289-296.
299. Chang, N. K.; Chang, S. H., High-Yield Synthesis of Carbon Nanocoils on Stainless Steel. *Carbon* 2008, 46, 1106-1109.
300. Tang, N. J.; Zhong, W.; Au, C. T.; Gedanken, A.; Yang, Y.; Du, Y. W., Large-Scale Synthesis, Annealing, Purification, and Magnetic Properties of Crystalline Helical Carbon Nanotubes with Symmetrical Structures. *Adv. Funct. Mater.* 2007, 17, 1542-1550.
301. Qi, X. S.; Zhong, W.; Deng, Y.; Au, C. T.; Du, Y. W., Synthesis of Helical Carbon Nanotubes, Worm-Like Carbon Nanotubes and Nanocoils at 450 Degrees C and Their Magnetic Properties. *Carbon* 2010, 48, 365-376.
302. Qi, X. S.; Xu, M. H.; Zhong, W.; Ye, X. J.; Deng, Y.; An, C. T.; Jin, C. Q.; Du, Y. W., Magnetic Properties and Large-Scale Synthesis of Novel Carbon Nanocomposites Via Benzene Decomposition over Ni Nanoparticles. *J. Phys. Chem. C* 2009, 113, 2267-2272.
303. Li, D. W.; Pan, L. J., Growth of Carbon Nanocoils Using Fe-Sn-O Catalyst Film Prepared by a Spin-Coating Method. *J. Mater. Res.* 2011, 26, 2024-2032.

304. Yang, S.; Chen, X.; Katsuno, T.; Motojima, S., Controllable Synthesis of Carbon Microcoils/Nanocoils by Catalysts Supported on Ceramics Using Catalyzed Chemical Vapor Deposition Process. *Mater. Res. Bull.* 2007, 42, 465-473.
305. Yang, S. M.; Ozeki, I.; Chen, X.; Katsuno, T.; Motojima, S., Preparation of Single-Helix Carbon Microcoils by Catalytic Cvd Process. *Thin Solid Films* 2008, 516, 718-721.
306. Zhang, M.; Nakayama, Y.; Pan, L. J., Synthesis of Carbon Tubule Nanocoils in High Yield Using Iron-Coated Indium Tin Oxide as Catalyst. *Jpn. J. Appl. Phys. Part 2 - Lett.* 2000, 39, L1242-L1244.
307. Fonseca, A.; Hernadi, K.; Piedigrosso, P.; Colomer, J. F.; Mukhopadhyay, K.; Doome, R.; Lazarescu, S.; Biro, L. P.; Lambin, P.; Thiry, P. A.; Bernaerts, D.; Nagy, J. B., Synthesis of Single- and Multi-Wall Carbon Nanotubes over Supported Catalysts. *Appl. Phys. A-Mater.* 1998, 67, 11-22.
308. Wang, X. H.; Hu, Z.; Wu, Q.; Chen, X.; Chen, Y., Synthesis of Multi-Walled Carbon Nanotubes by Microwave Plasma-Enhanced Chemical Vapor Deposition. *Thin Solid Films* 2001, 390, 130-133.
309. Yang, S.; Chen, X.; Kusunoki, M.; Yamamoto, K.; Iwanaga, H.; Motojima, S., Microstructure and Microscopic Deposition Mechanism of Twist-Shaped Carbon Nanocoils Based on the Observation of Helical Nanoparticles on the Growth Tips. *Carbon* 2005, 43, 916-922.
310. Takikawa, H.; Yatsuki, M.; Miyano, R.; Nagayama, M.; Sakakibara, T.; Itoh, S.; Ando, Y., Amorphous Carbon Fibrilliform Nanomaterials Prepared by Chemical Vapor Deposition. *Jpn. J. Appl. Phys. Part 1 - Regul. Pap. Short Notes Rev. Pap.* 2000, 39, 5177-5179.
311. Zhou, Y. C.; Dong, H. Y.; Wang, X. H.; Yan, C. K., Preparation of Tin Titanium Carbide by Solid-Liquid Reaction Synthesis and Simultaneous Densification Method. *Mater. Res. Innov.* 2002, 6, 219-225.
312. Dai, X. J.; Skourtis, C., Substrate Characteristics beneath Self-Aligned Carbon-Nanotube Forests. *J. Appl. Phys.* 2008, 103, 124305.
313. Lin, J. H.; Chen, C. S.; Rummeli, M. H.; Bachmatiuk, A.; Zeng, Z. Y.; Ma, H. L.; Buchner, B.; Chen, H. W., Growth of Carbon Nanotubes Catalyzed by Defect-Rich Graphite Surfaces. *Chem. Mater.* 2011, 23, 1637-1639.
314. Nel, A.; Xia, T.; Madler, L.; Li, N., Toxic Potential of Materials at the Nanolevel. *Science* 2006, 311, 622-627.
315. Esconjauregui, S.; Fouquet, M.; Bayer, B. C.; Ducati, C.; Smajda, R.; Hofmann, S.; Robertson, J., Growth of Ultrahigh Density Vertically Aligned Carbon Nanotube Forests for Interconnects. *Acs Nano* 2010, 4, 7431-7436.
316. Medina, H.; Lin, Y. C.; Jin, C. H.; Lu, C. C.; Yeh, C. H.; Huang, K. P.; Suenaga, K.; Robertson, J.; Chiu, P. W., Metal-Free Growth of Nanographene on Silicon Oxides for Transparent Conducting Applications. *Adv. Funct. Mater.* 2012, 22, 2123-2128.
317. Song, H. J.; Son, M.; Park, C.; Lim, H.; Levendorf, M. P.; Tsen, A. W.; Park, J.; Choi, H. C., Large Scale Metal-Free Synthesis of Graphene on Sapphire and

Transfer-Free Device Fabrication. *Nanoscale* 2012, 4, 3050-3054.